TUM

Technische Universität München

TUM School of Engineering and Design

Electrochemical Impedance Spectroscopy and Power Line Communications for Automotive Battery Management Systems

Thomas F. Landinger, M. Eng.

Abstract

Electromobility is gaining increasing momentum around the world. On the way to environment-friendly transportation, enhancing driving range and safety become critical tasks for modern automotive battery management systems (BMSs). As current BMSs rely on a limited number of measurement quantities, namely voltage, current, and temperature, prospective high performance and safety requirements are tough to meet. Therefore, this thesis proposes online Electrochemical Impedance Spectroscopy (EIS) as additional in-situ sensing technique for automotive traction batteries. EIS is a widely used technique for electrochemical system characterization and offers numerous possibilities for nondestructive battery state estimation, this way advancing smart BMS and smart cells. To demonstrate the capabilities of EIS, fundamental dynamic properties of lithium-ion (Li-ion) batteries are summarized and their characterization using EIS is outlined. For promoting the adoption of online EIS in future BMSs, state-of-the-art BMS functionalities are summarized and implementation options for online EIS are presented, considering possible interference scenarios.

High voltage (HV) traction batteries consist of hundreds of single Li-ion cells, whose monitoring demands for extensive data transfer and communications bus wiring throughout the battery pack. To counteract the increase of the wiring harness, this thesis proposes alternative communications concepts for BMSs without dedicated wires and emphasizes the concept of HV power line communications (PLC), which utilizes the existing HV power train infrastructure for communications. As HV PLC for in-battery communications is an emerging research area, this thesis discusses possible implementation options within automotive traction batteries, presents a proof of concept, investigates the coexistence between HV PLC and online EIS, and introduces a physical-based modeling approach of the HV battery power line network, which is used for simulations on the PLC channel transfer characteristics.

Due to demanding requirements on data rate, robustness, and electromagnetic compatibility, the frequency band of the PLC has to be allocated in the megahertz range. Therefore, PLC system design and channel modeling requires knowledge about the high frequency (HF) characteristics of Li-ion batteries, which are not sufficiently studied in existing literature due to frequency limitations of conventional EIS equipment. For this reason, this thesis develops a Li-ion battery characterization methodology for high frequencies up to 300 MHz, enabling HF impedance spectroscopy of various Li-ion cell types at different cell states. Using a physical-based modeling approach, various electrochemical and electrophysical battery processes relevant at high frequencies are determined such as the ionic shunt effect, the skin effect and other resistive-inductive effects. Furthermore, electromagnetic coupling mechanisms among cells within a battery pack are studied and their influence on the PLC channel transfer characteristics is evaluated.

The obtained findings on the HF characteristics of Li-ion cells facilitate assessing the influence of cell design and cell state on fast battery dynamics. The developed battery modeling approach can be reused for the simulation of further highly dynamic battery applications such as power converters and motor controllers. Moreover, the PLC proof of concept and the developed simulation environment can serve as a basis for future PLC system designs.

Kurzfassung

Die Elektromobilität gewinnt weltweit sichtlich an Dynamik. Ein umweltfreundliches Transportwesen stellt hohe Anforderung an Reichweite und Sicherheit moderner Batteriemanagementsysteme (BMSs). Da sich die Messgrößen aktueller BMSs auf Spannung, Strom und Temperatur beschränken, werden steigende Anforderungen an die Leistungsfähigkeit und Sicherheit zur Herausforderung. Die elektrochemische Impedanzspektroskopie (EIS) als weitverbreitete Messmethode zur Charakterisierung von Lithium-Ionen-Batterien kann zur erweiterten in-situ Zustandsbestimmung in zukünftigen BMSs verwendet werden und den Weg zur intelligenten Batteriezelle (engl. *Smart Cell*) ebnen. Dazu werden in dieser Arbeit fundamentale dynamische Eigenschaften von Lithium-Ionen-Batterien aufgezeigt und deren Charakterisierung mittels EIS veranschaulicht. Um den Einsatz von EIS in zukünftigen BMS-Generationen zu fördern, werden gegenwärtige BMS-Funktionalitäten zusammengefasst und ein Überblick der EIS-Implementierungsmöglichkeiten und der zu erwartenden Störszenarien gegeben.

Hochvolt- (HV-) Antriebsbatterien bestehen aus hunderten Einzelzellen, deren Überwachung große Datenmengen und eine weitläufige Datenbusverdrahtung innerhalb des Batteriepacks erfordert. Um dem Verdrahtungsaufwand entgegenzuwirken, werden in dieser Arbeit alternative Kommunikationskonzepte mit dem Fokus auf Hochvolt-Powerline-Kommunikation (HV-PLC) diskutiert. HV-PLC-Systeme verwenden zur Datenübertragung den vorhandenen HV-Antriebsstrang, wodurch der existierende verdrahtete Datenbus eingespart werden kann. Da die Thematik der HV-PLC für Intra-Batteriekommunikation größtenteils noch unerforscht ist, werden in dieser Arbeit mögliche Implementierungen diskutiert und die Machbarkeit nachgewiesen (engl. *Proof of Concept*). Darüber hinaus wird die Koexistenz zwischen HV-PLC und EIS untersucht und ein physikalisch motivierter Modellansatz der Hochvoltbatterie entwickelt, um die Kanalcharakteristik der PLC zu simulieren.

Aufgrund der hohen Anforderungen an die Datenrate, Robustheit und elektromagnetische Verträglichkeit muss das Frequenzband der PLC im Megahertz-Bereich allokiert werden. Daher erfordern der PLC-Systementwurf und die Kanalmodellierung fundierte Kenntnisse des Hochfrequenz- (HF-) Verhaltens von Lithium-Ionen-Zellen, welches aufgrund von Frequenzlimitierung bei EIS-Geräten bisher nicht ausreichend erforscht ist. In dieser Arbeit wir daher eine Messmethodik zur Charakterisierung von Lithium-Ionen-Zellen für hohe Frequenzen bis zu 300 MHz entwickelt, die eine HF-Impedanzspektroskopie verschiedener Zelltypen bei verschiedenen Zellzuständen ermöglicht. Über einen physikalisch motivierten Modellansatz werden HF-relevante elektrochemische und elektrophysikalische Effekte wie der Ionic-Shunt-Effekt, der Skin-Effekt und weitere resistiv-induktive Verlustprozesse erfasst. Zusätzlich werden elektromagnetische Verkopplungen zwischen benachbarten Batteriezellen und deren Einfluss auf die PLC-Übertragungscharakteristik untersucht.

Die gewonnenen Erkenntnisse zum HF-Verhalten von Lithium-Ionen-Batterien können genutzt werden, um den Einfluss von Zelldesign und -zustand auf das dynamische Zellverhalten zu beurteilen. Der eingeführte Modellansatz kann zur Simulation weiterer hochdynamischer Batterieanwendungen wie beispielsweise Leistungswandler und Motorenregler verwendet werden. Darüber hinaus kann der präsentierte Machbarkeitsnachweis der PLC für zukünftige Systementwürfe wiederverwendet werden.

Acknowledgement

List of Publications

Peer-Reviewed Journal Paper Contributions (Lead Author)

(1) T. F. Landinger, G. Schwarzberger, and A. Jossen. "A Physical-Based High-Frequency Model of Cylindrical Lithium-Ion Batteries for Time Domain Simulation". In: *IEEE Transactions on Electromagnetic Compatibility*, vol. 62, no. 4 (2020), pp. 1524–1533. DOI: 10.1109/TEMC.2020.2996414.

(2) T. F. Landinger, G. Schwarzberger, and A. Jossen. "High frequency impedance characteristics of cylindrical lithium-ion cells: Physical-based modeling of cell state and cell design dependencies". In: *Journal of Power Sources*, vol. 488, 229463 (2021). DOI: 10.1016/j.jpowsour.2021.229463.

(3) T. F. Landinger, G. Schwarzberger, G. Hofer, M. Rose, and A. Jossen. "Power Line Communications for Automotive High Voltage Battery Systems: Channel Modeling and Coexistence Study with Battery Monitoring". In: *Energies*, vol. 14, no. 7, 1851 (2021). DOI: 10.3390/en14071851.

Peer-Reviewed Conference Paper Contributions (Lead Author)

(1) T. F. Landinger, G. Schwarzberger, and A. Jossen. "A Novel Method for High Frequency Battery Impedance Measurements". In: *2019 IEEE International Symposium on Electromagnetic Compatibility, Signal & Power Integrity (EMC+SIPI)*. New Orleans, LA, USA, 2019, pp. 106–110. ISBN: 9781538691991. DOI: 10.1109/ISEMC.2019.8825315.

(2) T. F. Landinger, G. Schwarzberger, M. Rose, S. Dollhaeubl, G. Hofer, A. Pake Talei, and A. Jossen. "Power Line Communications in Automotive Traction Batteries: A Proof of Concept". In: *2020 IEEE International Symposium on Power Line Communications and its Applications (ISPLC)*. Málaga, Spain, 2020, pp. 1–5. ISBN: 9781728148168. DOI: 10.1109/ISPLC48789.2020.9115412.

Peer-Reviewed Conference Paper Contributions (Co-Author)

(1) H. Hackl, M. Ibel, T. F. Landinger, D. J. Pommerenke, and B. Auinger. "Li-Ion Cell Impedance Measurement Using Open/Short/Load Compensation for De-Embedding". In: *2021 IEEE International Joint EMC/SI/PI and EMC Europe Symposium*. 2021, pp. 190–195. ISBN: 9781665448888. DOI: 10.1109/EMC/SI/PI/EMCEurope52599.2021.9559223.

Online Article Contributions

(1) T. F. Landinger. "Battery Characterization for High Speed Signaling". In: *Signal Integrity Journal* (2019). Accessed on September 28, 2021. [Online]. URL: https://www.signalintegrityjournal.com/articles/1432-battery-characterization-for-high-speed-signaling.

Conference Contributions

(1) T. F. Landinger, S. Mikl, F. Rasras, G. Hofer, G. Schwarzberger, M. Rose, and A. Jossen. "Interference Scenarios during Single Cell Impedance Measurements in Automotive Battery Packs". In: *Kraftwerk Batterie 2021*. Accessed on September 28, 2021. [Online]. URL: https://battery-power.eu/wp-content/uploads/2021/04/Landinger-2021-Interference-Scenarios-during-Single-Cell-Impedance-Measurements.pdf.

List of Contents

List of Abbreviations

2-ASK .... binary amplitude shift keying

3-D .... three-dimensional

ADC .... analog-to-digital converter

AC .... alternating current

AWGN .... additive white Gaussian noise

BB .... broadband

BER .... bit error rate

BEV .... battery electric vehicle

BLE .... Bluetooth low energy

BMS .... battery management system

BMU .... battery management unit

BPLN .... battery power line network

CAN .... control area network

CEI .... cathode-electrolyte interphase

CENELEC .... Comité Européen de Normalisation Électrotechnique

CID .... current interrupt device

CISPR .... Comité International Spécial des Perturbations Radioélectriques

CMC .... cell monitoring circuit

CPE .... constant phase element

CT .... computed tomography

DC .... direct current

DSP .... digital signal processing

EDL .... electric double layer

EEC .... equivalent electrical circuit

EIS .... electrochemical impedance spectroscopy

EM .... electromagnetic

EMC .... electromagnetic compatibility

EMI .... electromagnetic interference

EU .... European Union

EV .... electric vehicle

FFT .... fast Fourier transform

FLW .... finite length Warburg

FSW .... finite space Warburg

GEIS .... galvanostatic electrochemical impedance spectroscopy

GND .... ground

HD-PLC .... high definition power line communication

HF .... high frequency

HV .... high voltage

IC	integrated circuit
IEEE	Institute of Electrical and Electronics Engineers
IEA	International Energy Agency
IGBT	insulated-gate bipolar transistor
IoT	internet of things
ISM	industrial, scientific and medical
ISO	International Organization for Standardization
LAN	local area network
Li-ion	lithium-ion
LV	low voltage
MoB/ MoT	master on bottom/ top
NB	narrowband
OCV	open-circuit voltage
OPERA	Open PLC European Research Alliance
OSL	open/ short/ load
PCB	printed circuit board
PEIS	potentiostatic electrochemical impedance spectroscopy
PHEV	plug-in hybrid electric vehicle
PLC	power line communications
PRBS	pseudo random bit sequence
PRIME	PoweRline Intelligent Metering Evolution
PTC	positive temperature coefficient
RFID	radio-frequency identification
RX	receiver
SEI	solid-electrolyte interphase
SMD	surface-mounted device
SNR	signal-to-noise ratio
SOA	safe operating area
SOC	state of charge
SOH	state of health
S-parameter	scattering parameter
TX	transmitter
UART	universal asynchronous receiver transmitter
UNB	ultra-narrowband
UPA	Universal Powerline Association
VNA	vector network analyzer
WBMS	wireless battery management system
Wi-Fi	wireless fidelity

List of Symbols

The following symbols are listed as defined within the main part of this thesis and may vary from each individual paper included in the thesis due to specific regulations set by the publishers or other unique conditions within the papers. Therefore, symbols used in the papers are defined once again individually within each paper.

Constants

F	Faraday constant 96,485 C mol^{-1}	
R	Universal gas constant 8.314 J mol^{-1} K^{-1}	

Greek Symbols

α	Symmetry factor	
Δ	Difference operator	
η	Cell overvoltage/ polarization	V
ϑ	Celsius temperature	°C
μ_i	Chemical potential	kJ $\cdot$ mol^{-1}
μ_i^0	Chemical standard potential	kJ $\cdot$ mol^{-1}
ν_i	Stoichiometric coefficients	
τ	Time constant	s
φ	Phase angle	rad
φ_0	Electric potential	V
$\Delta\varphi_{00}$	Electric standard potential	V
ω	Angular frequency	rad $\cdot$ s^{-1}

Latin Symbols

A_0	Capacitance parameter	A $\cdot$ s^n $\cdot$ V^{-1}
a_i	Thermodynamic activity	
C	Capacitance	F
c_i	Concentration	mol $\cdot$ dm^{-3}
D_i	Diffusion coefficient	cm^2 $\cdot$ s^{-1}
f	Frequency	Hz
$I; i(t)$	Direct current; time-varying current	A
$I(j\omega)$	Fourier transform of current	A $\cdot$ s^{-1}
$\hat{i}$	Current amplitude	A
j_0	Exchange current density	mA $\cdot$ cm^{-2}
$\vec{j}_i$	Diffusion flux density	mol $\cdot$ m^{-2} $\cdot$ s^{-1}
j_n	Faradaic current density	mA $\cdot$ cm^{-2}
L	Inductance	H
l_i	Diffusion length	m
n	Exponent of constant phase element	
n_i	Number of electrons	

R	Resistance	Ω
T	Absolute temperature	K
t	Time	s
$V;\ v(t)$	Direct current voltage; time-varying voltage	V
V_0	Cell equilibrium voltage	V
$V(j\omega)$	Fourier transform of voltage	$\text{V} \cdot \text{s}^{-1}$
$\hat{v}$	Voltage amplitude	V
W	Warburg element	
Z	Impedance	$\Omega + \text{j}\Omega$

Letter-like Symbols

$\mathscr{F}$	Fourier transform operator
$\mathfrak{I}$	Imaginary part operator
$\text{Li}+$	Lithium ion
$\mathfrak{R}$	Real part operator
∇	Gradient

Subscripts

0	Standard; certain value of variable
bat	Battery
C	Coupling
c	Concentration
cc	Cell-to-cell
ct	Charge transfer
$D0$	Limited diffusion
dc ; DC	Direct current
ddl	Diffuse double layer
dl	Double layer
FL	Finite length
FS	Finite space
i	Chemical species
L	Load
m	Master
N	Total number of battery cells
n	Faradaic current; battery cell number
ox	Oxidation
$rect$	Rectangular
red	Reduction
S	Shunt
s	Slave
sdl	Static Helmholtz layer
sei	Solid-electrolyte interphase
sin	Sinusoidal
W	Warburg
Δt	Time interval
Ω	Ohmic

1 Introduction

"The global electric vehicle fleet expanded significantly over the last decade, underpinned by supportive policies and technology advances" – proclaimed by the International Energy Agency (IEA) in 2020 [1], this statement concisely summarizes the ongoing journey towards environment-friendly mobility. As visible in Figure 1, the worldwide electric car stock referring to battery electric and plug-in hybrid electric vehicles (BEVs, PHEVs) surpassed 7.2 million in 2019, which is a year-to-year increase of 40% [1].

In 2018, the European Commission presented its strategic long-term vision for a prosperous, modern, competitive and climate neutral economy by 2050 [2]. The strategy proposes pathways for a long-term reduction of European Union (EU) greenhouse gas emissions to achieve the Paris Agreement temperature objectives, ratified by 181 parties in 2015, to hold global temperature increase well below 2 °C [3]. As the transport sector is responsible for a quarter of greenhouse gas emissions in the EU, the spread of low and zero emission vehicles is pushed by regulatory measures and adequate financial instruments [2]. It has been demonstrated that financial government incentives significantly boost the rate of diffusion of BEVs on the market [4], powering a climate-neutral economy for the long term.
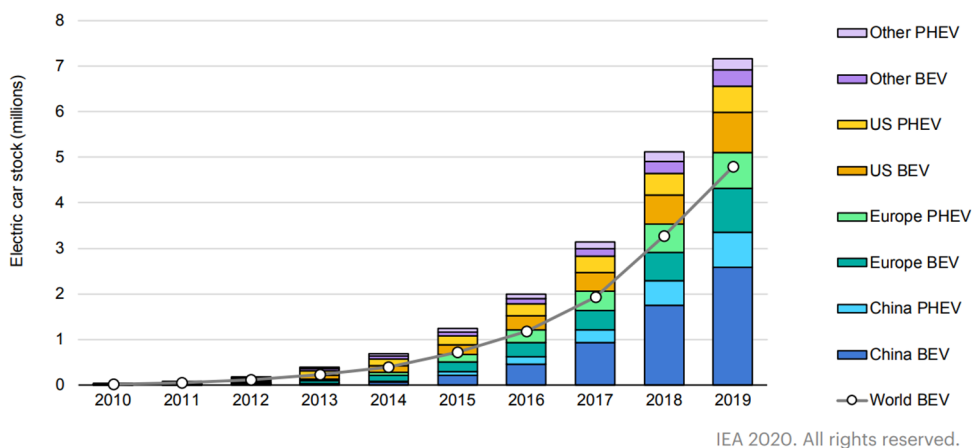
Figure 1: Global electric car stock, 2010–2019 [1]. © 2020 IEA.

Despite strong sales growth in the past decade, automotive market share of electric vehicles (EVs) still represents a small portion below 1% worldwide [1]. Limited driving range, long charging times, battery safety, sustainability, and purchase price are among the main concerns of motorists [5]. In order to further propagate electromobility globally, the automotive industry needs to address customer concerns by technological advances in next-generation EVs.

One of the most relevant components of EVs is their energy storage system, which is commonly based on electrochemical batteries [6]. The Lithium-ion (Li-ion) battery technology continues to spread rapidly among multitudinous applications and is also the state-of-the-art technology in today's EVs due to its high gravimetric and volumetric energy and power density, long lifespan, high voltage, and high efficiency [7, 8]. However, existing Li-ion traction batteries are reaching their performance limits,

intensifying the aforementioned concerns. In 2018 therefore, the large-scale, long-term European research initiative BATTERY 2030+ represented its vision of inventing the sustainable batteries of the future, to enable Europe to reach the goals of a climate-neutral society [9]. The vision includes the incorporation of new smart sensing technologies and self-healing functionalities into battery cells to ultimately create the "smart cell" by 2030.

1.1 Towards Smart Cells in Automotive Batteries

Li-ion batteries must be kept within their safe operating area (SOA), which is restricted by temperature, voltage, and current windows defined by the cell manufacturer [10]. Leaving the SOA, for example, by overvoltage (overcharge) or undervoltage (undercharge), the performance rapidly degrades and safety issues might occur such as thermal runaway, leading even to physical damages, explosions, or fires [8, 10, 11]. To avoid these issues, a battery management system (BMS) is inevitable to ensure a safe, efficient, and reliable operation of each individual cell [12]. Given the fact that the BMS must fulfill many tasks such as battery state estimation [6], (dis-)charge controlling, cell balancing [13], thermal management [14], and fault diagnosis [15], many research studies have been conducted on BMS applications [10, 16]. Large-format traction batteries in EVs are built of hundreds of single Li-ion cells grouped into smaller battery modules to ensure a long-lasting energy system with high power capability [17, 18]. To speed up charging and limit the power dissipation within the automotive power train, the system voltage is typically increased to 400 V or up to 800 V by connecting cells in series [19]. Due to the high voltage and high current requirements together with rising safety and reliability expectations, BMSs for EVs are complex systems containing sophisticated sense and control subsystems [20]. In nowadays BMSs, most widely a modularized architecture is used, where the number of monitoring channels of each subsystem is in accordance with the number of cells in a module [21].

However, current BMSs rely on a limited number of measurement quantities, namely cell terminal voltage, battery module voltage, battery pack main voltage and current, and local surface temperature [8, 10, 22]. Typically, state of charge (SOC) estimation requires high accuracy of cell voltage measurements in the range of 1 to 10 mV [10], which is especially challenging in a modularized or centralized BMS topology due to long sensing leads, which are susceptible to ohmic voltage drops and electromagnetic interference (EMI) [23]. Depending on the measurement precision, the remaining uncertainty in SOC estimation has to be considered in the BMS monitoring by additional safety margins, diminishing the SOA and limiting the available battery power [24].

Another key issue in state-of-the-art BMSs is the temperature monitoring on cell level. The number of temperature sensors implemented in large-format batteries is often limited to less than twenty sensors, leading to an average of only two temperature sensors per module [25, 26]. Beside implementation challenges such as positioning, thermal contacting, and wiring, the temperature on cell level can only be estimated by the usage of local surface temperature sensing combined with thermal modeling [25, 27]. For stable thermal dynamics, this approach is feasible, however, estimation errors strongly increase during transient disturbances [25]. Especially for highly dynamic applications such as fast charging, accurate temperature detection is essential to estimate and reduce the risk for battery failures, for example, caused by lithium plating [28]. However, due to heat transfer delay from

the cell's core to the surface (up to 10 °C temperature lag [29] or time delays of five minutes [30] for cylindrical Li-ion cells), this is not feasible in real-time, thus demanding additional safety margins that limit charging rates. Nevertheless, local hotspots need to be detected as quickly as possible because they can lead to thermal runaway, which calls for embedded temperature sensors or alternative fast temperature detection methods [31].

Summarizing, battery pack performance substantially depends on the accuracy of the BMS sensing and the knowledge of the SOA of each individual Li-ion cell within the pack. With current BMS implementations, a majority of the system capabilities are underutilized, degrading battery performance and efficiency [8]. From this perspective, next-generation BMSs need to solve shortage of measurement quantities and their validity to meet challenging global technical regulations, for example, passenger warning five minutes prior to the presence of a hazardous situation inside the passenger compartment such as fire, explosion, or smoke [32]. Beside the possible integration of sensors into Li-ion cells, also novel sensing methods are considered for technological progress of BMSs [8, 18, 31], which is in accordance with the BATTERY 2030+ Roadmap of Europe to accomplish smart cells by new sensing technologies [9]. On the way to smart single cells, many other benefits come along such as high system modularity and flexibility, strong fault tolerance by self-reconfigurable battery packs, and enhanced cycle life management, all together enabling a smart "plug-and-play" BMS [8].

1.2 Scope of this Thesis

Within the scope of this thesis, the implementation of online Electrochemical Impedance Spectroscopy (EIS) combined with High Voltage Power Line Communications (HV PLC) for automotive traction batteries is proposed as a promising strategy towards a smart and flexible plug-and-play BMS, which eventually enhances overall performance, safety, and the widespread adoption of EVs.

A very promising smart sensing technique is seen in Electrochemical Impedance Spectroscopy (EIS), which is used for battery impedance evaluation over frequency [9]. Great achievements have been made in characterizing and modeling the dynamic behavior of Li-ion battery cells using EIS in the laboratory environment as well as in onboard diagnosis, where it is often referred to as "online EIS" [18, 33–37]. EIS is a nondestructive measurement method, which can be used for in-situ battery state estimation, making it a powerful and interesting tool for next-generation automotive BMSs. The quantity of publications available utilizing EIS for SOC [38–41], state of health (SOH) [40, 42–44], and temperature [38, 39, 45–47] estimation demonstrates its high potential to enable smart cells and improve future BMSs in terms of safety and performance. However, EIS is still predominantly applied at the benchtop using cost-intensive calibrated galvanostats, potentiostats, or impedance analyzers [33].

The first goal of this thesis is therefore to point out possible implementation architectures, excitation options, and expected measurement obstacles of online EIS within automotive HV batteries.

A challenging task is seen in the coordination of hundreds of smart cells and the acquisition of measurement data due to the expected strong increase of sensors and real-time data. Although control area network (CAN) bus systems are widely used in today's BMSs [8, 10], its reuse in smart BMSs would strongly increase wiring harness and connector cost without gaining system flexibility. For this reason, efficient battery pack data compression methods are under investigation to reduce communication overhead [8, 48] as well as novel data communications concepts to reduce sensor wiring effort and system complexity [9, 18]. In this context, high voltage (HV) power line communications (PLC) for in-battery communications has been proposed as promising technique for next-generation automotive BMSs to cut wiring cost, reduce size and weight, and increase system flexibility [8, 49]. HV PLC utilizes the existing power connections inside the battery pack and the HV power lines for data transmission by superimposing a modulated communication signal [50]. Using HV PLC for the traction battery, multiple sensors and actuators can be accessed by the BMS without the need of a wired communications bus. With respect to autonomous driving, HV PLC could also be used as redundant communications link for fault indication to increase the safety level [50]. Moreover, PLC can also enable the communication between EVs and the charging infrastructure allowing vehicle-to-grid applications [51, 52]. Compared to wireless communications, the main advantages of PLC are its cost effectiveness – the communications infrastructure is already there in terms of the power line network [52] – and its higher security level offered by wired data transmission [31, 53].

Therefore, within the scope of this thesis, the implementation of online EIS combined with HV PLC for automotive traction batteries is proposed as promising strategy towards a smart and flexible plug-and-play BMS, enhancing overall EV performance and safety. The proposed single-cell-based BMS architecture is illustrated in Figure 2, where each Li-ion cell is equipped with a cell monitoring circuit (CMC) and a communications interface to the central battery management unit (BMU). The traditional sensing of voltage (V), current (I), and temperature (ϑ) is upgraded by online EIS, and
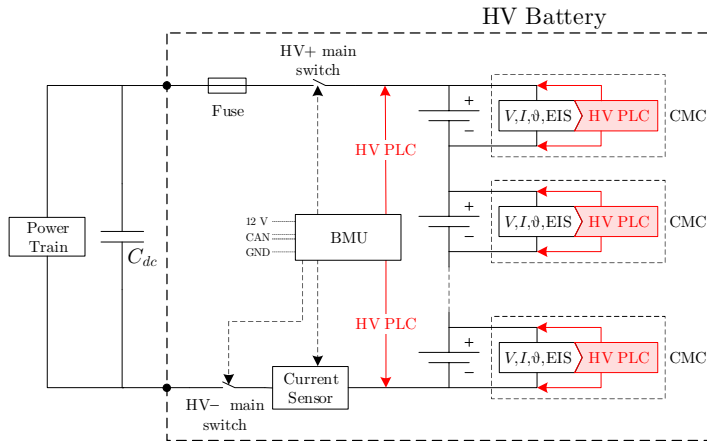
Figure 2: Proposed single-cell-based BMS architecture enabling smart cells by EIS, while saving communications wiring effort by HV PLC. The HV battery supplies the electric power train and the direct current (DC) link capacitor C_{dc}. The BMU is connected to the 12 V on-board power supply and the CAN of the EV. (Based on Ref. [54].)

the communication between CMCs and the BMU is realized by HV PLC. The BMU is responsible for data coordination, fault detection, state estimation, and controlling tasks such as cell voltage equalization and main switch control [22]. It is connected to the 12 V on-board power supply and linked to the central CAN of the EV.

While PLC is already established in smart electricity grids [55] and smart building applications [52], this is not the case for in-vehicle PLC. No dedicated technology for in-vehicle PLC has been developed up to the present and research reports are sparse [56]. In particular, HV PLC for traction batteries is still in an early pre-development stage and has been considered only by a few research groups in the past [31, 57–60]. To date, evaluation boards of PLC for batteries were mostly developed on a laboratory scale under specific low DC voltages using low data rates [31, 61–63]. However, the PLC system intended for communication within a single-cell-based BMS should support high data rates in the range of 2 Mbps [64, 65] to meet high update rates of measurement quantities. For example, the voltage of each cell within the battery pack should be acquired every 10–100 ms [58, 66].

> *The second goal of this thesis is therefore to demonstrate the feasibility of PLC over Li-ion batteries by means of a custom-made PLC modem with high data rates.*

To bring the proof of concept towards a real PLC system for traction batteries, a thorough understanding of the overall PLC channel transfer characteristics is required. Modeling the HV power line channel is essential to predict signal attenuation, select appropriate carrier frequencies, and optimize PLC modem design. Although a few channel models featuring PLC for batteries have been reported previously [57, 58, 60], to the present date, a PLC channel model validated by real PLC signals on Li-ion batteries is missing in literature.

> *The third goal of this thesis is therefore to develop a generic PLC channel model for a Li-ion battery pack validated by real PLC signals, which predicts channel transfer characteristics and facilitates PLC modem design.*

The most crucial component of the HV power line network is the battery pack itself comprising hundreds of single cells. Since PLC target frequencies are in the megahertz range to obtain high data rates [64], it is essential to identify the high frequency (HF) behavior of each battery cell, which is mainly determined by its impedance [57]. For impedance characterization, EIS is mostly used in the battery community due to its accuracy and nondestructive nature [67]. However, most published studies focus on typical EIS frequencies below 10 kHz relevant for electrochemical process identification [68]. Consequently, little work has been reported on the characteristics of Li-ion batteries above the typical EIS frequency range, which is denoted as "HF" in this thesis.

The PLC system design involves not only determining the battery's impedance for high frequencies but also quantifying the influence of cell design and cell state on the impedance. That means, a reliable and stable communication has to be ensured throughout a wide range of environmental conditions, which include ambient temperature, SOC, and different cell types. All of the mentioned conditions have been reported to significantly influence the cell's impedance behavior [39, 69], however, only taking EIS frequencies into consideration.

> *The fourth goal of this thesis is therefore to characterize and model the high frequency characteristics of Li-ion batteries and to quantify the impact of cell design and cell states dependencies on the impedance.*

Irrespective of its application, PLC always employs existing infrastructure optimized for power transfer [50]. Therefore, PLC inherently faces compatibility issues with the coexisting signals present on the power line network. In case of HV PLC for traction batteries, these are DC load currents, impulsive noise generated by the power electronics [70], as well as signals coming from the cell monitoring circuits. Considering the aforementioned monitoring tasks, especially the error-free coexistence between PLC and online EIS measurements is key to the success of the proposed plug-and-play BMS. Measurement data need be sent periodically to the BMU via PLC, while the communication must not interfere with the cell monitoring and vice versa.

> *The fifth and last goal of this thesis is therefore to examine the compatibility of PLC and the coexisting battery monitoring including online EIS.*

1.3 Outline of this Thesis

This thesis is structured according to the previously defined goals. A graphical outline is given by Figure 3 including the paper contributions presented in this thesis. After the introduction, Chapter 2 covers fundamentals on Li-ion batteries, focusing on the impedance-based description of established battery dynamics relevant for frequencies below 10 kHz. Moreover, typical battery impedance characterization methods such as EIS are presented. In Chapter 3, state-of-the-art BMS architectures and monitoring tasks are discussed as well as the concept of online EIS. Regarding BMS data transfer, three different communications concepts – wired, wireless, and power line – are presented and compared with an emphasis on PLC. Chapter 4 aims for characterizing and modeling the HF properties of cylindrical Li-ion battery cells. As little work has been published on this topic, this chapter is meant to advance scientific knowledge on very fast battery dynamics. In a first step, a novel methodology for HF battery impedance measurements is developed since existing techniques are restricted in either frequency or accuracy. As second step, a physical-based HF battery model is proposed, discussing HF-relevant loss processes occurring in Li-ion batteries. The last step includes determining cell design and cell state influences on the HF impedance behavior. Chapter 5 seeks for advancing the state of the art of BMS communications by employing PLC for automotive traction batteries on the way to a smart plug-and-play BMS. Therefore, it begins with a feasibility study proving the concept of PLC for a small-scale battery pack. Subsequently, using the findings of Chapter 4, a channel model of the battery power line network is developed and used for predicting the PLC channel transfer characteristics in a master-to-slave communication. Bringing EIS and PLC together, a final study investigates compatibility aspects and possible interference scenarios, giving suggestions for an error-free coexistence within the BMS. Finally, Chapter 6 concludes the thesis with a summary of the overall findings and an outlook.
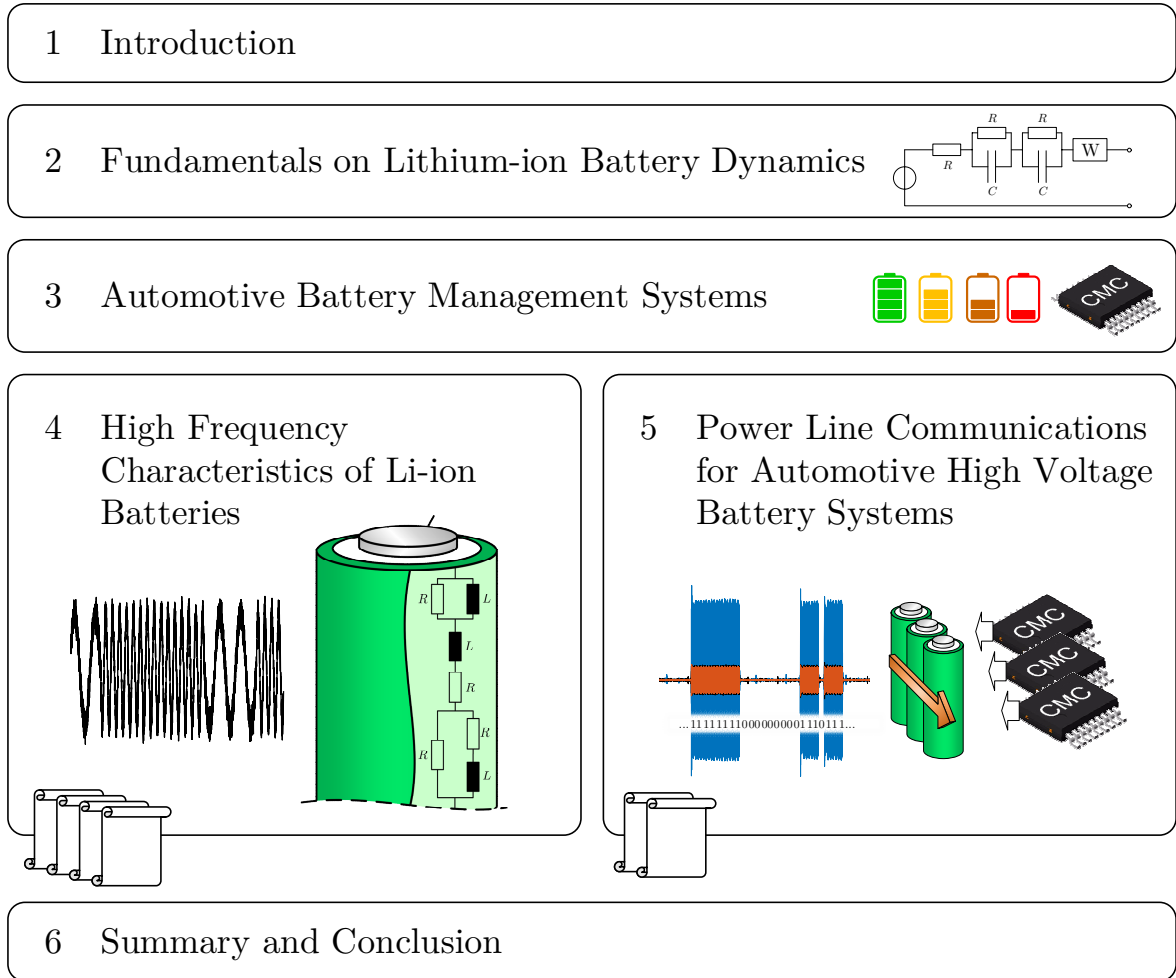
Figure 3: Graphical outline of this thesis including the presented paper contributions.

2 Fundamentals on Lithium-ion Battery Dynamics

This chapter gives insights into the fundamental dynamic properties of Li-ion batteries and how they can be modeled by impedance elements. It forms the basis for the following chapters, especially for Chapter 4 that focuses on the high frequency cell characteristics. Subsequently, commonly used battery impedance characterization methods are discussed.

The terminal voltage of a Li-ion battery under load differs from its equilibrium voltage due to a number of overpotentials caused by electrochemical and electrophysical effects occurring inside the battery [71]. As the overpotentials induce additional impedance seen at the terminals, the underlying effects are also called loss processes [69]. Figure 4 gives an overview of the electrochemical (orange colored) and electrophysical (blue colored) loss processes of a Li-ion battery. Each loss process can be classified according to a certain relaxation time, ranging from years over milliseconds to an instant in case of the ohmic resistance of the battery.

Fast time constants below 1 ms can be assigned mainly to electrophysical effects, which are of an inductive or resistive-inductive nature [69, 72]. According to Ohm's law, the voltage across an ohmic resistance follows the applied current without any time delay, that is, the time constant is zero. For this reason, the ohmic resistance is drawn vertically on the left-hand side of Figure 4. Purely external inductive effects caused by the current path geometry inside the battery [74] follow a current $i(t)$ with an instantaneous voltage response $v(t) = \frac{di(t)}{dt}$, having also a time constant of zero. As the apparent impedance Z of an inductance L depends on frequency ($Z = j2\pi f L$), the impedance contribution of the external inductance dominates the HF behavior of the cell and disappears for frequencies below
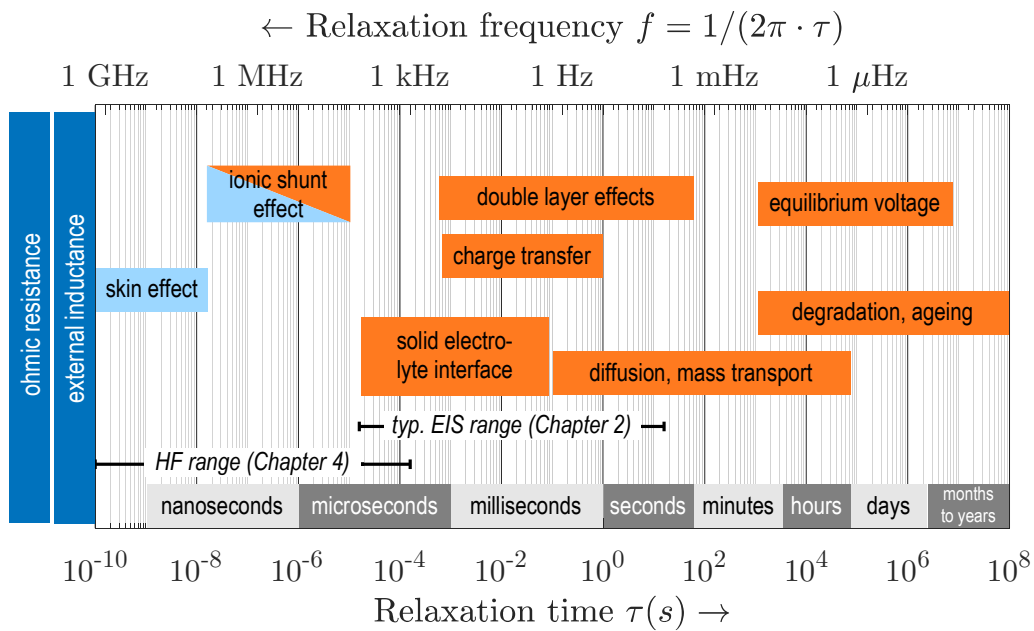
Figure 4: Electrochemical (orange) and electrophysical loss processes (blue, light blue) occurring in a Li-ion battery classified by their relaxation time ranges. For comparison, the corresponding relaxation frequency is given as second abscissa. (Based on Refs. [68, 74–76].)

1 kHz. The skin effect accounts for the uneven current distribution inside an electric conductor for fast time-varying currents [75]. The wound-up geometry of the electrode layers can be described by the ionic shunt effect, which is the only effect influenced by both electrochemical and electrophysical losses [73].

Beside fast electrophysical effects, typically slower electrochemical effects such as electric double layer capacitance, charge transfer resistance, and reactions at the solid-electrolyte interphase (SEI) can be observed, which exhibit time constants mainly in the milliseconds range up to half a minute [68, 74–76]. Mass transport effects show larger relaxation time constants starting at approximately 0.1 s and reaching several hours [74, 75]. The equilibrium voltage is subject to even slower changes caused by SOC variations through cyclic conditioning or self-discharge [74, 75]. Cell degradation and aging become typically obvious after several hours to days and can be monitored throughout years.

As pointed out in the introduction, one aim of this thesis is to illuminate very fast battery dynamics that are typically not covered by the battery research community. In the following section, therefore, only established dynamic battery characteristics are presented that are identifiable by EIS in the typical frequency range between 10 mHz and 10 kHz [68] as indicated in Figure 4. High frequency characteristics above 10 kHz are discussed in detail in Chapter 4.

2.1 Impedance-based Description of Battery Dynamics

Originally introduced by Oliver Heaviside in 1892, the term "impedance" refers to the ratio of the amplitude of a voltage to that of a current when their variations are simple-harmonic [77]. Accordingly, the impedance Z is determined as transfer function in the frequency domain by

$$Z(j\omega) = \frac{V(j\omega)}{I(j\omega)} = \frac{\mathcal{F}\{v(t)\}(j\omega)}{\mathcal{F}\{i(t)\}(j\omega)} \,, \tag{2.1}$$

where $v(t)$ is the cell terminal voltage, $i(t)$ the load current, $\mathcal{F}$ the Fourier transform operator, and ω the angular frequency, which equals $2\pi f$. Since a load current generates electric polarization losses within a Li-ion battery exhibiting specific relaxation time constants, the underlying loss processes are often described by impedance elements as done in the following.

In general, the equilibrium voltage of a Li-ion cell is given by the potential difference between the two Galvani potentials $\Delta\varphi_0$ of both positive and negative electrodes placed in the same solution [78]:

$$V_0 = \Delta\varphi_0(\mathrm{I}) - \Delta\varphi_0(\mathrm{II}) \,. \tag{2.2}$$

Using the Nernst equation, each Galvani potential can be expressed as potential difference between the two conducting phases of electrode and electrolyte:

$$\Delta\varphi_0 = \Delta\varphi_{00} + \frac{\mathrm{R}T}{n_i\mathrm{F}} \cdot \ln\left(\frac{a_{ox}^{\nu_{ox}}}{a_{red}^{\nu_{red}}}\right), \tag{2.3}$$

with the electric standard potential $\Delta\varphi_{00}$, the universal gas constant R, the absolute temperature T, the number of electrons n_i participating in the half-cell reaction, and the Faraday constant F [78, 79]. The activities $a_{ox}^{\nu_{ox}}$ and $a_{red}^{\nu_{red}}$ with their stoichiometric coefficients ν_{ox} and ν_{red} describe the effective concentrations of the active species i (i.e., lithium) in the oxidized and reduced components, respectively [78, 80]. Measuring the equilibrated Galvani potential of a single electrode in an

electrolyte is considered impracticable as the electrolyte potential cannot be measured directly [79, 81] and $a_{ox} = a_{red}$ is reached only by approximation in open circuit condition [82]. Therefore, the open-circuit voltage (OCV) measured across the cell terminals with minimum current flow is commonly used as approximation for the cell equilibrium voltage [82].

As stated above, the terminal voltage of a battery under a load current $i(t)$ differs from its equilibrium state. Considering the discharge case, the terminal voltage $v(t)$ is generally lower than the open circuit voltage due to potential drops η_i caused by the aforementioned dynamic loss processes:

$$v(t) = V_0 - \sum_i \eta_i = V_0 - i(t) \cdot R_\Omega + \eta_{sei}(t) + \eta_{ct}(t) + \eta_c(t) \ , \tag{2.4}$$

where R_Ω is the ohmic resistance of the cell, η_{sei} the overpotential due to the SEI on the anode, η_{ct} the activation polarization or charge transfer overpotential at anode and cathode, and η_c the concentration polarization at anode and cathode [81]. For reasons of clarity, Eq. (2.4) summarizes activation and concentration polarizations of both electrodes by one overpotential each, although they may exhibit different time constants in case of anode and cathode [87]. By normalizing Eq. (2.4) to the current, each of the overpotentials can be described by an impedance-based sub-circuit as depicted in Figure 5. In this description, high frequency overpotentials due to inductive or resistive-inductive effects are neglected as is often the case in literature because they are not relevant for electrochemical process identification. However, they play a crucial role in highly dynamic battery applications such as PLC for in-battery communications. For this reason, apart from the common battery dynamics presented in the following, HF-relevant battery effects are discussed separately in Chapter 4.
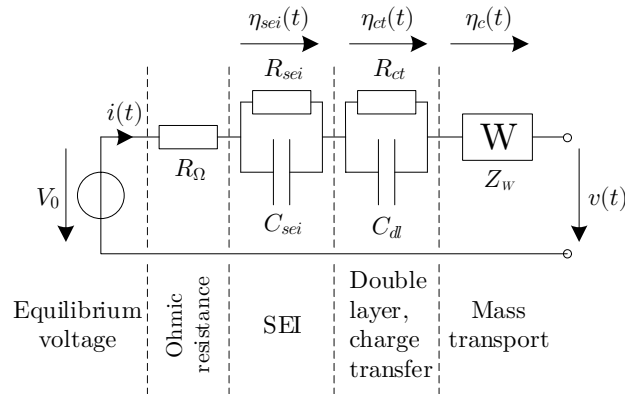
Figure 5: Impedance-based description of electrochemical battery dynamics considering time constants within microseconds to minutes typically covered by EIS measurements. (Based on Refs. [83–85] as one of the most commonly used modeling approaches [83].)

2.1.1 Helmholtz and Diffuse Double Layer

The Galvani potentials between the two conducting phases of electrode and electrolyte are connected with the formation of an electric double layer at the phase boundary [79]. From a chemical perspective, the solution pressure describes the natural tendency to balance the concentration of a species i between the active material and the surrounding electrolyte, that is, balancing their chemical potentials

$$\mu_i = \mu_i^0 + \mathrm{R}T \cdot \ln(a_i) \ , \tag{2.5}$$

with the chemical standard potential μ_i^0 and the activity a_i of the species [80]. For a Li-ion cell, this causes interfacial surface tension leading to a diffusion of charged lithium ions (Li+) between electrode and electrolyte. As an example, supposing that the anodic chemical potential of lithium (Li) exceeds the chemical potential of Li in the electrolyte, the oxidized Li+ diffuse into the electrolyte forming a layer of positive charge, whereas a negative charge remains at the anode surface [74]. As a consequence, the exchanged charge builds up an electric field hindering further Li+ transition, such that a balanced state between diffusion and migration will be reached. As such, a dynamic equilibrium between the electrochemical potentials of anode (I) and electrolyte (II) is reached:

$$\mu_i(\mathrm{I}) + n_i\mathrm{F} \cdot \varphi_0(\mathrm{I}) = \mu_i(\mathrm{II}) + n_i\mathrm{F} \cdot \varphi_0(\mathrm{II}) \ , \tag{2.6}$$

with the transferred charge quantity $n_i\mathrm{F}$ and the electric potentials $\varphi_0(\mathrm{I})$ and $\varphi_0(\mathrm{II})$ of electrode and electrolyte, respectively [79]. The electric potential difference $\Delta\varphi_0$ between $\varphi_0(\mathrm{I})$ and $\varphi_0(\mathrm{II})$ is caused by the electric field and can be calculated from Eq. (2.5) and Eq. (2.6), resulting in the Galvani potential given by Eq. (2.3). The potential at the conducting phase boundary does not change abruptly. Instead, the electric field keeps the diffused Li+ particles close to the phase boundary such that an electric double layer (EDL) is formed, in which the potential progresses gradually [80].

The EDL was originally modeled by Helmholtz with a fixed single layer having a linear potential progression [75], and was extended towards the bulk electrolyte solution by the Gouy-Chapman diffuse double layer [86] as illustrated in Figure 6 for the anode. Accordingly, the Helmholtz layer accounts for the static lithium ions right at the phase boundary and can be modeled as plate capacitor with the distance d_i of half of the diameter of the solvated Li+ [78]. Additionally, the diffuse double layer accounts for the thermal motion of Li+ in the EDL and can also be represented as capacitor connected in series [79]. Summarizing, the EDL can be modeled by a capacitor with the overall capacitance of

$$\frac{1}{C_{dl}} = \frac{1}{C_{sdl}} + \frac{1}{C_{ddl}} \ , \tag{2.7}$$
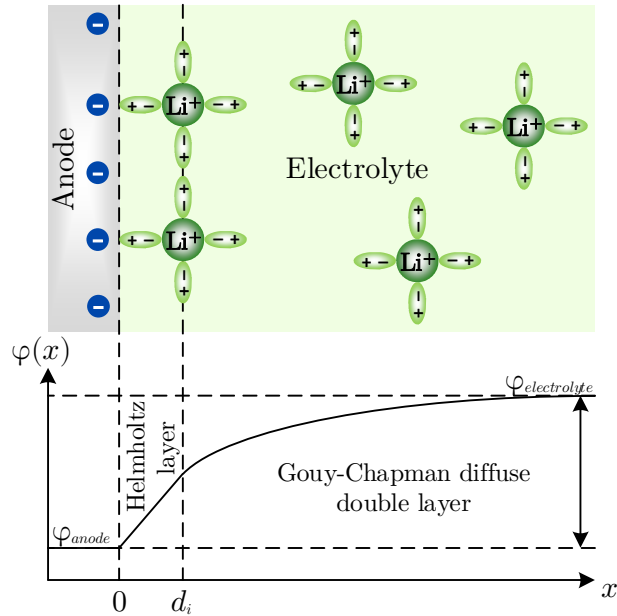
Figure 6: Electric double layer model by Helmholtz and Gouy-Chapman with the electric potential progression between anode (φ_{anode}) and electrolyte ($\varphi_{electrolyte}$). (Based on Refs. [74, 78].)

with the capacitances C_{sdl} and C_{ddl} of the static Helmholtz layer and the diffuse double layer, respectively [80]. In the impedance-based model of Figure 5, the capacitances of both anodic and cathodic EDLs are summarized in the simplest and most-common way by a single capacitor C_{dl} [78, 87]. To include the frequency dependence (also called frequency dispersion) of the EDL capacitance caused by surface roughness and atomic scale inhomogeneities, the capacitor is sometimes replaced by a constant phase element (CPE), which will be further treated in Section 2.2.2 [85, 88].

2.1.2 Charge Transfer

The previous section discussed EDL effects, which are connected with the dynamic electrochemical equilibrium voltage. The surface overpotential η_{ct} at the phase boundary of electrode and electrolyte is caused by the limited charge transfer reaction rate in case of an externally applied electric current, that is, when the equilibrium state is left [78]. In terms of electric potentials, an externally applied voltage across two electrodes will drive the electrochemical redox reaction such that forward and backward reactions take place simultaneously but with different reaction rates. The overall reaction rate of anode and cathode, respectively, is characterized by the faradaic current density j_n, which is given by the Butler-Volmer equation [80]:

$$j_n = j_0 \left[\exp\left(\frac{\alpha n \mathrm{F} \eta_{ct}}{\mathrm{R}T} \right) - \exp\left(-\frac{(1-\alpha)n\mathrm{F}\eta_{ct}}{\mathrm{R}T} \right) \right] , \tag{2.8}$$

where j_0 is the exchange current density, which depends on temperature, electrolyte composition, and electrode surface of the corresponding electrode. Large values of j_0 mean that a large current density can be obtained with a small surface overpotential. The apparent transfer coefficients or symmetry factor α relates how an applied potential favors one direction of reaction over the other. The reaction rate goes to zero at $\eta_{ct} = 0$ for any composition or reaction surface [80]. Figure 7 illustrates the Butler-Volmer relationship according to Eq. (2.8) for symmetric reaction rates ($\alpha = 0.5$).

For small $\eta_{ct} < 6$ mV, Eq. (2.8) can be linearized and the charge transfer resistance R_{ct} can be calculated as partial derivative [85]:

$$R_{ct} = \left[\left. \frac{\partial j_n}{\partial \eta_{ct}} \right|_{\eta_{ct}=0} \right]^{-1} = \frac{\mathrm{R}T}{n\mathrm{F}j_0} . \tag{2.9}$$

Since double layer effects and the charge transfer reaction occur in parallel, the model elements C_{dl}
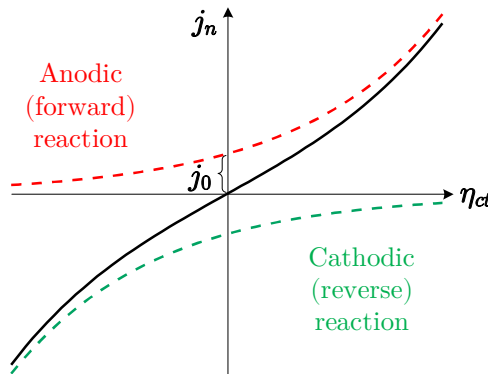
Figure 7: Graphical representation of the Faradaic current density according to the Butler-Volmer equation (2.8) with $\alpha = 0.5$. (Based on Ref. [82].)

and R_{ct} of Figure 5 are also placed in parallel. This means that at the phase boundary, the battery current is divided into a portion flowing into the charge transfer reaction and a part flowing into the EDL [75]. From a dynamic perspective, an applied current pulse will first charge C_{dl} and subsequently flow solely across R_{ct}. For higher frequencies, the RC-circuit behaves as a lowpass filter for the charge transfer reaction and the reaction will be shunted by C_{dl} [75]. This is further discussed in Chapter 4.

2.1.3 Ohmic Resistance

All key processes occurring in a galvanic cell such as Li-ion cells involve the conduction of charged particles between anode and cathode [71]. The ohmic resistance of a Li-ion battery accounts for the limited electric or ionic conductivity of the following components forming the current path:

(1) The electrolyte as the main contributor due to its limited ionic conductivity [89].

(2) The ionic conductivity of the separator soaked with electrolyte [90]. Additives in the electrolyte help to reduce the ohmic resistance by improving the wettability of the separator [91].

(3) The ionic and electric conductivity of the active materials of anode and cathode [71, 75].

(4) The electric conductivity of metallic components such as current collectors, tabs, and bonding wires [69]. Current collector foils and tabs are usually welded to minimize contact resistances [74].

(5) Contact resistances between active materials and current collectors as well as within active layers [68, 71, 75].

(6) Additional safety components such as current interrupt devices (CIDs) or positive temperature coefficient (PTC) thermistors, which are often implemented in commercially available Li-ion cells and inherently cause additional cell resistance [74, 92].

Commonly, the ohmic resistance of a cell can be modeled by a single resistor as depicted in Figure 5 by the circuit element R_{Ω}.

2.1.4 Solid-Electrolyte Interphase

The solid-electrolyte interphase (in some literature also called solid-electrolyte interface) is a passivating film layer that establishes primarily, but not exclusively, in the first charging cycle on the anodic graphite surface [93, 94], which is the most common anode material [93, 95]. The SEI formation can be explained by the graphite anode potential exceeding the thermodynamic stability window of the electrolyte during operation, leading to side reactions of the anode with the electrolyte solvents and salt [93, 96]. As a consequence, the reductive decomposition products of the electrolyte build up a passivating surface layer accompanied by irreversible loss of lithium inventory [94], which is typically in the range of 10% of the capacity [97]. The resulting SEI is illustrated in Figure 8 and has the purpose to prevent (1) the electrolyte compounds from further reduction on the lithiated anode surface, (2) the anode material from corrosion [94, 96], and (3) the co-intercalation of solvents with Li+ into the graphite structure avoiding graphite exfoliation [98]. Due to this essential protective character, the SEI is considered the foundation for properly working Li-ion batteries, and governs cell performance, safety, and lifetime [96, 99]. Its unique structure is permeable for lithium ions in first

approximation and rather impermeable for electrons and other electrolyte components [94]. However, the controlling of the formation, composition, and stability of the SEI is still under investigation in the Li-ion battery research community [93].

Although the SEI is permeable to lithium ions, its ionic conductivity is much lower compared to the bulk electrode [71]. Consequently, an additional overpotential due to the SEI can be observed under cell operation. The so-called SEI surface impedance can be modeled by an RC-circuit according to Figure 5, which is composed of the ionic resistance R_{sei} and the capacitance C_{sei} of the SEI layer, where the latter is defined by the dielectric constant, thickness and area of the layer [85].

It should be mentioned that also on the cathode side, a cathode-electrolyte interphase (CEI) is formed similar to the SEI on the anode [94, 100], but which has generally less impact on the cell performance [93].
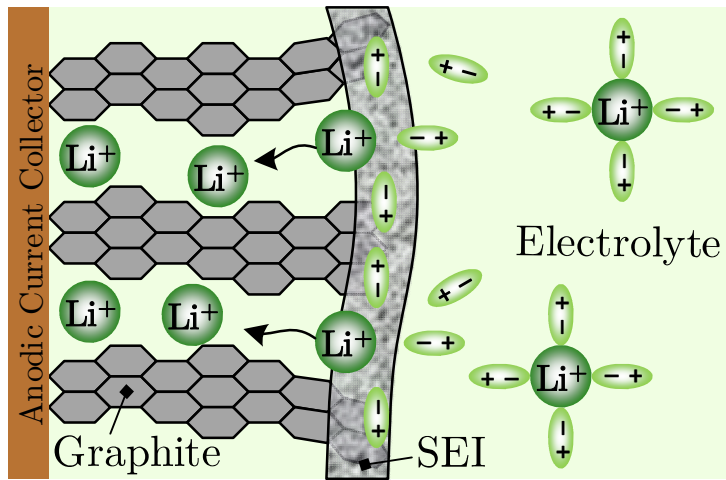
Figure 8: Schematic SEI working principle. Mainly in the first charging cycle, solvated lithium ions decompose during intercalation into the graphite structure, thereby forming the SEI, which acts as a barrier for further solvent molecules. (Based on Ref. [96].)

2.1.5 Mass Transport

Mass transport of lithium ions during operation can be done by (1) convection and stirring, (2) migration in an electric field, and (3) diffusion in a concentration gradient [79, 81]. Convection, which describes fluid flow, is small for Li-ion batteries due to small pore sizes of the electrodes and can therefore be neglected [74, 101]. Electric fields are small in the free electrolyte and ion migration is often prevented by solvate molecules covering the lithium ions [75]. Therefore, diffusion is the most important of the three processes and typically dominates the mass transport in batteries [75, 81]. Ion diffusion happens in the free electrolyte, within the porous electrode (both liquid phase) and inside the active material (solid phase or solid state [68]) [75, 102], and can be mathematically described by Fick's first law of diffusion [79, 103]:

$$\vec{j_i} = -D_i \cdot \nabla c_i \ , \tag{2.10}$$

with $\vec{j_i}$ being the diffusion flux density pointing in the direction of decreasing concentration, D_i the diffusion coefficient, and ∇c_i the concentration gradient. Under transient conditions, the

concentration distribution not only depends on the coordinates but also on time [79]. The rate of change in concentration over time is defined by Fick's second law of diffusion [81, 103]:

$$\frac{\partial c_i}{\partial t} = \nabla \cdot (D_i \cdot \nabla c_i) \ . \tag{2.11}$$

Equation (2.11) is valid for both the liquid and the solid phase, while c_i represents the lithium-ion concentration in the electrolyte and the lithium concentration in the solid active material [101].

The diffusion in Li-ion batteries can be characterized by the so-called Warburg impedance named after its founder E. Warburg [104], which relates the diffusion overpotential caused by a concentration gradient to the diffusion flux [105]. Two different Warburg impedances relevant for Li-ion batteries can be calculated by solving Fick's second law of diffusion given by Eq. (2.11) for different boundary conditions [85, 105]:

(1) The finite length Warburg (FLW) impedance characterizes the frequency dispersion for one-dimensional diffusion through a finite length layer with an ideal reservoir with fixed ion concentration c_i at one interface [105, 106]. The FLW is given by

$$Z_{W_{FL}} = \frac{R_{D0}}{\sqrt{j\omega\tau}} \tanh(\sqrt{j\omega\tau}) \ , \tag{2.12}$$

where $\tau = l_i^2/D_i$ is the diffusion time constant calculated from the limited diffusion length l_i and the diffusion coefficient D_i, and R_{D0} the diffusion resistance for $\lim_{\omega\to 0} Z_{W_{FL}}$ [85, 87, 106]. For Li-ion batteries, the FLW element can be used to describe the diffusion impedance from a thin electrode into the free electrolyte representing an ideal Li+ reservoir [75, 85].

(2) The finite space Warburg (FSW) impedance characterizes the frequency dispersion for one-dimensional diffusion through a finite length layer with zero flux at one interface, which is equivalent with a non-permeable or reflective wall [85, 87, 105]. The FSW is given by

$$Z_{W_{FS}} = \frac{\tau}{C_{D0}\sqrt{j\omega\tau}} \coth(\sqrt{j\omega\tau}) \ , \tag{2.13}$$

where C_{D0} is the diffusion capacitance, which is linked to the diffusion resistance R_{D0} via the diffusion time constant $\tau = R_{D0}C_{D0}$ [85, 87], and $\lim_{\omega\to 0} Z_{W_{FS}} = \tau/(3j\omega C_{D0}) = R_{D0}/3$ [105]. For Li-ion batteries, the FSW element can be used to describe the solid state diffusion of lithium ions towards the center of large electrode particles having a limited diffusion path [85].

In previously published works such as [107, 108], the finite space Warburg impedance is used to summarize diffusion characteristics of Li-ion batteries in one element highlighting that kinetics are limited by solid state diffusion [109]. However, there are also studies reported in literature such as [74, 110, 111], which use the finite length Warburg impedance for describing overall diffusion dominated by ion diffusion in the free electrolyte and the electrode pores.

2.2 Battery Impedance Characterization Methods

Determining the battery impedance is essential to identify dynamic battery processes as presented in Section 2.1 and to map them to an impedance-based battery model such as given by Figure 5. Although there exist many different battery impedance and resistance measurement techniques, they fall into two main categories: (1) Large signal impedance measurements by current pulses in the time domain and (2) small signal impedance measurements by Electrochemical Impedance Spectroscopy in the frequency domain [39, 112].

2.2.1 Time Domain: DC Current Pulse Method

DC current pulses are often applied for a straightforward estimation of the battery resistance [113–117]. It involves the excitation of the battery by a sharp large DC current pulse while monitoring the resulting transient cell voltage response. This allows for the calculation of an instantaneous, so-called "DC resistance" after the time interval Δt defined by

$$R_{DC,\Delta t} = \frac{\Delta V}{\Delta I} \, , \tag{2.14}$$

where ΔV is the cell voltage difference and ΔI the current difference, both measured after the time Δt elapsed since switching on the current pulse [113, 114]. A generic current pulse and the corresponding voltage response of the cell are given by Figure 9a, neglecting inductive cell effects, which will be discussed in Chapter 4. During the rising and falling edge of the pulse, the cell voltage follows the current in an instant showing an ohmic behavior. As indicated in Figure 9a, the cell's ohmic resistance R_Ω can be directly determined right after the rising edge using Eq. (2.14). After the current pulse has settled, the electrochemical overpotentials due to SEI, charge transfer and diffusion build up and also contribute to $R_{DC,\Delta t}$. The most important pulse parameters are the step height ΔI, which can reach high C-rates [114], and the time interval Δt, which is set to 10 s in many studies [117, 118] to address the corresponding time constants of the aforementioned overpotentials (see Figure 4). Other pulse parameters such as pulse direction, pulse shape, and rise and fall time have been reported to be negligible when determining $R_{DC,\Delta t}$ for short times $\Delta t < 1$ s [113], but may play a role for longer time intervals due to electrode potential differences [114].

Current pulse methods are typically used for battery series resistance estimation, offering a fast, direct, and model-free measurement approach [115, 116]. Furthermore, also a model-based approach can be used to identify cell model parameters by matching the model to the cell's transient voltage response [114]. However, estimation results may be inaccurate for fast-switching currents pulses due to noisy measurements [116] and the overlapping of different dynamic cell contributions in the pulse response, making their separation unfeasible [114, 119]. For a more distinct separation of fast battery dynamics such as SEI and charge transfer, EIS can be applied as presented in the following.
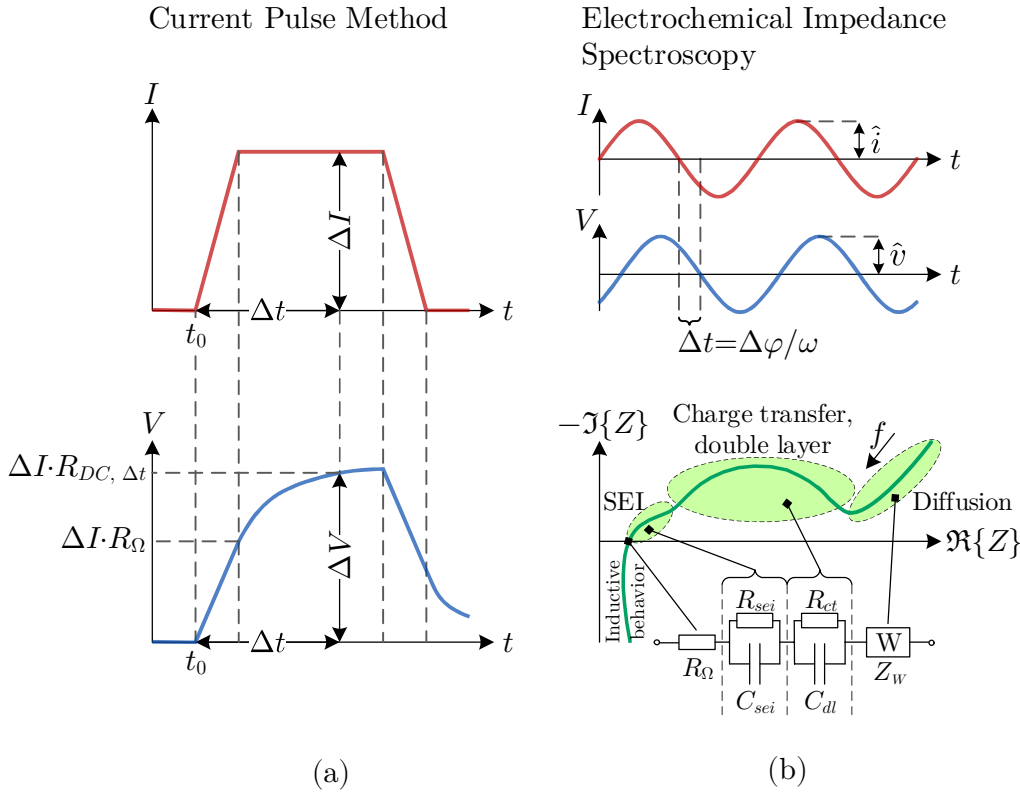
Figure 9: (a) Current pulse method and extraction of selected resistance values. (b) Electrochemical Impedance Spectroscopy with time domain signals (upper part) and resulting impedance locus drawn as Nyquist plot. The battery dynamics as described in Section 2.1 as well as the model elements of Figure 5 can be mapped to specific parts as depicted in the Nyquist plot. (Based on Refs. [112, 118].)

2.2.2 Frequency Domain: Electrochemical Impedance Spectroscopy

Electrochemical Impedance Spectroscopy is a non-invasive test method for impedance analysis at multiple frequencies. In recent years, EIS has become one of the most important characterization methods for electrochemical systems such as batteries or fuel cells [120]. The technique involves the periodic small signal excitation of the battery and measuring its response for determining the complex-valued battery impedance versus frequency given by

$$Z(j\omega) = |Z(j\omega)|e^{j\varphi(\omega)} = \Re\{Z(j\omega)\} + j \cdot \Im\{Z(j\omega)\} = \frac{V(j\omega)}{I(j\omega)} = \frac{\mathcal{F}\{v(t)\}(j\omega)}{\mathcal{F}\{i(t)\}(j\omega)} \,, \tag{2.15}$$

where $\Re$ and $\Im$ are the real and imaginary part operators, respectively. Sinusoidal current and voltage signals are often used for periodic excitation, though other waveforms such as rectangular, multi-sine, or random noise signals are possible [112]. Impedance spectra can also be acquired by time domain measurements using step signals and transform the measurement results into the frequency domain [120]. These and other excitation options will be presented in Section 3.2.1.

For sinusoidal signals as illustrated in Figure 9b, the complex-valued impedance defined by Eq. (2.15) can be further expressed by the amplitude relationship between voltage $\hat{v}$ and current $\hat{i}$ and their phase shift $\Delta\varphi$ for a certain angular frequency ω_0:

$$Z(j\omega_0) = |Z(j\omega_0)|e^{j\omega_0 \Delta\varphi} = \frac{\hat{v}}{\hat{i}}e^{j\omega_0[\varphi_v - \varphi_i]} \ . \tag{2.16}$$

The excitation can be either voltage (potentiostatic mode, PEIS) or current (galvanostatic mode, GEIS), though the galvanostatic mode is preferred for batteries to prevent SOC drift during measurements [112]. The resulting impedance locus is typically drawn in a Nyquist plot, where the negative imaginary part of the impedance is plotted versus the real part as depicted in the lower part of Figure 9b. This allows for assigning various dynamic battery processes to certain parts of the impedance curve as marked in Figure 9b. Moreover, the impedance-based model elements of Figure 5 can be traced in the impedance curve and values for the circuit parameters can be obtained by the usage of curve fitting algorithms such as complex nonlinear least squares [111]. A set of basic electrical circuit elements and their impedance curves in the Nyquist plot are shown in Figure 10. A simple ohmic resistor can be read out on the real axis of the Nyquist plot, whereas pure capacitive or
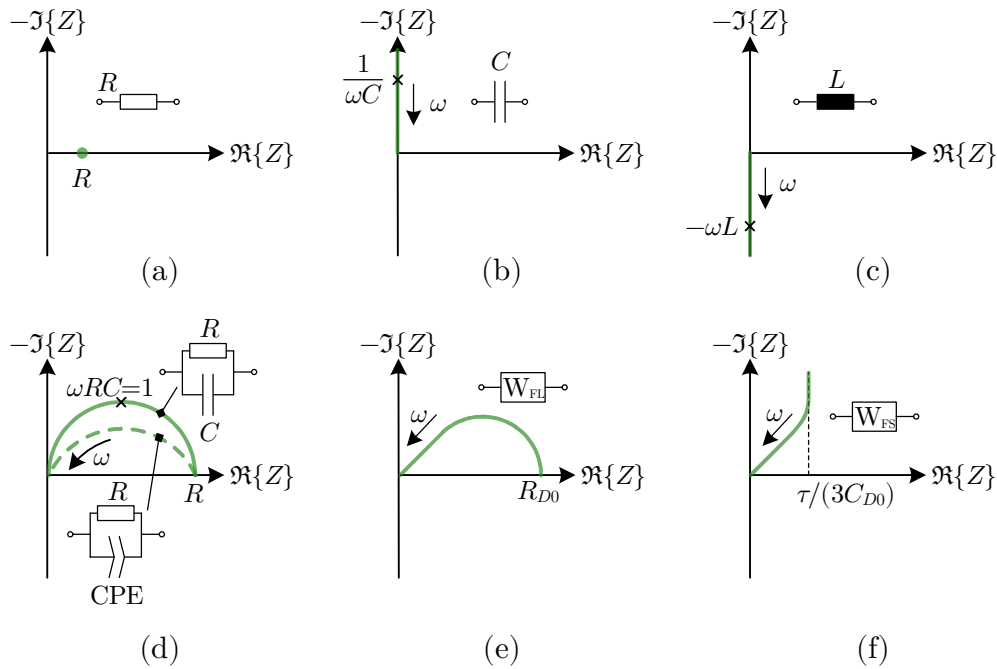
Figure 10: Impedance locus of commonly used model elements such as resistor (a), capacitor (b), inductor (c), parallel RC and ZARC element (d), finite length Warburg element (e), and finite space Warburg element (f) and extraction of certain model parameters. (Based on Refs. [85, 121].)

inductive elements appear as straight lines on the imaginary axis as visible in Figure 10a–c. In Figure 10d, the generic impedance curve of a parallel RC-circuit is depicted, which spans a semicircle in the upper half-plane of the Nyquist plot and reaches an impedance of zero for very high frequencies. In electrochemistry, impedance semicircles are often shifted as marked by the dashed green curve in Figure 10d. The shift is caused by frequency dispersion, meaning that the relaxation time constant is not single-valued but distributed around a mean value [87], which was proven by Ref. [105]. This can

be attributed mainly to the spatial extension of the liquid/ solid phase boundary for porous electrodes and rough surfaces [85].

Modeling a shifted semicircle is generally approached by a CPE and a resistor (R) in parallel, referred to as ZARC-element, which has the expression [85]

$$Z_{ZARC} = \ R \parallel Z_{CPE} = R \parallel \frac{1}{A_0 (j\omega)^n} \ , \tag{2.17}$$

with A_0 being a capacitance parameter and the exponent $n \in [-1; 1]$. Thereby, the CPE can be seen as a generalized impedance element since different values for n resemble resistive ($n = 0$), capacitive ($n = 1$), and inductive ($n = -1$) nature as well as Warburg characteristics ($n = \frac{1}{2}$). In Figure 10e and Figure 10f, the impedance locus of the two Warburg elements (FLW, FSW) presented in Section 2.1.5 are depicted, which follow a constant slope of 45 degrees and, for low frequencies, approach resistive or capacitive behavior in case of the finite length or finite space Warburg element, respectively.

Using the presented basic electrical circuit elements, physically meaningful battery models can be designed and parametrized by EIS measurements. Beside the presented model of Figure 5, two other models are frequently used, which are depicted in Figure 11. The model shown in Figure 11a is based on the well-known Randles equivalent circuit [122], which involves a Warburg element contributing to the particle surface impedance mainly due to solid state diffusion [85]. The other frequently used model given in Figure 11b is closely related to the model of Figure 5 and replaces the capacitors by CPEs, accounting for the aforementioned frequency dispersion for rough and porous electrodes [85].
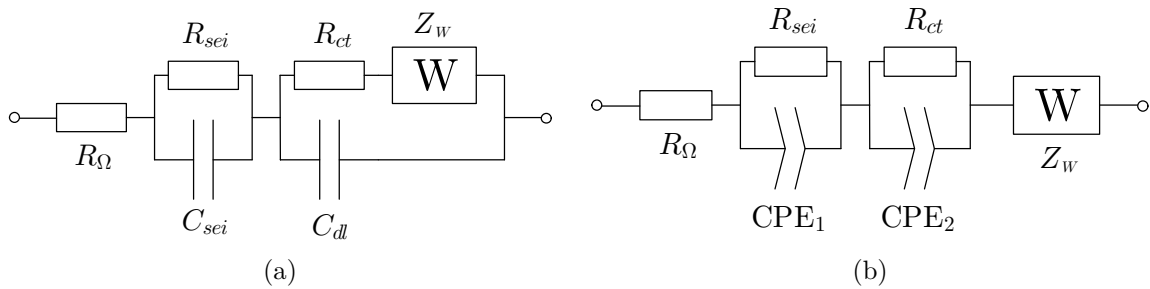
Figure 11: Frequently used impedance-based models for EIS analysis beside the model given in Figure 5. (Based on Ref. [83].)

As mentioned in Section 2.2.1, EIS is preferred for a detailed characterization of fast cell dynamics such as SEI and charge transfer because high slew rate current pulses and limited sampling rates lead to noisy measurement results [118, 120]. In contrast, slower cell dynamics like diffusion demand very long-lasting EIS measurements, which are susceptible to distortions and noise. Therefore, it is reported that measurement data quality for low frequencies ($f < 10$ Hz) is typically better when obtained from pulse methods rather than from EIS because long relaxation times are tracked more accurately [118, 120]. Pulse methods are also advantageous because signal generation is relatively simple and can be either active by using dedicated hardware or simply passive by reusing existing signals such as EV drive currents [116]. On the other hand, EIS measurements at single frequencies are very robust against disturbances, which will be shown in Section 3.2.3. By now, EIS is mostly used in the laboratory environment but gains increasing interest in the field of BMS for battery state estimation.

3 Automotive Battery Management Systems

Automotive BMSs are inevitable to keep each Li-ion cell of an HV traction battery within its safe operating area [123]. This chapter proposes online EIS and PLC for the smart management of battery systems and lists opportunities and challenges regarding its implementation in an EV. First, an overview of typical BMS topologies is given in Section 3.1. Subsequently, Section 3.2 discusses important implementation aspects of online EIS for traction batteries such as architecture, excitation options, and possible interference scenarios. Finally, existing and novel communications concepts for BMSs are introduced in Section 3.3 including a summary of state-of-the-art PLC technologies.

3.1 BMS Functionality and Topologies

Although there is no consensus about the definition of the term "BMS", the wide view is that BMS is any electrical or mechanical system that manages battery cells, modules, or packs to optimize performance and ensure safety and reliability [123]. The functionality includes (1) data acquisition, (2) safety protection, (3) battery state prediction, (4) charge/ discharge and equalization management, (5) communications, and (6) thermal management [18, 20].

The monitoring of individual cell voltages, temperatures, and battery pack current is a typical feature of an automotive BMS in order to forecast the battery's SOC and SOH [18, 124]. EV traction batteries consist of hundreds of single Li-ion cells, which require many measurement channels. Depending on the degree of modularity, the BMS can be realized by different topologies summarized in Figure 12. A centralized BMS (Figure 12a) is based on a single, monolithic system that provides measurement channels for each cell of the pack. It is beneficial in terms of compactness as it can be replaced as a whole in case of failures, and provides the lowest cost for very large volumes above ten thousand parts [66, 123]. However, the central BMU also has to support the high voltage of the battery pack, which leads to increased creepage and clearance distances [66]. State-of-the-art automotive BMSs often apply a modularized or semi-distributed topology as shown in Figure 12b, where a fixed number of cells forming a module is controlled by a slave BMS unit (also called module controller) containing multiple CMCs [8, 10, 123]. Acquired measurement data are sent to the central master BMU for further processing, though the master BMU could also be integrated in one of the module controllers [123]. The modularized BMS is more extendable than the centralized BMS and allows for more flexible scaling of individual modules with different size and form factors. Also wiring effort and high voltage requirements are eased, although this comes along with higher cost [123].

The sensing circuits of both centralized and modularized BMS architectures are typically not located directly next to the intended Li-ion cell [123]. This implies long measurement leads between individual battery cells and sensing circuits, which can easily pick up electromagnetic disturbances [23]. In the worst case, measurement data are only slightly distorted so that the BMU does not detect the false measurement but performs wrong state estimations [26]. The fully-distributed topology (Figure 12c) mitigates wiring effort and EMI through dedicated CMCs, which are integrated in the modules or directly placed on the cells [66, 123]. Instead of multiple measurement and control leads susceptible

to ohmic voltage drops and external interferences, only a communications link is needed between the CMCs and the central BMU. This enables low-noise voltage and temperature measurements on cell level with high resolution, offering the highest degree of information among the three BMS topologies. However, the fully-distributed BMS also significantly increases the overall hardware amount, maintenance effort, and cost.

Current battery management systems still face multiple challenges. SOC estimation is traditionally realized by Coulomb counting [125] or OCV modeling [126]. As Coulomb counting suffers from error accumulation [6] and OCV tracking in real-time is not feasible during EV operation, advanced SOC tracking uses a combination of both approaches including an impedance-based battery model to estimate the OCV during operation [12]. However, limited measurement quality and quantity, especially in modularized or centralized BMSs, lead to uncertainty of the battery model parameters [20]. Also real-time SOH estimation is an open topic in BMS research since current SOH estimation methods such as durability- and battery-model-based methods depend on the estimation quality of the model parameters [10, 12]. Beyond, SOC and SOH estimations are often performed on pack level (macro-scale) rather than on cell level (micro-scale), leaving a significant estimation uncertainty on cell level [8]. As mentioned in the introduction, also cell temperature tracking and hotspot detection in real-time is quite challenging due to the limited number of temperature sensors placed on the modules. For these reasons, BMS research increasingly seeks for novel detection methods of additional cell parameters. Among them, the internal resistance of the battery, or more generalized, its impedance is considered a promising cell parameter.
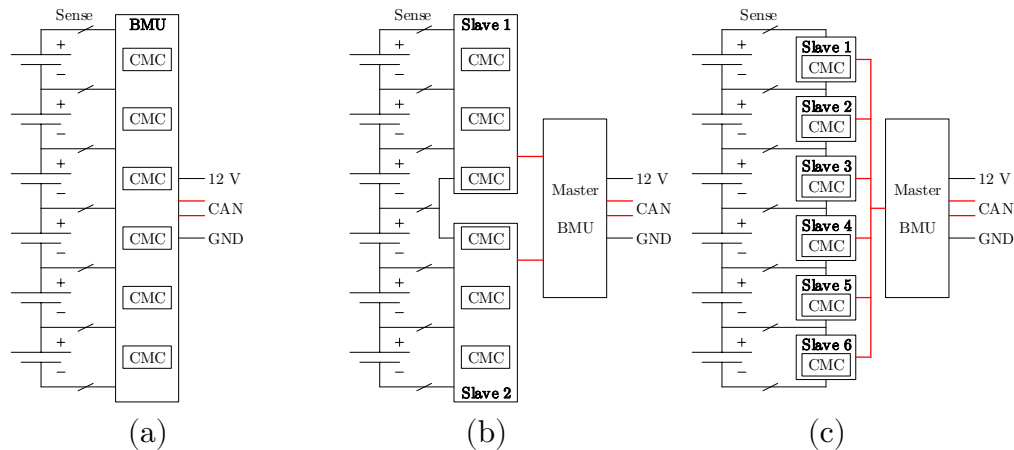
Figure 12: Different BMS architectures outlined on an exemplary small battery stack. Centralized (a), modularized/ semi-distributed (b), and fully-distributed (c) topology. (Based on Refs. [66, 123].)

3.2 Online Electrochemical Impedance Spectroscopy

The battery's impedance over frequency is a promising quantity for cell state estimation since it has been shown to be dependent on SOC [38–41], SOH [40, 42–44], and temperature [38, 39, 45–47]. Sensorless temperature detection could be done with EIS measurements around the intercept frequency of the impedance curve where the imaginary part approaches zero [47], or at higher frequencies [27, 45]. Knowledge of the impedance is also advantageous for battery model parametrization [20]. Model parameters could be updated online and used for real-time state

estimation [127, 128]. The SOH of the battery, for example, can be predicted by the change in ohmic resistance, charge transfer resistance, and Warburg impedance [129]. Furthermore, SOC prediction can be done directly by correlating impedance measurements with the SOC [42] or using a model-based approach parametrized by EIS measurements [41, 43].

In state-of-the-art BMSs, however, usually only the overall DC resistance of the battery is estimated by current pulse methods for the sake of power prediction or fault diagnosis [10, 127]. As described in Section 2.2.1, this method lacks a good separation of battery dynamic effects according to their relaxation times and is also influenced by the nonlinear charge transfer function characterized by the Butler-Volmer equation (2.8). In contrast, EIS performs impedance measurements at multiple frequencies around a defined working point, which can be adjusted by the superimposed DC load current [112, 127]. This way, EIS can accurately identify and separate dynamic battery effects, which makes it suitable for online battery model parameterization and state estimation [84, 112, 114]. However, the integration of online EIS as additional functionality into automotive BMSs faces several challenges, among them the biggest is to achieve reliable measurements while keeping implementation cost at a minimum [112]. In the following, different realization options and challenges are discussed.

3.2.1 Excitation Options for Online Electrochemical Impedance Spectroscopy

Valid EIS measurements need to fulfill the criteria of linearity, causality, and stationarity [84, 130], which is especially challenging in the highly dynamic and noisy automotive environment [27]. Electrochemical systems are inherently nonlinear due to the nonlinear current-voltage relationship of the charge transfer reaction (Eq. (2.8)) and diffusion processes, and may generate higher harmonics during excitation with a single frequency. However, sufficiently small perturbation ensures the system to remain in a pseudolinear region, keeping higher harmonic content in the system response low [84]. On the other hand, a tradeoff has to be found between linearity and a sufficiently high signal-to-noise ratio (SNR), where the latter demands for high excitation amplitudes [85]. For Li-ion batteries, the voltage response should not exceed 10 mV during a single-frequency excitation to ensure pseudolinearity [85].

Laboratory EIS measurements are commonly performed using the single-sine or also called frequency-sweep method, in which single frequency points are evaluated sequentially [84, 131, 132]. This offers good noise rejection, however, also leads to time-consuming measurements [37]. Especially at low frequencies in the millihertz range, this can cause non-steady-state behavior during measurements such as noticeable changes in cell voltage and SOC, which may violate the stationarity criterion [37, 131]. The aspect of stationarity is particularly crucial for EVs when considering large load currents present on the power lines. In this case, also the causality criterion may be violated because a change in the cell voltage may not be linked to the EIS excitation itself, but arises from an external source [118] such as a Joule heating due to high load currents and ohmic losses [133].

For the stated reasons, the majority of online EIS realizations apply broadband signals, where multiple frequencies are measured simultaneously to reduce the measurement time [84]. Denoted as time-domain-based EIS [134], the technique applies either stochastic, transient, or multi-frequency periodic signals for cell perturbation, containing rich harmonic content [135]. Stochastic signals have been used in the form of pseudo-random bit sequences (PRBSs) [135, 136] and random noise signals [37, 137].

As PBRSs are intended for linear system identification [138], ternary signals have been introduced to characterize nonlinear systems such as Li-ion cells, eliminating errors coming from even-order nonlinear distortions [139, 140]. Also transient signals such as current or voltage steps and pulses have been proposed for determining the impedance spectrum [120, 131, 141]. Since large current steps or pulses may change the operating point of the electrochemical system, multi-sine excitation has been proposed, combining the advantages of single-sine (accuracy, defined operating point) and broadband excitation (time efficiency) [37, 132, 134, 142, 143].

All time-domain-based EIS techniques involve the transformation of the measured voltage and current signals into the frequency domain [131]. Fourier transform or Fast Fourier transform (FFT) [134, 144, 145] and Laplace transform [141, 145] are frequently used mathematical methods for data processing. However, these methods inherently follow the frequency-time uncertainty principle, which means that frequency and time resolution of non-stationary signals are inverse proportional [131, 132]. To overcome this tradeoff, alternative techniques such as the Wavelet transform have been proposed, enabling both high time and frequency resolution [131, 146].

3.2.2 Implementation Options for Online Electrochemical Impedance Spectroscopy

In general, there are two implementation approaches for online EIS: (1) Active and (2) passive [84, 127]. In the first approach, either (1a) existing infrastructure or (1b) dedicated hardware is used to generate the excitation signal for EIS. The former (1a) mainly implies the reuse of existing switched-mode power supplies [112], involving battery chargers [34, 143], power converters [147, 148], motor controllers [37], or battery balancing units [33, 149] to generate periodic or stochastic excitation signals. The latter approach (1b) considers dedicated hardware for online EIS, where mostly random noise signals [137] or PRBSs [135, 136, 140] are applied because their hardware-based generation is relatively simple compared to continuous waveforms [150]. To avoid SOC drift during EIS, the galvanostatic approach is mostly used allowing for accurate charge balancing such as in Refs. [27, 34, 37, 127, 132]. On the other hand, passive EIS (2) exploits existing load currents present on the EV power lines for impedance measurements [128, 151–153]. Accordingly, passive EIS works without additional active signal generation and uses driving current profiles as signal source, which can be categorized as stochastic signals [153]. In comparison, active EIS is more cost-intensive than passive EIS due to hardware overhead, but excitation amplitudes and measurement frequencies can be set explicitly as desired. In contrast, passive EIS depends on the load current dynamics, which are mainly determined by the EV's powertrain and might contain only specific frequency components with unpredictable amplitudes [127, 154].

For both active and passive EIS, the voltage response measurement should be as close as possible to the cell to mitigate distortions [23] and ohmic voltage drops [155]. As state-of-the-art BMSs already involve the measurement of each individual cell voltage [11], existing CMCs could be reused for voltage response measurements in both cases [34].

The excitation of active EIS could be either centralized, where the signal is generated once on pack level [34] or distributed on cell level [8]. On the one hand, the centralized approach benefits from less

hardware effort, in particular when reusing existing power electronics, but requires overhead for data synchronization between the centralized current and distributed voltage measurements since non-synchronized measurements lead to relatively large impedance errors [128]. On the other hand, the distributed approach demands for significant hardware effort but offers high accuracy while synchronization is simple when using a monolithic solution for both current and voltage measurements. Such a monolithic EIS solution is provided by Infineon Technologies AG in the form of a prototype integrated circuit (IC), which evaluates the cell impedance in a frequency range from 10 Hz to 5 kHz using galvanostatic EIS with sinusoidal or rectangular periodic excitation. Intended for online EIS application, the IC is directly supplied by a single Li-ion cell and generates the excitation signal by the periodic on-off switching of a load resistor R_L as illustrated in Figure 13a. Analog-to-digital converters (ADCs) are used for direct voltage acquisition and indirect current acquisition using a shunt resistor R_S. By digital signal processing (DSP), the complex-valued impedance over frequency is calculated and can be sent to a central BMU by a serial bus communications system.

Due to the passive load excitation technique, the cell is always in the discharge region during the EIS measurement. Compared to sinusoidal excitation, periodic rectangular excitation has the advantage of less heat dissipation in the IC because the switching transistor does not need to operate in the linear region [33]. Also the controlling is simplified as no feedback control loop is needed for the on-off switching. Moreover, the fundamental amplitude of the periodic square wave with 50% duty cycle is $4/\pi$ (2.1 dB) higher than the fundamental amplitude of the periodic sine wave, while the average discharge current (or DC spectral component) is the same in both cases as visualized in Figure 13b. The derivation of this relationship can be found in the Appendix. As a consequence, the usage of a periodic rectangular EIS excitation could increase the SNR in an online application by 2.1 dB. Lower duty cycles below 50% would further amplify the ratio of fundamental to average current amplitude as shown in Figure 13b, but the increased peak current would demand a higher maximum current rating of the excitation circuit, this way increasing the component size.

(a)   (b)
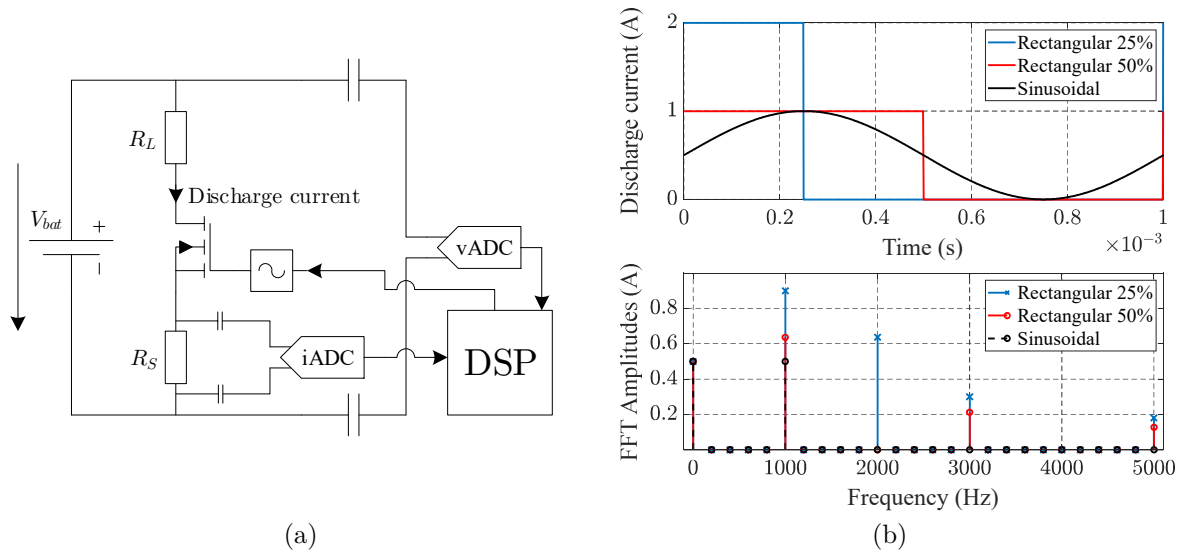
Figure 13: Galvanostatic EIS using the prototype IC by Infineon Technologies AG. (a) Excitation principle using on-off switching of a passive load connected to the battery with its terminal voltage V_{bat}. (b) Different excitation signals and their spectral components.

3.2.3 Interference Scenarios during Online Electrochemical Impedance Spectroscopy

As the ohmic resistance of Li-ion batteries is quite low in the range of tens of milliohms for cylindrical 18650 cells [73] and even lower for high-capacity prismatic cells [156], EIS voltage signals are typically small and online EIS becomes especially challenging in the noisy environment of electric vehicles. Interference of EIS measurements can be the result of (1) external disturbances or (2) internal disturbances. Typical interference scenarios are illustrated in Figure 14a. Power electronic systems are considered the main source of electromagnetic interference in EVs due to the high speed switching of power semiconductor devices such as insulated-gate bipolar transistors (IGBTs) [157]. As the power electronic systems are directly supplied by the battery, they are largely responsible for external disturbances of online EIS, marked by the red arrows in Figure 14a. However, noise experiments conducted with the Infineon prototype EIS IC on a cylindrical 18650 Li-ion cell revealed that reliable EIS results can be obtained even for slightly negative SNR values as shown in Figure 14b [158] by exploiting narrowband filter structures and FFT processing gain [159]. Other external disturbances such as PLC indicated by the orange arrow in Figure 14a can also have an impact on EIS measurements, which will be discussed in detail in Section 5.2.

Internal disturbances have their origin inside the battery pack and can be caused by leakage currents or crosstalk. As indicated by the blue arrows in Figure 14a, undesired branching of the EIS excitation current cannot be avoided in a distributed topology because the power line network outside of the battery pack offers an alternative current path for the local EIS excitation across the DC-link capacitor. To quantify the significance of the leakage current, EIS measurements were performed on a Li-ion cell placed in a battery module made of twelve prismatic cells with connected and unconnected DC-link capacitor [158]. The results depicted in Figure 14c suggest a rather small averaged measurement deviation of 3.3% for frequencies below the intercept frequency, however, due to the frequency-dependent impedance of the DC-link capacitor, the leakage current increases with frequency and the measurement deviation reaches 15.4% for 10 kHz. Since the measured voltage response of the cell is lower due to the reduced effective excitation current, which, however, cannot be noticed by the EIS device, the measured impedance tends to be lower than the true impedance as visible in Figure 14c. The leakage current effect could be avoided using a centralized EIS excitation, but it is expected that leakage currents can be neglected for complete traction batteries because increased ohmic resistance and wiring inductance make the current path across the DC-link capacitor undesirable.

Other internal disturbances arise from simultaneous EIS measurements of more than one Li-ion cell in close vicinity, which is known as radiated EMI or cell-to-cell crosstalk interference (green arrows in Figure 14a) [160]. Crosstalk experiments were conducted by performing EIS measurements simultaneously on three adjacent Li-ion cells within a battery module made of twelve prismatic cells as shown in the inset of Figure 14d [158]. The results of Figure 14d exemplify how strongly the EIS measurement of the middle cell is distorted, when online EIS is performed on the adjacent cells at the same time. It has been suggested that the crosstalk is caused by inductive coupling among neighboring cells [160], which is supported by the facts that the measurement error due to the crosstalk increases with frequency as visible in Figure 14d [158] and that is does not differ between electrically connected
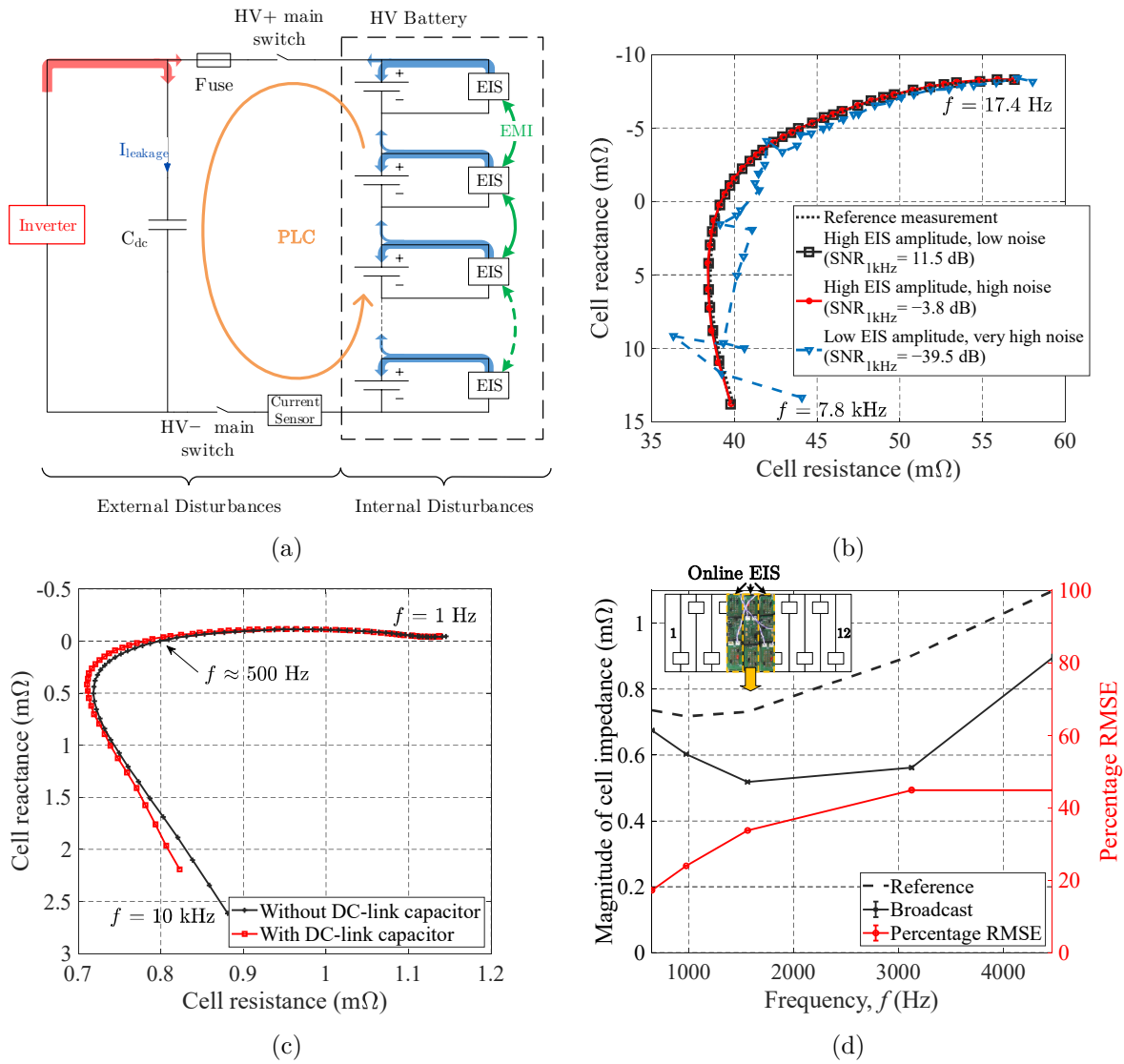
Figure 14: Interference scenarios during online EIS on single Li-ion cells within a distributed BMS architecture [158]. (a) Overview of online EIS disturbances within the electric power train. (b) Impact of additive white Gaussian noise (AWGN), marked by the red arrows in (a). (c) Impedance measurement deviation due to leakage current across the DC-link capacitor, marked by the blue arrows in (a). (d) Impedance measurement error due to cell-to-cell EMI (crosstalk) in terms of percentage root mean square error (RMSE), marked by the green errors in (a); for the reference measurement, only the middle EIS circuit was active, whereas for the broadcast measurement, all three EIS circuits were active as shown in the inset.

and unconnected cells [160]. It has also been shown that the crosstalk linearly increases with the excitation current and reduces for larger distances between the cells [160]. To avoid crosstalk, simultaneous EIS measurements should be therefore performed only at distant cells or at different frequencies. Alternatively, sequential EIS measurements could be an option, though this demands for more time compared to simultaneous measurements. As crosstalk is a linear [160] and deterministic [70] phenomenon, another option is to compensate for the crosstalk by including an EMI model in the EIS measurement algorithm [160].

3.3 In-Battery Communications Concepts

BMS communications implies internal communication among CMCs and the central BMU as well as external communication of the BMU with peripheral control units [66, 123]. In this section, existing and novel concepts for internal BMS communications, also referred to as in-battery communications [161], are presented. BMS communications needs to fulfill demanding system requirements. Measurement data of hundreds of single Li-ion cells need to be periodically sent to the BMU with high accuracy for precise state estimation [162], while update rates of up to 100 samples per second require real-time communications [66]. The often low-voltage communications system needs to be galvanically isolated from the high voltage of the power lines for safety purposes [124, 162] and has to be robust against EMI coming from the EV's power electronic systems [66, 163]. Eventually, the power consumption of the communications system should be as low as possible [163] and weight, size, and cost should be minimized [164].

3.3.1 Wired Communications

Existing automotive BMSs mostly employ a serial communications link for data transmission [66], whereby the CAN developed by Bosch in the 1980s [165] is widely used as serial bus system isolated from the rest of the CAN of the EV [124, 163, 166]. As illustrated in Figure 15a, the CAN bus operates in a master/ slave configuration, where the BMU represents the master and the module controllers or CMCs – depending on the BMS topology (see Section 3.1) – represent the slave BMS units [161]. The galvanic isolation between high and low voltage is mostly realized by capacitors or transformers [124]. The high acceptance of the CAN bus arises from its robustness against EMI due to twisted pair wiring and differential signaling [124, 163], high speed communications up to 1 Mbps enabling near-real time performance [66], and cost efficiency because only one isolation interface is required per BMS slave unit [163]. However, the CAN bus requires long wiring throughout the battery pack, which raises reliability concerns because any damage could lead to an interruption of the entire bus system. Instead of implementing costly redundant systems, the daisy-chain topology pictured in Figure 15b has been
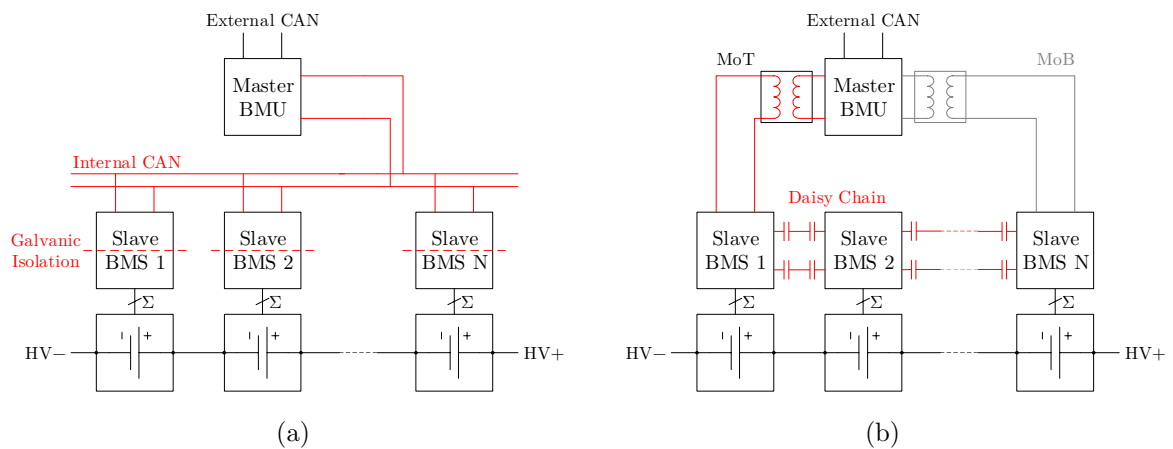
Figure 15: Wired-communications topologies of automotive BMSs. (a) Common serial bus system using isolated CAN in master/ slave configuration. (b) Alternative communications approach using the daisy-chain topology in master/ slave configuration. (Based on Refs. [163, 167, 168].)

proposed as a more reliable solution compared to conventional serial bus systems [163, 167]. Acting as a point-to-point bus between two slave BMS units, the communication signal travels only short distances and is repeated by every slave unit. The daisy-chain topology involves connecting the master on top (MoT) or on bottom (MoB) of the slave node stack as denoted in Figure 15b. To further increase the reliability, also a ring topology can be realized by connecting the master to both ends of the slave node stack [163]. The daisy-chain topology is considered more expensive than the conventional serial bus system since two costly isolated communications interfaces are required per slave unit [124, 163]. Still, due to the high reliability, several BMS monitoring ICs are commercially available that support daisy-chain communications such as the TLE9012AQU by Infineon Technologies AG [169], the MAX11068 by Maxim Integrated, Corp. [170], the bq76PL536A-Q1 by Texas Instruments, Corp. [171], and the LTC6803-3 by Analog Devices, Inc. [172].

Any wired communications system still requires a significant amount of wiring harness, which lets size and weight of the battery pack increase and may also cause reliability issues due to vibrations and fatigue [173]. Moreover, installation of the wiring harness complicates the battery pack assembly process and its maintenance, leading to additional cost [161]. To overcome these disadvantages, alternative communications media are currently under investigation in research and development. In the following, two novel communications concepts for BMS, namely wireless and power line communications, are presented. Although optical communications might be another solution for BMS communications thanks to its advantages of inherent galvanic isolation and EMI robustness [174], it is not included in this section due to the lack of reported research at this time.

3.3.2 Wireless Communications

Wireless in-battery communications solves the disadvantages of wiring harness, connectors, and galvanic isolation effort associated with wired communications, and offers the optional integration of sensors inside the battery cells [8, 175]. Particularly in the context of smart cells and the Internet of Things (IoT), wireless battery management systems (WBMS) gain increasing attention [176, 177]. Most of the reported WBMS approaches use the industrial, scientific and medical (ISM) 2.4 GHz band [178, 179], which is compliant with the Institute of Electrical and Electronics Engineers (IEEE) 802.15.4 standard [180]. Based on this standard, the ZigBee communication protocol was proposed for a wireless point-to-point communication for WBMS [181, 182]. Beyond, specific technologies for the ISM 2.4 GHz band have been employed such as wireless fidelity (Wi-Fi) [183] and Bluetooth Low Energy (BLE) [173]. In contrast, also sub-GHz ISM bands have been used for uplink-only communication from cell sensors to battery control units to minimize energy consumption, or in combination with a passive downlink using radio-frequency identification (RFID) technology at 13.56 MHz or with an active downlink using the 433 MHz ISM band [175, 184]. The average power consumption for an IEEE 802.15.4-compliant transceiver during data transmission was found to range from 26.8 to 54.0 mW, depending on the signal power level [179].

For wireless channel characterization, a battery emulator made of a metallic box was presented in Ref. [185], which emulates the free space within a battery pack for electromagnetic wave propagation. Different antenna types (wired helix, planar, ceramic/chip etc.) and frequency bands between 100 MHz and 3 GHz were analyzed in terms of channel transfer characteristics. As the metallic box

environment acts as a resonant cavity, a large amount of transmission modes was observed, leading to many resonant frequencies in the channel transfer function [185]. Further channel characterizations reported in Ref. [186] yielded increasing channel attenuation for larger distances between antennas as well as for a larger number of antennas. Finally, frequencies between 2.2 GHz and 2.6 GHz were found to be advantageous for a high number of antennas due to lower transmission power and reduced antenna size and cost [161, 186].

Some semiconductor companies already pronounced concepts or demos for wireless BMS, namely Analog Devices, Inc. [187], Maxim Integrated, Corp. [188], or even offer commercially available products such as the CC2662R-Q1 by Texas Instruments, Corp. [189]. However, there is still a need for optimization regarding wireless in-battery communications. On the one hand, it is still a challenging task to trade off a sufficient signal power level to avoid EMI caused by the EV's noisy environment [190] against minimum battery energy consumption. On the other hand, the electromagnetic compatibility (EMC) of wireless communications has to be assured to be compliant with automotive EMC regulations [178]. Communications coverage of all cells within the battery pack and reliability are still open topics [8]. Since there are no standards defining physical dimensions of automotive battery packs, their geometries and sizes differ largely, from which it is expected to significantly alter the wireless channel transfer characteristics [161]. However, the invariant channel topology of an assembled battery pack with fixed antenna locations might ease the channel estimation during operation.

3.3.3 Power Line Communications

PLC is considered another promising communications approach for automotive BMS as it combines several advantages of wired and wireless communications. Similarly to wireless communications, PLC comes along with the advantages of reduced wiring effort and weight [50, 59], less mechanical failure potential, eased maintenance, and the possibility of cell sensor integration without extra wiring [31]. In addition to these benefits, PLC still employs a wired communication utilizing the existing power line infrastructure, which makes it more cost-efficient [52] and more secure [31, 53] compared to wireless communications.

At present, PLC is widely employed in smart electricity grids [55] and smart home applications [52] with different standards available. Its spans from low-speed communications such as ripple control in electricity grids [50] to high speed communications such as power quality monitoring in buildings [52]. PLC technologies can be classified according to Refs. [50, 191] as follows.

(1) Ultra-Narrowband (UNB): Technologies that operate in the Ultra-Low Frequency (0.3–3 kHz) band or in the upper part of the Super-Low Frequency (30–300 Hz) band. UNB-PLC systems work at low data rates in the range of less than 100 bps but can convey information over tens to hundreds of kilometers.

(2) Narrowband (NB): Technologies that operate in the Very-Low Frequency, Low-Frequency, and Medium-Frequency bands (3–500 kHz). NB-PLC systems work at either low data rates of few kbps using single carrier technologies or at higher data rates up to 500 kbps using multicarrier technologies.

(3) Broadband (BB): Technologies that operate in the High-Frequency (2–30 MHz) and Very-High Frequency (30–300 MHz) bands. BB-PLC systems work at high data rates ranging from several Mbps to several hundreds of Mbps.

Standardization of PLC took a long journey [192], but there are regulations available such as standardization of NB-PLC for smart grid applications according to the Comité Européen de Normalisation Électrotechnique (CENELEC) standard EN 50065-1 [193]. Further initiatives, namely PoweRline Intelligent Metering Evolution (PRIME) [194] and G3-PLC [195] have proposed specifications for NB-PLC, which today provide the most commonly used international and open technology standards for advanced metering and grid control [191]. Considering BB-PLC, two worldwide standards, namely ITU-T G.hn [196] and IEEE 1901 [197], have been defined targeting in-home Local Area Networks (LANs) and internet access [192, 198]. Also in case of BB-PLC, several industry alliances were formed in the last decade proposing their own technology specifications, among them the Open PLC European Research Alliance (OPERA), the HomePlug Powerline Alliance, the Universal Powerline Association (UPA), the High Definition Power Line Communication (HD-PLC) Alliance, and The HomeGrid Forum [52, 191]. Due to the large number of specifications, IEEE 1901 has been defined to provide coexistence and interoperability between different PLC standards [197]. For further details about the latest standardization developments, the reader is referred to Ref. [191].

In contrast to PLC for smart grid and smart buildings, PLC for in-vehicle communications is considered only by a few research groups and no dedicated technology has been developed yet [56]. Reported literature about in-vehicle PLC can be divided into (1) traditional 12 V low voltage (LV) PLC for communication between EV peripherals such as dashboard and lights [56], and (2) PLC for in-battery communications denoted as "HV PLC" in this work, which was originally proposed in Ref. [49]. In fact, most of the reported works deal with traditional LV PLC such as Refs. [53, 56, 199, 200], also known as DC bus technology. However, LV PLC differs largely from HV PLC for in-battery communications as can be seen from Figure 16. In contrast to LV PLC, the topology of HV PLC is structured as a daisy-chain, where all PLC nodes are connected in series. Consequently, specific design aspects such as a missing common ground (GND) reference and low PLC access impedances require a new design concept for HV PLC that will be presented in Chapter 5. Because the access impedance of HV PLC is predominantly defined by the Li-ion cell impedance at high frequencies in the megahertz range, identifying HF characteristics of Li-ion cells is inevitable and will be addressed in Chapter 4.

(a)   (b)
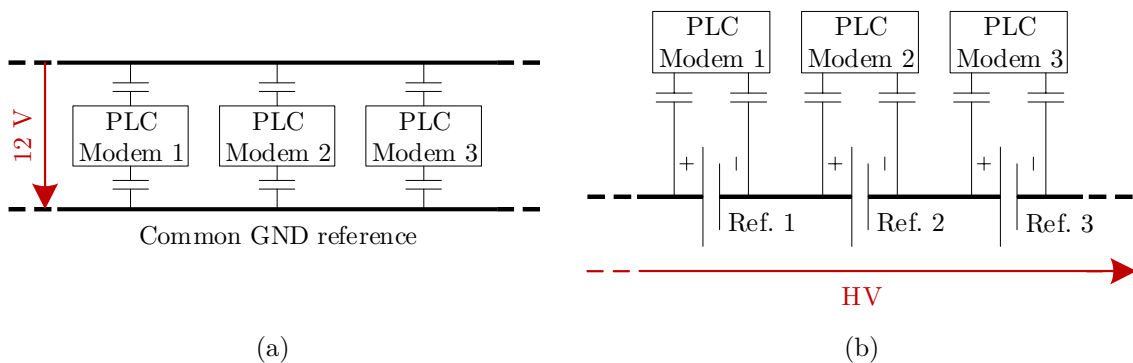
Figure 16: Different topologies for in-vehicle PLC. (a) Traditional DC bus technology used for LV PLC exhibiting one global ground reference. (b) Concept of daisy-chain HV PLC intended for in-battery communications exhibiting as many local ground references as PLC modems.

4 High Frequency Characteristics of Li-ion Batteries

As more and more dynamic battery applications start emerging such as fast charging [201], wireless power transfer [202], and power line communications [57], the high frequency behavior of Li-ion batteries receives growing interest. Important tasks include the prediction of battery performance degradation due to fast-switching power electronics [203] or verification of the electromagnetic compatibility of high voltage traction batteries [204]. Also PLC system design requires profound knowledge about the HF characteristics of Li-ion cells because PLC frequencies are allocated in the megahertz range to fulfill high requirements on data rate, robustness, and electromagnetic compatibility as will be pointed out in Chapter 5. Thereby, the HF cell impedance is the most important measure to examine the PLC system performance [57]. However, battery impedance characterization is typically motivated by electrochemical process identification, and EIS measurements therefore focus on the low frequency region below 10 kHz [68]. Due to this fact as well as EIS equipment limitations at high frequencies, there is only little work available investigating the HF properties of Li-ion batteries. For this reason, the often visible characteristic bend of the impedance curve in the Nyquist plot as shown in Figure 17 at frequencies above the intercept frequency is not fully understood. The observable increase in resistance has been interpreted in different ways in literature, for example, by the skin effect [74, 75], by the interaction between inductive and resistive losses in the jelly roll [69, 205], or simply by measurement errors due to parasitic inductances [112]. In the latter case, the bending is often ignored and ideal inductive behavior is assumed [206] as marked by the dashed red line in Figure 17.

The goals of this chapter are therefore to clarify the electrochemical or electrophysical effect responsible for the impedance curve bending, and also to model the overall HF behavior of Li-ion batteries up to 300 MHz, covering all frequencies of interest of the above-mentioned applications.
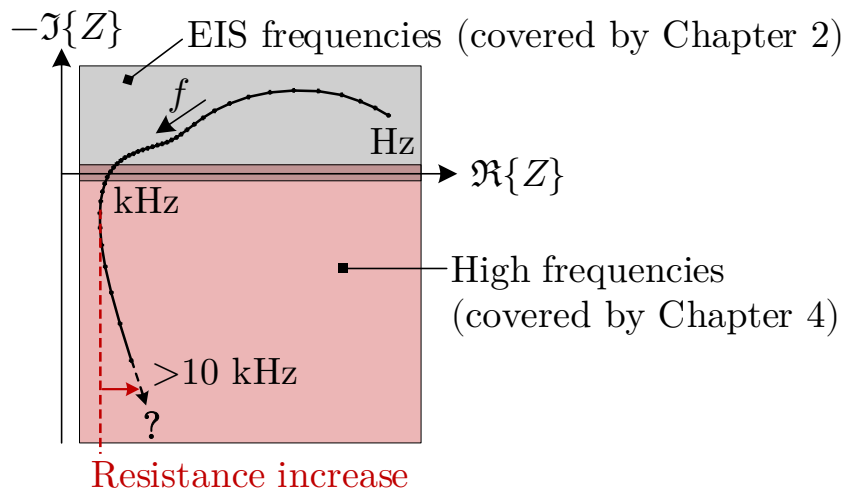
Figure 17: Typical impedance locus of a Li-ion cell determined by EIS measurements, focusing on electrochemical process identification. Frequencies larger than 10 kHz are often not covered and the visible characteristic resistance increase at higher frequencies is either ignored or attributed to various electrophysical effects. The further impedance locus will therefore be investigated in this chapter.

Section 4.1 introduces a novel methodology for battery impedance measurements, which overcomes frequency and accuracy restrictions of existing measurement techniques. In Section 4.2, the measurement methodology is applied to a cylindrical Li-ion cell for HF impedance characterization. HF-relevant electrochemical and electrophysical loss processes as summarized in Figure 4 are explicitly investigated and modeled as equivalent electrical circuit (EEC). Dependencies of the HF impedance behavior on cell design and cell state are investigated in Section 4.3 on eight different cylindrical Li-ion cells.

4.1 High Frequency Impedance Characterization Methodology

In this sections, a measurement methodology is developed for battery impedance characterization for high frequencies. Several circumstances make the battery impedance characterization of Li-ion batteries for high frequencies challenging. First, the low impedance of Li-ion batteries causes significant reflections of electromagnetic waves, which can lead to impedance measurement errors at high frequencies without proper calibration [207]. Secondly, because wavelengths shorten towards the dimensions of the battery, the physical length of the cell cannot be neglected anymore and the connection between the cell and the measurement equipment needs to be designed explicitly to remove systematic errors caused by connection impedances as well as inductive and capacitive coupling effects [207]. Both aspects are typically not covered by conventional EIS measurement equipment and are therefore addressed by the following two sections. Section 4.1.1 presents the development of the impedance measurement method, while Section 4.1.2 extends the method to a more generalized methodology for different battery types and more flexible calibration and compensation procedures.

4.1.1 A Novel Method for High Frequency Battery Impedance Measurements

This section introduces the paper *A Novel Method for High Frequency Battery Impedance Measurements* and is based on the paper without further reference.

The goal of this paper was to develop a measurement method for low impedances, which can deal with signal reflections, offers adequate calibration and de-embedding procedures, and is not restricted in high frequency. The resulting method employs a vector network analyzer (VNA) as primary measurement device, which measures the scattering parameters (S-parameters) of a two-port device for high frequencies. Different VNA techniques are available for impedance measurements, namely the reflect, the series-through, and the shunt-through method, all of which are optimized for different impedance value ranges [208]. Accordingly, the shunt-through method was used in the presented paper as it is optimized for low impedances [155]. For the impedance measurements, an ICR18650-26J Li-ion cell by Samsung SDI Co., Ltd. (Yongin, South Korea) [209] was used. The connection between cell and the coaxial-connector-based VNA measurement equipment was realized by a custom-built printed circuit board (PCB) as depicted in Figure 18, whereon the battery was mounted by soldering using a specific solder with low liquidus temperature to prevent the cell from harmful heating. Both VNA ports are connected to the same battery terminal as required by the shunt-through method. The current loop is closed by the bottom GND layer of the PCB. The measurement reference plane of the VNA was shifted by calibration and compensation procedures to plane B as indicated in Figure 18.
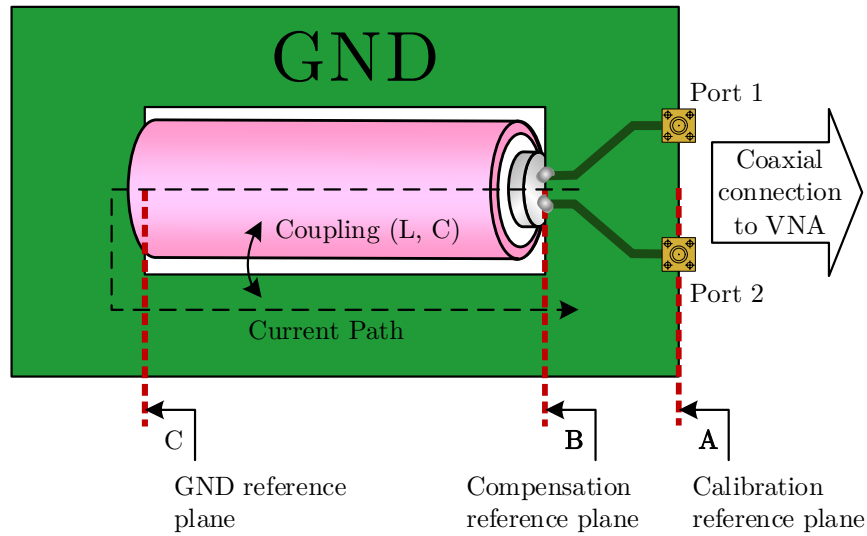
Figure 18: Principle structure of the battery PCB fixture used for the HF impedance measurements. The battery cell is mounted on the fixture by soldering. Depending on the reference plane used for the VNA measurement, all electrical components on the plane's left side are measured.

Impedance measurements conducted at reference plane B include all electrical components that are on the left side of the plane, including PCB trace impedances and electromagnetic coupling effects. Since the battery is only a part of this impedance, it was mathematically extracted from the measurement by de-embedding procedures. A reference measurement of a solid copper (Cu) cylinder combined with a three-dimensional (3-D) electromagnetic (EM) model were used for de-embedding of the cell impedance and for validation of the measurement method. The measured battery impedance of the ICR18650-26J is very low-ohmic for low frequencies (40 mΩ for 1 kHz), yet increases largely for high frequencies (40 Ω for 300 MHz) mostly due to the inductance of the cell.

Authors contribution   Development of the measurement method and execution of the experiments were performed by Thomas F. Landinger. Data processing and simulations were also conducted by Thomas F. Landinger. The printed circuit board was conceptualized by Guenter Schwarzberger and Thomas F. Landinger and was designed by Guenter Schwarzberger. Andreas Jossen supervised this work. The original draft was written by Thomas F. Landinger and was reviewed and edited by all authors.

A Novel Method for High Frequency Battery Impedance Measurements

Thomas F. Landinger, Guenter Schwarzberger, Andreas Jossen

A Novel Method for High Frequency Battery Impedance Measurements

Thomas F. Landinger, Guenter Schwarzberger
Infineon Technologies AG
Munich, Germany
thomas.landinger@infineon.com

Andreas Jossen
Institute for Electrical Energy Storage Technology
Technical University of Munich (TUM)
Munich, Germany
andreas.jossen@tum.de

Abstract—**Electrochemical Impedance Spectroscopy (EIS) is widely used to measure the impedance of lithium-ion (Li-ion) battery cells. The EIS focuses on frequencies from millihertz to kilohertz, since the electrochemical processes do not have shorter time constants. To investigate high frequency phenomena as the electromagnetic compatibility (EMC) of an automotive traction battery, impedance measurements also in the higher megahertz range are necessary. State-of-the-art EIS measurement devices for batteries do not meet the requirements of this application, as they can cause electromagnetic wave reflections and do not provide sufficient calibration techniques. In this paper, we present a method to determine the battery impedance for a wide frequency range from 1 kHz to 300 MHz. Using a vector network analyzer, two-port scattering parameters (S-parameters) of a 18650 Li-ion cylindrical cell are measured with the shunt-through method. The resulting cell impedance is 40 mΩ at 1 kHz and increases to 40 Ω at 300 MHz mainly due to the external inductance of the cell.**

Keywords—automotive traction battery, electrochemical impedance spectroscopy, 18650 cell, high frequency impedance, shunt-through method, partial inductance.

I. INTRODUCTION

Lithium-ion (Li-ion) battery cells are the state-of-the-art technology for electric vehicle (EV) traction battery systems. They offer the highest energy density among all commercially available battery types. The characterization of the dynamic behavior of a Li-ion cell is essential for designing the traction battery system. One frequently used technique for the characterization is the Electrochemical Impedance Spectroscopy (EIS). Using EIS, the cell is excited by single or multi tones and its response is measured. The magnitude and phase ratio of the force and sense signals give the complex impedance of the cell versus frequency [1]. Traditionally, EIS is performed up to several tens of kHz, since the chemical processes do not occur faster [2]. However, various research topics require battery impedance characterization also for high frequencies (HF) as far as several hundreds of MHz. For instance, knowledge about the battery's HF properties is necessary to determine the electromagnetic compatibility (EMC) of the high voltage traction battery [3] as well as predicting the influence of the power inverter's current ripples on the battery performance degradation [4]. Another benefit is to evaluate the battery's capability for power line communications (PLC), wherein the battery serves as a transmission channel and data are sent over the high voltage power line [5, 6].

For measuring the HF impedance of a battery cell, the traditional EIS is no longer sufficient since there is a huge impedance mismatch between source, load and characteristic line impedances. In the galvanostatic mode, for example, the EIS force and sense ports are high ohmic, whereas the battery cell is low ohmic. This leads to multiple reflections, which may distort the measurement. Additionally, conventional cables are used that are mechanically not fixed. This leads to scattered reflections as the characteristic line impedance varies along the cables. In addition, inductive coupling between force and sense leads is a problem when using conventional cables. Not every EIS measurement device offers calibration techniques. However, as wavelengths become short and in the dimensions of the wire lengths, the calibration is crucial for correct measurements.

To overcome these problems, an HF alternative to the EIS is necessary. In literature, there are commonly three different approaches reported. The most straightforward way is to measure voltage and current in the time domain, as done in the EIS, but with HF-capable devices [7]. However, for wideband impedance measurements this solution may be time-consuming. As a second solution, researchers use dedicated impedance analyzers for HF battery impedance measurements [5, 7 – 11]. They provide a high accuracy but often have a limited frequency range. To overcome this limitation, the third way is to connect a vector network analyzer (VNA) to the battery, measure the scattering parameters (S-parameters), and convert them into impedance values. The authors in [6] and [12] both did a 1-port reflection measurement that has typically a lower accuracy than a 2-port measurement. In [3], the authors performed a 2-port measurement with the series-through method. However, as Li-ion batteries have very low impedances in the milliohm range, VNA suppliers do not recommend this setup. Instead, in this work we measure the battery impedance of an 18650 cell using an Agilent E5061B VNA together with the shunt-through method as suggested in [13]. This method has not been applied to Li-ion batteries before.

As important as the measurement method is the connection of the cell to the measurement device. The battery's physical length makes the definition of a measurement reference plane difficult. In [12], a cylindrical fixture was designed to provide a return path to the battery current and so allowing the definition of a reference plane at one pole of the cell. The disadvantage of this approach is a complex de-embedding procedure. Consequently, in this paper we develop a novel cell fixture that eases the de-embedding work significantly. In addition, the novel method accounts for the external inductance of the cell, which was not done in previous high frequency cell impedance studies.

This paper is organized as follows: section II introduces the shunt-through method and shows how the method is implemented in the measurement setup. In section III, the cell fixture is presented. Section IV points out how we removed the fixture's impact on the measurement. In section V, the results for an 18650 cell are presented and validated. The paper concludes with section VI.

II. Measurement Setup

A. Measurement Method

The VNA shunt-through method is the HF equivalent to the dc four-terminal sensing also known as Kelvin sensing, which makes it the best choice for low impedance measurements [14]. Fig. 1 shows the measurement setup. Both VNA ports are connected via a dc block to the positive battery pole and form a Kelvin probe. Port 1 serves as a current source and port 2 is used to measure the voltage across the battery. Due to the small impedance of the cell, most of the current will be reflected back to port 1 leading to a reflection coefficient S_{11} close to one. Hence, a slight change in the cell impedance does not lead to a reliably detectable change in S_{11}.
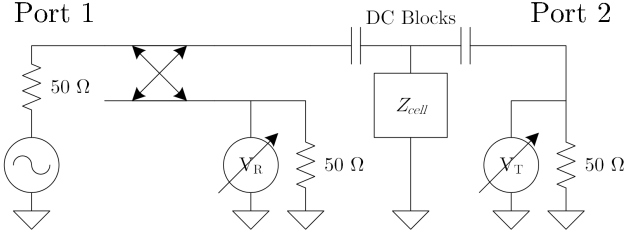
Fig. 1. Measurement setup using the VNA shunt-through method.

If we instead measure the voltages V_T and V_R and calculate the transmission coefficient S_{21} with

$$S_{21} = V_T / V_R , \qquad (1)$$

we get valuable information about the small voltage across the battery. The sensitivity of S_{21} is much higher than that of S_{11} since S_{21} is close to zero and a slight change in the cell impedance will lead to a relatively large change in S_{21}. With

$$Z_{cell} = \tfrac{1}{2} Z_0 \cdot S_{21} / (1 - S_{21}) \qquad (2)$$

we get the impedance Z_{cell} of the cell for the characteristic impedance Z_0, which is 50 Ω in this work.

B. Dynamic Range

Typically, VNAs provide a wider frequency range than impedance analyzers, with comparable accuracy [13]. The latter is only true if the dynamic range of the VNA is sufficient for the measurement. If we assume a minimum impedance of 40 mΩ of the investigated 18650 cell, S_{21} can be derived from (2) and the maximum insertion loss (IL) of the cell is

$$IL = 20 \cdot \log_{10} (|S_{21}|) = -55.93 \text{ dB} \qquad (3)$$

In order to protect the VNA against dc stress, inner dc blocks are inserted between the battery and the VNA ports. The dc blocks contain a series capacitor each, which are specified by a maximum insertion loss of 1 dB above 1 kHz. Altogether, the excitation signal coming from port 1 undergoes an attenuation of almost 58 dB. The dynamic range subtracted from the maximum output power of the port, defines the smallest signal power level that the VNA

can detect out of the noise floor. In our case, the VNA reaches a dynamic range of 100 dB above 1 kHz [15]. With the maximum output power of 10 dBm, this results in a minimum detectable signal power level of − 90 dBm. For the cell measurement, the power level of the excitation signal is set to − 17 dBm, which is a tradeoff between maximizing the signal to noise ratio and ensuring the battery state to remain in the linear condition. Using the maximum insertion loss of (3), the resulting minimum power level at port 2 is −75 dBm, which is well detectable by the VNA.

III. Cell Fixture Developement

Since the battery cannot be connected directly to the coaxial-connector based test system, a printed circuit board (PCB) fixture was designed and is shown in Fig. 2. Two microstrip lines with the characteristic impedance of 50 Ω connect the SMA jacks X1 and X2 with the positive pole of the battery. The lines are placed in an angle of 90 degrees to each other to reduce coupling effects between the force (X1) and the sense (X2) path. The battery itself is located in the cutout of the PCB. The negative pole of the cell contacts the ground (GND) plane of the PCB providing a return path for the battery current. Fig. 3 shows the current distribution on the PCB, which was simulated with a three-dimensional (3D) model using CST Microwave Studio. A solid copper cylinder with the same dimensions as the battery serves as a cell dummy in the simulation. The current flows through the cylinder, back at the edges of the cutout and beneath the microstrip line back to the SMA connectors. To obtain the cell impedance data, the influence of the PCB fixture needs to be compensated.

Fig. 2. Printed circuit board cell fixture with microstrip traces and SMA connectors. X1 is connected to port 1 and X2 is connected to port 2 of the VNA.
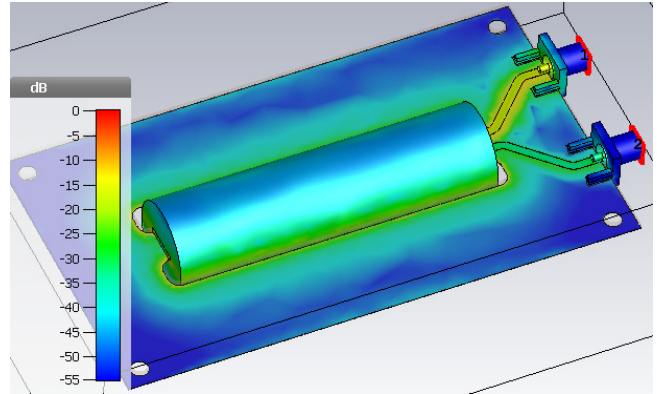
Fig. 3. Normalized current distribution on the PCB for 100 MHz during X1 excitation.

IV. CALIBRATION AND ERROR CORRECTION

To remove the fixture's impact on the measured impedance data, we used calibration and port extension procedures, which are provided by the VNA, and a novel de-embedding procedure that was developed in this work.

A. Calibration and Port Extension

A short, open, load and thru (SOLT) calibration was performed to remove all systematic errors in the coaxial section of the test system. To shift the measurement reference plane to the positive pole of the cell, the automatic port extension (APE) was performed, which is a response calibration that corrects for both delay and loss of the microstrip lines. For the response calibration, we used an open standard.

B. De-Embedding Procedure

During the measurement, the excitation current flows through the battery to the negative pole and back on the ground plane of the PCB to the SMA connector. The physical dimensions of the battery cell cause a non-negligible delay and loss of the signal on its way back on the ground plane. For instance, a sinusoidal signal with a frequency of 200 MHz has a wavelength of 72 cm for a typical microstrip line with a relative permittivity ε_r of 4.3. The length of the 18650 cell, which is 6.5 cm, leads to a phase shift of more than 32 degrees. In other words, the resistance and the inductance of the signal's return path on the ground plane affect the measurement significantly and therefore cannot be neglected. If the physical length of the battery stays below the critical length, which is 1/10 of the wavelength as a rule of thumb, the return path on the ground plane can be modeled as a simple RL lumped element circuit, which is illustrated in Fig. 4. Since there are two ways for the current to return – to either the right or the left of the cell – the ground self-partial inductance L_{gnd} and the ground resistance R_{gnd} are considered twice. The elements C_{TL} and L_{TL} model the microstrip transmission line, which the automatic port extension procedure already accounts for. The SMA ports are labeled with X1 and X2, respectively. For the sake of simplicity, the cell is modeled as a simple RL series circuit, which is sufficient for the subsequent considerations. Since only frequencies beyond 1 kHz are investigated, including the
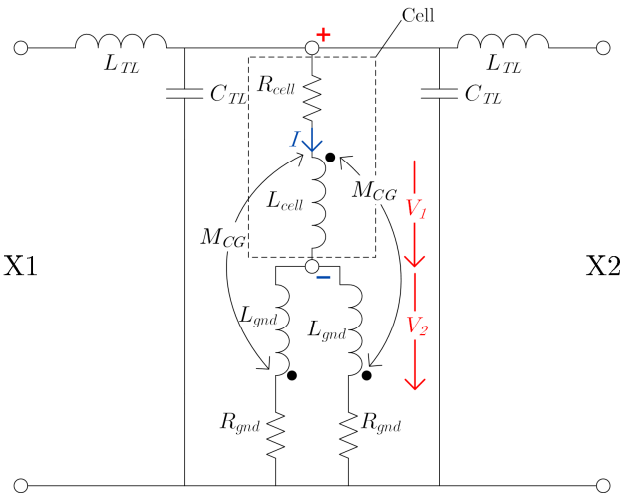
Fig. 4. Schematic of the PCB fixture.

capacitive behavior of the cell in the de-embedding procedure is redundant. The cell and the ground return path together form a current loop, which results in an effective loop inductance L_{eff}. As reported in [16], the return lead of a current loop partly compensates for the external magnetic field of the signal lead. Thus, the measured effective loop inductance L_{eff} of the cell in the PCB is smaller than the self-partial inductance L_{cell} of the cell. This phenomenon is due to inductive coupling and is described by the concept of mutual inductance [17]. Of course, a self-partial inductance cannot be measured directly, because the test current always needs a return path. To de-embed L_{cell} from the loop inductance, the mutual inductance M_{CG} between L_{gnd} and L_{cell} has to be considered. Using Kirchhoff's laws and Faraday's law of induction, the voltages V_1 and V_2 indicated in Fig. 4 can be expressed as

$$V_1 = I \cdot j\omega L_{cell} - I/2 \cdot j\omega M_{CG} - I/2 \cdot j\omega M_{CG}, \quad (4)$$

$$V_2 = I/2 \cdot j\omega L_{gnd} - I \cdot j\omega M_{CG}. \quad (5)$$

With Ohm's law, (4) and (5) can be reformulated and by including the resistances the measured effective impedance is

$$Z_{eff1} = R_{cell} + j\omega (L_{cell} - M_{CG}) + R_{gnd}/2 + j\omega (L_{gnd}/2 - M_{CG}). \quad (6)$$

In order to extract the elements R_{cell} and L_{cell}, a second impedance measurement of a known reference is necessary. In addition, the reference must have the same external inductance as the cell. As stated in [12], the cell's external inductance can be modeled by a conducting cylinder with almost the same diameter as the battery. In this work, a solid copper cylinder was manufactured as reference impedance, which has the same dimensions as the 18650 cell. The measured effective impedance of the copper cylinder in the PCB fixture can be written in the same way as (6) by

$$Z_{eff2} = R_{Cu} + j\omega (L_{Cu} - M_{CG}) + R_{gnd}/2 + j\omega (L_{gnd}/2 - M_{CG}) \quad (7)$$

where R_{Cu} is the resistance and L_{Cu} the self-partial inductance of the copper cylinder. If we now calculate the difference between (6) and (7), the resistance and self-partial inductance of the ground plane as well as the mutual inductance cancel out, because they have the same values in both measurements. The mutual-partial inductances M_{CG} in (7) remain unchanged due to the same external magnetic field of the cylinder. Solving (6) – (7) for the cell impedance:

$$Z_{cell} = R_{cell} + j\omega L_{cell} = Z_{eff1} - Z_{eff2} + R_{Cu} + j\omega L_{Cu}. \quad (8)$$

The copper cylinder's complex impedance can be derived analytically. Due to the skin effect, both the resistance and the inductance of the copper cylinder are frequency dependent. The resistance can be divided into a constant dc part and a variable ac part, which increases with the frequency. Due to the thickness of the cylinder, the dc part is only a few micro-ohms and can be neglected. The cylinder's self-inductance comprises an internal and an external inductance. For low frequencies, the sum of both parts form the cylinder's self-inductance. For higher frequencies, the magnetic field within the cylinder is negligible and only the
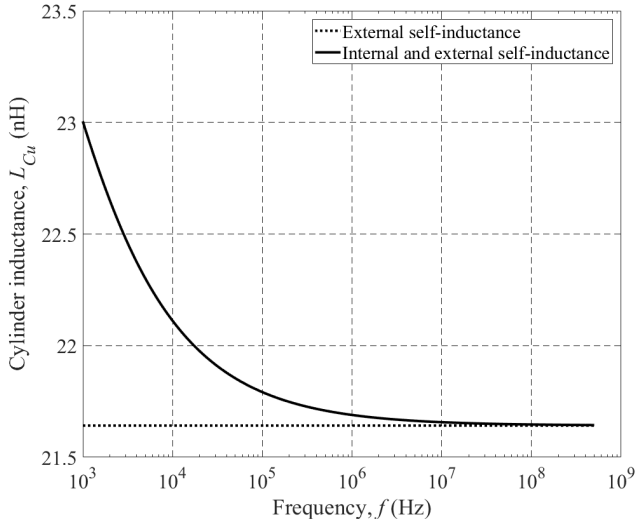
Fig. 5. Analytical self-inductance of the copper cylinder comprising internal and external inductance.
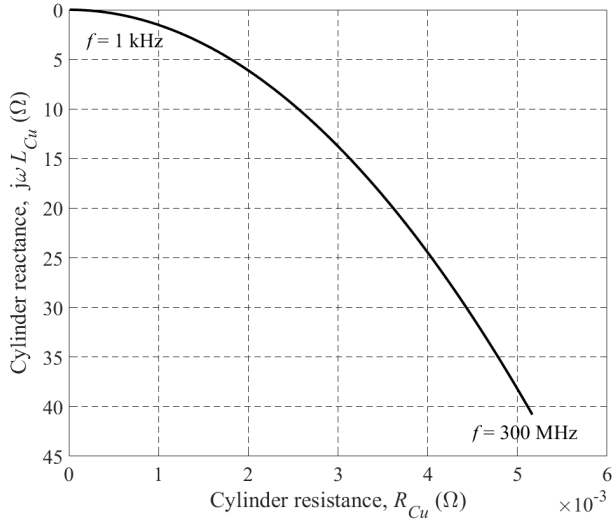
Fig. 6. Analytical impedance spectrum of the copper cylinder.
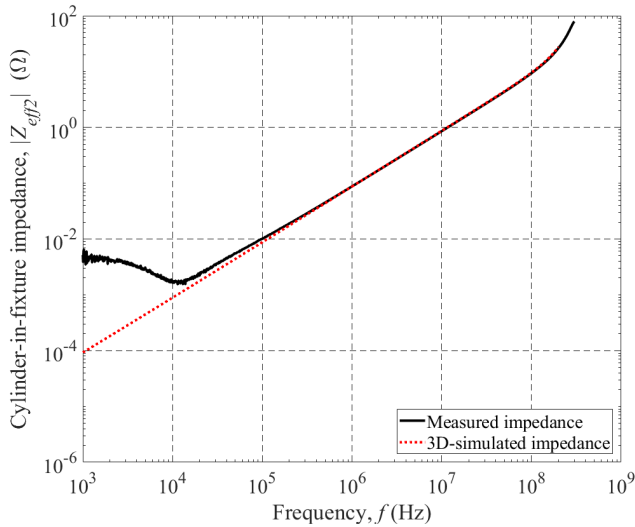
Fig. 7. Measured and 3D-simulated impedance of the copper cylinder mounted on the PCB fixture.

external magnetic field defines the self-inductance. Using formulas from [10] and [18], the cylinder's self-inductance was calculated. The external and the complete self-inductance of the copper cylinder are illustrated in Fig. 5 and the resulting impedance spectrum is shown in Fig. 6.

The capacitive coupling between the cell and the ground return path is not yet included in the de-embedding procedure. By adding coupling capacitances in parallel to the RL ground circuits in Fig. 4, it can be shown that (8) also accounts for capacitive coupling, since the capacitances eventually cancel out in the subtraction of the two impedance measurement data.

V. RESULTS AND VALIDATION

The impedance measurement was carried out on a new Samsung 18650 Li-ion cell with a state of charge (SOC) of 50 % in the frequency range from 1 kHz to 300 MHz. First, we measured the impedance of the copper cylinder mounted on the PCB fixture, which is shown together with the 3D simulation result in Fig. 7. To illustrate the comparison correctly in Fig. 7, the APE of the VNA was switched off since the simulation does not provide this feature. This can be noticed from the curve bending at the highest frequency decade in Fig. 7. For the evaluation, the APE was switched on again. There is a large deviation between measurement and simulation in the lower frequency range, which is due to the simplified 3D model of the cylinder, which is only a one-dimensional high frequency surface impedance model [19]. For higher frequencies the simulation result matches the measurement result and thus validates it. Secondly, we measured the impedance of the cell mounted on the PCB fixture, which is illustrated in terms of magnitude and phase in Fig. 8 and 9. As final step, the synthesis according to (8) was done and can also be seen in Fig. 8 and 9. The magnitude of the de-embedded cell impedance starts with 40 mΩ at low frequencies and increases up to 40 Ω at 300 MHz, which is mainly because of the cell's reactance as signified in the Fig. 10. The increase of the de-embedded impedance is higher than that of the cell-in-fixture impedance. This is due to the external inductance of the cell, which is compensated when the cell is mounted on the PCB fixture. For validation, the cell impedance at 1 kHz was also measured by a Zahner Zennium EIS measurement device and exhibited 40 mΩ, too.

VI. CONCLUSIONS

In this paper, we presented a novel method to determine the high frequency impedance of a Li-ion battery cell from 1 kHz to 300 MHz. Vector network analysis was applied to measure the cell impedance with the shunt-through method. A microstrip based PCB fixture enabled a reliable connection between the cell and the coaxial-connector based measurement equipment. To remove the fixture's impact on the measurement, a second reference impedance was measured. For this aim, a solid copper cylinder was fabricated. The resulting cell impedance is higher than in previously published data, since the external inductance of the cell is included in the measurement. The external inductance accounts for most of the inductance at high frequencies. The next steps are to fit different battery models to the impedance measurement results and investigate the influence of different cell connectors.

Fig. 8. Measured impedance magnitude of the cell mounted on the PCB fixture and de-embedded impedance using (8).

Fig. 9. Measured impedance phase of the cell mounted on the PCB fixture and de-embedded phase using (8).

Fig. 10. Impedance spectra of the cell mounted on the PCB fixture and de-embedded impedance using (8)

REFERENCES

[1] E. Barsoukov and J. R. Macdonald, Eds., *Impedance Spectroscopy: Theory, Experiment, and Applications*. Hoboken, New Jersey: John Wiley & Sons, Inc., 2005.

[2] A. Jossen, "Fundamentals of battery dynamics," *Journal of Power Sources*, vol. 154, no. 2, Mar., pp. 530-538, 2006.

[3] M. Reuter, S. Tenbohlen and W. Köhler, "Influence of a traction battery's input impedance on conducted emissions of an automotive HV inverter," *2013 International Symposium on Electromagnetic Compatibility*, Brugge, 2013, pp. 229-234.

[4] M. J. Brand, M. H. Hofmann, S. S. Schuster, P. Keil and A. Jossen, "The Influence of Current Ripples on the Lifetime of Lithium-Ion Batteries," in *IEEE Transactions on Vehicular Technology*, vol. 67, no. 11, pp. 10438-10445, Nov. 2018.

[5] I. Ouannes, P. Nickel and K. Dostert, "Cell-wise monitoring of lithium-ion batteries for automotive traction applications by using power line communication: battery modeling and channel characterization," *18th IEEE International Symposium on Power Line Communications and Its Applications*, Glasgow, 2014, pp. 24-29.

[6] A. P. Talie, W. A. Pribyl and G. Hofer, "Electric Vehicle Battery Management System Using Power Line Communication Technique," *2018 14th Conference on Ph.D. Research in Microelectronics and Electronics (PRIME)*, Prague, 2018, pp. 225-228.

[7] T. Doersam, S. Schoerle, E. Hoene, K. -. Lang, C. Spieker and T. Waldmann, "High frequency impedance of Li-ion batteries," *2015 IEEE International Symposium on Electromagnetic Compatibility (EMC)*, Dresden, 2015, pp. 714-719.

[8] C. Bolsinger, J. Brix, M. Dragan and K.P. Birke, "Investigating and modeling the transmission channel of a prismatic lithium-ion cell and module for powerline communication," *Journal of Energy Storage*, vol. 10, Apr., pp. 11-19, 2017.

[9] M. Raya and R. Vick, "A simulation method to determine the RF impedance of batteries," *2017 International Symposium on Electromagnetic Compatibility - EMC EUROPE*, Angers, 2017, pp. 1-5.

[10] E. Hoene, S. Guttowski, R. Saikly, W. John and H. Reichl, "Rf-properties of automotive traction batteries," *2003 IEEE International Symposium on Electromagnetic Compatibility, 2003. EMC '03.*, Istanbul, 2003, pp. 425-428 Vol.1.

[11] M. S. Tabbakh, F. Morel, R. Mrad and Y. Zaatar, "High frequency battery impedance measurements for EMI prediction," *2013 IEEE International Symposium on Electromagnetic Compatibility*, Denver, CO, 2013, pp. 763-767.

[12] A. R. Ruddle, J. Chen and Y. X. Teo, "Measurement of rf impedance for automotive 18650 cylindrical lithium ion cells," *2017 International Symposium on Electromagnetic Compatibility - EMC EUROPE*, Angers, 2017, pp. 1-6.

[13] Keysight Technologies, Appl. Note 5991-0213EN, pp. 1-17.

[14] Keysight Technologies, Appl. Note 5989-5935EN, pp 1-19.

[15] Agilent Technologies Technical Staff, *Agilent E5061B Network Analyzer Help*, Agilent Technologies, 2010.

[16] F. B. J. Leferink and M. J. C. M. van Doom, "Inductance of printed circuit board ground planes," *1993 International Symposium on Electromagnetic Compatibility*, Dallas, TX, USA, 1993, pp. 327-329.

[17] C. L. Holloway and E. F. Kuester, "Net and partial inductance of a microstrip ground plane," in *IEEE Transactions on Electromagnetic Compatibility*, vol. 40, no. 1, pp. 33-46, Feb. 1998.

[18] E. B. Rosa, "The Self and Mutual Inductances of Linear Conductors," *Bulletin of the Bureau of Standards*, vol.4, no.2, pp. 301-311, 1908.

[19] Dassault Systèmes, "CST Studio Suite ® 2018 Help". [Online]. Available: https://www.cst.com/products/cstmws. [Accessed: Dec. 04, 2018].
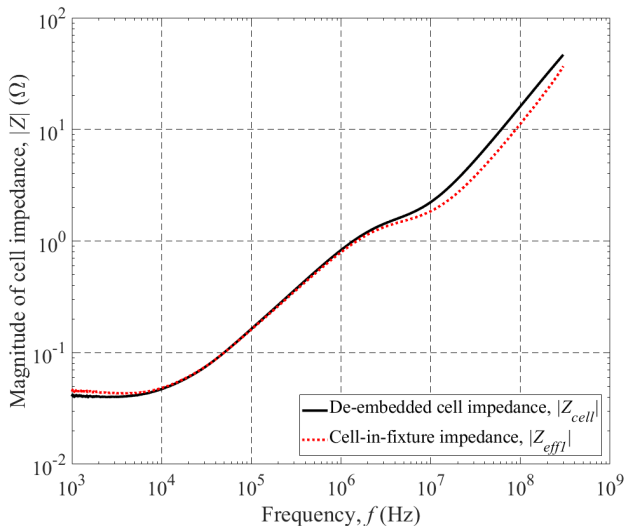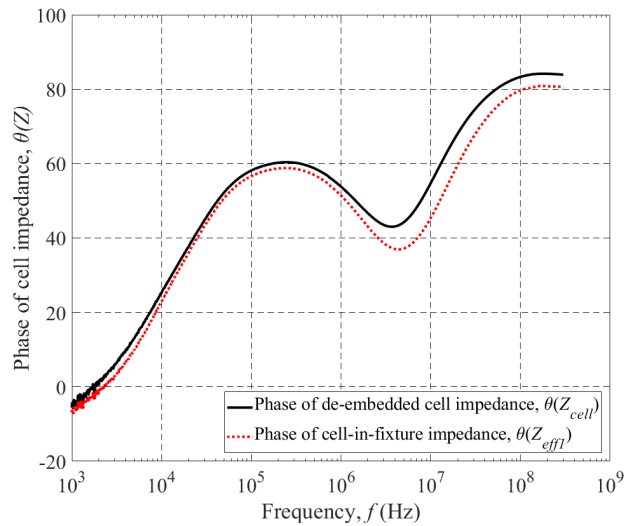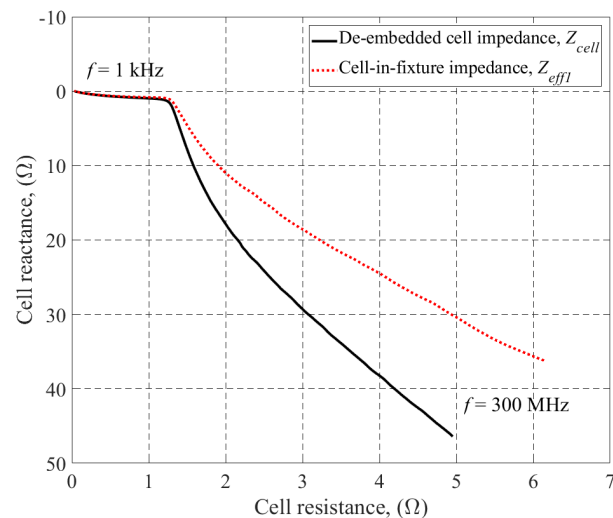
4.1.2 Li-Ion Cell Impedance Measurement Using Open/Short/Load Compensation for De-Embedding

This section extends the impedance measurement method of the previous section to a more generalized methodology and is based on the paper *Li-Ion Cell Impedance Measurement Using Open/Short/Load Compensation for De-Embedding* without further reference.

The extended measurement methodology is based on the VNA shunt-through method as applied in Section 4.1.1. However, the custom-built PCB of Figure 18 was replaced by a more generalized PCB that includes a battery cell holder for connecting the cell to the coaxial-connector based VNA. The usage of a cell holder makes the methodology more flexible and effortless since no soldering is required and the cell under investigation can be changed easily. A more general Open/ Short/ Load (OSL) compensation procedure was used for systematic error correction and de-embedding. Calibration standards ("Open", "Short", 50 Ω "Load") were designed as surface-mounted devices (SMDs) as well as cylindrical standards having the physical dimensions of an 18650 Li-ion cell (diameter of l8 mm, length of 65 mm). The latter calibration standards offer the advantage that a second measurement of a reference impedance (such as the Cu cylinder used in Section 4.1.1) is not necessary anymore and the VNA impedance measurement directly yields the de-embedded cell impedance after the OSL compensation.

Using both sets of aforementioned calibration standards, the OSL compensation approach was successfully validated by comparing impedance measurements of a Samsung ICR18650-26J Li-ion cell with a 3-D EM model, which was made of the PCB, the cell holder contacts, and the measured battery impedance imported as lumped-port element.

In order to demonstrate the robustness and flexibility of the OSL compensation procedure, different load impedances were connected in parallel to the battery cell. The impedance measurement results and therefore also the compensation procedure appeared to be load-independent. In other words, the HF impedance of the battery was shown to be load-independent within the considered frequency (10 kHz to 1 GHz) and load current range (below 10 mA). For example, a parallel load of 3 kΩ || 100 pF mimicking an IC powered by the battery was demonstrated not to influence the HF characteristics of the cell.

Authors contribution Conceptualization was done by Herbert Hackl and Thomas F. Landinger. Development of the measurement method and simulations were performed by Herbert Hackl. Reference data obtained by the original measurement method of Section 4.1.1 were provided by Thomas F. Landinger. Execution of the experiments, data processing, and visual presentation were performed by Martin Ibel. Scientific council was provided by David J. Pommerenke. Supervision and funding acquisition were in the responsibility of Bernhard Auinger. The original draft was written by Herbert Hackl and was reviewed and edited by all authors.

Li-Ion Cell Impedance Measurement Using Open/Short/Load Compensation for De-Embedding

Herbert Hackl, Martin Ibel, Thomas F. Landinger, David J. Pommerenke, Bernhard Auinger

Li-Ion Cell Impedance Measurement Using Open/Short/Load Compensation for De-Embedding

1st Herbert Hackl, 2nd Martin Ibel
[1]Silicon Austria Labs
TU-Graz SAL GEMC Lab, Austria
[2]Graz University of Technology, Austria
herbert.hackl, martin.ibel@silicon-austria.com

3rd Thomas F. Landinger
Infineon Technologies AG
Munich, Germany
thomas.landinger@infineon.com

4th David J. Pommerenke[3,1]
[3]Graz University of Technology
Institute of Electronics
Graz, Austria
david.pommerenke@tugraz.at

5th Bernhard Auinger[1,2]
bernhard.auinger@silicon-austria.com

Abstract—**Knowledge of battery cell impedance is crucial for the design of many modern applications, as well as for predicting their electromagnetic compliance. For detailed 3D simulation of battery packs, single cells are commonly replaced with simplified bodies enhanced by internal impedance data obtained from measurement on real cells. Thereby it is necessary to exclude all influence of the measurement setup, i.e. to de-embed the cell impedance from exterior properties. In this work, two approaches are presented to extract the impedance of an 18650 Lithium-ion (Li-ion) cell from within a battery holder on a printed circuit board (PCB), using Open/Short/Load compensation (OSLC) and a copper cylinder as reference. By adding components in series and parallel to the cell, it is verified that the extraction result is not impacted by PCB circuitry, and also that the cell's impedance is load-independent. Eventually, the test setup including Li-ion cell is replicated as electromagnetic (EM) simulation project. Two measurement-based methods to model the cell are compared, suitable for both 3D or circuit simulation. The frequency range under consideration is from 9 kHz to 1 GHz, whereas the presented approach proves reliable up to 200 MHz.**

Index Terms—**battery, high frequency impedance, 18650 cylindrical cell, Lithium-ion, Open/Short/Load compensation (OSLC), 3D simulation, S-parameter**

I. INTRODUCTION

Modeling of printed circuit boards (PCBs) and on-board circuitry is an always necessary task in daily electronics engineering and simulation of electronic magnetic compatibility (EMC). Many applications include batteries mounted to the PCB, nowadays often Li-ion types. When the battery is part of the circuit, it is inevitable to model its behavior in order to enable simulation of the complete system. Thus, battery modeling is a vivid field of research. In this work, the focus is on deriving a model of the cell's impedance based on S-parameter measurement.

Generally, there are two approaches to model battery cells for simulation: Often, the cell is regarded as a component within an electric network. Information of the cell's impedance and transient response is e.g. required to predict current ripples produced by power electronic devices switching a battery-powered line [1]. Here, the cell can be reduced to an equivalent circuit model. On the other hand, when modeling battery packs composed of many individual cells, the geometry becomes

additionally relevant, as (parasitic) coupling between cells will affect the overall impedance of the pack. An approach for suchlike problems is 3D simulation of the complete battery pack as discussed in [2]: For computational speed-up single cells are replaced with simplified bodies, e.g. conductive cylinders, which represent the cell's 'external' impedance, i.e. the capability to couple to its environment by mutual inductance or capacitive means. The 3D model is linked to an description of the real cell's 'internal' impedance, e.g. described with an equivalent circuit or lumped impedance port.

Methods to obtain the impedance of cylindric battery cells based on measurement and de-embedding were presented before. For instance, [3] designed a brass tube fixture, which impact on the measurement results is respected with an analytically derived equivalent circuit. The method was validated by the use of different sized tubes which all lead to the same cell impedance. [4] used a special PCB fixture were the cell needs to be soldered into. It featured well matched $50\,\Omega$ transmission lines which allowed to move the VNA calibration plane towards the battery by the VNA's built-in port extension function. The mutual inductance between cell and PCB was compensated by reference measurement with a copper cylinder dummy. The process is mathematically sound, but it was not validated whether the de-embedding yields the 'true' cell impedance. The method was applied in [5] to analyze eight different commercially available types of 18650 Li-ion cells. It shows that the internal geometrical structure has considerable impact on the high-frequency impedance (while state-of-charge has not). Thus, doing application-oriented simulation, a new cell model needs to be extracted whenever the battery type changes. Necessary workflow should to be effortless and used fixtures often reusable. No soldering should be required.

This work presents an alternative to above mentioned approaches, which does not require special fixture designs. The method first presented in [4] is extended by a more generalized way of de-embedding applying Open/Short/Load compensation (OSLC), which allows to obtain the cell impedance even when the battery holder is mounted anywhere on the PCB. The device used for demonstration is a single Lithium-ion cell of type Samsung ICR18650-26J in a battery holder mounted

Fig. 1. Photo of the PCB used in this work. It enables 2-port shunt-through S-parameter measurement, as well as connection of SMD loads in parallel and/or series to the battery holder. The PCB's bottom layer is a solid GND plane. Underneath most of the battery holder is another GND plane on the top layer, used to connect 'Short' and 'Load' between battery plus pole (left) and GND during OSL compensation with soldered standards, see Fig. 2.
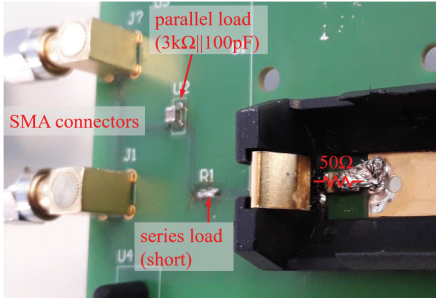
Fig. 2. Detail of the test PCB: Parallel and series SMD loads can be connected to the battery (here: $3\,\mathrm{k\Omega}\|100\,\mathrm{pF}$ in parallel to the cell). The photo shows the soldered connection of a $50\,\Omega$ standard for 'Load' compensation. Similar 'Short' standard was realized with a solder bridge.

to a simple PCB, see Fig. 1. Two different procedures are demonstrated in Sections II-A and II-B, one using common SMD (surface mount device) 'Short' and $50\,\Omega$ 'Load' (also called 'Match') standards, the other with specifically designed 18650 cylinder-sized calibration standards.

Furthermore, the PCB allows to add series or parallel loads. By applying the same procedure while mounting different loads, it is verified, that proposed method reliably removes the PCB's impedance from the wanted cell impedance. At the same time it is shown, that the battery cell impedance is load-independent (within considered frequency and load current range).

The purpose of de-embedding the battery is to use the cell-specific impedance data for simulation. Thus, the de-embedded data is validated in Section III by 3D simulation of the test PCB including battery and comparison of the simulated overall setup impedance to the original measurement result.

II. CELL IMPEDANCE DE-EMBEDDING BY OPEN/SHORT/LOAD COMPENSATION

An application-typical installation is employed, i.e. the cell is placed inside a PCB-mounted battery holder. For broadband measurement with a vector network analyzer (VNA) an interface PCB was designed as shown and described by Fig. 1. Soldered to the board is a battery holder for one 18650 cylindrical cell. (Similar PCB-mounted holders were used for PLC demonstration in [6].) The concept is visualized
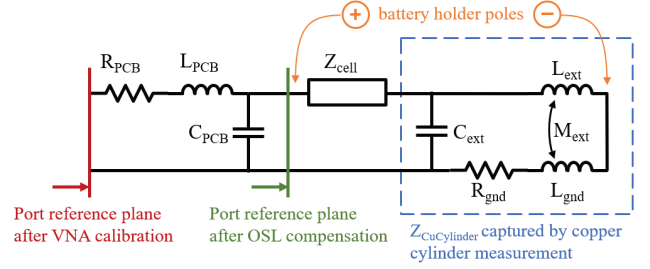
Fig. 3. OSL compensation is used to move the measurement's reference plane from the SMA connectors, i.e. the VNA calibration plane, towards the battery holder. Therewith, PCB parasitics as well as battery loads are excluded from the measurement result.

by Fig. 3: Accessible for VNA measurement are only the SMA connectors. After normal 2-port calibration of the VNA with connected coaxial cables, the SMA interface is the measurement port's reference plane (red). Open/Short/Load compensation (OSLC) [7] additionally to the VNA calibration allows to move the measurement's reference plane from the red to green marking. This is where the battery cell's plus pole is located. Ideally, OSLC removes all circuit components in between red and green reference planes, including the test fixture residuals, i.e. the PCB itself. We will test the limits of the procedure by adding series or parallel loads and comparison of the de-embedded cell impedance for loaded and unloaded scenarios later in this work.

The 2-port shunt-through method is employed (meaning both measurement ports are connected to the battery plus pole), because it is best suited for broadband measurement of very low impedances [8]. The device's impedance is calculated from the measured S_{21} parameter by

$$Z_{\mathrm{ShuThr}} = \frac{1}{2} \cdot Z_0 \cdot \frac{S_{21}}{1 - S_{21}} \qquad \text{where } Z_0 = 50\,\Omega. \quad (1)$$

For Open/Short/Load compensation the measurement is conducted without any device under test (DUT, i.e. the battery cell) but with calibration standards instead, being close to $0\,\Omega$ 'Short', close to $50\,\Omega$ 'Load' or nothing connected at all 'Open'. Afterwards, the DUT is connected and measured, yielding Z_{DUTmeas}. The impact of the PCB and additional loads is compensated according (2) [7], with the impedances being derived from (1) for respective measurement method. Z_{StdLoad} is the ideal value of whatever was used as 'Load' standard before, here $50\,\Omega$.

$$Z_{\mathrm{DUT,OSLC}} = Z_{\mathrm{StdLoad}} \frac{(Z_{\mathrm{Open}} - Z_{\mathrm{Load}})(Z_{\mathrm{DUTmeas}} - Z_{\mathrm{Short}})}{(Z_{\mathrm{Load}} - Z_{\mathrm{Short}})(Z_{\mathrm{Open}} - Z_{\mathrm{DUTmeas}})} \tag{2}$$

Depending on the size and position of the standards used for OSLC, more or less components of the setup are compensated as test fixture residuals. When OSL standards are connected directly between the battery holder's plus pole and GND, as in Fig. 2, then the reference plane is moved to the location illustrated by the green plane in Fig. 3. Application of (2) now yields the impedance measured in between plus pole

and GND. Alternatively, OSL standards could be connected in between the battery holder's plus and minus poles. Then, application of (2) would extract the impedance between these poles. In the next subsections both approaches are investigated.

A. OSLC with Soldered Standards and Copper Cylinder Reference

1) Workflow: Due to the specific layout of the used PCB, it is possible to connect the footprint of the holder's plus pole directly with the top layer GND plane by soldered 'Short' and 'Load' standards. As calibration standards a high precision $50\,\Omega$ SMD resistor (Load), a solder bridge (Short) or the untouched PCB (Open) are used, see Fig. 2. Such compensation will move the reference for measurement to the green plane of Fig. 3. As illustrated, $Z_{\text{DUT,OSLC}}$ measured at this location includes not only the cell's internal impedance Z_{cell}, but also the return path from the cell's minus pole via the GND plane R_{GND}, L_{GND}, mutual inductance M_{ext} between cell housing L_{ext} and L_{GND}, as well as capacitive coupling C_{ext} between cell and PCB.

Based on [4] and [9] it is assumed that a copper cylinder of 18650 size will resemble similar mutual inductive and capacitive coupling towards the PCB as the battery cell. Latter can thus be modeled as a series circuit of Z_{cell} and $Z_{\text{CuCylinder}}$ (3). (The model of [9] is a slightly smaller cylinder within a casing which is eventually found to be negligible.)

$$Z_{\text{cell-in-fixture,OSLC}} = Z_{\text{cell}} + Z_{\text{CuCylinder,OSLC}} \tag{3}$$

The workflow for cell impedance extraction is:

1) measure OSL standards Z_{Short}, Z_{Open} and Z_{Load} directly soldered to the PCB
2) place the copper cylinder in the battery holder and compensate the measurement result applying (2) to obtain $Z_{\text{CuCylinder,OSLC}}$
3) place the Li-ion cell in the battery holder and compensate the measurement result applying (2) to obtain $Z_{\text{cell-in-fixture,OSLC}}$. Use (3) to extract the internal cell impedance Z_{cell}.

The quality of the OSLC is assessed by plotting the measured values of Z_{Short}, Z_{Open}, Z_{Load} and the uncompensated cell-in-fixture Z_{DUTmeas} in Fig. 4. The 'Open' and 'Short' traces span a region of confidence (ROC). As long as the 'Load' trace is well above 'Short' and below 'Open', the compensation is regarded to yield a trustworthy result. The impact of additional loop inductance introduced by inserting the cell into the battery holder is well visible in this plot by the resonance frequency shift compared to the 'Short' trace, which exhibits the uncompensated PCB trace inductance L_{PCB} only. Also, the second order resonance at $500\,\text{MHz}$ (with DUT) or $600\,\text{MHz}$ (open PCB trace) is clearly visible. With this simple OSL compensation it is not possible to mitigate second-order effects.
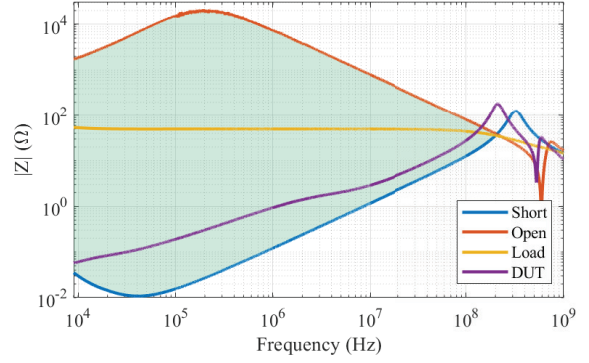
Fig. 4. Region of confidence (RoC) (transparent) for OSLC with standards soldered on PCB as shown in Fig. 2. DUT is the uncompensated Z_{DUTmeas} of the Li-ion cell inside the fixture. RoC upper frequency limit is $200\,\text{MHz}$.

2) Extraction Results With Different Loading Conditions: In [3] it is reported that impedance measurements from $100\,\text{kHz}$ to $200\,\text{MHz}$ on a 18650 Li-ion cell under unloaded condition, i.e. DC open circuit, or while drawing a DC current of appr. $70\,\text{mA}$ are indistinguishable. Therefore, it is assumed that loading conditions have no impact on the broadband cell impedance. However, existing works cover only DC loading and limited frequency range. Thus, with the following experiment of adding series and parallel loads on the PCB two question are addressed:

- verify whether described OSLC approach really enables to remove all influence of the PCB, and
- verify that the Li-ion cell's impedance is load-independent also for frequency-variant loading and within $9\,\text{kHz}$ to $1\,\text{GHz}$.

The complete workflow was repeated three times with following loading conditions. The extraction results are summarized by Fig. 5.

1) unloaded, i.e. no additional components on the PCB
2) $85\,\text{nH}$ series load added into the PCB trace. This increases the fixtures impedance at high frequency far beyond the wanted DUT value.
3) parallel load of $3\,\text{k}\Omega\|100\,\text{pF}$ added between battery plus pole and ground plane. This will continuously draw a DC current of about $1\,\text{mA}$ from the battery and becomes very low-ohmic at around $100\,\text{MHz}$. This loading condition should mimic an IC being powered from the cell.

The fact that de-embedding always yields the same internal cell impedance Z_{cell} regardless of the PCB circuitry validates proposed approach. Also, the cell impedance is load-independent over the complete frequency range, as expected.

It is visible from Fig. 5 that parallel loads with pronounced resonance behavior, like a capacitor, will in the region of its self-resonance disturb the compensation. However, the used $100\,\text{pF}$ was judged by the authors to be the maximum relevant value to mimic an IC input connected to the battery cell. Lower capacitor values will result in resonance well above
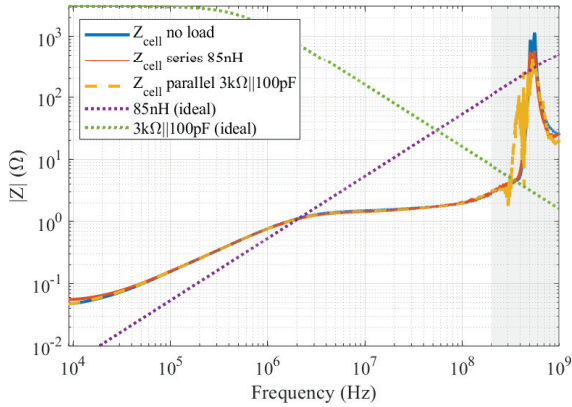
Fig. 5. Extracted cell impedances using OSLC with standards soldered to the PCB and (3). Loads are connected in series or parallel to the cell, compare Fig. 2. The well matching results verify, that proposed approach is capable of de-embedding the cell's impedance irrespective of the PCB circuitry. Shaded area is outside the RoC of Fig. 4.

the considered frequency range. Though, with the presented OSLC approach it might not be possible to mitigate the impact of large buffer capacitors (like $> 1\,\mathrm{nF}$) parallel to the battery. The approach also doesn't work with series loads much higher than the cell impedance, e.g. $100\,\Omega$.

B. OSLC Along Battery Holder with Cylinder Standards

1) Workflow: The extraction of Z_cell based on OSLC with soldered calibration standards as described above requires an additional reference measurement with a copper cylinder to obtain and exclude the 'external' cell impedance. As an alternative, this section presents compensation by use of self-built 18650-sized calibration standards, which mimic the battery cell. The idea is to have all external influences, i.e. the value of $Z_\mathrm{CuCylinder}$, already captured by the OSL measurements. The workflow is as follows:

1) Measurement of OSL standards, where 'Short' is a copper cylinder, 'Open' is the empty battery holder, and 'Load' is a two-part copper cylinder with internal $50\,\Omega$ SMD resistor as shown by Fig. 6.
2) Measurement of the Li-ion cell in the battery holder and compensation by (2) directly yields Z_cell.

Again the ROC is plotted in Fig. 7. ('Open' and 'DUT' traces are identical to Fig. 4.) The fact that 'Short' and 'DUT' traces are now similar above $20\,\mathrm{MHz}$ proves that the 'external' impedance of the copper cylinder used as 'Short' standard is similar to that of the battery cell DUT inside same fixture. The additional 'internal' cell impedance Z_cell is visible by the higher impedance at low frequencies and by the $200\,\mathrm{MHz}$ resonance being less pronounced than with the 'Short' cylinder. As before, it is obvious from this figure too, that OSLC is ineffective for frequencies higher than $500\,\mathrm{MHz}$.

2) Extraction Results With Different Loading Conditions: Again, the PCB was equipped with loads and OSLC with cylinder standards was repeated to verify if the procedure does
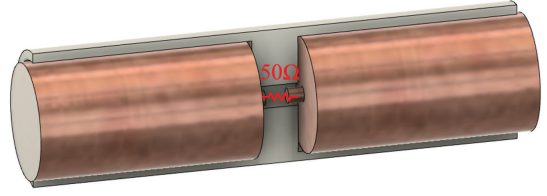
Fig. 6. 18650 copper cylinder with internal $50\,\Omega$ resistor used as 'Load' standard. The cylinder has a 3D-printed plastic mantle to mimic the battery cells outer isolation.
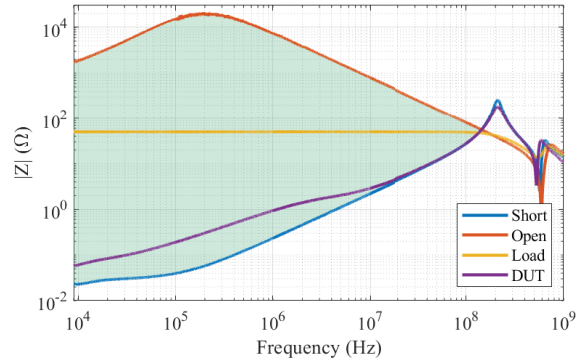
Fig. 7. Region of confidence (RoC) (transparent) for OSLC with 18650-sized copper cylinder standards. DUT is the Li-ion battery cell. RoC upper frequency limit is $145\,\mathrm{MHz}$.

reliably extract only the cell impedance. The unspectacular inductive series load was omitted this time but replaced with an additional $3\,\mathrm{k}\Omega\|10\,\mathrm{nF}$ parallel load. Results are shown in Fig. 8. As before, the de-embedding result proves load-independent but is partially deteriorated when the load's impedance is in the same order of magnitude as the cell's. Above $100\,\mathrm{MHz}$ however, results are not as well matching as in case of OSLC with soldered standards. This is because the copper cylinder 'Short' standard shows almost identical impedance as the cell in this frequency range (compare Fig. 7) irrespective of the loading, hence it is numerically impossible to differentiate load from cell.

III. VALIDATION BY USAGE IN SIMULATION

Fig. 9 gives a direct comparison of cell impedances obtained with both OSLC approaches for the unloaded case. The de-embedding result is mostly independent of the OSLC method used. What was not validated yet is, whether this de-embedded data is really useful for simulation of a battery cell. It is scope of this section.

The demonstration is done using exactly the same test PCB used for measurement before. The PCB layout data was imported to ANSYS HFSS [10] by means of the ODB++ design files and extended with a simple 3D model of the battery holder's metallic parts only, i.e. the springs, and SMA connectors, see Fig. 10. 2-port S-parameters are simulated at the SMA connectors denoted by the turquoise arrows. As before during measurements, the PCB impedance is calculated from the S-parameters by (1).
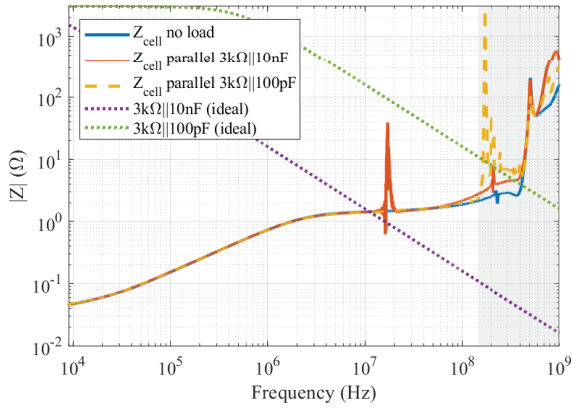
Fig. 8. Extracted cell impedances using OSLC with 18650 cylinder standards. Different loads were connected in parallel to the cell. At high frequencies load compensation does not work as well as with soldered OSL standards (compare Fig. 5). However the matching results still verify, that proposed approach is capable of de-embedding the cell's impedance irrespective of the PCB circuitry. Shaded area is outside the RoC of Fig. 7. The $3\,\mathrm{k}\Omega||10\,\mathrm{nF}$ load soldered to the PCB is self-resonant at $14\,\mathrm{MHz}$, $3\,\mathrm{k}\Omega||100\,\mathrm{pF}$ at $210\,\mathrm{MHz}$, which causes distortion of the de-embedding result close to respective frequencies.

(a)

(b)

Fig. 10. Simulation models to validate the de-embedded cell impedances. Top: The cell is not modeled but replaced with a lumped port between the battery holder's poles. The port is assigned the impedance data from OSL compensated cell-in-fixture measurement $Z_{\mathrm{cell\text{-}in\text{-}fixture,OSLC}}$ of Section II-A). Bottom: The cell is modeled as copper cylinder with series lumped port, holding the extracted impedance Z_{cell} of Section II-A or II-B.

Fig. 9. Measured cell-in-fixture and copper-cylinder-in-fixture impedance, both compensated by direct OSLC with soldered standards, Z_{cell} as result from (3), and Z_{cell} as result from fixture compensation with cylinder standards. The shaded area marks the minimum limit of confidence given by the latter.
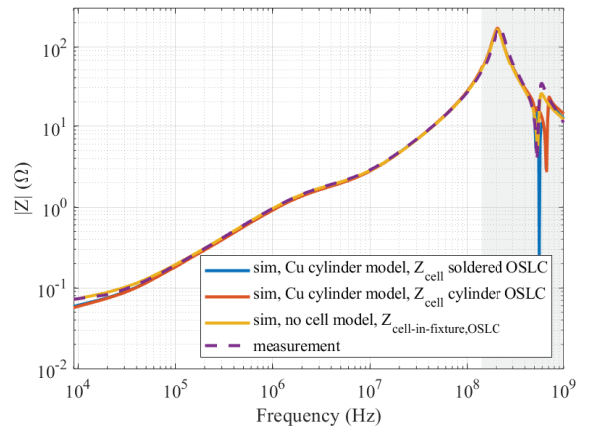
Fig. 11. Measured and simulated PCB overall impedance with the unloaded Li-ion cell in the battery holder, obtained by 2-port shunt-through method applying (1). Red and blue traces use the simulation model of Fig. 10(b) and the cell internal impedance data obtained with the approaches of Sections II-A or II-B (given by the yellow and violet traces of Fig. 9). The simulation yielding the yellow trace used the model of Fig. 10(a) and the complete cell-in-fixture impedance $Z_{\mathrm{cell\text{-}in\text{-}fixture,OSLC}}$ (blue trace of Fig. 9).

Fig. 10(a) shows the simulation setup without battery model. The turquoise rectangular port between battery plus pole and top layer GND plane is exactly where OSL compensation was done in Section II-A. The compensated measurement result $Z_{\mathrm{cell\text{-}in\text{-}fixture,OSLC}}$ can be directly assigned as lumped port impedance in the simulation model. Then, the 3D simulation of the PCB includes all setup related parameters, i.e. everything that was de-embedded by OSLC during measurement, while the on-board lumped port with impedance $Z_{\mathrm{cell\text{-}in\text{-}fixture,OSLC}}$ adds real world data of the battery cell and its interaction with the fixture to the model. Because $Z_{\mathrm{cell\text{-}in\text{-}fixture,OSLC}}$ was de-embedded from the rest of the setup during measurement, it is possible to change the PCB layout in simulation without invalidating the measured cell-in-fixture impedance - at least

as long as the direct vicinity of the cell is unaltered. Also, it is possible to extract a 3-port S-parameter description from the 3D model and use that for circuit simulation, with the 1-port cell data assigned to respective port on schematic level. Because the cell impedance is load-independent, simulations with various circuitry will not invalidate the measured cell-in-fixture impedance.

Validation of the approach was done both described ways, i.e. by assigning the data $Z_{\mathrm{cell\text{-}in\text{-}fixture,OSLC}}$ directly in the 3D model of the unaltered PCB Fig. 10(a) or by first exporting

3-port S-parameters to a circuit simulator and connecting the cell-in-fixture impedance there. Both simulations yield the same results, namely the yellow trace of Fig. 11, which overlaps almost exactly with the measured result.

Alternatively, Fig. 10(b) shows a simulation setup where the cell body is respected as solid copper cylinder. This is aligned with above de-embedding using a copper cylinder for reference measurement. If, e.g. an aluminum cylinder was used during de-embedding, we would use same material for the simulation model. Now, the 'internal' Z_{cell} is added as tiny lumped port in between spring connector and cylinder face. The resulting series connection represents (3) and is therewith a perfect reproduction of foregoing measurement procedure. As described in the introduction, the advantage of including a 3D representation of the cell body in simulation is, that this way also changes of the cell's direct vicinity, e.g. another cell placed close-by, correctly influences the cell-in-fixture impedance. The values of Z_{cell} from both described OSLC workflows where assigned to the cell port visible in Fig. 10(b), yielding the blue and red traces of Fig. 11, respectively. The results are equivalent up to $400\,\mathrm{MHz}$ where the OSLC approach with soldered standards of Section II-A performs slightly better, as was already expected from the discussion of Fig. 4 and Fig. 7. The fact that only the yellow trace matches the measurement precisely at both low and high frequencies might mean that the contact resistance between copper cylinder and holder springs is underestimated in the simulation model (low frequency error) and that the 'external' cell impedance is not accurately depicted in simulation, possible due to the missing battery holder model in Fig. 10(b) (high frequency error).

IV. CONCLUSION

Two workflows were presented to de-embed the impedance of a 18650 Li-ion cell from within a battery holder mounted to a PCB. The method is based on measurements only, i.e. no simulation of PCB characteristics is required. Instead, properties of the fixture are regarded by Open/Short/Load compensation, using SMD calibration standards soldered to the PCB, or 18650-sized cylinder standards placed in the battery holder. Proposed procedure can reliably mitigate the impact of PCB circuitry for frequencies up to $145\,\mathrm{MHz}$ or $200\,\mathrm{MHz}$, depending on the used standards. This was demonstrated by considering RoC plots and different loading conditions. OSLC with standards soldered to the PCB works for slightly higher frequencies than the self-built 18650 standards, because the 'Short' compensation with a copper cylinder standard is too similar to the wanted cell impedance for high frequencies.

The drawback is, that soldered standards require PCB modification which is time consuming and might even be impracticable. Additionally, it is necessary to compensate the coupling of battery towards PCB by reference measurement with a copper cylinder of same size. More convenient is to use calibration cylinders of the cell's size. Such need to be produced first, of course, but enable completely solder-free fixture compensation. Therewith they offer highest flexibility for quick cell de-embedding at any PCB with battery holder.

The correctness of extracted cell impedances was showcased by application in simulation. When the de-embedded cell impedance data was used for 3D simulation of the unloaded scenario, both approaches yielded similar results consistent with measurement up to almost $400\,\mathrm{MHz}$. We conclude that, although simulation above $200\,\mathrm{MHz}$ is outside the confident range, it still may have informative character. The absolute maximum frequency will depend on the specific application.

REFERENCES

[1] P. K. P. Ferraz, R. Schmidt, D. Kober, and J. Kowal, "A high frequency model for predicting the behavior of lithium-ion batteries connected to fast switching power electronics," *Journal of Energy Storage*, vol. 18, pp. 40 – 49, 2018.

[2] A. R. Ruddle, Y. X. Teo, and J. Chen, "Electromagnetic modelling strategies for emc analysis of automotive traction batteries," in *2017 International Conference on Electromagnetics in Advanced Applications (ICEAA)*, Sep. 2017, pp. 1395–1398.

[3] A. R. Ruddle, J. Chen, and Y. X. Teo, "Measurement of rf impedance for automotive 18650 cylindrical lithium ion cells," in *2017 International Symposium on Electromagnetic Compatibility - EMC EUROPE*, 2017, pp. 1–6.

[4] T. F. Landinger, G. Schwarzberger, and A. Jossen, "A novel method for high frequency battery impedance measurements," in *2019 IEEE International Symposium on Electromagnetic Compatibility, Signal Power Integrity (EMC+SIPI)*, July 2019, pp. 106–110.

[5] T. F. Landinger, G. Schwarzberger, and A. Jossen, "High frequency impedance characteristics of cylindrical lithium-ion cells: Physical-based modeling of cell state and cell design dependencies," *Journal of Power Sources*, vol. 488, p. 229463, 2021. [Online]. Available: http://www.sciencedirect.com/science/article/pii/S037877532100015X

[6] T. F. Landinger, G. Schwarzberger, M. Rose, S. Dollhaeubl, G. Hofer, A. P. Talei, and A. Jossen, "Power line communications in automotive traction batteries: A proof of concept," in *2020 IEEE International Symposium on Power Line Communications and its Applications (ISPLC)*, 2020, pp. 1–5.

[7] Keysight Technologies. (2020) Impedance measurement handbook, 6th edition. [Online]. Available: https://www.keysight.com/at/de/assets/7018-06840/application-notes/5950-3000.pdf

[8] S. M. Sandler, "Extending the usable range of the 2-port shunt through impedance measurement," in *2016 IEEE MTT-S Latin America Microwave Conference (LAMC)*, 2016, pp. 1–3.

[9] Y. X. Teo, J. Chen, and A. R. Ruddle, "Predicting the rf impedance of cells in parallel for automotive traction battery applications," in *2019 International Symposium on Electromagnetic Compatibility - EMC EUROPE*, Sep. 2019, pp. 438–443.

[10] ANSYS Inc. ANSYS Electromagnetics. [Online]. Available: www.ansys.com

4.2 Physical-based High Frequency Model of Cylindrical Li-Ion Batteries

This section introduces the article *A Physical-Based High-Frequency Model of Cylindrical Lithium-Ion Batteries for Time Domain Simulation* and is based on the paper without further reference.

The impedance measurement method developed in Section 4.1.1 was applied to a Samsung ICR18650-26J Li-ion cell to enable the HF impedance spectroscopy of cylindrical Li-ion cells up to 300 MHz. Several HF-relevant electrochemical and electrophysical effects were identified by a combined approach of impedance-based modeling and geometrical considerations based on computed-tomography (CT) scans of the considered cell. It is shown that the cell impedance at high frequencies is governed by resistive and inductive loss processes, which originate mainly from the geometrical structure of the cell and additionally from the skin effect for very high frequencies above 10 MHz. It is found that the initial impedance curve bending in the Nyquist plot above the intercept frequency is caused by the ionic shunt effect, which describes the quasiparallel interconnection between ionic currents in the electrolyte and electrical currents along the current collector windings. The overall cell inductance derived from the cell impedance by $L = \Im\{Z_{cell}\}/(2\pi f)$ is frequency-dependent as illustrated in Figure 19. As indicated, the jelly roll inductance dominates the inductive cell behavior at the lower frequency decades, whereas at the higher frequency decades, the overall cell inductance is governed by the cylindrical cell geometry and resembles the inductance of a hollow Cu cylinder with the same dimensions as of the 18650 cell. The presented impedance-based battery model for high frequencies will be further modified and used for PLC channel modeling in Chapter 5.
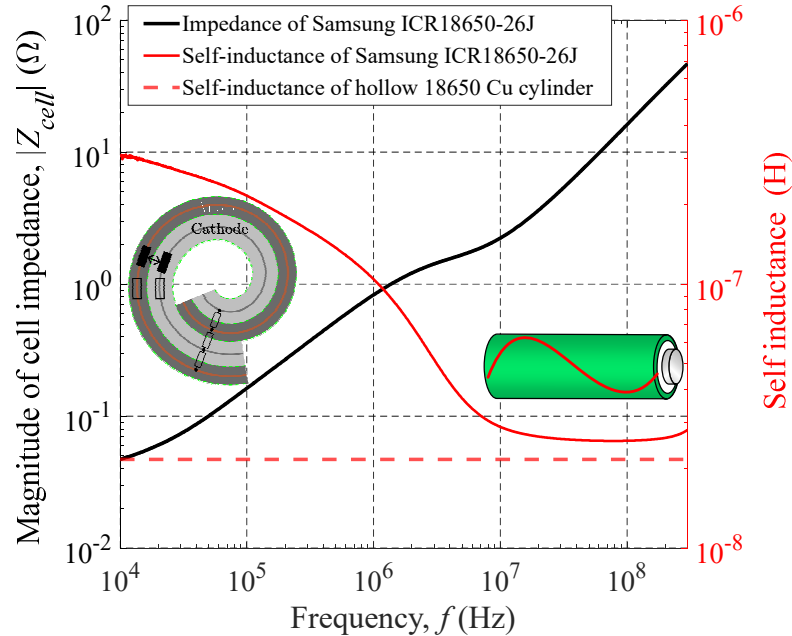
Figure 19: High frequency impedance characteristics of the investigated Samsung ICR18650-26J Li-ion cell. The overall cell inductance derived from $L = \Im\{Z_{cell}\}/(2\pi f)$ can be approximated by a hollow Cu cylinder with the dimensions of the 18650 cell.

Authors contribution   Development of the impedance measurement method and execution of the experiments were performed by Thomas F. Landinger. Data processing, battery modeling, and simulations were also conducted by Thomas F. Landinger. The printed circuit board was conceptualized by Guenter Schwarzberger and Thomas F. Landinger and was designed by Guenter Schwarzberger. Andreas Jossen supervised this work. The original draft was written by Thomas F. Landinger and was reviewed and edited by all authors.

A Physical-Based High-Frequency Model of Cylindrical Lithium-Ion Batteries for Time Domain Simulation

Thomas F. Landinger, Guenter Schwarzberger, Andreas Jossen

Permanent weblink:

https://doi.org/10.1109/TEMC.2020.2996414

A Physical-Based High Frequency Model of Cylindrical Lithium-Ion Batteries for Time Domain Simulation

Thomas F. Landinger, Guenter Schwarzberger, and Andreas Jossen

Abstract—**Lithium-ion (Li-ion) batteries in electric vehicles are exposed to high slew rate currents originating from the power electronics. Modern gallium nitride (GaN) and silicon carbide (SiC) based power converters generate high switching frequencies, which propagate toward the battery. To predict the battery's impact on conducted emissions, we need to determine the battery's behavior over a high frequency (HF) bandwidth. Traditional battery characterization techniques such as Electrochemical Impedance Spectroscopy (EIS) focus on frequencies below 10 kHz. This paper proposes a novel method to characterize the battery beyond typical EIS frequencies. Using the proposed approach, we investigate and model the dynamic behavior of cylindrical Li-ion batteries from 1 kHz to 300 MHz. HF characterization of the cell is enabled by a novel measurement technique applying vector network analysis (VNA) and measuring the S-parameters of the cell. We design a specific fixture to connect the cell to the VNA and remove fixture errors by de-embedding procedures. The cell's HF impedance originates from several loss processes such as the skin effect, the ionic shunt effect and simple ohmic-inductive effects. First in literature, all these effects are measured and summarized in an equivalent electrical circuit model, which predicts the cell's impact on HF current pulses.**

Index Terms—**battery impedance, EIS, electrochemical impedance spectroscopy, VNA, shunt-through measurement method, high frequency impedance**

I. INTRODUCTION

Electrochemical Impedance Spectroscopy (EIS) is widely used to characterize and model the dynamic behavior of lithium-ion (Li-ion) battery cells [1]. The typical frequency range of the EIS lies between 10 mHz and 10 kHz [2] and hence focuses mainly on the electrochemical processes, which do not exhibit faster time constants [3]. To evaluate higher frequency issues such as how a battery affects conducted emissions coming from the inverter in an electric vehicle [4] or how high speed power line communications signals can be sent over a battery [5], a high bandwidth model of the cell becomes necessary.

The EIS measurement equipment is optimized for low frequencies and faces several measurement obstacles when the frequency increases further. Inductive and capacitive coupling effects between connecting leads disturb the measurement, and

additionally, multiple reflections cause errors to due standing electromagnetic waves [6]. This makes high frequency (HF) impedance measurements and their interpretations difficult, as it is not easy to distinguish between measurement errors and the battery impedance itself [2]. When it comes to the measurement of high frequency properties of Li-ion battery cells, an HF-capable measurement setup is necessary. Many methods have been proposed to measure the HF impedance of electronic devices and circuits, the most common of which are current and voltage measurements, or balancing and resonating networks [7]. The current voltage (I-V) method is broadly applied with dedicated impedance analyzers to measure the cell's HF impedance [8–10] and is also used in traditional EIS [1]. As dedicated impedance analyzers have a limited frequency range, vector network analysis gets an increasing interest regarding broadband impedance measurements [7], and is therefore selected for the cell's HF characterization in this work.

Already above some kilohertz, cylindrical cells show an inductive and slightly dissipative behavior, which leads to the often visible inductive impedance arc in the positive imaginary half-plane of the impedance locus or Nyquist plot [2, 3]. In literature, the HF inductive characteristic is often modeled by a simple inductor as in [3, 11, 12]. In this case, the inductive impedance arc is ignored and declared to be a measurement artefact, e.g. caused by the parasitic current shunt inductance of the measurement setup [13]. Only a few publications tend to interpret the inductive impedance arc to be related to the battery itself. Already three decades ago, Laman *et al.* [14] published a paper on the inductive properties of cylindrical batteries. They found that the HF inductive characteristics of cylindrical cells mainly arise from the spirally wound geometry of the current collectors and the position of the anodic and cathodic tabs. More recently, Osswald *et al.* [15] investigated the inductive properties of different cell tab patterns located along the current collectors and found a strong correlation between the maximum impedance value and the windings enclosed by the tabs. Schindler *et al.* [16] proposed a very detailed battery model in form of a transmission line model based on the mathematical concept of spirally wound cells published in [17]. They concluded that the inductive impedance arc in the Nyquist plot was a result of the interaction between inductive losses in the

electrical domain and resistive losses in the electrochemical domain. As a drawback, this model requires much information about the physical dimensions of the cell, which are often unknown. Ferraz *et al*. [18] proposed three less complex HF cell models, which still consider physical factors of influence. However, at the end they could not decide whether the resistive inductive behavior of the current collectors or the skin effect causes the inductive impedance arc. The skin effect is often stated to be the only reason for the high frequency related increase in resistance as in [3, 19].

In this paper, we extend our previously published HF battery characterization method [6], and show that the inductive and resistive characteristics of cylindrical cells at high frequencies are a combination of the electrochemical and electrophysical phenomena cited above.

To address the above stated HF measurement obstacles, Section II introduces our novel measurement method [6] using a vector network analyzer (VNA) instead of an EIS measurement device, which allows us to largely exclude high frequency caused measurement errors. In Section III, a test fixture is presented to connect the cell to the VNA. Section IV illustrates how fixture errors are removed to de-embed the cell impedance. In Section V, a cylindrical Li-ion cell ICR18650-JM by the Samsung SDI Co., Ltd. is characterized in the frequency range from 1 kHz to 300 MHz. In Section VI, we discuss the measurement results and their electrophysical and electrochemical meaning. First in literature, the cell's HF resistive and inductive behavior is separated into different loss processes, which are assigned to lumped elements of an equivalent electrical circuit (EEC) HF battery model. We derive the loss processes from the battery's geometry on the one hand and from the measurement results on the other hand. In Section VII, the EEC HF model is validated in the time domain by stimulating the cell with HF current pulses and measuring the voltage response. The paper concludes with Section VIII. As a remark, most of the physical quantities and equations presented in Sections II, III, and IV are frequency dependent, but we chose not to denote this dependency explicitly to ease the notation.

II. Impedance Measurement Technique

As stated in the introduction, vector network analysis is utilized to characterize the broadband impedance of the cell. Two different VNA approaches are shown in Fig. 1a and Fig. 1b. Regarding the basic reflect method (Fig. 1a), a VNA transmits a known sinusoidal signal toward the unknown battery impedance Z_{bat} and sweeps the signal over the desired frequency range. Depending on the cell's impedance, a part of the transmitted signal will be reflected back scaled by the reflection coefficient

$$\Gamma = \frac{V_b}{V_a} = \frac{Z_{bat} - Z_0}{Z_{bat} + Z_0} , \tag{1}$$

which is also known as the scattering parameter (S-parameter) S_{11}. The objective of the VNA is to determine the scattering parameters of the device under test by measuring the incident
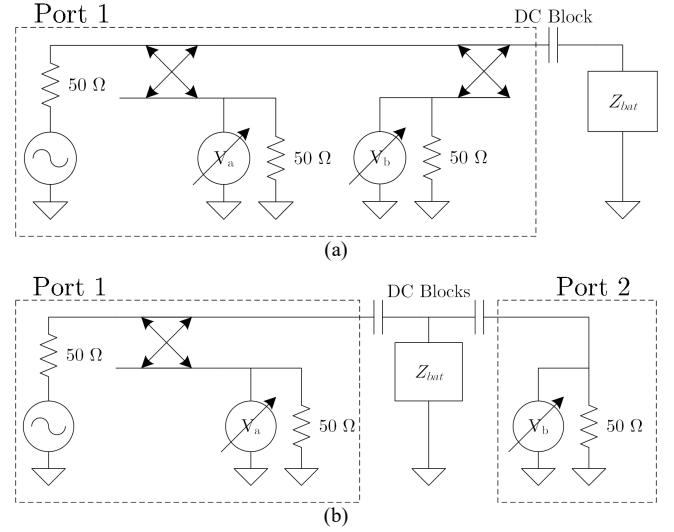
Fig. 1. VNA setups for different impedance measurement methods. (a) VNA reflect method. (b) VNA shunt-through method. The crossed arrows indicate the directional couplers.
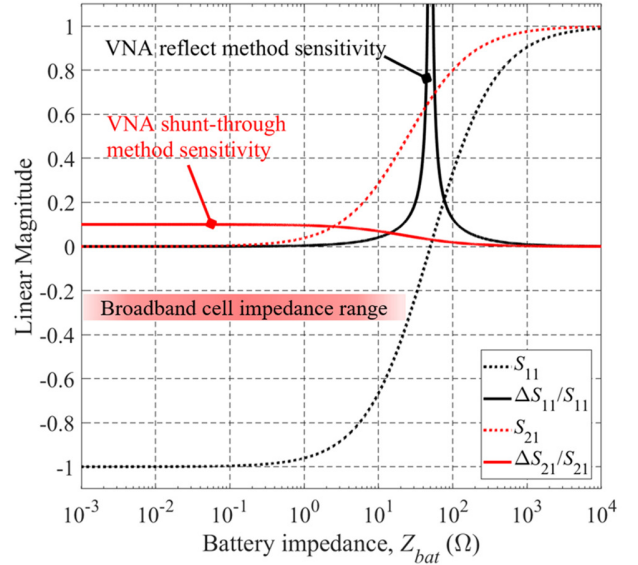
Fig. 2. Measurement sensitivities of the VNA reflect method (S_{11} data) and the VNA shunt-through method (S_{21} data) depending on a real battery impedance. Shown are the absolute values of the S-parameters derived from (2) and (3) and their corresponding change $\Delta S_{i1}/S_{i1}$ for a 10 % change in Z_{bat}.

and reflected voltage waves V_a and V_b, respectively. Using the VNA reflect method, the unknown impedance can be calculated from the scattering parameter S_{11} as

$$Z_{bat} = Z_0 \frac{1 + S_{11}}{1 - S_{11}} = Z_0 \frac{V_a + V_b}{V_a - V_b} . \tag{2}$$

The VNA setup for the shunt-through method is indicated in Fig. 1b. The cell is connected in a tee-configuration to the VNA and two-port scattering parameters are measured. Port 1 serves as a current source and port 2 measures the voltage across the battery. Due to the low impedance of the cell, most of the incident voltage wave will be reflected back to port 1 leading to

an S_{11} close to –1. However, a small portion of the signal is transmitted to port 2, which determines S_{21}. Using the information of S_{21}, the impedance Z_{bat} can be calculated with

$$Z_{bat} = \frac{Z_0}{2} \frac{S_{21}}{1 - S_{21}} . \qquad (3)$$

The VNA-reflect method requires only a one-port measurement and offers a wide frequency range. However, its impedance range is rather narrow and centered at the characteristic impedance Z_0 due to the varying S_{11} measurement sensitivity. Fig. 2 illustrates the sensitivity in terms of change in S_{11} for a 10 % change in Z_{bat} assuming a real battery impedance. The lower the cell impedance, the further the S_{11} measurement sensitivity decreases. Since the impedance of a single 18650 Li-ion cell is in the milliohm range for several frequency decades, the VNA reflect method is not sufficient to measure the low-ohmic cell impedance accurately enough. To overcome this problem, the VNA shunt-through method is an effective alternative. The sensitivity of the VNA shunt-through method is also depicted in Fig. 2 and exhibits a significantly higher value than the VNA reflect method. In particular, it has to be noted that the percentage change in S_{21} equals the percentage change in Z_{bat} for impedance values smaller than 1 Ω, which covers the typical cell impedance range as denoted in Fig. 2. Consequently, in this work we use the VNA shunt-through method for measuring the cell impedance as it offers a much higher measurement sensitivity for small impedances. Beside the sensitivity, the VNA shunt-through method has another benefit. As can be seen in Fig. 1b, the tee-connection of the cell forms a Kelvin probe, which is also known as four terminal sensing. Because force and sense leads are separated, their parasitic impedances consisting of resistance and self-inductance are not part of the measured impedance Z_{bat}, which has a great relevance for measuring low-value impedances [7]. Regardless of the measurement method, the dc blocks depicted in Fig. 1 are necessary to protect the measurement equipment against incoming dc current from the battery.

III. CELL CONNECTION

To achieve reproducible and accurate HF measurement results, the device under test (DUT) should be directly connected to the VNA by coaxial connectors and leads. This provides a stable and reliable mechanical connection and enables the application of transmission line theory [20] and therefore the usage of calibration and de-embedding procedures to remove systematic errors. However, the physical dimensions of the battery force us to leave the coaxial domain and thus to separate the signal and return conductors, which leads to varying line parameters along the transmission line such as inductance per length. To obtain a reproducible measurement setup nevertheless, we designed and manufactured a two-layer printed circuit board (PCB) cell fixture that connects the cell to the coaxial-connector based test system in a stable way. The PCB is displayed in Fig. 3a and has two 50 Ω microstrip lines on the top layer connecting the cell's positive terminal to the

(a)

(b)
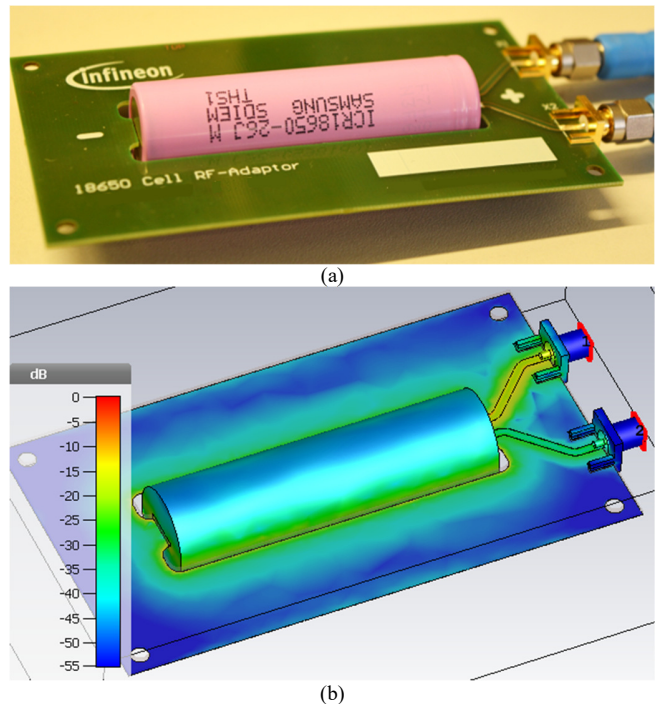
Fig. 3. PCB fixture for connecting the cell to the VNA test system. (a) PCB layout. (b) Simulated normalized current distribution for excitation at port X1 with f = 100 MHz [6].

inner conductor of the two coaxial Sub-Miniature-A (SMA) jacks X1 and X2. The signal return plane on the PCB's bottom side connects the cell's negative terminal to the return conductor of X1 and X2. The PCB is axial symmetric, therefore either X1 can be used as force port and X2 as sense port or vice versa. The microstrip lines are routed in an angle of 90° to each other to reduce force and sense coupling effects to a minimum. The cell itself is placed in the cutout of the board. The PCB's characteristics were simulated using the 3D electromagnetic wave simulation tool CST Microwave Studio. A solid copper (Cu) cylinder with the dimensions of an 18650 cell was inserted as a cell dummy to run the simulation. This results essentially in a short circuit, which can be seen from the simulated S_{11}-trace starting at the impedance value zero in Fig. 4. For higher frequencies, the reflection coefficient moves away from its starting point mainly due to an increase in the cylinder impedance. As another result, in Fig. 3b the normalized current distribution on the PCB's conducting layers is shown for an excitation signal coming from port X1. The current flows through the microstrip lines and the cylinder and back to X1 on the signal return plane at the edges of the cutout creating the lowest possible current loop inductance.

In fact, the part of the current's return path, which is in parallel with the cylindrical cell, will cause a reduction of the measured cell inductance by inductive coupling, which has to be considered in the de-embedding procedure later.

The battery is mounted on the PCB by soldering, as it offers the lowest contact resistance and highest maximum tensile force among common cell joining techniques [19]. To avoid any damage through heat impact, the cell's electrochemically
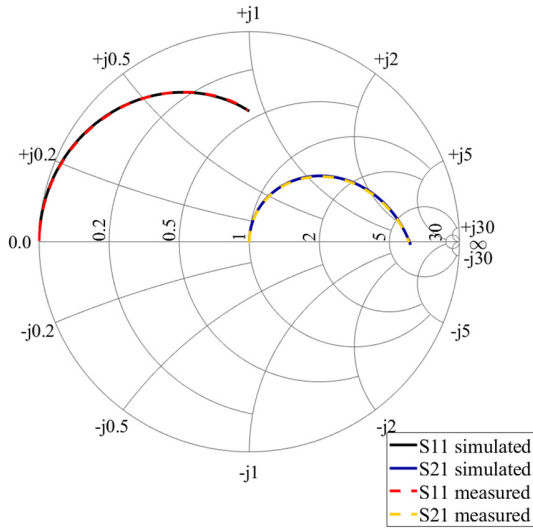
Fig. 4. Simulated and measured S-parameters of the PCB fixture with the copper cylinder mounted. The reference planes are at X1 and X2. Axes values are normalized impedances.

Fig. 5. De-embedding model of the cell and the PCB fixture. The greyed out transmission line elements are considered by the APE procedure.

active materials must not undergo a temperature above 80 °C [21]. Therefore, we used a special solder with a low liquidus temperature of 124 °C by the Chemet GmbH.

IV. Error Correction and De-Embedding

If we want to de-embed the cell impedance from the cell-in-fixture impedance measurement, we first need to define the term 'cell impedance'. As stated earlier, the cell exhibits physical dimensions leading to electrical delays, which are not negligible for HF impedance measurements. Since we start our impedance measurement at 1 kHz, which is generally the region of the cell's intercept frequency with the x-axis in the Nyquist plot initiating the inductive behavior, we do not consider the low-frequency relevant capacitive part of the cell impedance [1, 2]. On the other hand, the inductive part is most essential for the HF impedance measurement. An inductance can only be measured in a closed current loop resulting in a loop inductance. Of course, the desired cell inductance L_{bat} is only a part of this current loop and corresponds to a self-partial inductance as defined in [22, 23]. Together with the cell's ohmic resistance R_{bat}, these two parts form the cell impedance to be de-embedded:

$$Z_{bat} = \Re\{Z_{bat}\} + j\Im\{Z_{bat}\} := R_{bat} + j\omega L_{bat}. \quad (4)$$

The elements R_{bat} and L_{bat} model the overall ohmic-inductive behavior of the cell and will be divided into several portions for the cell model development in Section VI.

For the de-embedding procedure, we modeled the PCB and the battery by equivalent electrical circuits. The resulting schematic is illustrated in Fig. 5. On the one hand, equation (4) already defines the de-embedding model used for the battery. On the other hand, the PCB de-embedding model needs to account for the loss and delay of the excitation signal along its path on the signal return plane. When a signal propagates along
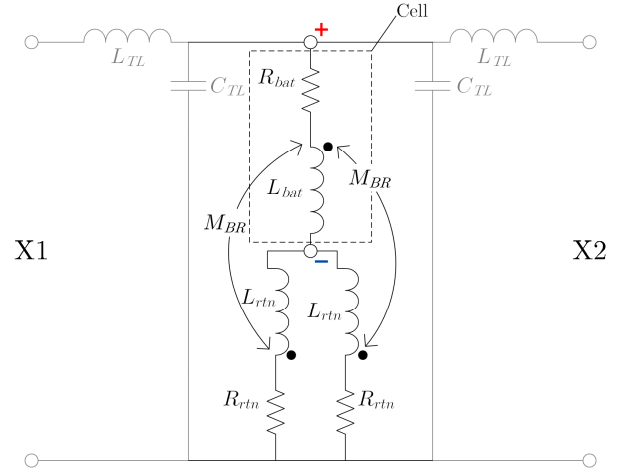
the signal return plane from the negative to the positive battery pole, it will undergo a non-negligible phase shift. For instance, a 200 MHz sinusoidal signal will be phase-shifted by more than 25°, considering the 18650 cell's length of 65 mm and a typical microstrip line with a relative permittivity ε_r of 4.3. If the signal wavelength λ is ten times the signal path length or longer, the signal path can be approximated by a simple lumped element RL circuit. This modeling approach results in a frequency limit, which is dependent on the cell's length l, the effective dielectric constant ε_{eff} of the microstrip line and the speed of light c_0:

$$f_{max} \approx \frac{c_0}{10 \cdot l\sqrt{\varepsilon_{eff}}} \approx \frac{c_0}{10 \cdot l\sqrt{(\varepsilon_r - 1)/2}} \quad (5)$$

For a typical microstrip line ($\varepsilon_{eff} \approx 2.65$) and an 18650 cell ($l = 65mm$), the frequency is limited to 283 MHz. Using this modeling approach, we can model the signal return path by the two lumped elements R_{rtn} and L_{rtn}, which account for loss and delay, respectively. Since the current flows on both sides around the battery, R_{rtn} and L_{rtn} are considered twice in Fig. 5. In addition, the schematic in Fig. 5 contains twice the elements C_{TL} and L_{TL} to represent the microstrip transmission lines. These elements are greyed out as the automatic port extension (APE) procedure provided by the VNA already accounts for them [6]. Most of the signal's path on the return plane is in parallel to the cell and will compensate partly for the external magnetic field of the battery as reported in [22]. This is due to inductive coupling effects and can be modeled by the concept of mutual inductance [23]. Therefore, we include twice the mutual inductance M_{BR} between L_{bat} and L_{rtn} in the de-embedding model as illustrated in Fig. 5. The small parts of the return path, which are perpendicular to the cell, will not affect the measured cell inductance because there is no mutual inductance between perpendicular signal path segments [23].

Capacitive coupling between the cell and the return path is assumed to be in the range of some picofarads due to the large distances, small cross section areas, and an $\varepsilon_r \approx 1$ of air. This

leads to a relatively high impedance in the investigated frequency range and can be neglected in the de-embedding model.

The resulting total impedance Z_{tot} of the model without considering the microstrip lines is

$$Z_{tot} = R_{bat} + j\omega(L_{bat} - M_{BR}) + \frac{R_{rtn}}{2} + j\omega(\frac{L_{rtn}}{2} - M_{BR}), \quad (6)$$

which will be set equal to the VNA measurement result acquired by (3) of the overall cell-in-fixture impedance. Solving this equation for the battery impedance reveals many unknown parasitic elements. A way to extract the battery impedance part (4) from (6) is a second measurement of a known reference impedance, which has the same magnetic field interaction with the PCB's conducting layers as the battery. Thereby, the inductive coupling effects remain the same among both measurements and the mutual inductances cancel out during the subtraction of the two measurement results. As reference, we chose a solid copper cylinder with the outer 18650 cell dimensions, which is equivalent to the one used in the simulation in III, and performed a second impedance measurement. Using the results of the cell- and the cylinder-in-fixture impedance measurement, Z_{tot1} respectively Z_{tot2} , the battery impedance can be derived by

$$Z_{bat} = Z_{tot1} - Z_{tot2} + R_{Cu} + j\omega L_{Cu} , \quad (7)$$

where R_{Cu} is the resistance and L_{Cu} the self-partial inductance of the copper cylinder. Both components are frequency dependent due to the skin effect and can be analytically calculated. More details on the de-embedding procedure can be found in [6].
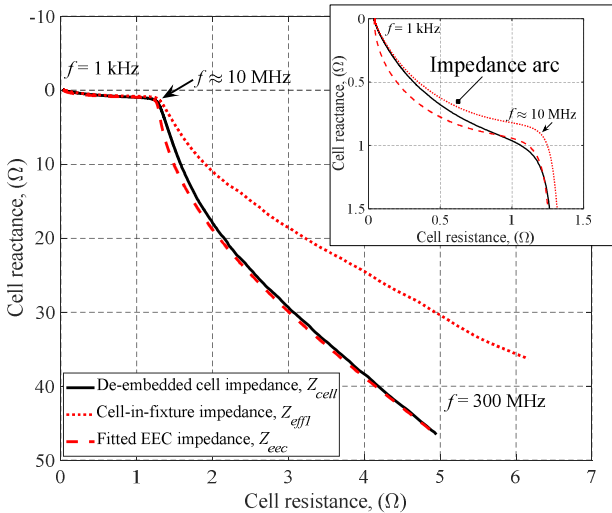
V. MEASUREMENT RESULTS AND DISCUSSION

We chose as representative commercial cell a new cylindrical ICR18650-JM Li-ion high energy cell by the Samsung SDI Co., Ltd. Using an Agilent E5061B VNA, both the battery and the copper cylinder reference were measured while being mounted on the PCB fixture. The cell impedance was derived using (7). The cell was measured at room temperature (23°C) with a state of charge of 50 % and a state of health of 100 %. The measurement is performed over a frequency range from 1 kHz to 300 MHz and takes about three minutes with the lowest intermediate frequency bandwidth (IFBW) of 10 Hz. The low IFBW together with a source power of 0 dBm leads to a sufficiently high dynamic range while still fulfilling the linearity criterion, which states that the inner battery impedance behaves linearly for cell over-potentials below 10 mV [1]. The cell fixture is connected via two short coaxial leads and dc blocks to the VNA. During the measurement, we observed common mode current flowing on the outer surface of the shield of the VNA coaxial cables. This led to a significant increase in the measured impedance for frequencies below 10 kHz. The sheath waves could be eliminated by encompassing the coaxial cables with ferrite cores.

For the validation of the measurement method, different source power levels between 0 dBm and -20 dBm fulfilling the linearity criterion have been applied. All of them led to the same cell impedance result, thus confirming the robustness of the method. For further validation of the proposed method, the measured S-parameters of the Cu cylinder were compared with the simulation results in III as shown in Fig. 4. The comparison indicates a close match between measurement and simulation and hence demonstrates the effectiveness of the method. The final measurement results are indicated in a Nyquist plot (Fig. 6) and additionally in a Bode plot (Fig. 7) since in the former the frequency information is not visible. Regarding

Fig. 6. Impedance spectra of the battery cell mounted on the PCB fixture and de-embedded cell impedance using (7). The dashed line represents the impedance spectrum of the fitted EEC battery model shown in Fig. 8. The inset highlights the inductive impedance arc in the lower frequency region.
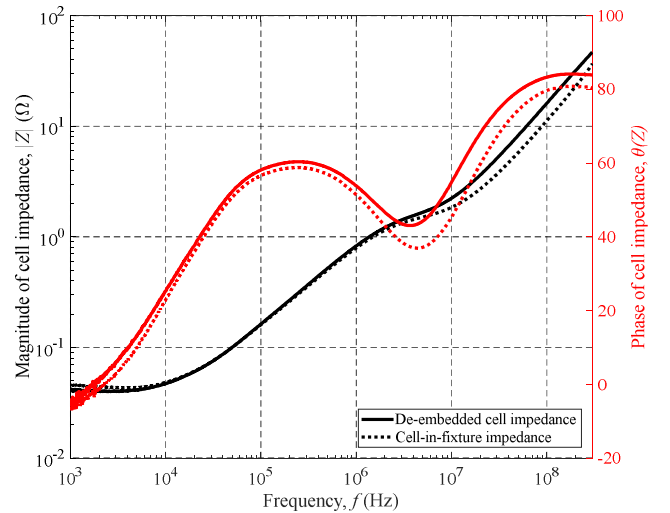
Fig. 7. Magnitude (black) and phase (red) of the measured cell-in-fixture impedance and the de-embedded cell impedance using (7).

Fig. 7, the impedance increases from 40 mΩ at 1 kHz up to 40 Ω at 300 MHz mainly due to the inductive reactance, which can be noticed from the phase progression reaching almost an angle of +90° at 300 MHz. The 1 kHz cell impedance value was also measured with a Zahner Zennium electrochemical workstation and exhibited the same value as measured with the HF method. At frequencies lower than 2 kHz the remainder of the cell's double-layer capacity is visible, which shunts the charge transfer reaction for higher frequencies [3]. The de-embedded cell impedance magnitude is higher than the cell-in-fixture impedance magnitude as the fixture compensates partly for the external magnetic field of the cell. Although our chosen upper measurement frequency limit of 300 MHz is higher than the frequency limit of the de-embedding model, which was stated in Section IV-B to be 283 MHz, there is no negative impact noticeable on the results above this frequency. I.e. the de-embedding model depicted in Fig. 5 has still a large frequency margin above the proposed frequency limit and therefore exhibits a good reliability for the chosen frequency band.

VI. HIGH FREQUENCY BATTERY MODEL

In this section, we propose an HF EEC battery model, which represents high frequency related electrophysical and electrochemical loss processes occurring in a cylindrical battery that have been reported in literature. In previous works, there have been two different approaches for HF battery modeling. The first approach defines a battery model in such a way that it fits the measurement result best. This fitting approach is straight forward and yields well-fitting circuit models, mostly a serial L or an RL circuit, but often lacks physical and chemical interpretations of the circuit elements. It is commonly known that the inductive behavior of the cell originates from the spirally wound current collectors and the connections inside the cell [15, 24]. The second approach is therefore based on the physical structure of the battery and requires a lot of information about the cell's geometry, which is often unknown. We therefore design our HF battery model by combining both the information of our measurement results and the available information about the structure of the battery and assign each EEC element a certain loss process occurring in the cell. The resulting EEC battery model is depicted in Fig. 8 and consists of frequency independent RL elements.

Using computed tomography (CT), the cell was scanned to gain insight into the internal structure, which is pictured in Fig. 9. A tab located at the outside of the electrode windings connects the cell's negative terminal to the active material whereas the positive terminal has a tab placed in the middle of the windings. To form a cylindrical cell, the metallic current collectors are coated on both sides with the active electrode material and are rolled up with a separator in between to form the jelly roll. Fig. 9 and Fig. 10a illustrate the cell's internal structure by a cross-sectional view. Tabs are attached to the current collectors and are usually connected by several bonds to the battery poles [16]. The position of the tabs on the current collectors is crucial for the inductive behavior of the cell [15], because more windings lead to an increase in inductance [14, 16]. From the Nyquist plot in Fig. 6 it can be seen, that the
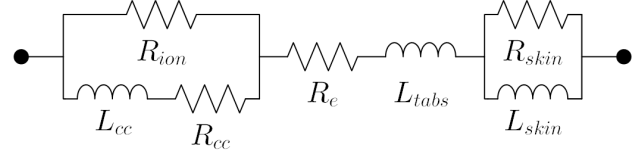
Fig. 8. Structure of the high frequency EEC battery cell model.

TABLE I
HIGH FREQUENCY BATTERY MODEL CIRCUIT ELEMENTS

Element	Quantity	Fitted EEC value range
R_e	Electrolyte resistance and polarization losses	30…40 mΩ
R_{cc}	Current collector resistance	3…7 mΩ
R_{ion}	Radial ionic resistance	1.0…1.5 Ω
L_{cc}	Current collector effective inductance	130…140 nH
L_{tabs}	Tabs and bonds self inductance	15…22 nH
R_{skin}	Skin surface resistance	10…15 Ω
L_{skin}	Internal inductance	3…6 nH

impedance path forms an inductive arc (visible in the magnified inset) before increasing steadily in both real and imaginary part. Different processes can be allocated to these observations and are modeled by lumped electrical elements. It should be noted that although we map the loss processes to lumped circuit elements, they inherently have a distributed characteristic, which is visible from the battery structure in Fig. 10a and 10b.

A. The ohmic resistance

As in traditional EIS, the ohmic resistance is defined as the resistance in the Nyquist plot, where the imaginary part of the impedance is zero. This happens at the so-called intercept frequency, which is 2 kHz for the investigated 18650 Li-ion cell, as noticeable in Fig. 7 from the zero-phase point. In our EEC HF battery model (Fig. 8), the ohmic resistance is divided into two resistive parts related to different battery components. As the first part, the electrochemical resistance R_e mainly
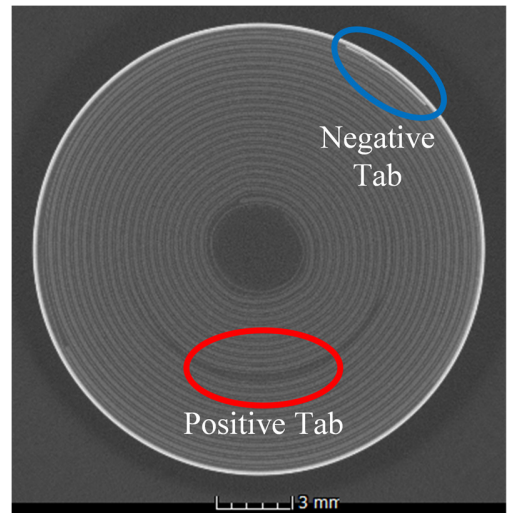
Fig. 9. CT scan of the investigated cell. The positions of the tabs are indicated.

accounts for the electrolyte resistance. Besides, R_e models contact resistances between the active electrodes and the current collectors, which also cause polarization losses [2]. The second part is the electrical resistance of the current collectors due to their limited conductivity and is modeled by R_{cc}. As stated earlier, the charge transfer resistance R_{ct} is not part of the HF battery model, as it is shunted by the cell's double-layer capacity C_{dl} for higher frequencies.

B. The inductive impedance arc

At the intercept frequency, the cell reactance $\Im\{Z_{bat}\}$ vanishes and the current only sees the resistances of R_e and R_{cc}. (There might be small capacitive and inductive contributions, but which cancel each other out.) The conventional current path (green arrow in Fig. 10b) at this frequency runs along the aluminum (Al) current collector, crosses the active electrode areas and the separator at a certain location in the jelly roll and flows along the Cu current collector to the tab. For increasing frequency, additional loss processes occur. The fast time-varying current causes an additional voltage drop along the current collectors due to their self-inductance. As the inductive reactance of the collectors increases with frequency, another current path becomes obvious. An increasing quantity of ionic branch currents flows radially between the jelly roll layers thus shunting the inductive reactance of the current collectors. The ionic branch currents are indicated by the red arrows in Fig. 10a and 10b, exemplifying the quasiparallel interconnection between ionic and electrical currents. This ionic shunt effect leads to the inductive impedance arc in the Nyquist plot as depicted in the inset of Fig. 6. Laman *et al.* [14] proved this statement by characterizing and comparing two cells: one with electrolyte and one without electrolyte. The cell without electrolyte does not show the arc in the impedance spectrum because it lacks the dissipative Li-ion flow mechanism. The Li-ions migrating through the jelly roll layers see multiples of the resistance R_e, which is modeled as the ionic resistance R_{ion} in our EEC. At the highest point of the impedance arc, the ionic current through the jelly roll layers equals the electric current through the current collectors. For modeling the inductive impedance arc, Ferraz *et al.* [18] proposed an inductive ZARC-element, which can be approximated by a chain of RL-elements in analogy to the capacitive ZARC-element [1]. Based on the above described ionic shunt effect, we model the impedance arc with one RL-circuit composed of the resistance R_{cc} and the effective inductance L_{cc} of the current collectors, in parallel with the ionic resistance R_{ion} as shown in Fig. 8. The effective inductance L_{cc} results from the self-inductance of the positive (Al) and negative (Cu) current collectors and their coupling through mutual inductance [16]. As described in [14], if the tabs of anode and cathode are placed at the opposite ends of the jelly roll as depicted in Fig. 10a, the currents in the current collectors flow in parallel leading to a large effective inductance L_{cc}. If the tabs are at the same end of the jelly roll, L_{cc} will be much less due to antiparallel current flow.

C. The skin effect

Due to electromagnetic field effects, a time-varying current tends to concentrate near the surface of a conductor, which is known as the skin effect. As a consequence, the higher the frequency of the current, the less is the penetration depth of the current leading to a reduction of the effective cross section of
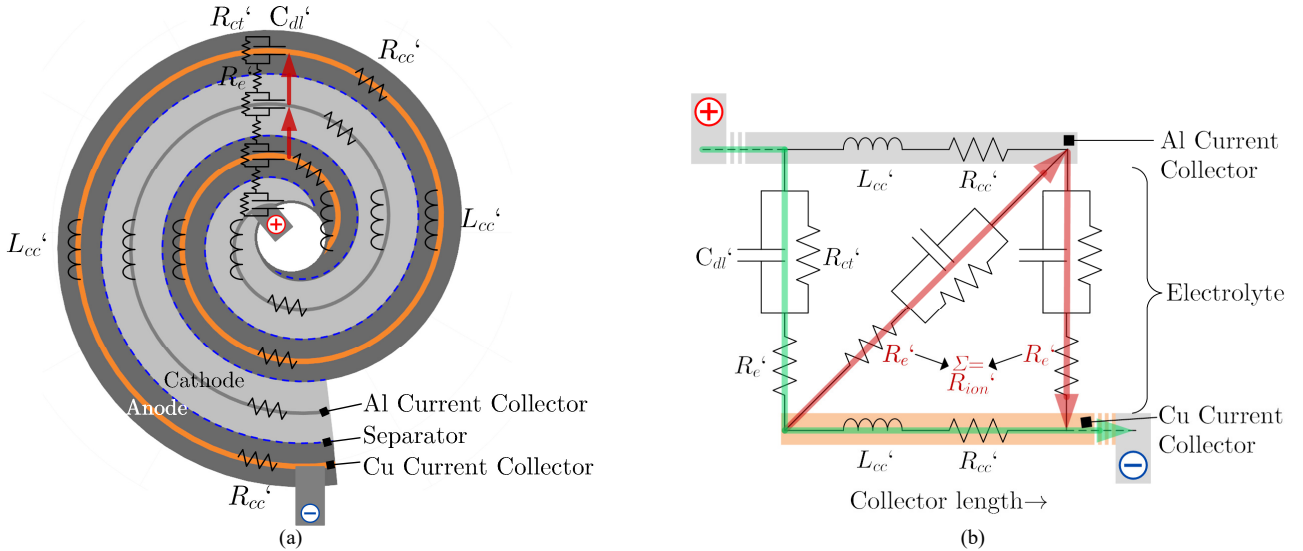
Fig. 10. Internal structure of a typical cylindrical cell with the positive tab (+) located in the center and the negative tab (-) at the outermost winding. In (a) the distributive nature of the inductance and resistance of the current collectors is shown and designated by apostrophized elements (') implying quantity per length. The exemplary chain of double layer capacitances C_{dl}' with charge transfer resistances R_{ct}' in parallel and the electrochemical resistances R_e' is based on the commonly used electrochemical EEC dynamic battery model [3] and indicates the HF radial ionic current flow (red arrows). The RC circuits are negligible for the regarded high frequency range and only a multiple of R_e' remains as R_{ion}'. (b) is a fraction of the entire transmission line (a) and illustrates the two different current paths: the conventional (green arrow) and the HF relevant path (red arrows). This eventually leads to an RL parallel circuit for high frequencies.
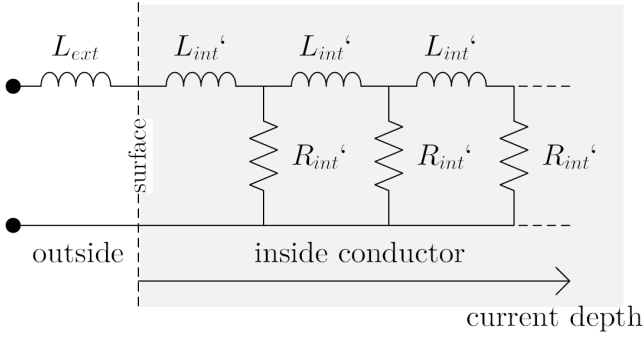
Fig. 11. External and internal impedance of a conductor, illustrated by distributed circuit elements. Adapted from [26].

the conductor. The penetration depth for cylindrical conductors can be calculated by

$$d_{skin} = \frac{1}{\sqrt{\pi\sigma\mu f}} \, , \qquad (8)$$

with the conductivity σ and the permeability μ of the material. The reduced current depth causes an increase in internal resistance R_{int} and a decrease in internal inductance L_{int}, as the magnetic flux penetration depth inside the conductor shrinks. Together R_{int} and L_{int} form the frequency dependent internal impedance, which is also known as the surface impedance [25]:

$$Z_{int}(\omega) = R_{int}(\omega) + j\omega L_{int}(\omega) = \frac{l}{w} \sqrt{j\omega\mu/\sigma} \, , \qquad (9)$$

where l is the length and w the circumference of the conductor. Fig. 11 illustrates how the internal resistance and inductance are distributed in the conductor as an RL transmission line with the frequency-constant elements R_{int}' and L_{int}'. From (9) we see that the surface impedance depends on the square root of the frequency and that the real and imaginary parts are identical. This leads to an angle of 45° in the Nyquist plot and can be interpreted as an inductive Warburg impedance in analogy to the Warburg impedance used for modeling the slow diffusion processes in a Li-ion cell [3]. This interpretation is also in accordance with the transmission line character visible in Fig. 11. Despite the frequency dependency of the surface impedance, we model the skin effect by the two frequency independent lumped elements R_{skin} and L_{skin} in Fig. 8, which is a good tradeoff between simplicity and fitting accuracy. Eventually a parallel RL-circuit will form a semi-circle, but for the considered frequency range, this topology is sufficient.

The skin effect can be noticed in Fig. 6 at high frequencies above the inductive impedance arc, which lies at approximately 10 MHz. It is superimposed by the reactance growth due to the external inductance, which leads to an angle of more than 45°. The skin effect occurs in the conducting materials of the cell, in particular in the current collectors, whose typical thickness lies between 10 to 20 µm [26]. Solving (8) for the frequency, the skin effect becomes evident starting from 10.9 MHz for a
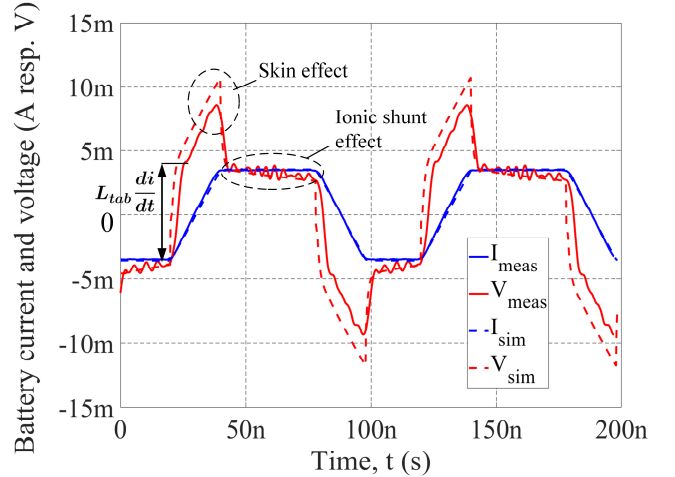
Fig. 12. Measured and simulated cell voltage and current versus time.

20 µm thick copper current collector ($\sigma = 58 \cdot 10^6$ S/m and $\mu = \mu_0 = 4\pi \cdot 10^{-7}$ H/m). This matches our observations of the impedance measurement results.

D. The external inductance

According to (9), the phase of the internal impedance remains always at an angle of 45°. However, the external magnetic flux outside of the conductor dominates the increase in reactance, which eventually results in a maximum phase shift of nearly 90° as noticeable in Fig. 7. The external inductance represents the external magnetic flux and composes the already introduced current collector inductance L_{cc} and additionally the inductance L_{tabs} of the remaining conducting cell components, which are not shunted by the ionic current flow presented in Section VI-B. These components are mainly the tabs and bonds and the physical cell length, which always leads to an inductive contribution.

VII. MODEL PARAMETRIZATION AND VALIDATION

The proposed HF EEC battery model was fitted using the well-known least square (LS) method [27]. The fitted model parameters are summarized in table I, where also a range of fitting values is given for each parameter.

Since the cell characterization was performed in the frequency domain using network analysis, we chose to validate the HF EEC model in the time domain. Therefore, we excited the cell by a trapezoidal current pulse with a frequency of 10 MHz and an edge time of 20 ns and measured the voltage response. The current source is realized by a signal generator together with a series resistor of 30 Ω, which is also used as shunt resistor to measure the current. The current source is connected to the cell mounted on the PCB fixture. The setup was simulated using the SPICE-simulator SIMetrix together with the HF EEC battery model. The results are shown in Fig. 12. When the current starts to rise, the voltage immediately shows a step-like increase in accordance with the law of inductance $u(t) = L \cdot di(t)/dt$. If we calculate the respective inductance, we obtain the same value as L_{tabs}, which is

responsible for the immediate voltage step. The shape of the positive and negative voltage peaks originates from the RL circuit representing the skin effect, as the edge time of 20 ns corresponds to a frequency of 50 MHz. After the skin effect has settled, the instantaneous impedance is approximately 1 Ω, which can be calculated by applying Ohm's law at $t = 50$ ns, for instance. This value matches the Nyquist curve shown in Fig. 6 and is mainly caused by the radial ionic resistance. During the constant current phase, the ionic shunt effect can be noticed from the slow voltage drop, which is caused by a decrease in the instantaneous reactance of L_{cc}. The small oscillations of the voltage signal are due to parasitic measurement effects. The slight differences between the measured and the simulated voltage response in Fig. 12 can be addressed to the distinction between measured cell-in-fixture and de-embedded cell impedance. The latter is used for the model fitting and thus will not completely match the cell-in-fixture measurement.

VIII. Conclusion

In literature, cylindrical Li-ion battery cells have been investigated mainly at frequencies below 10 kHz using electrochemical impedance spectroscopy. To open up high frequency impedance spectroscopy of these cells, we developed a novel HF fixture to mount a single battery so it can be characterized with a 2-port VNA method for frequencies as high as 300 MHz. Different electrochemical and electrophysical effects such as the ionic shunt effect or the skin effect could be measured and allocated to different frequency ranges. The presented cell model can be used for simulations of the cell's electromagnetic interference (EMI) behavior and for modeling a cell-based power line communications channel. Since all of the inspected high frequency effects are of an resistive or inductive nature, they strongly depend on the cell's design and geometry. Future work will focus on their dependency on the structure, state of charge and temperature.

References

[1] E. Barsoukov and J. R. Macdonald, *Impedance spectroscopy: Theory, experiment, and applications,* 2nd ed. Hoboken N.J.: Wiley-Interscience, 2005.

[2] J. Illig, J. P. Schmidt, M. Weiss, A. Weber, and E. Ivers-Tiffée, "Understanding the impedance spectrum of 18650 LiFePO4-cells," *Journal of Power Sources*, vol. 239, pp. 670–679, 2013.

[3] A. Jossen, "Fundamentals of battery dynamics," *Journal of Power Sources*, vol. 154, no. 2, pp. 530–538, 2006.

[4] M. Reuter, S. Tenbohlen, and W. Kohler, "Influence of a Traction Battery's Input Impedance on Conducted Emissions of an Automotive HV Inverter," in *2013 IEEE International Symposium on Electromagnetic Compatibility (EMC Europe)*, Brugge, Belgium, 2013, pp. 229–234.

[5] Y. Maryanka, "Wiring reduction by battery power line communication," in *IEE Seminar on Passenger Car Electrical Architecture*, Birmingham, UK, Jun. 2000, p. 8.

[6] T. F. Landinger, G. Schwarzberger, and A. Jossen, "A Novel Method for High Frequency Battery Impedance Measurements," in *2019 IEEE International Symposium on Electromagnetic Compatibility, Signal & Power Integrity (EMC+SIPI)*, New Orleans, LA, USA, Jul. 2019 - Jul. 2019, pp. 106–110.

[7] L. Callegaro, *Electrical impedance: Principles, measurement, and applications*. Boca Raton: CRC Press, 2013.

[8] C. Bolsinger, J. Brix, M. Dragan, and K. P. Birke, "Investigating and modeling the transmission channel of a prismatic lithium-ion cell and module for powerline communication," *Journal of Energy Storage*, vol. 10, pp. 11–19, 2017.

[9] T. Doersam *et al.,* "High frequency impedance of Li-ion batteries," in *IEEE International Symposium on Electromagnetic Compatibility (EMC), 2015: 16-22 Aug. 2015, Dresden*, Dresden, Germany, op. 2015, pp. 714–719.

[10] E. Hoene, S. Guttowski, R. Saikly, W. John, and H. Reichl, "Rf-properties of automotive traction batteries," in *2003 IEEE International Symposium on Electromagnetic Compatibility, 2003. EMC '03*, Istanbul, Turkey, May. 2003 - May. 2003, 425-428 Vol.1.

[11] S. Buller, M. Thele, R.W.A.A. DeDoncker, and E. Karden, "Impedance-Based Simulation Models of Supercapacitors and Li-Ion Batteries for Power Electronic Applications," *IEEE Trans. on Ind. Applicat.*, vol. 41, no. 3, pp. 742–747, 2005.

[12] S. M. Mousavi G. and M. Nikdel, "Various battery models for various simulation studies and applications," *Renewable and Sustainable Energy Reviews*, vol. 32, pp. 477–485, 2014.

[13] R. Koch, *On-line Electrochemical Impedance Spectroscopy for Lithium-Ion Battery Systems: Estimation, Compensation and Avoidance of Measurement Deviations*. München: Universitätsbibliothek der TU München, 2017.

[14] F. C. Laman, M. W. Matsen, and J. A. R. Stiles, "Inductive Impedance of a Spirally Wound Li/MoS[sub 2] Cell," *J. Electrochem. Soc.*, vol. 133, no. 12, p. 2441, 1986.

[15] P. J. Osswald *et al.,* "Current density distribution in cylindrical Li-Ion cells during impedance measurements," *Journal of Power Sources*, vol. 314, pp. 93–101, 2016.

[16] S. Schindler and M. A. Danzer, "Influence of cell design on impedance characteristics of cylindrical lithium-ion cells: A model-based assessment from electrode to cell level," *Journal of Energy Storage*, vol. 12, pp. 157–166, 2017.

[17] M. Guo and R. E. White, "Mathematical model for a spirally-wound lithium-ion cell," *Journal of Power Sources*, vol. 250, pp. 220–235, 2014.

[18] P. Korth Pereira Ferraz, R. Schmidt, D. Kober, and J. Kowal, "A high frequency model for predicting the behavior of lithium-ion batteries connected to fast switching power electronics," *Journal of Energy Storage*, vol. 18, pp. 40–49, 2018.

[19] M. J. Brand, "Lithium-ion battery cells and systems under dynamic electric loads," Dissertation, Techn. Univ; Herbert Utz Verlag GmbH; Technische Universität München, München.

[20] M. Steer, *Microwave and RF design: A systems approach*. Raleigh, NC: SciTech Pub, 2010.

[21] M. Brand *et al.,* "Electrical safety of commercial Li-ion cells based on NMC and NCA technology compared to LFP technology," in *2013 World*

Electric Vehicle Symposium and Exhibition (EVS27), Barcelona, Spain, Nov. 2013 - Nov. 2013, pp. 1–9.

[22] F.B.J. Leferink and M.J.C.M. van Doom, "Inductance of printed circuit board ground planes," in *1993 International Symposium on Electromagnetic Compatibility*, Dallas, TX, USA, Aug. 1993, pp. 327–329.

[23] C. L. Holloway and E. F. Kuester, "Net and partial inductance of a microstrip ground plane," *IEEE Trans. Electromagn. Compat.*, vol. 40, no. 1, pp. 33–46, 1998.

[24] R. Mingant *et al.,* "EIS Measurements for Determining the SoC and SoH of Li-Ion Batteries," in Las Vegas, NV, 2011, pp. 41–53.

[25] H. A. Wheeler, "Formulas for the Skin Effect," *Proc. IRE*, vol. 30, no. 9, pp. 412–424, 1942.

[26] P. Oßwald, "Advanced Thermodynamic Measurements as Degradation Tracking Technique in Lithium-Ion Cells," Dissertation, Universitätsbibliothek der TU München, München, 2017.

[27] S. M. Kay, *Estimation theory,* 19th ed. Upper Saddle River, NJ: Prentice Hall PTR, 2011.

Thomas F. Landinger received the B.Eng. and M.Eng. degree in electrical engineering and information technology from the Rosenheim Technical University of Applied Sciences, Rosenheim, Germany, in 2016 and 2018, respectively. He is currently pursuing the Ph.D. degree in electrical and computer engineering at the Technical University of Munich, Germany.

In 2017, he was with the Mixed Signal ASICs Development Group of Rohde & Schwarz GmbH, Munich, Germany as a Master Student. Since 2018, he has been a Ph.D. candidate with the Infineon Technologies AG, Munich, Germany, where he works on robust battery management systems. His research interests include automotive electronics, battery characterization and modeling, system simulation, power line communications and high frequency measurement techniques.

Guenter Schwarzberger received his Diploma degree in electrical engineering from the Technical University of Munich, Germany, in 1994.

From 1994 to 2004, he engaged in mixed signal semiconductor test as a Test Engineer, Applications Manager and later Product Manager with SZ Testsysteme. In 2004, he joined Infineon Technologies AG, Munich, Germany, where he has held various positions in Technical Marketing and Application Engineering for automotive power semiconductors. Since 2015, he has been Senior Staff Engineer Automotive System Engineering with focus on electromobility and battery topics.

Andreas Jossen received the Diploma and Doctoral degree in electrical engineering from the University of Stuttgart, Germany. He earned his doctorate dealing with management of photovoltaic plants using energy storage systems.

From 1994 to 2010, he was a Group Leader of the battery system technology group with the Center for Solar Energy and Hydrogen Research, ZSW, Ulm, Germany. Since 2010, he has been a Full Professor at the Institute for Electrical Energy Storage Technology at the Technical University of Munich, Germany. His research activities include modeling, simulation, and characterization of rechargeable batteries, such as battery topologies, state determination, and control of battery systems.

4.3 Cell State and Cell Design Dependencies

This section introduces the article *High frequency impedance characteristics of cylindrical lithium-ion cells: Physical-based modeling of cell state and cell design dependencies* and is based on the paper without further reference.

In Section 4.2, HF impedance measurements were conducted on a specific type of 18650 Li-ion cell at a certain ambient temperature and SOC. In this section, the HF impedance characteristics of eight different 18650 high power and high energy Li-ion cells were investigated using the measurement method of Section 4.1.1 and the modeling approach of Section 4.2 for a more profound HF impedance spectroscopy of cylindrical Li-ion cells. The impedance-based HF battery model of Section 4.2 was parametrized for all investigated cell types as well as for various temperature and SOC conditions.

HF impedance analysis of the different 18650 Li-ion cells revealed a strong correlation with the internal cell structure. Cylindrical Li-ion cells are manufactured by coating the metallic current collector foils by the active electrode materials, placing separators in between, and winding up the stacked layers of separator/ anode/ separator/ cathode into a jelly roll [13]. Tabs are attached to the current collectors to connect the cathode to the positive cap and the anode to the negative outer casing of the cell [13]. Depending on the number of current collector windings and the tabs located along the windings, the eight investigated 18650 Li-ion cells differed widely in their jelly roll inductance from tens to hundreds of nanohenries. Moreover, it has been found that cylindrical high energy cells having thick electrode layers and less windings exhibit a smaller jelly roll inductance than corresponding high power cells with the same tab arrangement.

In literature, it is usually concluded that temperature and SOC hardly influence the resistive-inductive cell characteristics above the intercept frequency [47, 210]. However, impedance investigations over temperature and SOC are often restricted in frequency not exceeding 1 MHz [38, 47, 210]. Therefore, in this section, selected Li-ion cells were characterized up to 300 MHz for different ambient temperatures from 0 °C to 40 °C in intervals of 10 °C and at various SOC conditions from 10% to 90% in intervals of 20%. HF impedance spectroscopy revealed a temperature dependence of the cell impedance in the lower megahertz range due to temperature-dependent ionic current flow in the electrolyte, supporting the existence of the ionic shunt effect found in Section 4.2. Other frequency regions did not show a temperature dependence. SOC was found not to influence the HF cell behavior except for one investigated cell showing a slight SOC dependence for frequencies below 1 MHz, most probably due to anodic volume change during cyclic conditioning. Above 1 MHz, no SOC influence could be observed.

Authors contribution Development of the impedance measurement method and execution of the experiments were performed by Thomas F. Landinger. Data processing, battery modeling, and simulations were also conducted by Thomas F. Landinger. The printed circuit board was conceptualized by Guenter Schwarzberger and Thomas F. Landinger and was designed by Guenter Schwarzberger. Andreas Jossen supervised this work. The original draft was written by Thomas F. Landinger and was reviewed and edited by all authors.

High frequency impedance characteristics of cylindrical lithium-ion cells: Physical-based modeling of cell state and cell design dependencies

Thomas F. Landinger, Guenter Schwarzberger, Andreas Jossen

Permanent weblink:

`https://doi.org/10.1016/j.jpowsour.2021.229463`

High frequency impedance characteristics of cylindrical lithium-ion cells: Physical-based modeling of cell state and cell design dependencies

Thomas F. Landinger [a,*], Guenter Schwarzberger [a], Andreas Jossen [b]

[a] *Infineon Technologies AG, Am Campeon 1-15 85579, Neubiberg, Germany*
[b] *Technical University of Munich, Germany*

GRAPHICAL ABSTRACT
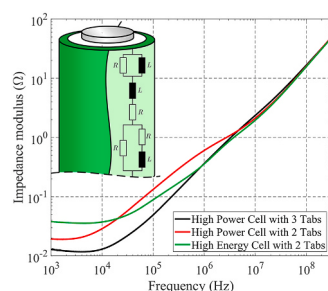
ARTICLE INFO

ABSTRACT

High frequency (HF) properties of lithium-ion (Li-ion) batteries receive growing attention, as an increasing number of highly dynamic loads are present in today's hybrid or battery electric vehicles (HEV, BEV). In this paper, we address the need for a better understanding of the HF characteristics of cylindrical Li-ion cells. First in literature, the impact of cell design, ambient temperature and state of charge (SOC) is investigated in a uniquely wide frequency range from 1 kHz to 300 MHz. Impedance measurements performed on eight different 18650 Li-ion cells show a strong correlation with the cell geometry including cell design (high power, high energy cell) and tab positioning along the current collectors. Moreover, the impedance response of the cells varies with temperature above 1 MHz indicating an increasing contribution of ionic current flow as the inductive reactance of the jelly roll becomes larger. SOC variations indicate only slight impedance changes below 1 MHz, most likely due to electrode volume change. The results are summarized in a physical-based HF battery model, which can be used for simulating highly dynamic battery applications such as battery power line communications (PLC) and impulsive noise investigations on the automotive high voltage (HV) power train.

1. Introduction

Electromobility is regarded as a strong driving force towards environment-friendly mobility. Its future success is directly linked to the performance of the automotive traction battery, which needs to supply a variety of loads. Lithium-ion (Li-ion) batteries are implemented in most of today's electric and hybrid vehicles due to their high specific energy and energy density [1]. To enhance performance and safety, a battery

---

management system (BMS) monitors the battery pack by sensors attached to the cells, which are commonly connected by a serial communication bus [2]. As this demands a huge amount of wiring, power line communication (PLC) has recently been proposed as an attractive alternative communication technique among cell sensor circuits [3–7]. Thereby, the high voltage (HV) automotive power lines including the traction battery are utilized as transmission channel, and the serial communication bus can either be omitted to save costs or used as a redundant communication system.

Predicting the performance of PLC over the traction battery requires knowledge about the battery's impedance for high frequencies in the megahertz range. On cell level, Electrochemical Impedance Spectroscopy (EIS) [8] is widely used to determine the complex-valued cell impedance over frequency. However, EIS is generally limited in frequency since regular EIS equipment mainly utilizes impedance measurement techniques, which are optimized for low-frequency relevant electrochemical process identification [8]. This makes high frequency (HF) impedance measurements and their interpretations difficult, as measurement errors such as inductive artefacts coming from the EIS equipment may distort the results [9]. As the typical frequency range of EIS lies below 10 kHz [9], we denote frequencies above 10 kHz as 'HF'. For HF cell characterization in the megahertz range, we previously proposed an alternative HF-capable impedance measurement technique, which can deal better with HF phenomena such as signal reflections and coupling effects [10]. For PLC performance prediction, it is also essential to quantify how the battery's HF impedance depends on different cell designs and how it changes over a wide range of ambient temperature and the state of charge (SOC).

Only a few publications are available dealing with the cell's behavior at high frequencies from a physical point of view. Laman et al. [11] investigated the HF properties of cylindrical cells up to 10 MHz, which had the anodic tab attached to the outermost and the cathodic tab to the innermost electrode winding[1]. By adding a second anodic tab to the innermost winding, they found that the spiral geometry of the electrodes and the tab positions significantly contributes to the cell's inductance and consequently to its HF impedance.

Osswald et al. [12] confirmed these findings by assessing the inductive behavior of a cylindrical 26650 cell with EIS measurements among different tab positions along the current collectors. They concluded that the maximum impedance value at high frequencies strongly correlates with the electrode windings enclosed by the tabs.

More recently, Schindler et al. [13] investigated an 18650 cell by three electrode impedance measurements up to 1 MHz. Based on measurements and geometrical information gained from microscopical cross sections, they proposed a detailed planar transmission line model, which can predict the impact of the cell design on the battery's impedance. Beside inductive loss processes, they recognized another HF relevant resistive loss process due to radial ionic current flowing between the jelly roll layers. The study concluded that the cell design (power/energy cell) significantly changes the cell's resistive-inductive behavior for high frequencies.

In [14], Ferraz at al. proposed three high frequency cell models considering the skin effect as potential reason for the resistive HF behavior of the cell. By evaluating the cell impedance up to a frequency of 1 MHz, they found the resistive-inductive cell characteristics not to correlate substantially with SOC.

All of the cited previous studies provide valuable information about the cell's properties at elevated frequencies. However, none of them investigated frequencies higher than 10 MHz, which are of interest for PLC over the traction battery. Yet, Hoene et al. [15] investigated cell properties for frequencies higher than 10 MHz, but simplified the cell by a solid cylindrical conductor model, which does not give a detailed

insight into the cell. For this reason, in Ref. [16], we investigated the cell's resistive-inductive characteristics up to a frequency of 300 MHz. Using a novel measurement method for HF low-ohmic impedances, we were able to detect several high frequency related loss processes including the skin effect, which we summarized in a physical-based battery model. The presented approach was applied to one specific 18650 Li-ion cell, but only at a certain temperature and SOC.

To the best knowledge of the authors, no literature is available quantifying the impact of cell design, temperature and SOC on the cell's HF behavior in the megahertz range. This is critical because the battery directly affects the PLC performance, which might deteriorate for varying ambient conditions.

In this paper, we address this issue and examine how much the cell's HF impedance varies with different factors of influence. The cited previous works [11–14] already considered the cell geometry to be essential for the HF behavior of Li-ion cells. For this reason, we investigate different high power and high energy 18650 cells in a frequency range from 1 kHz to 300 MHz. Cross-sectional views of the cells are analyzed regarding tab positions and number of windings, and the cells' impedances versus frequency are obtained by vector network analyzer (VNA) measurements [17]. Moreover, we evaluate how the cells' HF impedances depend on different temperatures and SOCs and how these dependencies can be addressed by our physical-based HF battery model.

In Section 2, we present typical high frequency characteristics of cylindrical Li-ion cells found in previous literature and introduce our modeling approach. Section 3 presents the experimental setup used for the HF cell characterization. The results for different cell geometries, temperatures and SOCs are evaluated and discussed in Section 4. The paper concludes with Section 5.

2. Battery model for high frequencies

In Fig. 1a, we propose an equivalent electrical circuit (EEC) model of a single cylindrical Li-ion cell for high frequencies. The battery's typical AC impedance response is shown in the Nyquist plot in Fig. 1b. The EEC model addresses several resistive or inductive effects, which are visible at different frequency regions in the Nyquist plot. The goal of the model is to describe the frequency dependent physical effects in a compact form by lumped elements, which are frequency independent. It should be noted that the model describes the battery's AC impedance only for frequencies higher than the intercept frequency with the real axis in the Nyquist plot. It does not include slower cell dynamics such as double layer effects and diffusion, which exhibit a capacitive nature and can be found in the negative imaginary half plane of the Nyquist plot (indicated by the dashed impedance curve in Fig. 1b). Since the double layer capacitance will shunt the charge transfer reaction resistance for higher frequencies [18], this effect is also not relevant for HF battery modeling. Consequently, solely resistive and inductive loss processes determine the high frequency behavior of cylindrical cells. They can be allocated in either the electrochemical or the electrophysical domain.

It is commonly accepted that the inductive cell properties arise mainly from the spirally wound geometry of cylindrical cells [11–13]. Fig. 2a illustrates the jelly roll structure in a cross-sectional view. Copper (Cu) and aluminum (Al) current collectors are coated by the active electrode materials on both sides creating anode and cathode, respectively. To form the jelly roll, the electrodes are rolled up with separator foils placed in between [19]. Caused by this geometry, the current collectors exhibit an inductive nature, which is distributed along the collector windings and denoted as $L_{cc}'(f)$ in Fig. 2a. More specifically, $L_{cc}'(f)$ represents the self-inductance of each current collector segment and describes the voltage drop along the segments due to a time-varying current. The frequency dependency of $L_{cc}'(f)$ arises from the skin effect, which forces the current to concentrate on the outer surface of electrical conductors for higher frequencies (for further details see below).

As the cathodic and anodic current collector segments are closely attached to each other, their magnetic fields interact and mutual

---

[1] A graphical representation of the tab pattern can be found in Fig. 3 with reference to the Molicel IHR18650A.
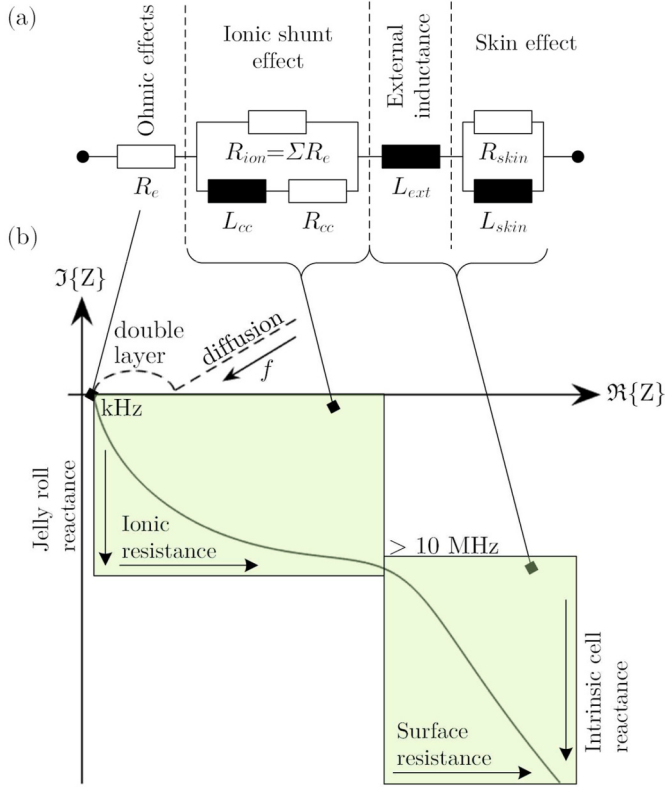
Fig. 1. (a) Physical-based high frequency EEC-model of a cylindrical Li-ion battery. The model represents the high frequency relevant loss processes, which can be found at different frequency ranges in the Nyquist plot (b). The dashed section of the cell's impedance locus indicates the low frequency relevant electrochemical effects, which are not part of the model (a).

Fig. 2. Structure of a typical cylindrical Li-ion cell: (a) Cross-sectional view of the spiral geometry. (b) Representation of (a) as planar transmission line. From (b) it becomes evident that ohmic effects in the electrochemical domain are in parallel with resistive-inductive effects in the electrophysical domain. The point P in both (a) and (b) indicates the same position along the Al current collector. The locally distributed nature of the circuit elements is signified by apostrophes (') implying quantitiy per length. The frequency dependency of the elements L_{cc}' and R_{cc}' is caused by the skin effect.

inductive coupling was observed in previous studies [11,13]. The mutual inductance M' in Fig. 2a accounts for this phenomenon. Regarding the manufacturing of cylindrical cells, tabs are attached to the current collectors to connect the cathode to the positive cap and the anode to the negative outer casing of the cell [19]. Depending on the position of the tabs along the current collectors, the tabs will enclose more or less windings leading to a higher or lower jelly roll net inductance consisting of self and mutual inductance [12]. This will be investigated deeper in Section 4.1.

The limited conductivity per length of the current collectors is indicated by the resistor R_{cc}'(f) in Fig. 2a, which is also frequency dependent due to the skin effect as previously reported in Refs. [18,20, 21]. In Ref. [22], the proximity effect was found to be a possible reason for the increasing cell resistance at high frequencies. Thereby, electrical conductors in close proximity mutually induce eddy currents forcing the overall current concentration to be higher at the non-facing surfaces of the conductors [23]. Regarding the spirally wound cell geometry, anodic and cathodic current collectors are mutually stacked. From this symmetric structure, we suppose that the proximity effect will cancel out in cylindrical battery cells and can be neglected.

The locally distributed resistor R_e' accounts for the ohmic losses occurring in the electrochemical domain and its interface to the electrophysical domain. R_e' is mainly determined by the ionic conductivity of the electrolyte, but also includes the transition resistance between active electrodes and current collectors [9,18,24]. As first component in the EEC model (Fig. 1a), the resistor R_e sums up the locally distributed ohmic resistance R_e'. The value of R_e can be estimated at the intercept frequency with the real axis of the Nyquist plot in Fig. 1b, albeit small capacitive and inductive contributions might be still present cancelling each other out [25].

The local distribution of the elements L_{cc}', R_{cc}', and R_e' along the

spiral from Fig. 2a can be re-drawn as a planar transmission line, which is depicted in Fig. 2b. From this representation, the parallel interconnection between the electrophysical losses along the current collectors and the electrochemical losses in the electrolyte becomes obvious. This was first found in Ref. [11] and was thoroughly investigated in Ref. [13]. In the Nyquist plot (Fig. 1b), the parallel conjunction leads to a resistive-inductive impedance arc spanning frequencies from kHz up to some MHz. The arc can be explained by the increasing reactance of the current collectors for increasing frequencies. The higher the frequency, the more ionic current radially shunts the electrode windings through the jelly roll layers, seeing multiples of the electrolyte resistance R_e' [11]. Based on the observations in the Nyquist plot and the knowledge about the cell structure, we can model this ionic shunt effect by a lumped element RL parallel circuit, which is the second part of the EEC model in Fig. 1a. It comprises the net inductance L_{cc} and resistance R_{cc} of the current collectors in parallel with the ionic resistance R_{ion}, which can be seen as the total resistance of the stacked active material and the electrolyte located between the tabs.

It should be noted that although the presented cell loss processes do have an inherently distributed nature and are partly frequency dependent, we model them by lumped and frequency-constant EEC elements to obtain a compact and comprehensive battery model.

Still, the frequency dependency caused by the skin effect is included in the EEC model of Fig. 1a by another frequency constant RL circuit (R_{skin} and L_{skin}). This third EEC sub circuit accounts for the diminishing penetration depth d_{skin} (also known as skin depth) of a time varying current for increasing frequencies. For cylindrical conductors, d_{skin} can be calculated according to Ref. [26] by

$$d_{skin} = \frac{1}{\sqrt{\pi \sigma \mu f_{skin}}} \tag{1}$$

with the frequency f_{skin}, the electrical conductivity σ, and the magnetic permeability μ of the conductor. The decreased penetration depth leads to an increase in internal resistance and reactance per length according to

$$R_{int}'(f) + j2\pi f \cdot L_{int}'(f) = \frac{1}{w}\sqrt{j2\pi f \cdot \mu / \sigma} \,, \tag{2}$$

where $L_{int}'(f)$ is the internal inductance per length and w the circumference of the conductor. The internal resistance $R_{int}'(f)$ per length is also known as surface resistance. Equation (2) is derived in Ref. [26] by establishing the frequency dependent current density distribution inside the conductor. From (2), it can be seen that the complex internal impedance is proportional to the square root of the frequency. This would lead to an impedance curve progression with an angle of $+45°$ in the Nyquist plot similar to the $-45°$ diffusion branch described by the Warburg impedance (see Fig. 1b). However, external inductance contributions arising from the tabs and bonding wires are superimposed leading to a steeper reactance increase as visible in Fig. 1b. In the EEC model, the lumped elements describing the skin effect are denoted as R_{skin} and L_{skin} to distinguish them from the true line parameters $R_{int}'(f)$ and $L_{int}'(f)$.

Additionally for very high frequencies, the signal propagation delay due to the physical length of the cell becomes evident. When a signal propagates from one cell terminal to the other, it undergoes a phase delay, which can be regarded as the intrinsic cell inductance, which is another external inductance. The intrinsic cell inductance and the external inductance due to tabs and bonding wires are summarized by the fourth and last EEC model element L_{ext}. All EEC model components including their physical meaning are summarized in Table 1. For a deeper explanation including the model validation, the reader is referred to Ref. [16].

3. Experimental

In this work, impedance measurements were performed on eight different commercially available 18650 cylindrical Li-ion cells in the frequency range from 1 kHz to 300 MHz. The essential electrical parameters of the investigated high power and high energy cells are listed

Table 1
EEC battery model elements of Fig. 1a and their physical meaning.

Circuit Element	Electrochemical or -physical effect
R_e	Ohmic resistance of electrolyte and interface between active electrodes and current collector
R_{cc}	Electrical resistance of current collectors
R_{ion}	Ionic resistance of the electrolyte layers
L_{cc}	Net self-inductance of the current collectors (external inductance)
L_{ext}	Tab and bonding wire inductance, intrinsic cell inductance (external inductance)
R_{skin}	Internal (surface) resistance
L_{skin}	Internal inductance

in Table 2. The impedance measurements were carried out with an Agilent E5061B vector network analyzer (at present Keysight Technologies, Inc., USA) using the shunt-through VNA method, which is specialized for broadband low-ohmic impedance measurements [27]. The frequency span was swept with the least available bandwidth of 10 Hz to provide best accuracy, which is ensured to be below 10% according to the manual of the VNA. 1601 measurement points were recorded, which corresponds to 292 points per frequency decade. The excitation power of the VNA was chosen to be -17 dBm (20 µW), which is a tradeoff between a sufficient signal-to-noise ratio and keeping the cells within the linear region (10 mV criterion [8]). Each cell was mounted on a printed circuit board (PCB) fixture to connect it properly to the VNA by coaxial connectors and leads. By measuring a reference impedance, which we chose to be a solid copper cylinder with the same dimensions as the cell, we were able to de-embed the cell impedance from the entire measurement setup. For more details about the HF measurement method, the reader is referred to our previous work [10].

Beside the measurement method accuracy, the HF impedance deviation among cells of the same type has to be considered to provide reliable results. Four cells of the same type were characterized using the HF measurement method and found to deviate by 4% below 100 MHz and 18% between 100 MHz and 300 MHz with respect to their HF impedance. These values are well below the impedance variations presented in the results and discussion section 4 thus accounting for reliable results.

All tests were performed within the first few cycles of the cells and the SOC was kept at 50% except for the investigations on SOC dependences in Section 4.3. Thereby, electrochemical long-term changes can be excluded during the measurements.

To gain insight into the structure of the cells, each cell was investigated by X-ray computed tomography (CT) and cross-sectional scans were obtained, which are illustrated in Fig. 3. Thereby, the tab positions along the windings and the number of windings could be determined, which are presented in Section 4.1.

For temperature investigations, the cells were placed inside a Voetsch VT 7004 climate chamber (Weiss Umwelttechnik GmbH, Germany), which provides a controlled thermal environment. For each temperature setting of the chamber, a period of 2 h was chosen for temperature equilibration of the cells to obtain a homogenous temperature distribution [28]. In addition to the HF VNA impedance measurements, EIS measurements in the low-frequency region were performed at each temperature using a Zahner Electrochemical Workstation Zennium (ZAHNER-elektrik GmbH & Co. KG, Germany).

To charge and discharge the cells to certain SOC values, the ATGB 1200 battery test equipment (Batteryuniversity GmbH, Germany) was used. Table 3 summarizes the steps performed for the cell characterization at different SOCs. After a constant current/constant voltage (CCCV) charge and discharge capacity check, the cells were charged to reach the desired SOC. Subsequently, 2 h of rest were chosen for cell temperature setting. Since only frequencies higher than 1 kHz are considered, electrochemical relaxation processes are not expected to influence the impedance measurement as they only affect frequencies below 500 Hz [29].

4. Results and discussion

The section is divided into three subsections each of them discussing one factor of influence (geometry, temperature, state of charge) on the cell impedance, which have been observed during the measurements.

4.1. Geometry dependency

Four essential geometrical cell aspects reported in previous literature to affect the resistive-inductive behavior of cylindrical Li-ion cells were investigated how they change the HF cell characteristics: the number of tabs, the position of the tabs [11–13], the cell design (high power or high

Table 2

Electrical parameters[a] and cell design parameters of the investigated 18650 Li-ion cells. For tabs located in the jellyroll, the corresponding winding number is given in parentheses, counted from inside to outside.

Cell	Nominal discharge capacity	Maximum continuous discharge current	Cathode	Anode	Number of windings	Mandrel	Group
Samsung INR18650–25R	2500 mAh	20 A	In jellyroll (15)	Cell center and can	27	No	**A**
Sony US18650VTC4	2100 mAh	30 A	In jellyroll (12)	Cell center and can	24	Yes	
Sony US18650VTC5	2600 mAh	30 A[b]	In jellyroll (13)	Cell center and can	24	Yes	
Panasonic NCR18650B	3350 mAh	6.2 A[b]	In jellyroll (11)	At can	17	Yes	**B**
Panasonic NCR18650E	2250 mAh	20 A[b]	In jellyroll (16)	At can	23	Yes	
LG INR18650 MJ1	3500 mAh	10 A	Cell center	At can	19	No	**C**
Molicel IHR18650A	1950 mAh	4 A	Cell center	At can	18	Yes	
A123 APR18650M1A	1100 mAh	30 A	In jellyroll (15)	In jellyroll (15)	22	Yes	**D**

[a] Values from datasheets unless otherwise stated.

[b] Information from suppliers, not verified.
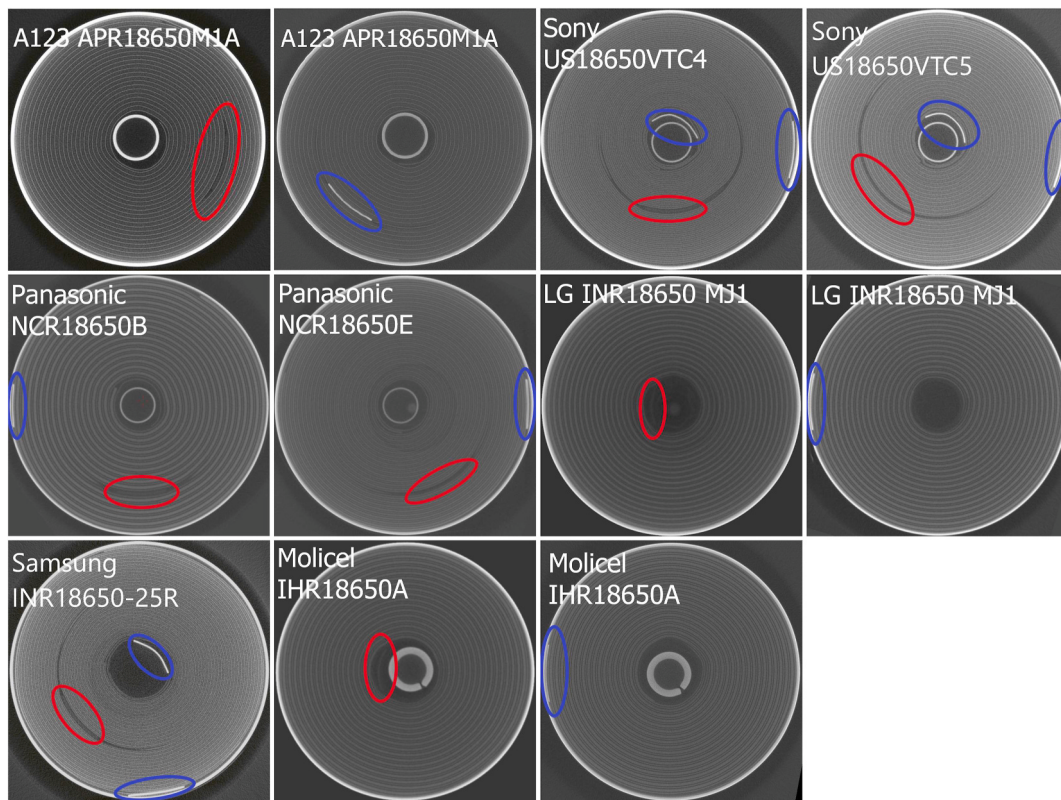
Fig. 3. CT cross sections of the investigated cells. The positions of the tabs are indicated by red (cathode) and blue (anode) markers. In some cases, two different CT scans of the cell are required to determine all tab positions. This is because the tabs are not visible together in one cross-sectional view since they do not range sufficiently along the length of the cell. All scans are viewed from the negative cell terminal. (For interpretation of the references to colour in this figure legend, the reader is referred to the Web version of this article.)

energy) [11,13,30,31] and the presence of a mandrel [12]. The cell design mainly implies the electrode thickness and number of windings [31], whereas the mandrel is a steel rod that is inserted for the winding process during manufacturing [12].

Prior to the HF measurements, CT cross sectional views illustrated in Fig. 3 were analyzed regarding tab positions, number of windings and whether a mandrel is located in the center of the cell. The resulting tab positions are marked in the CT scans and the found geometry data of the cells are summarized in Table 2. Depending on the tab positions along

the current collectors, the cells were divided into four different groups A, B,C, and D.

Before analyzing the results, the inductive nature of the spirally wound geometry of the cell has to be understood, which determines most of the overall HF cell impedance. The inductive contributions due to the cell's geometry can be separated into three parts. The first part is the spiral structure of the cell, which causes the main part of the overall cell inductance due to circumferential current flow [12,13]. To the best knowledge of the authors, no closed formula for calculating the

Table 3
Steps of the HF cell characterization for different SOCs.

Step	Parameter	End Criterion
CCCV Charge	I_{CC} = 1C (0.5C), V_{CV} = 4.2 V	$I_{CV} \leq 0.05$C
Pause	time t	$t = 5$ min.
CCCV Discharge	I_{CC} = 1C, V_{CV} = 2.5 V	$I_{CV} \leq 0.05$C
Pause	time t	$t = 5$ min.
CC Charge	I_{CC} = 1C (0.5C)	$Q = 10, \ldots, 90\%$
Pause	time t	$t = 2.0$ h
HF Impedance Measurement	$P = -$ 17dBm, 1 kHz $\leq f \leq 300$ MHz	Sweep end, $t = 5$ min.

inductance of a spirally wound planar conductor is available in literature. The approximation by a set of concentric cylinders as done in Refs. [11,13] was reported in Ref. [32] to be valid only when little current flows in circumferential direction. This applies to metallized film capacitors, where the electrode face ends are continuously connected to the tabs by a metal spray [32] leading to a current flow solely in longitudinal direction. However, this is not the case for cylindrical battery cells, where the tabs are connected to the current collectors only at specific points along the windings.

The second part addresses the inductive coupling between positive and negative current collectors, which is illustrated in Fig. 4. Depending on the tab positions, the current in both collectors is in either parallel or antiparallel relationship and induces a positive or negative voltage drop with respect to the voltage drop caused by the collector's self-inductance L_+ or L_-. If the currents are in parallel as in Fig. 4a, the mutual coupling inductance M adds up the self-inductance of the current collectors and the net inductance of the segment is

$$L_{par} = (L_+ + M) || (L_- + M) . \tag{3}$$

For the readers' convenience, we depicted the detailed mathematical part of equations (3)–(5) in the appendix part of this work and only give the final form - relevant in the following – here.

Regarding the other case, when the tabs are located face-to-face at one end of the collectors as indicated in Fig. 4b, the currents are in opposite directions (their sum is zero) and M gets a negative sign.

As reported in Ref. [13], the inductive coupling factor $k := M/\sqrt{L_+ L_-}$ between the current collectors is close to 1 due of the tight alignment of the electrode layers. Supposing equal currents on both collectors, a coupling factor of nearly 1, and equal inductance values of L_+ and L_- inserted in (3), the net inductance of the segment from Fig. 4a is

$$L_{par} \approx (2L_+) || (2L_+) = L_+ , \tag{4}$$

whereas in the case of antiparallel current flow as in Fig. 4b, the net inductance is close to zero:

$$L_{npar} \approx (L_+ - L_+) + (L_+ - L_+) = 0 . \tag{5}$$

Regarding Fig. 4, the current density changes along the current collectors and is different for (a) and (b). However, as the coupling factor k is close to 1, this has no impact on the net inductance of the segments.

The third part of the geometry-caused inductive contribution is the physical length of the cell, which causes a current flow in longitudinal direction from one battery terminal to the other. It can be approximated by the inductance of a hollow cylinder, which can be calculated by

$$L_{cyl} = \frac{\mu_0}{2\pi} l \left(\ln \left(\frac{2l}{r} \right) - 1 \right) . \tag{6}$$

Equation (6) was originally given by Rosa [33] developing the concept of partial inductance, and can be found in inductance textbooks such as in Ref. [34]. Using the cell's length $l = 6.5$ cm and radius $r = 9$ mm and the permeability $\mu_0 = 4\pi \cdot 10^{-7}$ of free space, equation (6) yields an inductance of 21.7 nH. This so-called intrinsic cell inductance causes an additional phase shift especially in the very high frequency range

above 100 MHz, where the signal wavelength reaches the dimensions of the 18650 cell.

4.1.1. Cell impedance measurements

Fig. 5 presents the HF impedance measurement results of the investigated cylindrical Li-ion cells. The results are separated into four sub-figures a,b,c,d according to the aforementioned four groups of cells A,B,C, and D with different tab patterns as indicated. In Fig. 5d, beside group D, also one representative cell from each of the other groups A,B,C is added to allow a comparison among different groups.

For each 18650 cell, the HF EEC battery model of Fig. 1a was fitted to the corresponding impedance measurement using the randomize and simplex algorithms provided by EC-Lab® Software (BioLogic, France). The relevant fitted inductance and ohmic resistance values are summarized in Table 4. Since the chosen battery model aims to describe the HF behavior in a highly compact manner yet with physical meaning, there remains a deviation between measurement and model. A typical model fit and its mean square deviation from the measurement is pictured in the appendix. Since the time constants of the loss processes are largely distinct from each other, overfitting issues did not occur. For the following analysis, the frequency range is separated into three ranges: Low frequency range I (1 kHz–20 kHz), high frequency range II (20 kHz–10 MHz) and very high frequency range III (10 MHz–300 MHz).

As visible in the Bode plots of Fig. 5a–d, depending on each cell's ohmic resistance, the impedance magnitude starts at low-ohmic values in frequency range I and strongly increases due to the resistive-inductive properties of the cell for higher frequencies in range II and III. This can also be seen from the impedance phase reaching almost an angle of 90° for 300 MHz. Frequency range II highlights the different inductive properties of different cell designs and tab patterns, whereas in range III, interestingly all cells exhibit more or less the same impedance magnitude and phase. The observations in range III match the fitted values of the external inductance L_{ext} in Table 4, which are only slightly higher than the hollow cylinder inductance of 21.7 nH calculated by (6) using the 18650 cell diameter. From this, we can conclude that above approximately 70 MHz, the cell design and tab patterns do not significantly affect the HF impedance anymore and the current is forced towards the outermost winding of the cell, where it sees the lowest possible cylinder inductance.

As the inductive parts contribute much more to the impedance growth than the resistive parts, the Nyquist plots of Fig. 5a–d also highlight the increase separated in real and imaginary part. From the Nyquist plots, we can allocate the resistive-inductive impedance arc in frequency range II revealing the ionic shunt effect. The arc broadens for cells with higher ohmic resistance because the ionic currents see more resistance when shunting the electrode layers. In frequency range III, the resistance of the cells still increases, which can be addressed to the skin effect. The characteristic bending in the Nyquist plots marks the transition from frequency range II to III.[2] The impedance bending is most probably due to the settling ionic shunt effect and the initiating skin effect. Solving (1) for the skin frequency f_{skin} using a typical Cu current collector ($\sigma = 58 \cdot 10^6$ S/m, $\mu = \mu_0 = 4\pi \cdot 10^{-7}$ H/m, $d_{skin} = 13~\mu$m $= d_{Cu}$) leads to $f = 25$ MHz. Due to the definition of the skin depth being the depth where the current density has decreased to $1/e \approx 37\%$ of the surface value, the skin effect is expected to be already noticeable at frequencies below 25 MHz. This matches our observations in the Nyquist plots, where the skin effect becomes obvious between 10 and 20 MHz. As copper has a much higher conductivity than aluminum ($\sigma = 3.7 \cdot 10^6$ S/m), we conclude that the anodic current collector mostly defines the skin

---

[2] One exception is the A123 APR18650M1A, where the bending point is at a much higher frequency. Although both tabs are located inside the jelly roll, they are not located quite face to face as can be seen from the corresponding cross sections in Fig. 3. This might cause an increased ionic current flow leading to the visible impedance arc.
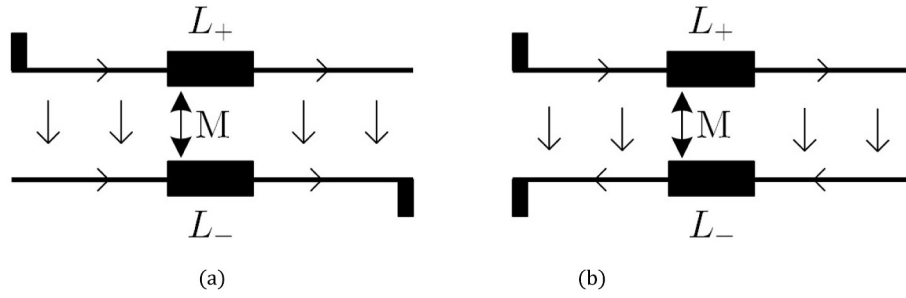
Fig. 4. Mutual coupling between the current collectors for parallel (a) and anti-parallel (b) current flow depending on the tab position.
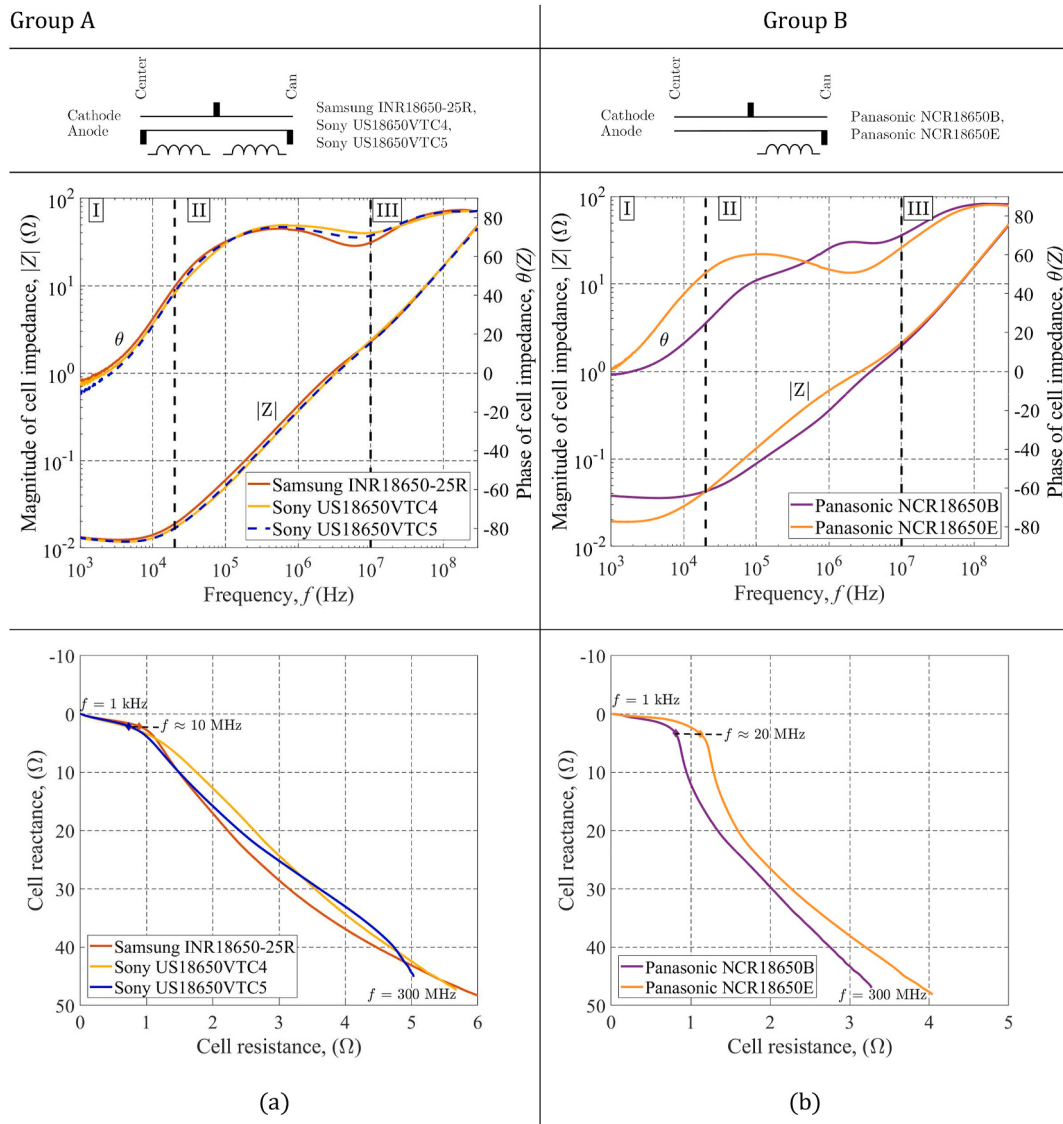
Fig. 5. HF impedance measurement results of eight different 18650 Li-ion cells grouped according to their tab patterns as indicated in (a–d). A Bode plot and a Nyquist plot illustrate the results for each group. In (d), one cell of each group/tab pattern is added enabling a comparison among different groups.

effect characteristics in frequency range III. The varying fitted values of the internal inductance L_{skin} in Table 4 may be due to different current collector thicknesses of the cells, but may also be due to fitting variance. For a deeper inspection, the thickness of the collectors of all cells would need to be determined, which is beyond the scope of this work. How the different cell geometries further affect the HF cell impedance is

discussed in the following.

4.1.2. Tab position

Regarding the mixed group results shown in Fig. 5d, the Bode plot reveals how different tab positions along the current collectors affect the cell impedance. As stated above, frequency range II provides insight on

Group C

Mixed Group = Group A-D
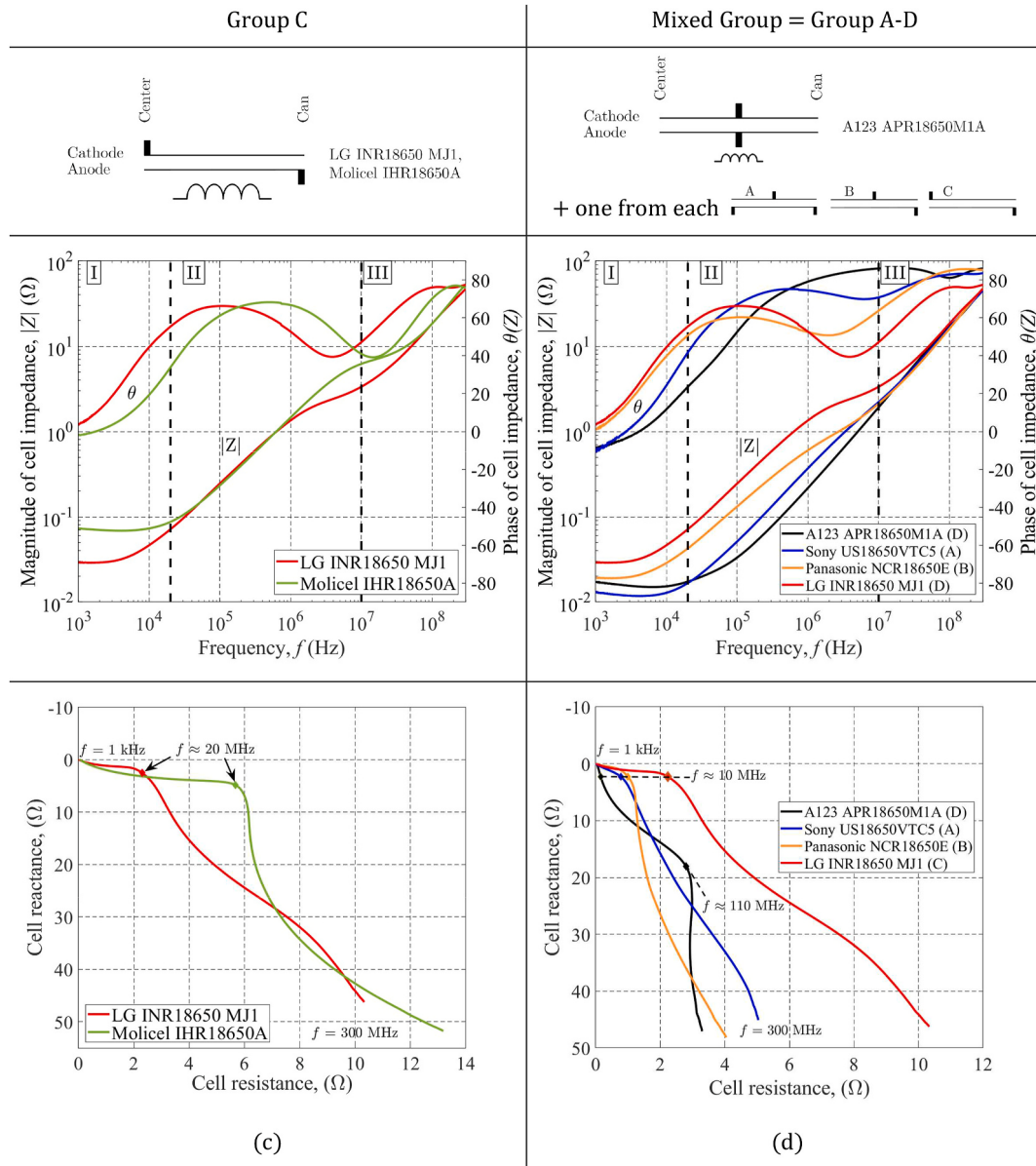
Fig. 5. (*continued*).

Table 4

Measured ohmic resistance and fitted inductance model parameters of the EEC model (Fig. 1a).

Cell	R_e (mΩ)	L_{cc} (nH)	L_{skin} (nH)	L_{ext} (nH)	Group
Samsung INR18650–25R	12.6	38.6	4.6	22.4	A
Sony US18650VTC4	12.0	22.2	4.7	21.9	
Sony US18650VTC5	11.9	27.6	4.5	22.2	
Panasonic NCR18650B	29.3	33.1	3.4	22.0	B
Panasonic NCR18650E	19.4	81.5	3.8	22.0	
LG INR18650 MJ1	29.5	226.8	8.9	21.3	C
Molicel IHR18650A	70.4	197.3	5.5	23.2	
A123 APR18650M1A	15.2	14.8	7.6	24.3	D

how geometry aspects change the impedance characteristics. In case of Fig. 5d, range II indicates that the cell impedance is higher the more distance lies between the positive and negative tabs. In case of the A123 APR18650M1A (group D), the tabs are placed in the middle of the jelly roll (see Fig. 3) and the cell shows the least impedance, followed by

groups C, B and A. Because the complex impedance Z is linked to the inductance L via $Z = j2\pi f_0 L$, a higher impedance at a certain frequency f_0 in the Bode plot corresponds to a higher inductance at f_0. From this, we can conclude that more windings enclosed by the tabs lead to a higher overall jelly roll inductance, which is in accordance with the previous findings in Refs. [11–13]. This is also confirmed by the fitted L_{cc} values in Table 4, which increase from 14.8 nH in case of the A123 APR18650M1A to 226.8 nH in case of the LG INR18650 MJ1, which has the highest jelly roll inductance among the investigated cells.

4.1.3. Number of tabs

Comparing the representative cells of group A (three tabs) and B (two tabs) in the Bode plot of Fig. 5d, group A exhibits slightly lower impedance values in frequency range II. Also the fitted jelly roll inductances L_{cc} (Table 4) of the cells from group A are lower than those from group B except for the Panasonic NCR185650B, which has significantly less windings (see Table 2). When looking back at the inductive coupling illustrated in Fig. 4 and equations (4) and (5), one can conclude that only collector segments with parallel current flow contribute to the jelly roll inductance. Consequently, in case of group B, only the collector

segments in between the tabs are essential for the overall inductance. Another reason for the negligible inductance of segments not being between tabs as drawn in Fig. 4b, could be a non-uniformly decreasing current density with increasing distance to the tabs, which was found in Ref. [12]. The three-tab arrangement of group A can be seen as two parallel inductances as drawn below the tab pattern in Fig. 5a, whose net inductance is smaller than a single inductance. Therefore, we can conclude that more tabs reduce the inductance of the spirally wound cell.

When looking at the Nyquist plot of Fig. 5d, the Sony US18650 VTC5 (group A) exhibits a higher real part than the Panasonic NCR18650E (group B) for very high frequencies. As described in Section 2, the ionic shunt effect leads to current flowing radially between the jelly roll layers. Therefore, the smaller real part may be caused by the smaller radial distance between the tabs in case of the Panasonic cell, which is visible in the corresponding cross sections in Fig. 3.

4.1.4. Cell design (high energy, high power)

The investigated 18650 Li-ion cells are either optimized for high power capability or high energy density, which can be deduced from the electrical parameters given in Table 2. To examine the influence of the cell design, a high energy (NCR18650B) and a high power (NCR18650E) cell by the Panasonic Energy Company are compared, whose impedance results are given in Fig. 5b (group B). To achieve a high energy density in cylindrical Li-ion cells, the electrodes are typically thicker than for high power cells [31,35], which is visible in the CT cross sections of the Panasonic cells in Fig. 3. Since thicker electrodes experience higher losses, the ohmic resistance R_e is higher thereby limiting the maximum power [35]. In contrast, high power cells like the Panasonic NRC18650E have thin electrodes to minimize R_e. The thin electrode layers leads to a higher amount of windings for high power cell as visible in Fig. 3. Therefore, we expect higher ohmic and inductive losses for high power cells at high frequencies, which was also reported in Ref. [13]. When looking at the results in Fig. 5b, the Bode plot reveals the different frequency characteristics. In frequency range I, the high power cell exhibits a smaller impedance, which increases faster than the high energy cell leading to a higher impedance in range II. In range III, both cells have quite similar impedance characteristics. We can conclude that the higher amount of windings of the high power cell leads to an increased current collector inductance L_{cc} (see Table 4), which causes the impedance to increase faster with frequency than for the high energy cell. These findings are in accordance to a cylindrical coil (solenoid), where the inductance increases with more windings ($L \propto N^2$) [36]. The mechanism behind can be explained by magnetic flux linkage, which increases with additional windings and thus does the inductance. For more information, the reader is referred to electromagnetics textbooks such as [36]. From the Nyquist plot, also the increased ohmic losses at high frequencies due to more windings become visible.

4.1.5. Presence of mandrel

As visible in Fig. 3 and summarized in Table 2, several of the investigated Li-ion cells have a center pin also called mandrel, which is used for the winding process of the jelly roll during manufacturing. Looking at the cell group A, the mandrel's influence on the HF cell behavior can be assessed since there are three cells with quite similar geometries expect for the mandrel. As there is no significant difference visible between the impedance results in Fig. 5a, it is expected that the mandrel has no influence on the HF cell impedance. The slightly higher impedance of the Samsung INR18650-25R in frequency range II in the Bode plot of Fig. 5a is most likely due to the higher amount of windings as listed in Table 2.

4.2. Temperature dependency

For temperature investigations, two 18650 cells from Table 2 were

selected having different electrical and chemical properties: the Samsung INR18650-25R having a cathode composed of nickel manganese cobalt (NMC[3]) and the Panasonic NCR18650B having a nickel–cobalt–aluminum (NCA[3]) composed cathode. In Fig. 6, Nyquist plots (a, b) and a Bode plot (c) illustrate the cell impedance for different temperatures. Fig. 6b and c only include the impedance curves of the Samsung cell to ensure readability, yet the impedance curves of the Panasonic cell show comparable results. In Fig. 6a, the real part of the impedance and the ohmic resistance at the intercept frequency significantly increase with decreasing temperature. Moreover, the transition from capacitive to inductive cell behavior is shifted to higher frequencies, which can be seen from the phase progression in Fig. 6c. These observations were also reported in previous literature [12,37,38] and can be accounted for by reduced charge transfer kinetics [39] and lowered electrolyte conductivity [40]. The latter dominates the temperature behavior of the ohmic resistance [41], whereas the conductivity variation of the metallic current collectors is negligible in the regarded temperature range [42]. Considering the impedance modulus in Fig. 6c, the curves for different temperatures overlay exactly in the entire frequency range except of a remarkable 15 MHz band centered around 10 MHz as indicated by the magnifying inset. In this band, the impedance significantly increases for lower temperatures suggesting a temperature effect dominated by the electrolyte conductivity. As found in the geometry section 4, the highlighted 15 MHz band is the frequency region, where ionic branch currents start flowing radially across the electrode layers shunting the current collector segments. Based on these findings, we suppose that the ionic branch currents see more or less electrolyte resistance depending on the temperature, which leads to the visible impedance spread in Fig. 6c. This can also be observed in the HF Nyquist plot of Fig. 6b, where the resistive-inductive impedance arc broadens for decreasing temperature leading to a higher real part of the cell impedance. Regarding the phase progression in Fig. 6c, we see that the characteristic phase minimum at some megahertz shifts to higher frequencies for lower temperature. From this, we assume that the ionic shunt effect is also shifted to higher frequencies for decreasing temperatures. This is because the higher electrolyte resistance forces the current to keep flowing on the collectors, and ionic branch currents caused by increasing collector reactance tend to initiate at higher frequencies. For frequencies above the highlighted 15 MHz band, the impedance modulus in Fig. 6c seems to be equal again for all temperatures. However, the strong increase in the imaginary part overshadows the impedance's real part in the Bode plot. From the HF Nyquist plot in Fig. 6b, it becomes clear that the real part remains temperature dependent also for higher frequencies.

The temperature dependency of the resistance of the electrolyte can be approximated by an Arrhenius behavior [40,42,43].

$$R_{ion} = \lambda \cdot e^{\frac{E_A}{k_B T}}, \tag{7}$$

with the activation energy E_A, the proportionality constant λ (Ω^{-1}) and the Boltzmann constant k_B. In Fig. 6d, impedance and resistance values of the investigated cells measured at 10 MHz are depicted in an Arrhenius plot. In addition, the fitted ionic resistance R_{ion} of the HF-EEC model describing the resistive-inductive impedance arc is added to Fig. 6d. All impedance curves exhibit an Arrhenius-like behavior and their activation energies lay between 0.04 eV and 0.12 eV as marked in the figure. The fitted R_{ion} has a significantly higher E_A than the measured values, likely because it models the ionic shunt effect over a broad frequency band. The measured values only represent one frequency point and do not account for the frequency shift of the entire ionic shunt effect for varying temperatures. There is also an Arrhenius-like behavior observed for the impedance modulus. This can be confirmed by the fact that the real part of the impedance is dominated by the temperature dependent

---

[3] Values from material safety datasheets.
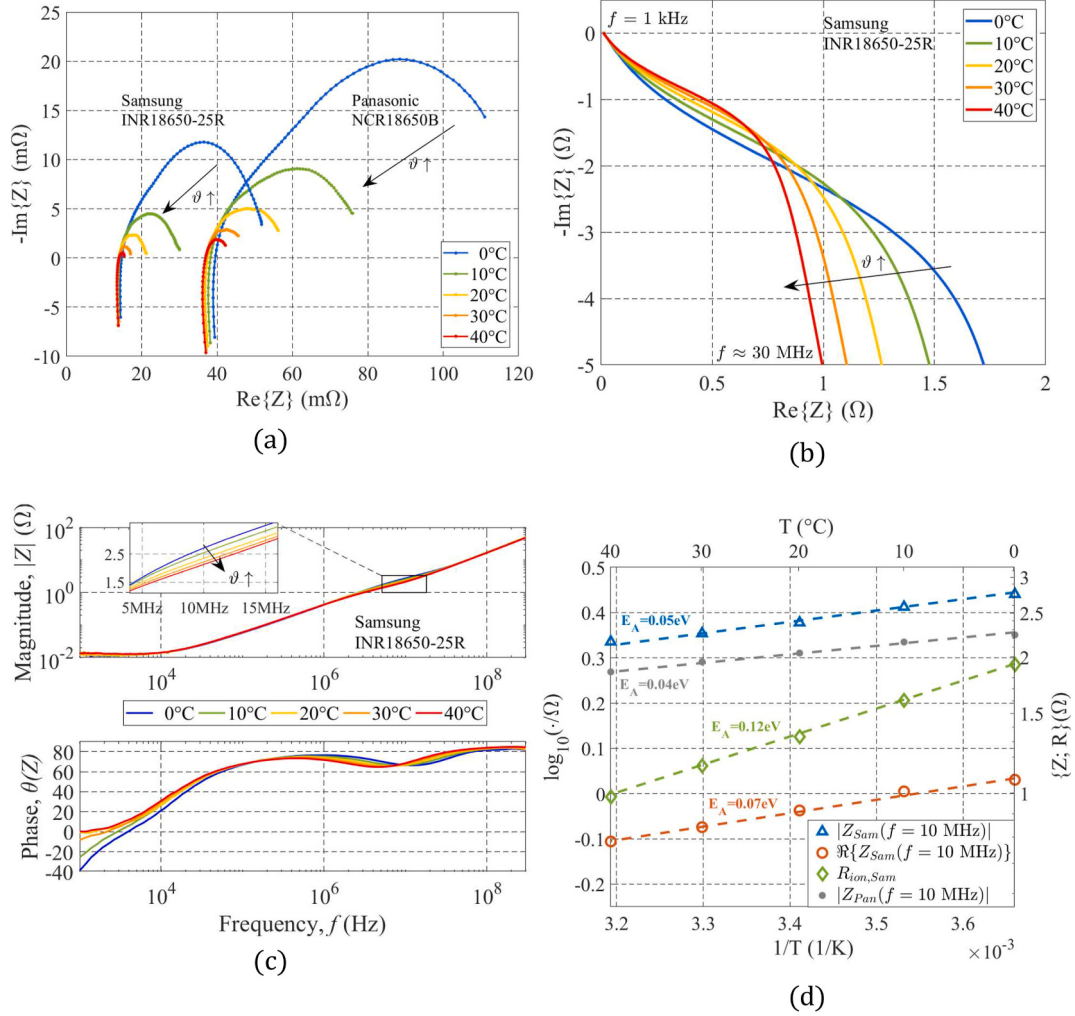
Fig. 6. Temperature dependency of the cell impedance for two different cylindrical 18650 Li-ion cells: EIS Nyquist plot (a) of both cells, HF Nyquist plot (b) and Bode plot (c) of Samsung INR18650-25R for different temperatures. Arrhenius plot (d) of selected impedances, namely Z_{Sam} (impedance of Samsung cell), its real part $\Re\{Z_{Sam}\}$, and Z_{Pan} (impedance of Panasonic cell) at 10 MHz. In addition, the fitted ionic shunt resistor $R_{ion,Sam}$ of the EEC HF model is depicted for the Samsung cell.

electrolyte resistance, whereas the imaginary part is mostly determined by the inductive cell properties, which are nearly temperature independent. The determined activation energies are in the same order of magnitude as previously found in Ref. [42], where the authors attributed the temperature dependency of the ohmic resistance mainly to the temperature dependent electrolyte conductivity. In conclusion, the found Arrhenius-like behavior underlines that the temperature-dependent electrolyte conductivity is mainly accountable for the HF impedance variation with temperature by 20% from 0 °C to 40 °C at frequencies above some megahertz.

4.3. State of charge dependency

For PLC, it is important that the communication performance does not vary with different SOCs. Therefore, the dependency of the HF cell impedance on SOC was investigated based on SOC variations (10%–90%) of the same cells already considered for the temperature investigations in Section 4.2. Fig. 7 illustrates the impedance measurement results for different SOCs in a Nyquist plot (a) for both cells and two Bode plots (b, c) each for one cell. In Fig. 7d, the SOC dependency of the cell impedance for selected frequencies is depicted. Regarding the Samsung INR18650-25R, both the Nyquist (Fig. 7a) and the Bode plot (Fig. 7b) do not indicate any significant impedance change within the considered SOC range. There are little variations in the Nyquist plot

most likely caused by measurement uncertainty. As found in literature, the cell impedance is nearly independent of SOC for frequencies higher than the intercept frequency [9,37,42,44]. It is also reported, that the ohmic resistance of the cell remains constant [9] or exhibits only small changes [9,38,43]. Interestingly, the Panasonic NCR18650B behaves differently from the Samsung cell as can be seen from Fig. 7a and d. The ohmic resistance increases by 15% from 33 mΩ (90% SOC) to 38 mΩ (10% SOC). Moreover, the cell impedance increases for low SOC values over a wide frequency range up to 1 MHz, mainly due to an increase in the real part (see magnifying inset of Fig. 7a). However, for higher frequencies, no SOC dependency can be observed. In contrast to the cyclic conditioning listed in Table 3, in a second experiment, the SOC was additionally adjusted by fully charging and then discharging the cell until reaching the desired SOC. This lead to the same results as for the procedure according to Table 3, thus excluding hysteresis effects. Although the effect is likely caused by another resistive effect, the behavior is different from the observations of the temperature dependency in Section 4.3 and therefore cannot be attributed to the electrolyte conductivity. Unfortunately, we found only little research dealing with cell dynamics and their SOC dependency in the regarded high frequency range. Typical cell dynamics such as double layer effects can be excluded because their large relaxation time cannot be assigned to the investigated high frequencies [29,42]. There are some previous studies available, which investigated Li-ion intercalation into graphite
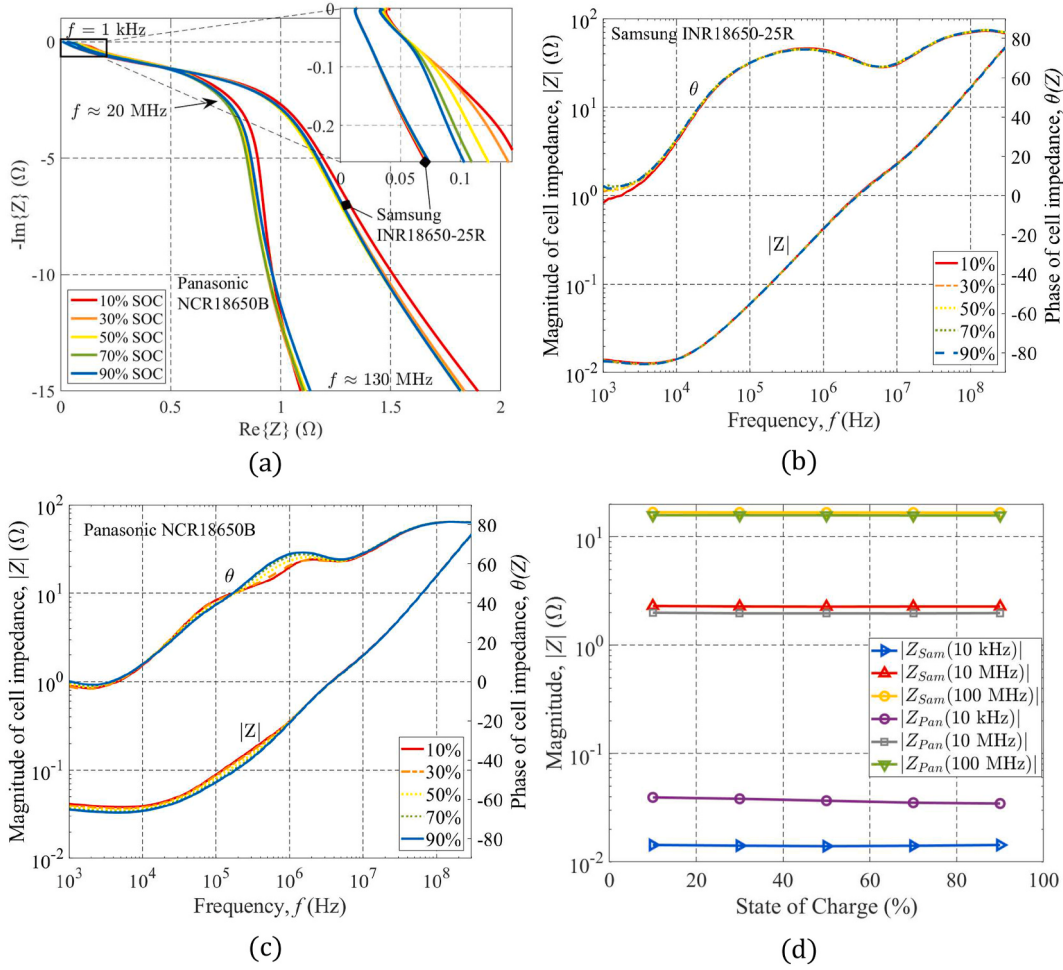
Fig. 7. SOC dependency of the cell impedance for two different cylindrical 18650 Li-ion cells: HF Nyquist plot (a) and Bode plots (b, c) of Samsung INR18650-25R and Panasonic NCR18650B, respectively. (d) Impedance of both cells over SOC for selected frequencies.

materials using EIS [45,46]. The studies could attribute the high frequency signature of the cell to contact resistance between the graphite electrode and the current collectors [45], or resistance within the bulk electrode [46]. Considering the different behavior of the Samsung INR18650-25R and the Panasonic NCR18650B, we assume that the specific cell technology including the thick electrode layers of the Panasonic cell account for the impedance change with SOC. More precisely, we suppose that the delithiation of the thick graphite anode, which dominates the volume change during cyclic conditioning [47], reduces the anode volume, leading to a higher contact resistance between active electrode and current collector.

Another reason for the increased impedance could be the additional heat resistance layer (HRL) that is inserted between negative electrode and separator of the NCR18650B [48], and the contact resistance between HRL and anode, which might depend on the volume change of the electrode, too.

Regardless of the mentioned possible reasons, for frequencies higher than 1 MHz, the additional contact or layer resistance has no more influence, because we assume that it is shunted by the fast time-varying current through capacitive coupling.

5. Conclusion

In this work, we investigated the resistive-inductive behavior of a variety of high power and high energy 18650 Li-ion cells. First in literature, we considered how cell geometry, temperature and SOC influence the cell's impedance characteristics over a wide frequency range

from 1 kHz to 300 MHz. By applying impedance measurements and modeling the cell characteristics from a physical point of view, we were able to address the following cell design aspects:

- Cylindrical high energy cells with thick electrode layers have less windings leading to a smaller jelly roll inductance than corresponding high power cells with the same tab arrangement (similar to solenoids, where $L \propto N^2$).
- The tab pattern significantly contributes to the resistive-inductive cell behavior. More windings enclosed by the tabs lead to a higher jelly roll inductance, which let the impedance significantly increase for high frequencies. More tabs along the current collectors can reduce the jelly roll inductance.
- A mandrel inserted in the center of the jelly roll was found not to influence the cell's impedance characteristics in the investigated frequency range.
- As the anodic current collector has a higher conductivity than the cathodic collector, we assume that it is the major contributor to the skin effect characteristics of the cell initiating above some megahertz.

These conclusions are linked to macroscopic cell geometry aspects and are therefore mainly independent from materials chemistry, except of a small contribution of the materials chemistry to the ohmic resistance. Besides, electrochemical reactions are regarded negligible for the HF signal response of the battery.

Considering a frequency of 10 MHz relevant for PLC, the geometrical

differences among the investigated cells lead to impedance values ranging from 1.8 Ω for group D to 6.2 Ω for group C cells.

Beside the cell's ohmic resistance, also the cell impedance above a frequency of 10 MHz showed a temperature dependency. This can be attributed to temperature dependent ohmic losses, which are caused by ionic current flow between the electrode layers forced by high current collector reactances. Other geometrical aspects such as current collector inductance did not show any temperature dependency. In case of the Samsung INR18650-25R, a temperature reduction from 40 °C to 0 °C lead to an impedance increase from 2.1 Ω to 2.7 Ω at 10 MHz.

It is commonly assumed that the SOC hardly influences the high frequency cell characteristics, which was also found in this work. However, one of the investigated cells exhibited a slight SOC dependency for frequencies below 1 MHz, most probably caused by anodic volume change during cyclic conditioning. Above 1 MHz, no SOC influence could be observed.

These findings can be used for predicting the influence of different cell designs on its inductance and impedance characteristics and can help for selecting the appropriate cell for applications, where HF signals are present. For future PLC design, the results can be used to optimize the PLC transceiver performance with respect to different types of cells. For example, to maximize the capacity of the PLC link, the transceiver output impedance has to be adjusted to the battery load impedance such that the PLC voltage across the battery is maximized [49]. This can be realized by an additional capacitor compensating for the positive imaginary part of the battery impedance at the PLC carrier frequency. Furthermore, the dynamic output current of the transceiver can be adapted to a specific cell to obtain a good tradeoff between PLC channel capacity and energy consumption.

CRediT authorship contribution statement

Thomas F. Landinger: Conceptualization, Methodology, Validation, Formal analysis, Investigation, Writing - original draft, Writing - review & editing, Visualization. **Guenter Schwarzberger:** Resources, Writing - review & editing. **Andreas Jossen:** Writing - review & editing, Supervision, Project administration, Funding acquisition.

Declaration of competing interest

The authors declare that they have no known competing financial interests or personal relationships that could have appeared to influence the work reported in this paper.

Appendix A. Net inductance derivation of current collector segments

A.1 Parallel current flow (Fig. A.8a).
The voltages across the inductances of the positive (L_+) and negative (L_-) current collector segments are given by[4]

$$V_+ = j\omega L_+ \cdot I_+ + j\omega M \cdot I_-,$$
$$V_- = j\omega L_- \cdot I_- + j\omega M \cdot I_+. \qquad (A.1)$$

The impedance between the tabs can be expressed as

$$Z = \frac{V_+ + V_2}{I} = \frac{V_1 + V_-}{I} = Z_+ \| Z_- = \frac{Z_+ \cdot Z_-}{Z_+ + Z_-}, \qquad (A.2)$$

where

$$Z_+ := \frac{V_+ + V_2}{I_+} = \frac{j\omega L_+ \cdot I_+ + j\omega M \cdot I_- + RI_+}{I_+}, \qquad (A.3)$$

$$Z_- := \frac{V_1 + V_-}{I_-} = \frac{RI_- + j\omega L_- \cdot I_- + j\omega M \cdot I_+}{I_-}. \qquad (A.4)$$

For the common case of supposing identical inductances $L_+ = L_-$ and equally distributed R, the currents get $I_+ = I_- = I/2$, and eq (A.2) can be rearranged using (A.3) and (A.4). to

$$Z = \frac{(j\omega L_+ + j\omega M + R) \cdot (R + j\omega L_- + j\omega M)}{j\omega L_+ + j\omega M + R + R + j\omega L_- + j\omega M} = (j\omega L_+ + j\omega M + R) \| (j\omega L_- + j\omega M + R). \qquad (A.5)$$

For high frequencies, $R \ll \omega L$, and eq. (A.5) can be simplified to

$$Z = (j\omega L_+ + j\omega M) \| (j\omega L_- + j\omega M) := j\omega L_{par} \qquad (A.6)$$

which solely contains the net inductance of the current collector segment:

$$L_{par} = (L_+ + M) \| (L_- + M), \qquad (A.7)$$

As reported in Ref. [13], the inductive coupling factor $k := M/\sqrt{L_+ L_-}$ for tightly aligned current collectors is close to 1, thus the net inductance for parallel current flow is

---

[4] For a better readability, the frequency dependency of the quantities voltage, current and impedance is explicitly not shown.

$$L_+ \approx L_-,$$

$$L_{par} = (L_+ + M)\|(L_- + M) \overset{k\approx 1}{=} (2L_+)\|(2L_+) = L_+. \tag{A.8}$$

A.2 Antiparallel current flow (Fig. A.8b).

The voltages across the inductances of the positive (L_+) and negative (L_-) current collector segments are given by

$$V_+ = j\omega L_+ \cdot I_+ - j\omega M \cdot I_-,$$
$$V_- = j\omega L_- \cdot I_- - j\omega M \cdot I_+. \tag{A.9}$$

Since $I_+ = I_-$ and $k \approx 1$, the voltages can be calculated by

$$V_+ \approx j\omega L_+ \cdot I_+ - j\omega L_+ \cdot I_+ = 0,$$
$$V_- \approx j\omega L_- \cdot I_- - j\omega L_- \cdot I_- = 0. \tag{A.10}$$

Since the voltages across the inductances are zero for antiparallel current flow, the net inductance of the current collector segment is zero:

$$L_{npar} := (L_+ - L_+) + (L_+ - L_+) = 0. \tag{A.11}$$

(a)   (b)
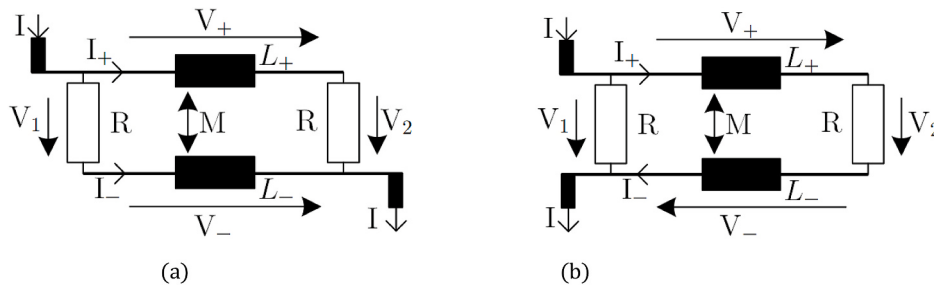
Fig. A.8. Current collector segments including mutual inductive coupling for parallel (a) and anti-parallel (b) current flow depending on the tab position. The resistances represent the resistance between positive and negative collector segments.

Appendix B. Fitting Accuracy of the EEC Model of Fig. 1a
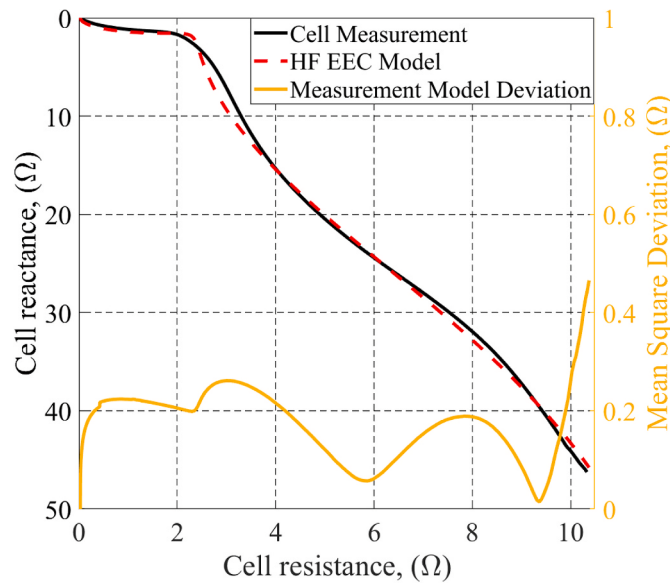
Fig. B.9. HF impedance measurement result and fitted EEC model of LG INR18650 MJ1. The mean square deviation between measurement and model is typical among the investigated cells.

References

[1] G.E. Blomgren, The development and future of lithium ion batteries, J. Electrochem. Soc. 164 (2017) A5019–A5025, https://doi.org/10.1149/2.0251701jes.

[2] H.J. Hong, J.R. Sevillano, C. Kain, G. Hofer, K. Felber, W.K. Chan, Alternatives in battery communication protocols, in: SAE Technical Paper Series, SAE International400 Commonwealth Drive, Warrendale, PA, United States, 2017.

[3] Y. Maryanka, Wiring reduction by battery power line communication, in: IEE Seminar on Passenger Car Electrical Architecture, IEE, Birmingham, UK, 21/6/2000, p. 8.

[4] O. Opalko, Powerline-Kommunikation für Batteriemanagement-Systeme in Elektro- und Hybridfahrzeugen, KIT Scientific Publishing, Karlsruhe, 2017.

[5] I. Ouannes, P. Nickel, K. Dostert, Cell-wise monitoring of Lithium-ion batteries for automotive traction applications by using power line communication: battery modeling and channel characterization, in: 2014 18th IEEE International Symposium on Power Line Communications and its Applications (ISPLC), Glasgow, United Kingdom, IEEE, Piscataway, NJ, 2014, pp. 24–29.

[6] A.P. Talie, W.A. Pribyl, G. Hofer, Electric vehicle battery management system using power line communication technique, in: 2018 14th Conference on Ph.D. Research in Microelectronics and Electronics (PRIME), IEEE, Prague, 2018, pp. 225–228 [S. l.], 2/7/2018 - 5/7.

[7] C. Bolsinger, J. Brix, M. Dragan, K.P. Birke, Investigating and modeling the transmission channel of a prismatic lithium-ion cell and module for powerline communication, Journal of Energy Storage 10 (2017) 11–19, https://doi.org/10.1016/j.est.2016.12.001.

[8] E. Barsoukov, J.R. Macdonald, Impedance Spectroscopy, John Wiley & Sons, Inc, Hoboken, NJ, USA, 2018.

[9] J. Illig, J.P. Schmidt, M. Weiss, A. Weber, E. Ivers-Tiffée, Understanding the impedance spectrum of 18650 LiFePO4-cells, J. Power Sources 239 (2013) 670–679, https://doi.org/10.1016/j.jpowsour.2012.12.020.

[10] T.F. Landinger, G. Schwarzberger, A. Jossen, A novel method for high frequency battery impedance measurements, in: 2019 IEEE International Symposium on Electromagnetic Compatibility, Signal Integrity and Power Integrity, New Orleans, LA, USA, IEEE, [Piscataway, New Jersey], 2019, pp. 106–110.

[11] F.C. Laman, Inductive impedance of a spirally wound Li/MoS[sub 2] cell, J. Electrochem. Soc. 133 (1986) 2441, https://doi.org/10.1149/1.2108430.

[12] P.J. Osswald, S.V. Erhard, A. Noel, P. Keil, F.M. Kindermann, H. Hoster, A. Jossen, Current density distribution in cylindrical Li-Ion cells during impedance measurements, J. Power Sources 314 (2016) 93–101, https://doi.org/10.1016/j.jpowsour.2016.02.070.

[13] S. Schindler, M.A. Danzer, Influence of cell design on impedance characteristics of cylindrical lithium-ion cells: a model-based assessment from electrode to cell level, Journal of Energy Storage 12 (2017) 157–166, https://doi.org/10.1016/j.est.2017.05.002.

[14] P. Korth Pereira Ferraz, R. Schmidt, D. Kober, J. Kowal, A high frequency model for predicting the behavior of lithium-ion batteries connected to fast switching power electronics, Journal of Energy Storage 18 (2018) 40–49, https://doi.org/10.1016/j.est.2018.04.024.

[15] E. Hoene, S. Guttowski, R. Saikly, W. John, H. Reichl, Rf-properties of automotive traction batteries, in: IEEE International Symposium on Electromagnetic Compatibility, 2003. EMC '03, Istanbul, Turkey, vol. 1, IEEE, 2003, pp. 425–428, 16/5/2003.

[16] T.F. Landinger, G. Schwarzberger, A. Jossen, A physical-based high-frequency model of cylindrical lithium-ion batteries for time domain simulation, IEEE Trans. Electromagn C. 62 (2020) 1524–1533, https://doi.org/10.1109/TEMC.2020.2996414.

[17] N. Shoaib, Vector Network Analyzer (VNA) Measurements and Uncertainty Assessment, Springer International Publishing, Cham, s.l., 2017.

[18] A. Jossen, Fundamentals of battery dynamics, J. Power Sources 154 (2006) 530–538, https://doi.org/10.1016/j.jpowsour.2005.10.041.

[19] Y. Wu, S. Saxena, Y. Xing, Y. Wang, C. Li, W. Yung, M. Pecht, Analysis of manufacturing-induced defects and structural deformations in lithium-ion batteries using computed tomography, Energies 11 (2018) 925, https://doi.org/10.3390/en11040925.

[20] M.J. Brand, Lithium-ion Battery Cells and Systems under Dynamic Electric Loads, Dissertation, München, 2018.

[21] C. Ropeter, Verhalten von Batterien bei impulsförmigen Strombelastungen unter Berücksichtigung des Skineffekts. Zugl.: Clausthal, Techn. Univ., Diss., 2006, Shaker, Aachen, 2007.

[22] J. Wang, K. Zou, C. Chen, L. Chen, A high frequency battery model for current ripple analysis, in: Twenty-Fifth Annual IEEE Applied Power Electronics Conference and Exposition (APEC), 2010, Palm Springs, CA, USA, IEEE, Piscataway, NJ, 2010, pp. 676–680.

[23] J.A. Tegopoulos, E.E. Kriezis, Eddy Currents in Linear Conducting Media, Elsevier, Amsterdam, 1985.

[24] M. Park, X. Zhang, M. Chung, G.B. Less, A.M. Sastry, A review of conduction phenomena in Li-ion batteries, J. Power Sources 195 (2010) 7904–7929, https://doi.org/10.1016/j.jpowsour.2010.06.060.

[25] S.S. Zhang, K. Xu, T.R. Jow, EIS study on the formation of solid electrolyte interface in Li-ion battery, Electrochim. Acta 51 (2006) 1636–1640, https://doi.org/10.1016/j.electacta.2005.02.137.

[26] H.A. Wheeler, Formulas for the skin effect, Proc. IRE 30 (1942) 412–424, https://doi.org/10.1109/JRPROC.1942.232015.

[27] Agilent Technologies, Appl. Note 5989-5935EN: Ultra-low Impedance Measurements Using 2-Port Measurements, Inc., USA, 2007.

[28] P.J. Osswald, M.d. Rosario, J. Garche, A. Jossen, H.E. Hoster, Fast and accurate measurement of entropy profiles of commercial lithium-ion cells, Electrochim. Acta 177 (2015) 270–276, https://doi.org/10.1016/j.electacta.2015.01.191.

[29] F.M. Kindermann, A. Noel, S.V. Erhard, A. Jossen, Long-term equalization effects in Li-ion batteries due to local state of charge inhomogeneities and their impact on impedance measurements, Electrochim. Acta 185 (2015) 107–116, https://doi.org/10.1016/j.electacta.2015.10.108.

[30] M. Guo, R.E. White, Mathematical model for a spirally-wound lithium-ion cell, J. Power Sources 250 (2014) 220–235, https://doi.org/10.1016/j.jpowsour.2013.11.023.

[31] J.B. Quinn, T. Waldmann, K. Richter, M. Kasper, M. Wohlfahrt-Mehrens, Energy density of cylindrical Li-ion cells: a comparison of commercial 18650 to the 21700 cells, J. Electrochem. Soc. 165 (2018) A3284–A3291, https://doi.org/10.1149/2.0281814jes.

[32] J. Ho, T.R. Jow, S.A. Boggs, Implications of advanced capacitor dielectrics for performance of metallized film capacitor windings, in: Proceedings of the 2008 IEEE International Power Modulators and High Voltage Conference, Las Vegas, NV, USA, IEEE, Piscataway, NJ, 2008, pp. 556–559.

[33] E.B. Rosa, The self and mutual inductance of linear conductors, Bulletin of the Bureau of Standards 4 (2) (1908) 332–333.

[34] F.W. Grover, Inductance Calculations, Dover Publications, Newburyport, 2013.

[35] R. Zhao, J. Liu, J. Gu, The effects of electrode thickness on the electrochemical and thermal characteristics of lithium ion battery, Appl. Energy 139 (2015) 220–229, https://doi.org/10.1016/j.apenergy.2014.11.051.

[36] N. Ida, Engineering Electromagnetics, Springer International Publishing, Cham, 2015.

[37] L.H.J. Raijmakers, D.L. Danilov, J.P.M. van Lammeren, M.J.G. Lammers, P.H.L. Notten, Sensorless battery temperature measurements based on electrochemical impedance spectroscopy, J. Power Sources 247 (2014) 539–544, https://doi.org/10.1016/j.jpowsour.2013.09.005.

[38] D. Andre, M. Meiler, K. Steiner, C. Wimmer, T. Soczka-Guth, D.U. Sauer, Characterization of high-power lithium-ion batteries by electrochemical impedance spectroscopy. I. Experimental investigation, J. Power Sources 196 (2011) 5334–5341, https://doi.org/10.1016/j.jpowsour.2010.12.102.

[39] T.R. Jow, S.A. Delp, J.L. Allen, J.-P. Jones, M.C. Smart, Factors limiting Li + charge transfer kinetics in Li-ion batteries, J. Electrochem. Soc. 165 (2018) A361–A367, https://doi.org/10.1149/2.1221802jes.

[40] K. Oldiges, D. Diddens, M. Ebrahiminia, J.B. Hooper, I. Cekic-Laskovic, A. Heuer, D. Bedrov, M. Winter, G. Brunklaus, Understanding transport mechanisms in ionic liquid/carbonate solvent electrolyte blends, Phys. Chem. Chem. Phys. 20 (2018) 16579–16591, https://doi.org/10.1039/c8cp01485j.

[41] X. Zhang, Thermal analysis of a cylindrical lithium-ion battery, Electrochim. Acta 56 (2011) 1246–1255, https://doi.org/10.1016/j.electacta.2010.10.054.

[42] J.P. Schmidt, S. Arnold, A. Loges, D. Werner, T. Wetzel, E. Ivers-Tiffée, Measurement of the internal cell temperature via impedance: evaluation and application of a new method, J. Power Sources 243 (2013) 110–117, https://doi.org/10.1016/j.jpowsour.2013.06.013.

[43] W. Waag, S. Käbitz, D.U. Sauer, Experimental investigation of the lithium-ion battery impedance characteristic at various conditions and aging states and its influence on the application, Appl. Energy 102 (2013) 885–897, https://doi.org/10.1016/j.apenergy.2012.09.030.

[44] C.T. Love, M.B.V. Virji, R.E. Rocheleau, K.E. Swider-Lyons, State-of-health monitoring of 18650 4S packs with a single-point impedance diagnostic, J. Power Sources 266 (2014) 512–519, https://doi.org/10.1016/j.jpowsour.2014.05.033.

[45] Y.-C. Chang, H.-J. Sohn, Electrochemical impedance analysis for lithium ion intercalation into graphitized carbons, J. Electrochem. Soc. 147 (2000) 50, https://doi.org/10.1149/1.1393156.

[46] M. Holzapfel, A. Martinent, F. Alloin, B. Le Gorrec, R. Yazami, C. Montella, First lithiation and charge/discharge cycles of graphite materials, investigated by electrochemical impedance spectroscopy, J. Electroanal. Chem. 546 (2003) 41–50, https://doi.org/10.1016/S0022-0728(03)00144-X.

[47] L.K. Willenberg, P. Dechent, G. Fuchs, D.U. Sauer, E. Figgemeier, High-precision monitoring of volume change of commercial lithium-ion batteries by using strain gauges, Sustainability 12 (2020) 557, https://doi.org/10.3390/su12020557.

[48] Panasonic Industrial Devices Sales Europe, Lithium - Ion/NNP + HRL Technology: NCR18650B Datasheet.

[49] M. de Piante, A.M. Tonello, On impedance matching in a power-line-communication system, IEEE Trans. Circuits Syst. II 63 (2016) 653–657, https://doi.org/10.1109/TCSII.2016.2530218.

5 Power Line Communications for Automotive High Voltage Battery Systems

In this chapter, the concept of PLC for in-battery communications is presented with an emphasis on the proof of concept, PLC channel modeling, and coexistence analysis.

Established PLC standards have been introduced in Section 3.3.3. Among them, the IEEE 1901 standard [197] describes the power line medium of in-home PLC by four major aspects, which mostly apply also for in-battery HV PLC:

(1) Pre-existence: The power line medium is a pre-existent, shared medium differing largely from other wired communications, which usually define their own media. Consequently, the PLC technology has to be able to adapt to dynamic network topologies due to switching of different loads and varying size of the power line network. This aspect is partly alleviated for HV PLC, since the topology of an assembled HV traction battery does not change. However, electric loads are still dynamically changing.

(2) Adversity: As the main purpose of the power line network is to deliver electric power from source to sink in the most efficient way, it provides suboptimal conditions for communications. Therefore, PLC standards cannot specify the characteristics of the target medium. As a consequence, channel characterization has to be conducted for any specific case.

(3) Openness: The power line medium is an open, unlicensed medium. The disadvantage is, however, that the medium is "open" and therefore susceptible to noise at all frequencies, for example, generated by the automotive power electronics in case of HV PLC.

(4) Regulatory variation: The frequency bands and power spectra permitted for PLC are generally defined by country-specific regulations. In case of HV PLC for traction batteries, car manufacturers need to comply with automotive EMC standards like the Comité International Spécial des Perturbations Radioélectriques (CISPR) 25 standard [211] and the International Organization for Standardization (ISO) 11452-2 standard [212], which have to be included in the individual requirements specifications.

In addition to the mentioned challenges for HV PLC, the communications system has to meet further requirements coming from the BMS specifications such as proposed by Table 1 [58].

Table 1: Communications requirements of an automotive BMS, monitoring one hundred Li-ion cells [58].

Data rate	2 Mbps
Voltage resolution	14 bit
Temperature resolution	11 bit
Latency of voltage measurement	10 ms
Latency of temperature measurement	100 ms
Bit error rate	10^{-3}

Table 1 does not include resolution and latency requirements on online EIS measurements, however, similar requirements on an impedance value at a given frequency are expected.

Considering the single-cell-based BMS architecture proposed in Figure 2, two different master/ slave configurations are conceivable for HV PLC, leading to the two different PLC topologies depicted in Figure 20. Since the power line network represents a shared medium, a half-duplex communication (one direction of communication at a time) is employed as master-to-slave (downlink) or slave-to-master (uplink) communication similar to the communication within a wired serial bus system as covered in Section 3.3.1. Figures 20a and 20b represent the first topology in case of downlink and uplink, respectively, where the PLC master modem is connected in parallel to the entire battery stack and the slave modems are connected in parallel to the single Li-ion cells. This topology benefits from a power-efficient downlink because the master modem sees the relatively large impedance of the entire battery pack at its output. Additionally, the master modem is already galvanically isolated from the HV system and can be directly connected and supplied by the EV's low voltage system. However, as the master modem is connected to HV+ and HV−, it is increasingly susceptible to electromagnetic interference and needs to be tested according to the aforementioned EMC regulations. Figures 20c and 20d show an alternative topology in case of downlink and uplink, respectively, where the master modem is attached to a single Li-ion cell just as the slave modems, this way mitigating EMC constraints. On the downside, because the master modem is responsible for coordinating the entire communication traffic, its increased power consumption would lead to an SOC disbalance within the battery pack, degrading the performance of the entire traction battery. Therefore, in the following, the first PLC topology is further investigated.

As mentioned in Section 3.3.3, no dedicated technology for the daisy-chain-structured HV PLC for traction batteries as shown in Figures 16b and 20 has been developed yet. Few research articles are available dealing with in-battery PLC on a laboratory scale, which generally use two different

(a)   (b)   (c)   (d)
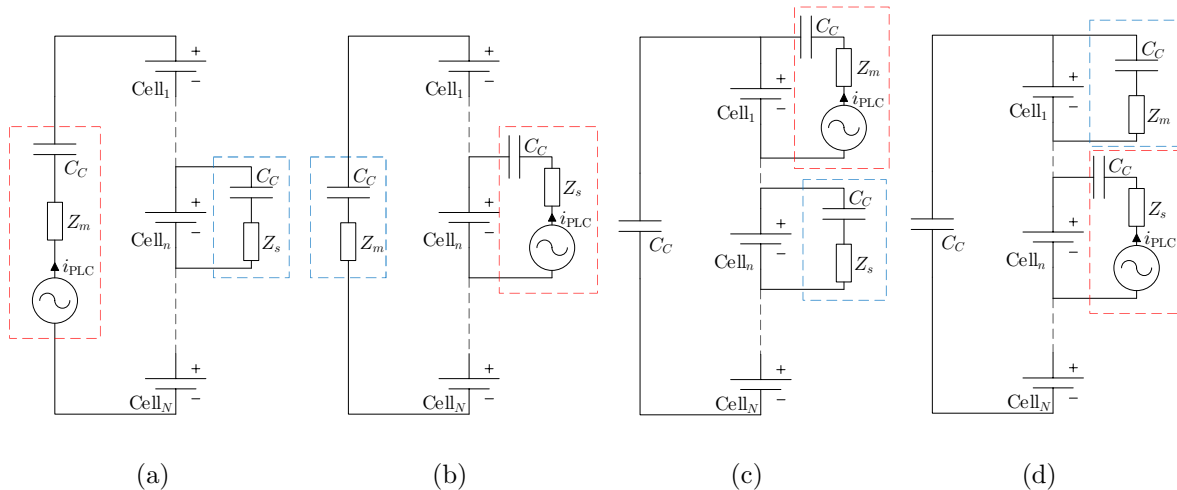
Figure 20: Different PLC topologies depending on the position of the master PLC modem. Master outside the stack in case of downlink (a) and uplink (b). Master inside the stack in case of downlink (c) and uplink (d). For simplicity, only single coupling capacitors denoted as C_C are shown. Z_m and Z_s represent the source impedances of master and slave, respectively. The dashed red boxes indicate the transmitting modems, whereas the dashed blue boxes indicate the receiving modems.

implementation approaches. Accordingly, reported works either (1) reuse established PLC technologies as listed in Section 3.3.3 or (2) utilize only the PLC physical layer combined with existing bus technologies, for example, emulating the signaling method of the CAN bus by PLC also known as CAN over PLC [50]. For the former approach (1), the HomePlug Green PHY standard [213] developed by the HomePlug Powerline Alliance has been proposed as promising solution due to its robust real-time performance [214], and has been considered also for PLC between EVs and charging stations [52]. For the latter approach (2), commercial solutions for serial universal asynchronous receiver transmitter (UART) over PLC are offered by Yamar Electronics, Ltd. (Tel Aviv, Israel) reaching medium data rates up to 115.2 kbps [215] and are applied in research works such as Refs. [31, 216, 217]. The company also offers CAN over PLC with higher data rates up to 1.4 Mbps [215], but which operate only in the traditional DC bus technology as depicted in Figure 16a. As a consequence, custom-made PLC solutions have been proposed in literature, however, data rates are still limited to hundreds of kbps [63, 218, 219]. In conclusion, a custom-made solution for in-battery PLC with a proprietary protocol optimized for battery monitoring data transmission with rates of 2 Mbps [64, 65] is desired to be competitive with conventional wired BMSs.

Therefore, Section 5.1 begins with a proof-of-concept study of PLC for in-battery communications using custom-made PLC modems. Since the PLC channel modeling is an important task to predict transfer characteristics and facilitate PLC modem design, Section 5.2 develops a PLC channel model based on the physical-based HF battery model of Section 4.2 and extends the model to account for electromagnetic coupling effects and contact resistances. The channel model is validated by the PLC proof-of-concept demonstrator of Section 5.1. Subsequently, the compatibility of PLC and the coexisting battery monitoring is investigated to ensure interoperability.

5.1 Hardware Proof of Concept

This section introduces the paper *Power Line Communications in Automotive Traction Batteries: A Proof of Concept* and is based on the paper without further reference.

The goal of this paper was to prove the concept of PLC for a small-scale battery pack using custom-made PLC modems reusable for future monolithic designs. Therefore, a block-based design approach was applied for the PLC modem development with separated blocks for transmitter (TX), receiver (RX), and power supply unit. The modem was designed to operate at voltages down to 2.25 V to be directly supplied by a single Li-ion cell. Regarding multiple Li-ion cells, each PLC modem attached to a single cell has its own local ground, which equals the negative terminal of the corresponding cell as illustrated in Figure 20. To reject common mode interferences such as noise signals shifting the local ground reference, an effective filter structure was included in the power supply unit of the modem. For the TX path, UART data were modulated using on-off-keying, which is the simplest form of binary amplitude shift keying (2-ASK). The sinusoidal carrier signal was generated by a Hartley oscillator having a frequency of 20.40 MHz, and was modulated by the UART data and fed into a fully differential amplifier. Using coupling capacitors, the amplified communication signal was coupled onto the PLC physical layer, which is mainly formed by the Li-ion battery cells as will be discussed further in Section 5.2.

For the RX path, the PLC signal was decoupled by capacitors and fed into a differential variable gain amplifier followed by an active bandpass filter. The demodulation was realized by an envelope detector composed of a passive rectifier and a lowpass filter stage. The demodulated signal was digitized by an active comparator stage with adaptive hysteresis and offset subtraction, and was fed into a microcontroller for data processing.

For the system verification, two PLC modems were attached to a small-scale battery pack consisting of six serially connected cylindrical Li-ion cells according to the first PLC topology (PLC master outside the stack, PLC slave inside the stack) presented in Figures 20a and 20b. The used Samsung ICR18650-26J Li-ion cells were of the same type that was characterized and modeled in Section 4.2. In a transmission test of 1000 data packets among master and slave PLC modem, the bit error rate (BER) was found to be zero.

Authors contribution Conceptualization of the PLC modems was done by Stefan Dollhaeubl, Guenter Hofer, and Thomas F. Landinger. PCB design and assembly were performed by Stefan Dollhaeubl. Experiments and data processing were conducted by Stefan Dollhaeubl and Thomas F. Landinger. Matthias Rose and Andreas Jossen supervised this work. The original draft was written by Thomas F. Landinger and was reviewed and edited by all authors

Power Line Communications in Automotive Traction Batteries: A Proof of Concept

Thomas F. Landinger, Guenter Schwarzberger, Matthias Rose, Stefan Dollhaeubl, Guenter Hofer, Arash Pake Talei, Andreas Jossen

Power Line Communications in Automotive Traction Batteries: A Proof of Concept

Thomas F. Landinger,
Guenter Schwarzberger, Matthias Rose
Infineon Technologies AG
Munich, Germany
thomas.landinger@infineon.com

Stefan Dollhaeubl, Guenter Hofer,
Arash Pake Talei
Infineon Technologies Austria AG
Graz, Austria
guenter.hofer@infineon.com

Andreas Jossen
Institute for Electrical Energy Storage Technology
Technical University Munich
Munich, Germany
andreas.jossen@tum.de

Abstract—**Power line communication (PLC) in automotive traction batteries is considered an attractive alternative to the serial-bus communication used in state-of-the-art battery management systems (BMS). PLC uses the battery power line as communication medium and saves additional wires, connectors and isolation effort. In this work, we present a proof of concept for a battery PLC in a small-scale battery pack. From a hardware approach, we develop a PLC modem, which modulates UART data using on-off-keying (OOK) and couples it onto the battery power line. To test the PLC, we design a demonstrator consisting of two PLC modems connected to a small-scale battery pack. The PLC is verified by a master-to-slave communication with an exemplary data transmission of multiples of 12 byte data packets.**

Keywords—*power line communication, PLC, electric vehicle, battery management system, BMS*

I. Introduction

As hybrid and battery electric vehicles (HEV, BEV) have started replacing vehicles with combustion engines, there is a growing interest in the traction battery as the essential energy source. Enhancing the BEV's range as well as the battery's lifetime while reducing battery costs are in the main focus of the industry. State-of-the-art battery packs consist of multiple stacked lithium-ion (Li-ion) cells to obtain the high voltage (HV) and parallel cells to provide the required energy storage capacity. The basic topology of a traction battery is illustrated in Fig. 1. As the abuse of Li-ion cells can be dangerous, a battery management system (BMS) is necessary to keep each battery cell in a safe state. The BMS monitors each cell regarding its temperature and voltage and provides balancing capabilities to maximize the battery's efficiency and range. For cell sensing, the central BMS unit has to communicate with the individual cell sensor circuits (CSC) over a reliable communication channel to perform state estimations such as state-of-charge (SOC) and state-of-health (SOH). This is usually realized by a serial communication link connecting the central BMS unit with the CSCs [1]. Beside the conventional bus topology, also other topologies such as the daisy-chain topology are used [2]. Recently, power line communication (PLC) has been considered as an attractive alternative to replace the serial communication link through a data communication over the battery chain [3–6]. In this approach, the data stream is modulated onto the power line and no additional wires are needed. As the power line channel is optimized for power transmission, it provides a harsh environment for communication due to many noise sources, which degrade the communication quality hugely [7].

Since the stacked cells in the traction battery force the PLC link to be serial, the architecture differs largely from conventional parallel PLC such as used in power grids and very little research has been published on this topic. Ouannes et al. proposed a high frequency model of a prismatic battery cell to simulate the PLC channel transfer characteristics in a battery stack [4]. In [5, 8], Opalko specialized on the coupling of the PLC signal into the system using Rogowski coils, disturbance investigations and measurements on real battery modules. Bolsinger et al. [6] proposed another high frequency battery model of a prismatic cell for PLC channel simulations. Summing up, the reported publications give valuable information about PLC channel modeling and noise investigations. However, a real implementation and analysis of a PLC over batteries is missing in literature.

In this work, we present a proof of concept for a single carrier PLC over a small battery stack consisting of six 18650 Li-ion battery cells by the Samsung SDI Co., Ltd. To demonstrate the PLC's performance, we design an innovative PLC modem, and establish uplink and downlink communication within the battery stack. The paper is organized as follows: Section II gives a short overview of the traction battery and the expected impedance of a single battery cell. In section III, we introduce our novel concept of the PLC hardware, presenting the system architecture and the PLC modem. The concept is evaluated in section IV by determining the bit error rate during a test communication. The paper concludes with section V.
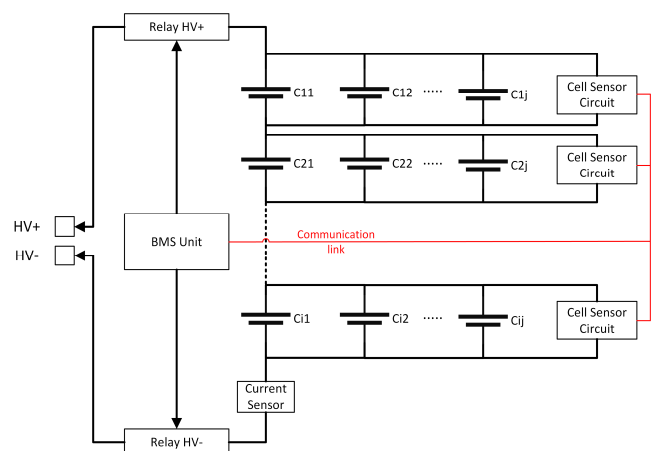
Fig. 1. Typical architecture of an HV battery system. Cell sensor circuits monitor cell parameters such as temperature and voltage. The PLC seeks to replace the serial communication links (red).
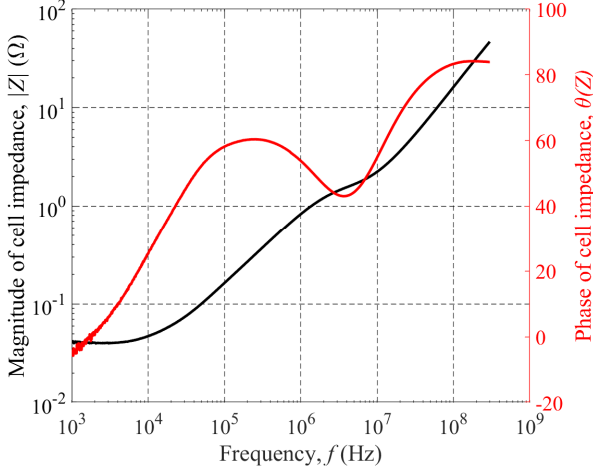
Fig. 2. Impedance modulus (black) and phase (red) of a single Li-ion Samsung ICR18650-26JM cell [9].

II. Traction Battery and Cell Impedance

A. Traction Battery

As the goal of this work is to clarify if PLC is a feasible approach to realize a communication within a battery system, the battery system itself has to be regarded. Fig. 1 shows a simplified topology of a traction battery with i cells in series and j cells in parallel. The BMS unit communicates with the CSCs, measures the current flowing through the stack and controls the main relay switches.

B. Cell Impedance

For the design of an effective PLC modem, the access impedance of the battery power line needs to be known. As the access impedance depends mainly on the cell impedance itself, the used battery cell ICR18650-26JM was characterized for a wide frequency range from 1 kHz to 300 MHz. Therefore, we developed a novel cell impedance measurement method using a vector network analyzer in shunt-through configuration, which was presented in [9]. Based on scattering parameter (S-parameter) measurements of the cell, we derived the magnitude and phase of the impedance over frequency. The results depicted in Fig. 2 show that the cell is very low-ohmic at low frequencies. To achieve a sufficiently high PLC voltage

Fig. 3. Setup and architecture of the PLC demonstrator. The master modem is connected to the positive and negative poles of the small-scale battery pack, whereas the slave modem is connected to and supplied by cell 2.

signal level at the cell, a high amount of current would be needed. Hence, low frequencies are not preferable for PLC coupling onto a battery. Due to its inductive behavior, which is visible from the positive impedance phase in Fig. 2, the cell impedance increases for higher frequency significantly and the coupling becomes easier. As target PLC carrier frequency, we chose 20 MHz, which is a good tradeoff between a reasonably high access impedance of the cell and low electromagnetic emissions, which would increase for higher frequencies and might violate legal limits. The electromagnetic compatibility of HV components is tested according to CISPR 25 [10].

III. Methodology

A. PLC Architecture

The constructed demonstrator has the architecture pictured in Fig. 3. The term "master" specifies the PLC modem as the only one that has a wired connection to the BMS unit outside of the battery pack. The slave PLC modems are located at the cells and have connections only to the cell. They do not need an external power supply, as they are supplied by the cell itself. In Fig. 3, an exemplary slave PLC modem is located at the second cell and the PLC signal is coupled onto the battery power line using coupling capacitors C_C. For the receive chain, sensing resistors R_S are placed at the modem's PLC interface. The coupling capacitors at the master modem together with the jumper close the ac current loop, hence enabling the PLC communication. For safety reasons, fuses denoted as F1 to F6 are inserted between all cells. To indicate the on-state, a light emitting diode (LED) D1 is placed in parallel to the master interface with a series resistor R_D. As the power line is a shared medium and a single carrier modulation is used, the communication can only work in one direction at a time (half-duplex). This means that there are two cases:

a. Master to Slave Communication

The master injects the communication signal into the positive and negative terminals of the stack, which results in a current flow through the cells. As the cell impedance is very low, it is preferred to let most of the current flow through the cell and let the sensing resistor be significantly higher than the cell impedance at the used carrier frequency. The resulting voltage V_S over the sensing resistor R_S of the slave reveals the modulated carrier and can be estimated by a simple voltage divider:

$$|V_S| \,/\, |V_G| \approx |Z_{cell}| \,/\, (N \cdot |Z_{cell}|) = 1/6 \; or \; 15.6 \text{ dB}, \quad (1)$$

with the stack voltage V_G, the magnitude $|Z_{cell}|$ of the frequency dependent cell impedance and the number of cells N. Of course, parasitic effects such as capacitive coupling between the cells and lead inductances are neglected in this estimation and would need to be quantified for a more thorough signal strength prediction.

b. Slave to Master Communication

If the communication direction is reversed, the result is a similar voltage divider. However, an issue arises: The low cell impedance necessitates high current amplitudes to achieve a significant voltage level at the cell. In addition, when the slave PLC modem imprints a current into the communication loop, most of the current will flow through the slave cell itself. Since the impedance of a single cell is significantly lower than the overall stack impedance, only a small part of the current will flow across the stack and the master's sensing resistor. As a
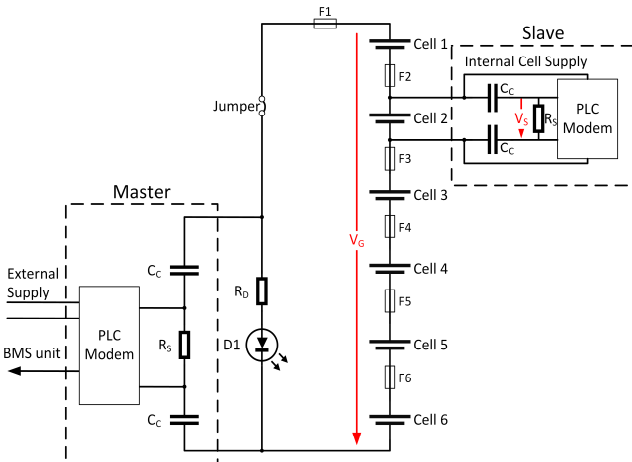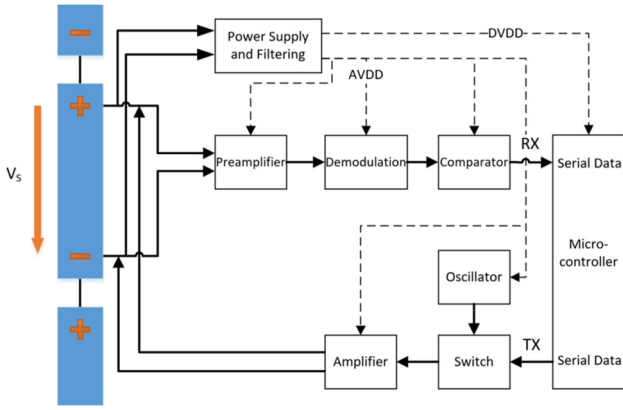
Fig. 4. Proposed concept for the PLC modem. The diagram shows the block based design approach with the modulator located at the bottom and the demodulator above. Analog (AVDD) and digital (DVDD) supplies are provided for the blocks.

consequence, the efficiency of the uplink will be much worse than the downlink. This could be improved in a multi-cell PLC system, where multiple cells in series are seen as one communication node. For instance, a PLC between battery modules will lower the total device-count and increase the access impedance, resulting in a better current transfer characteristic. Another alternative could be the serial coupling of the PLC signal, where the current is induced by Rogowski coils as reported in [8]. Thereby, the unwanted second current loop can be eliminated. As a drawback, the coils would need to be placed around the cell connectors making the module assembling process more complex and expensive.

B. PLC Modem Design

The applied block-based design approach is shown in Fig. 4 and completely separates the transmit (TX) and the receive (RX) chain. This enables the reuse of single blocks of the design in later revisions. The modem has its own power supply unit (PSU), which is directly supplied by the attached cell. The PSU contains filters to reject the PLC carrier signal and other common mode disturbances, and provides an analog (AVDD) and digital supply (DVDD) for the individual blocks. The TX chain is based around an oscillator, which generates the carrier signal. The serial universal asynchronous receiver transmitter (UART) data coming from the microcontroller let the oscillator switch on and off, depending on the logic level. The resulting on-off-keying (OOK) signal is the simplest form
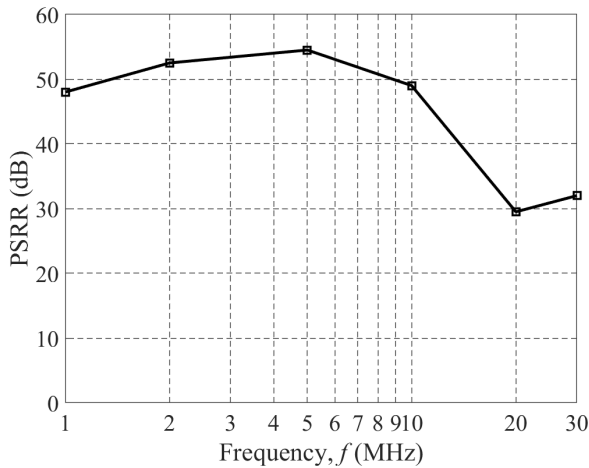
of amplitude shift keying (ASK) and provides an easy-to-implement narrowband communication system [11]. The OOK signal is then fed into an amplifier that drives the signal into the cell and the battery stack. Regarding the RX chain, a pre-amplifier first amplifies the incoming signal for the demodulation process, which is realized by an envelope detector. The signal is then fed into a comparator, which performs the analog-to-digital conversion to provide the RX UART data for the microcontroller. For sending user commands, the PLC master modem is controlled by an external terminal, which runs on a computer connected via a virtual communication (COM) port.

IV. RESULTS

The verification of the demonstrator is divided into a block and an overall system test. The block verification was performed at one PLC modem connected to a single cell. This means that both the TX and RX chain of the PLC modem were active and the self-demodulation was tested. For the system verification, two PLC modems were connected to the battery stack according to Fig. 3 to test the communication.

A. Block Verification

a. Power Supply Unit (PSU)

The PSU is based around a low dropout (LDO) regulator and provides a 3.060 V analog and digital supply with a low quiescent current of 0.83 mA. This helps to minimize the cell discharging during operation. For each PLC modem, it is important to have a stable power supply with a local ground reference. The supply rails should not be affected by the communication on the power line, hence the ground reference needs to be sufficiently decoupled from the PLC signal. This is ensured by common mode and differential mode filters at the input stage. The power supply rejection ratio

$$PSRR(f) = 20 \cdot log_{10}(V_{in}(f) / V_{out}(f)) \qquad (2)$$

was evaluated in the frequency range from 1 MHz to 30 MHz and is plotted in Fig. 5. The PSU was loaded by a 300 Ω resistor to provide the minimum load current of 10 mA. From Fig. 5, we expect the PLC carrier to be attenuated by 30 dB at 20 MHz.

b. Modulator

The carrier signal is generated by a Hartley oscillator, which comprises an LC resonant circuit with 1.1 uH and 54 pF. The resulting carrier frequency is 20.40 MHz with a total harmonic distortion (THD) of 2.0 %. The oscillator signal is switched on and off using an analog switch with a keying

Fig. 5. Power supply rejection ratio of the PSU. The PLC carrier frequency (20 MHz) is expected to be attenuated by 30 dB.
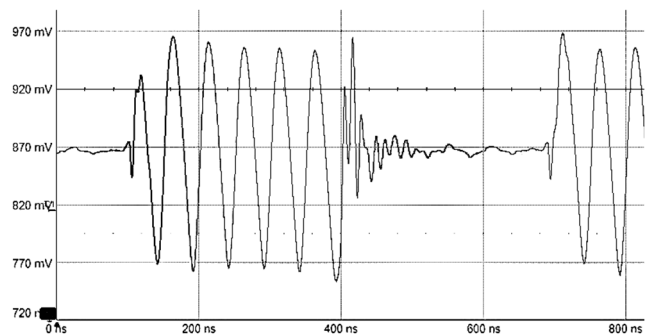
Fig. 6. On-off-keying signal after the analog switch. From the switching time of 300 ns it can be inferred that a bitrate above 3 Mbit/s is possible.
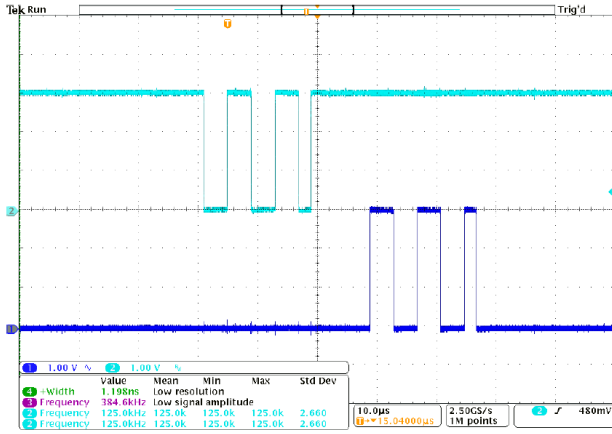
Fig. 7. Conversion of the UART data (cyan) coming from an external terminal to the power line interface (PLC-UART, blue).

time of 300 ns, which can be seen from Fig. 6. This leads to a bitrate of more than 3.3 Mbit/s, which exceeds a rate of 2 Mbit/s proposed for automotive BMS applications as in [5]. Nevertheless, for the system verification in section IV-B, the bitrate was reduced to 500 kbit/s to achieve a sufficient signal-to-noise ratio (SNR). The switch is controlled by the UART interface of the microcontroller, which is an XMC1404 boot kit by the Infineon Technologies AG. In case of the master, the UART data comes from an external terminal such as a computer. As shown in Fig. 7, the data needs to be inverted by the microcontroller to form PLC-UART data, because the modulator's analog switch takes a "high" level to switch the carrier on and a "low" level to disable it. This prevents the UART idle state, which is a "high" level, from transmitting a permanent carrier and saves energy. After the switch, the OOK signal is amplified by a fully differential amplifier with a gain of 3 and is coupled to the cell via serial capacitors. The resulting TX signal measured at the cell is shown in Fig. 8 and has an amplitude of approximately 250 mV$_{pp}$.
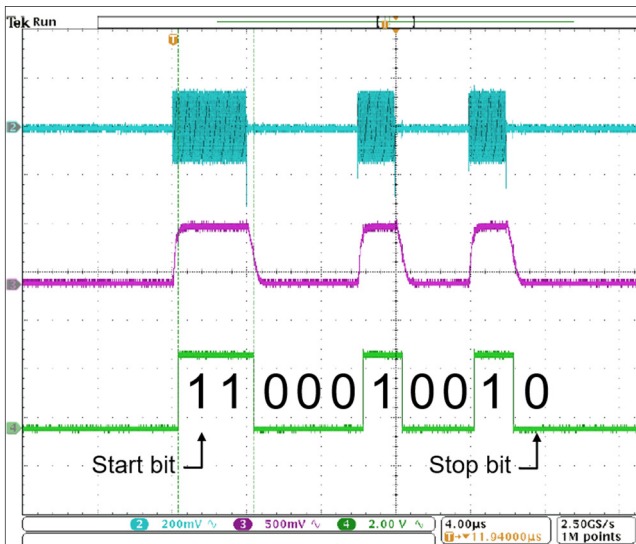
Fig. 8. TX signal measured at the cell (cyan), demodulated signal after the envelope detection (pink) and after the conversion to the digital domain (green). The example shows the transmission of the ASCII character 'v' (hexadecimal 0x76, UART 0b 0111 0110) by one PLC-UART frame (0b 1000 1001, inverted UART frame) including one start and one stop bit as signified.
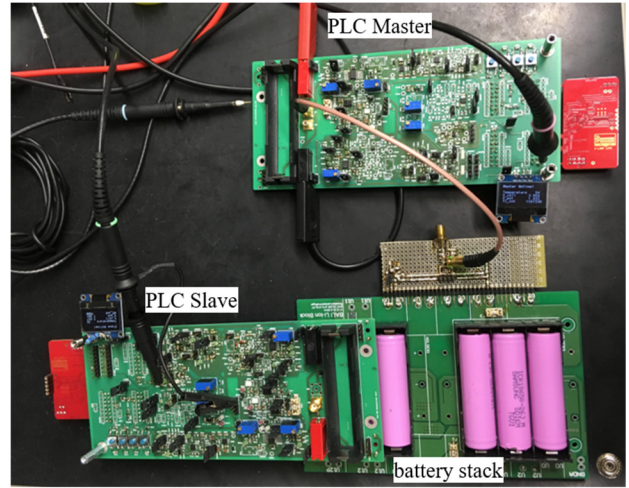
Fig. 9. Setup for the system verification and the proof of concept according to Fig. 3. The small battery stack consists of six 18650 cells. The PLC slave modem is plugged onto cell 2 (not visible as it is hidden under the board).

c. Demodulator

At the receiver, the PLC-signal is decoupled from the cell by capacitors and fed into a pre-amplifier, which is a differential variable gain amplifier (VGA). The adaptive gain is beneficial for this application, as the final amplitude of the RX signal cannot be estimated accurately beforehand. The gain control voltage can either be set with a potentiometer or from an external source. In addition, the VGA can be used in an automatic gain control (AGC) circuit in the future. The pre-amplifier's output needs to provide at least 500 mVpp for the subsequent envelope detector to ensure its reliable operation. Before the demodulation, the pre-amplified signal is passed to an active bandpass filter, which removes out-of-band noise from the signal. The passband of the filter is centered at the PLC carrier frequency with a bandwidth of 7 MHz. Afterwards, the signal is fed into a simple passive diode detector followed by a lowpass filter to perform the demodulation. The demodulated signal is converted into the digital domain using a comparator stage with an adaptive hysteresis and offset subtraction, and is passed to the microcontroller. The demodulated and digitized signals are shown in Fig. 8.

B. System Verification

The setup for the proof of concept is pictured in Fig. 9. According to Fig. 3, the master PLC modem is connected in parallel to the battery stack and the slave PLC modem sits at the second cell of the stack.

a. Physical Layer

The RX and TX signal amplitudes of both master and slave were measured using an oscilloscope and are listed in table I.

TABLE I
PLC SIGNAL STRENGTH AND ATTENUATION

Direction	Quantity	Value
Downlink	TX signal	250 mV$_{pp}$
	RX signal	35 mV$_{pp}$
	Attenuation	17 dB
Uplink	TX signal	100 mV$_{pp}$
	RX signal	45 mV$_{pp}$
	Attenuation	7 dB

The values are sorted by master-to-slave (downlink) and slave-to-master (uplink) communication. As can be seen from table I, the downlink attenuation exceeds the theoretical value calculated by (1). This is caused by additional losses such as contact resistances, coupling effects and the fuses between the cells. A more thorough channel estimation is therefore planned in future. Although the efficiency of the uplink is worse than that of the downlink as explained in section III-A-b, the signal attenuation is lower. This is due to the master's sensing resistor, which is significantly higher than the cell impedances and increases the voltage drop across it.

b. Data Link Layer

To show the functionality of the power line communication, two commands were implemented. They consist of a single 8-bit address (one UART frame) that is transmitted by the master. The slave responds to the commands according to table II.

TABLE II
PLC MASTER COMMANDS

Address	Description
0x31	Slave transmits 256 UART frames with data 0x00 to 0xFF
0x32	Slave transmits a measurement data packet (12 bytes) including - internal temperature of microcontroller (1 byte) - cell voltage (4 bytes) - test potentiometer voltage - CRC8 (1 byte)

Considering the command 0x32, the slave's cell voltage, the internal temperature of the microcontroller and the voltage of a test potentiometer are transmitted to the master. The test potentiometer is mounted on the XMC1404 boot kit board and provides a variable voltage between 0 V and DVDD for the analog digital converter (ADC) of the microcontroller, which can be seen in Fig. 10. To detect errors during the data transmission, a cyclic redundancy check (CRC) is performed and added to the data [12]. In our case, we use the standard CRC8 with polynomial 0x07 and initial value 0x00.

To test the packet transmission, 1000 data packets were requested from the master by repetitive sending the 0x32 command. Exactly 1000 packets were sent back from the slave and received by the master. During the test, the voltage of the test potentiometer mounted on the slave modem was altered to demonstrate that the communication is working. Based on the
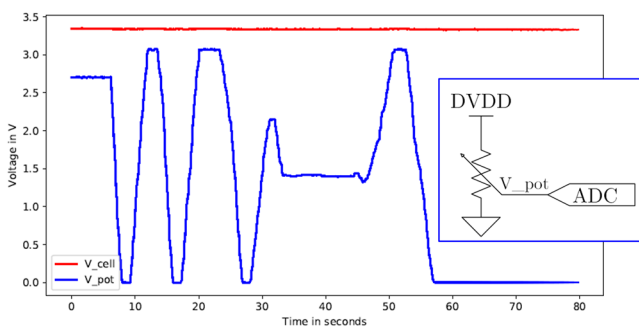
Fig. 10. Test of the measurement data packet transmission over the power line. Cell voltage V_cell (red) and test potentiometer voltage V_pot (blue) of the PLC slave modem are plotted over time. The potentiometer voltage is fed to the ADC of the microcontroller as can be seen from the inset.

received data packets, the voltage curve over time together with the cell voltage are shown in Fig. 10. In addition, by evaluating the CRCs, the bit error rate (BER) could be derived and no bit errors were found. These results demonstrate that PLC over a battery stack is actually possible.

V. CONCLUSION

In this paper, we presented a proof of concept for a power line communication over serially connected battery cells. Therefore, we developed a PLC modem, which transmits UART data frames using two-level ASK. Two modems, a master and a slave, were connected to a small-scale battery pack consisting of six 18650 cells to form a demonstrator. The physical layer as well as the data link layer of the communication were verified. In a transmission test of 1000 data packets, the BER was zero. To advance in battery PLC in future, the communication system needs to be very robust against excessive noise coming from DC/AC and DC/DC converters. This has to be verified by rigorous testing and a deep noise investigation. The high noise levels might necessitate more robust modulation methods as well as forward-error correction (FEC) techniques and redundancy.

REFERENCES

[1] P. Weicker, *A systems approach to lithium-ion battery management*. Boston: Artech House, 2014.

[2] H. J. Hong *et al.,* "Alternatives in Battery Communication Protocols," in *SAE Technical Paper Series*, 2017.

[3] A. P. Talie, W. A. Pribyl, and G. Hofer, "Electric Vehicle Battery Management System Using Power Line Communication Technique," in *2018 14th Conference on Ph.D. Research in Microelectronics and Electronics (PRIME)*, Prague, 2018, pp. 225–228.

[4] I. Ouannes, P. Nickel, and K. Dostert, "Cell-wise monitoring of Lithium-ion batteries for automotive traction applications by using power line communication: battery modeling and channel characterization," in *18th IEEE International Symposium on Power Line Communications and Its Applications*, Glasgow, United Kingdom, 2014, pp. 24–29.

[5] O. Opalko, B. Simon, D. Alonso, and K. Dostert, "Physical layer and multi-carrier analysis for power line communication networks in Li-ion batteries for electric and hybrid vehicles," in *2015 IEEE Vehicular Networking Conference (VNC): Date: 16-18 Dec. 2015*, Kyoto, Japan, 2015, pp. 243–250.

[6] C. Bolsinger, J. Brix, M. Dragan, and K. P. Birke, "Investigating and modeling the transmission channel of a prismatic lithium-ion cell and module for powerline communication," *Journal of Energy Storage*, vol. 10, pp. 11–19, 2017.

[7] L. Lampe, A. M. Tonello, and T. G. Swart, *Power Line Communications*. Chichester, UK: John Wiley & Sons, Ltd, 2016.

[8] O. Opalko, D. Alonso, and K. Dostert, "Measurements on Rogowski coils as coupling elements for power line communication in traction lithium-ion batteries," in *2015 International Symposium on Power Line Communications and Its Applications (ISPLC)*, Austin, TX, USA, 2015, pp. 29–34.

[9] T. F. Landinger, G. Schwarzberger, and A. Jossen, "A Novel Method for High Frequency Battery Impedance Measurements," in *2019 IEEE International Symposium on Electromagnetic Compatibility, Signal Integrity and Power Integrity*, New Orleans, LA, USA, 2019, pp. 106–110.

[10] CISPR 25, "Radio disturbance characteristics for the protection of receivers used on board vehicles, boats and on devices - Limits and methods of measurement," IEC/DIN-EN 55025, Brussels, Belgium, 2008.

[11] M. Steer, *Microwave and RF design: A systems approach*. Raleigh, NC: SciTech Pub, 2010.

[12] W. Peterson and D. Brown, "Cyclic Codes for Error Detection," *Proc. IRE*, vol. 49, no. 1, pp. 228–235, 1961.

5.2 Channel Modeling and Coexistence Study with BMS Monitoring

This section introduces the paper *Power Line Communications for Automotive High Voltage Battery Systems: Channel Modeling and Coexistence Study with Battery Monitoring* and is based on the paper without further reference.

The goal of this paper was to introduce an equivalent electrical circuit modeling approach for the battery power line network (BPLN) based on the HF battery model of Section 4.2, and to validate the resulting PLC channel model using the proof-of-concept demonstrator of Section 5.1. The applied modeling approach is visualized in Figure 21. Accordingly, the PLC master modem communicates with an arbitrary PLC slave connected to cell i via the PLC channel, which is represented mainly by the BPLN and additional wiring for the PLC modems. The physical-based battery model of Section 4.2 concentrated on the HF characteristics of a single Li-ion cell. In contrast, the BPLN consists of multiple Li-ion cells that experience electromagnetic coupling effects, which were identified in the paper by experiments and 3-D EM simulations. The coupling was modeled by mutual inductances M and coupling capacitances C_{cc} as visible in Figure 21. Moreover, the electrical connection between the cells was modeled by RL-elements. The entire PLC channel model was validated with real-world PLC signals generated by the custom-made PLC modems developed in Section 5.1.
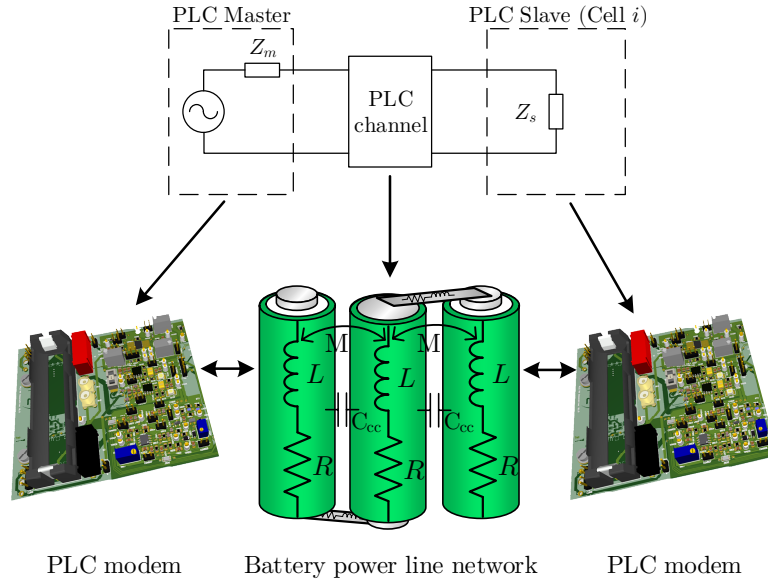
Figure 21: Principle structure of the PLC channel model based on the physical-based HF battery model of Section 4.2 and the PLC demonstrator of Section 5.1.

In the second part of the paper, the coexistence between PLC and the battery monitoring infrastructure was evaluated. Although the frequency bands of online EIS and PLC are apart from each other, coexistence issues could arise due to nonlinearity and periodicity effects as shown in Figure 22. On the one hand, PLC must not interfere with battery monitoring tasks such as high

precision voltage measurements or online EIS. Compatibility experiments revealed that the periodic repetition of PLC data packets generates narrowband disturbances that can fall into the EIS frequency band as indicated by the blue arrow in Figure 22. Disturbances could be simply avoided by selecting PLC packet rates unequal to online EIS measurement frequencies or by effective filter structures. DC monitoring was found not to be distorted by PLC signals. On the other hand, PLC should not be distorted by the cell monitoring circuits. The nonlinear current-voltage relationship of the charge transfer reaction can cause higher harmonics during EIS measurements with large signal excitation [220] as indicated by the dashed green arrow in Figure 22. Since nonlinearity effects were found only below frequencies of 200 Hz [220] and EIS measurements should fulfill the linearity criterion as discussed in Section 3.2.1, it was concluded that this effect does not lead to compatibility issues. Also the harmonic content of rectangular current excitation as proposed in Section 3.2.2 (see Figure 13b) were pointed out not to interfere with PLC signaling. However, it was found that monitoring circuits attached to a Li-ion cell can alter the cell's HF impedance characteristics at certain frequencies, most probably due to the specific filter characteristics of the CMCs.
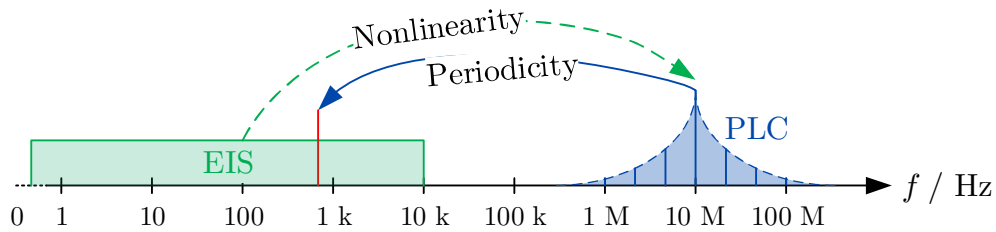
Figure 22: Spectral representation of potential coexistence issues between EIS and PLC signals.

Authors contribution   Conceptualization and design of the experiments and the modeling approach were done by Thomas F. Landinger. Experiments, simulations, and data processing were also performed by Thomas F. Landinger. Matthias Rose and Andreas Jossen supervised this work. The original draft was written by Thomas F. Landinger and was reviewed and edited by all authors.

Power Line Communications for Automotive High Voltage Battery Systems: Channel Modeling and Coexistence Study with Battery Monitoring

Thomas F. Landinger, Guenter Schwarzberger, Guenter Hofer, Matthias Rose, Andreas Jossen

Permanent weblink:

https://doi.org/10.3390/en14071851

Power Line Communications for Automotive High Voltage Battery Systems: Channel Modeling and Coexistence Study with Battery Monitoring

Thomas F. Landinger [1,2,*], **Guenter Schwarzberger** [2], **Guenter Hofer** [3], **Matthias Rose** [2] **and Andreas Jossen** [1]

1 Institute for Electrical Energy Storage Technology, Technical University of Munich (TUM), Arcisstr. 21, 80333 Munich, Germany; andreas.jossen@tum.de

2 Infineon Technologies AG, Am Campeon 1-15, 85579 Neubiberg, Germany; guenter.schwarzberger@infineon.com (G.S.); matthias.rose@infineon.com (M.R.)

3 Infineon Technologies Austria AG, Development Center Graz, Babenberger Str. 10, 8020 Graz, Austria; guenter.hofer@infineon.com

* Correspondence: thomas.landinger@infineon.com; Tel.: +49-89-234-36621

Abstract: As electric vehicles are gaining increasing worldwide interest, advances in driving range and safety become critical. Modern automotive battery management systems (BMS) compete with challenging performance and safety requirements and need to monitor a large amount of battery parameters. In this paper, we propose power line communications (PLC) for high voltage (HV) traction batteries to reduce the BMS wiring effort. By modeling a small-scale battery pack for frequencies up to 300 MHz, we predict the PLC channel transfer characteristics and validate the results using a PLC hardware demonstrator employing a narrowband single-carrier modulation. The results demonstrate that battery PLC is a demanding task due to low access impedances and cell coupling effects, yet transfer characteristics can be improved by optimal impedance matching. PLC for HV BMS not only saves weight and cost, but also improves flexibility in BMS design. PLC enables single-cell monitoring techniques such as online electrochemical impedance spectroscopy (EIS) without additional wiring. Online EIS can be used for in-situ state and temperature estimation saving extra sensors. This work unveils possible coexistence issues between PLC and battery monitoring. In particular, we demonstrate that certain PLC data or packet rates have to be avoided not to interfere with EIS measurements.

Keywords: battery management systems; lithium-ion battery; electric vehicles; power line communications; electrochemical impedance spectroscopy; physical layer model; coexistence study

1. Introduction

The ever-increasing demand for safe and clean energy is pushing the development of innovative electrical energy storage and transportation systems. Electromobility has clearly become a key innovation topic over the last decade. One of the most essential modules of hybrid and battery electric vehicles (HEVs, BEVs) is the traction battery system. It limits both the power and the mileage of the electric vehicle (EV). Lithium-ion (Li-ion) batteries are most widely applied in EVs due to their high energy density, long lifespan and high efficiency [1,2]. As Li-ion batteries are sensitive to misapplications such as over or under voltage, a battery management system (BMS) has to ensure a safe, efficient, and reliable operation [3]. For battery state estimation such as state of charge (SOC) and state of health (SOH), the BMS requires external sensors attached to the cells, which traditionally measure voltage, current, and temperature [4]. In general, the BMS is implemented using a centralized or distributed topology, where the latter can be based on a multi or single-cell approach [5]. The single-cell approach offers the highest battery system modularity and variability and enables advanced single-cell monitoring techniques such

as electrochemical impedance spectroscopy (EIS). From this perspective, the single-cell approach forms the foundation for the emerging field of smart cells and smart battery systems as recently reviewed in [6]. EIS is a powerful nondestructive method widely used for electrochemical process characterization, and gains significant interest in BMS applications, thereby often referred to as "online EIS" [7–10]. Using EIS, the battery cell's complex impedance over frequency is determined by exciting the cell with an AC signal and measuring its response [11]. The quantity of publications available correlating EIS with SOC [12–14], SOH [14,15], and temperature [12,13,16,17] estimation demonstrates its high potential to improve future BMS designs in terms of safety and performance. A complete review of EIS applications utilized for commercial Li-ion cells can be found in [18].

Despite the benefits coming along with a single-cell-based BMS such as gaining additional cell information by the usage of EIS, the effort for additional wiring and hardware let the complexity and cost of the BMS increase. Data acquired by sensors attached to the cells need to be periodically sent to the central battery management unit (BMU), which is typically done via a serial communication bus system [19].

Recently, high voltage (HV) power line communication (PLC) has been proposed as an attractive and innovative communication technique to improve cost efficiency and reduce weight and wiring overhead in the battery system [20–24]. For HV PLC, the dedicated HV power lines including the HV battery are utilized as a communication channel by superimposing a modulated carrier signal. In this way, the existing serial communication bus could either be omitted or used as a redundant communication system to reduce failure risks. Putting it together, PLC over the traction battery could enable a single-cell-based BMS featuring EIS for advanced state estimation without the need for additional wiring.

We therefore propose a BMS architecture as illustrated in Figure 1, where each cell is equipped with a cell monitoring circuit (CMC) and a communication interface. The communication between the CMCs and the BMU is realized by PLC, and the traditional sensing of voltage (V), current (I), and temperature (ϑ) is upgraded by EIS monitoring circuits.
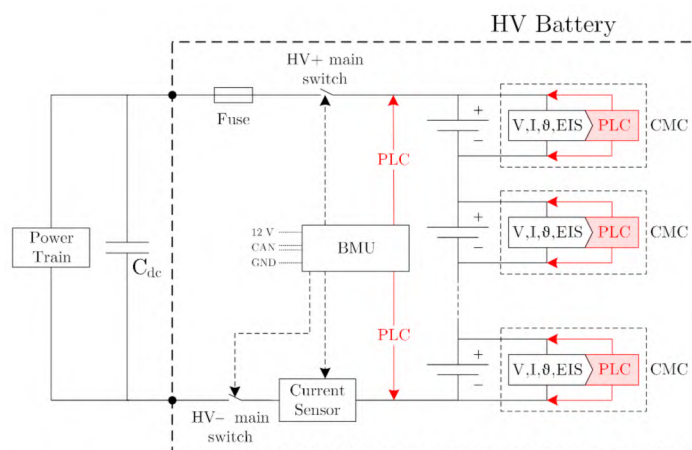
Figure 1. Proposed BMS architecture enabling single-cell monitoring including EIS, while saving additional wiring effort by employing HV PLC. The HV battery supplies the electric power train and the DC-link capacitor C_{dc}. The BMU is connected to the 12 V on-board power supply and the control area network (CAN) of the EV.

Several challenges come along with integrating PLC and EIS into the battery system. Besides the characterization of the PLC channel and development of a suitable PLC modem, also the compatibility between PLC and the coexisting battery monitoring including EIS needs to be clarified. Beyond this, the HV power line channel provides a harsh environment for data communication as it is optimized for power transmission and suffers from many noise sources such as motor drives and DC/DC converters [25,26]. Specifically, the HV traction battery contains hundreds of single Li-ion cells to obtain sufficient energy and

power capability [27]. This leads to an extensive number of PLC nodes, which is still accompanied by low PLC access impedances due to low-ohmic cell impedances [28].

While research on PLC for smart grids (e.g., [29]) and in-vehicle low voltage (LV) PLC (e.g., [26,30,31]) is already well advanced, HV PLC for automotive battery systems is still an emerging research field, where only little work has been published. The main reasons are its high Automotive Safety Integrity Level (ASIL) requirements [22] and the specific serial channel topology that is entirely different to conventional PLC systems, where all PLC modems are connected in parallel between the power line rails [32].

Takanashi et al. [33] developed an HV PLC system that can control multiple power electronic devices in real time. Although they evaluated the PLC channel characteristics of the HV power line, they did not consider a PLC within the HV battery pack.

First, Ouannes et al. [21] proposed an HV PLC for the potential application in an automotive BMS. By characterizing and modeling a prismatic Li-ion cell, they were able to predict the channel transfer characteristics of an HV PLC system. Continued in [34], the authors specialized on the physical layer performance analysis using different single and multi-carrier modulation techniques.

Bolsinger et al. [22] introduced a high frequency model of a prismatic Li-ion cell to simulate the PLC channel transfer characteristics in an HV battery stack and investigated serial and parallel PLC coupling methods.

In [24,35], Opalko et al. concentrated on PLC signal coupling using Rogowski coils, channel performance simulations, and disturbance investigations. For modeling the PLC channel, they extended the circuit-based model from [21] by a three-dimensional (3-D) electromagnetic (EM) model of the battery pack environment.

The cited previous works did not consider hardware implementations of PLC for battery cells. Still, small-scale PLC demonstrators for BMS applications can be found in various works [23,32,36] proving the concept of PLC for cylindrical Li-ion cells.

However, it becomes noticeable that the cited works concentrated on either PLC channel modeling or hardware implementation, and a comparison between predicted and actual channel characteristics on an implemented PLC system is missing in literature.

In this work, we address this issue by developing a novel bottom-up PLC channel model parametrized by high frequency (HF) impedance measurements and 3-D EM simulations on cylindrical 18650 Li-ion cells. Including coupling effects among adjacent cells, the cell-based model is scaled up to predict the channel transfer characteristics of a small battery pack, which is validated by using a real hardware PLC demonstrator that we have presented in [32].

To the best knowledge of the authors, there is no literature available investigating the compatibility of PLC and the coexisting BMS monitoring, which inherently share the same power lines. Thus, in the second part of this work, we will analyze the coexistence between PLC and BMS monitoring tasks such as voltage and online-EIS measurements and give suggestions how to avoid interference.

This paper is structured as follows: Section 2 presents the PLC hardware demonstrator. Section 3 introduces the PLC channel model components giving an insight into the high frequency properties of cylindrical Li-ion cells and their physical interpretation. In addition, capacitive and inductive coupling mechanisms are examined in detail by measurements and 3-D EM simulations. In Section 4, the model components are arranged to a complete PLC channel model to simulate the channel transfer characteristics. For the model validation, the PLC hardware demonstrator is used to compare the predicted with the actual channel characteristics. The coexistence between PLC and battery monitoring is investigated in Section 5, and Section 6 concludes the paper with a summary.

2. PLC Hardware Demonstrator

In our previous work [32], we developed a small-scale PLC demonstrator proving the concept of a single-cell-based PLC system. As illustrated in the schematic view of Figure 2a and the photograph of Figure 2b, a PLC system was designed involving six serially con-

nected ICR18650-26J Li-ion cell with a nominal capacity of 2600 mAh (value from the datasheet) by Samsung SDI Co., Ltd. (Yongin, South Korea). Two printed circuit boards (PCBs) were developed each containing a PLC modem, PLC coupling networks and a stable power supply unit. The slave PCB is connected to and directly supplied by a single 18650 Li-ion cell, whereas the master PCB is attached in parallel to the small-scale battery pack being supplied externally. The PLC signal is fed into the HV power lines by coupling capacitors denoted as C_c, thus high DC voltages are not a concern for the AC-coupled low voltage PLC signal. The PLC demonstrator employs a narrowband single carrier modulation using on-off keying (OOK) also known as binary amplitude shift keying (2-ASK). Narrowband communication was selected because of its high reliability and energy efficiency. The carrier frequency was chosen to be 20 MHz for the following reasons:

(1) The PLC system needs to meet high data rate requirements of 2 Mbps as reported in [33,35]. High data rates are required because voltage and current measurements of all cells within the pack need to be updated every 50–100 ms [5].

(2) Li-ion battery cells provide a low-ohmic access impedance to PLC devices. In consistence with [37], the access impedance defines the impedance seen by a PLC modem connected in parallel to a PLC access point, which in our case is a single Li-ion cell as indicated in Figure 2a. Due to their rolled-up geometrical structure, cylindrical Li-ion cells inherently exhibit an inductive nature for frequencies above some kilohertz [38]. Considering the inductive reactance $X_L = 2\pi f L$, high frequencies are favorable to obtain a higher access impedance. As will be discussed in Section 3.1, frequencies above 1 MHz are preferred.

(3) The HV power lines are corrupted by various electrical devices connected to the network, which generate impulsive noise [26]. Noise investigations on the voltage and current harmonic content of the HV power lines [31,33,39] revealed that the noise power decreases significantly for increasing frequency and can even be considered as "white" for narrow frequency bands above approximately 10 MHz.

(4) The PLC system needs to comply with electromagnetic compatibility (EMC) regulations. For HV components, the EMC is tested according to CISPR 25 [40]. To keep radiated electromagnetic emissions to a minimum, PLC frequencies have to be selected as low as possible, which is contrary to (1)–(3), demanding a tradeoff between the stated points.

(a)   (b)
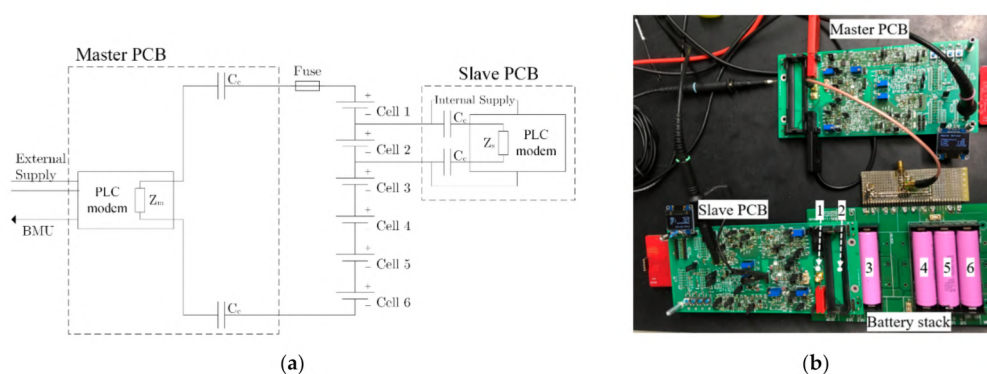
Figure 2. PLC hardware demonstrator composed of a small-scale battery pack and both a master and a slave PCB comprising PLC modems and coupling circuits: (**a**) Schematic representation; (**b**) Photograph of the laboratory setup [32]. The slave board is connected to cell 2 as indicated in (**a**) by putting the PCB on top of the stack (**b**).

For proving the concept of PLC over battery cells, the hardware demonstrator was designed to establish a PLC link among a master and a slave modem connected to the battery pack as in Figure 2a. In various test scenarios, battery parameters such as cell voltage were recorded by the microcontroller on the slave PCB and periodically sent to the master upon request in a half-duplex communication. Data packets containing 12 bytes

of data and a cyclic redundancy check (CRC) were sent to the master, while no bit errors were found. More information on the hardware implementation and verification can be found in [32]. To develop the presented proof-of-concept board further towards an actual PLC system for HV batteries, we will introduce our PLC channel modeling approach in the following Section.

3. PLC Channel Model Components

PLC system development requires a thorough understanding and modeling of the channel transfer characteristics. To gain broadband information about the PLC channel, a wide frequency range from 10 kHz to 300 MHz is considered in the following.

Commonly, there are two main approaches for PLC channel modeling reported in literature: deterministic and statistical [25]. The first approach relies on a detailed description of the network topology including accurate data link models, whereas the second approach uses statistical descriptions of the topology, often supplemented by extensive measurement campaigns used for model fitting [25]. Conventional in-home PLC systems usually require statistical modeling because the number of PLC coupling points and its locations within the system can vary [30].

In contrast, automotive HV batteries are large-format systems that are built from Li-ion cells connected in series, parallel or mixed configurations to obtain the necessary power for the traction motor and auxiliary systems [41]. Once implemented in the EV, the HV battery does not change its topology because no additional, unpredictable loads can be connected to the system except of an electric charger. Hence, we can consider the battery PLC system as static [24] enabling us to apply a deterministic channel modeling approach.

In the following, we present our bottom-up modeling approach, which is based on circuit-based models of (1) the battery cell, (2) coupling mechanisms among cells, and (3) the electrical connection between cells. The model components are derived from measurements and 3-D EM simulations and aim to describe the small-scale battery pack presented in the previous Section. Although it is quite common to use transmission line theory for PLC channel modeling [25], we applied circuit-based modeling throughout this work to obtain a meaningful PLC channel model allowing physical interpretations of the results. This is reasonable because the physical dimensions of the battery pack components are well below the considered wavelengths.

3.1. High Frequency Model of a Single Battery

As the development of EVs advances, an increasing number of highly dynamic loads such as DC/DC converters and motor drives are being connected to the HV battery. To predict their impact on conducted emissions in the HV power lines, high frequency modeling of batteries recently gained increasing attention [42]. However, as most of the reported HF battery models such as [21,22,43,44] are limited in frequency and follow a black-box approach, we presented a novel physical-based model of cylindrical Li-ion cells valid for frequencies from 1 kHz to 300 MHz in [45]. The derived equivalent electrical circuit (EEC) model is depicted in Figure 3a and can be considered as a grey-box model as it gives insights into different resistive-inductive effects occurring inside the battery in specific frequency bands. Besides, the physical-based model elements are related to the geometrical structure of the cell. In general, cylindrical Li-ion cells are manufactured by coating metallic current collector foils with the active electrode materials to form anode and cathode, which are wound with separator foils in between into a jelly roll. The rolled-up layers are usually placed into a firm metal casing, where metallic tabs connect the cathode to the positive terminal and the anode to the negative terminal and cell casing [46]. Typically, additional safety devices such as current interrupt devices (CIDs) are implemented [47].

(a)

(b)
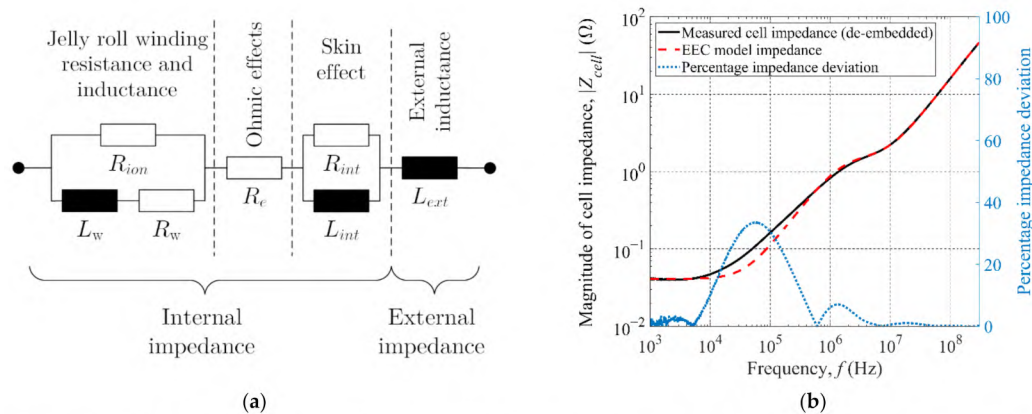
Figure 3. High frequency characterization of a cylindrical battery cell: (**a**) Physical-based EEC battery model including internal and external cell impedance valid from 1 kHz to 300 MHz; (**b**) Measured and modeled HF impedance response versus frequency and percentage deviation.

The spiral structure inherently leads to an increased inductive behavior of the cell for high frequencies (already starting above some kilohertz), which is modeled by the inductance L_w and the resistance R_w of the current collector windings, and the ionic resistance R_{ion} of the stacked electrode layers. Remaining external inductive effects due to tabs, bonding wires, and the cell's electrical length are summarized in the component L_{ext}. The resistance R_e summarizes ohmic effects caused mainly by the limited electrolyte conductivity and contact resistances within layers and between layer interfaces. For frequencies above 10 MHz, the current penetration depth in the collector foils decreases due to electromagnetic field effects, which is known as the skin effect. The increasing current concentration on the conductor's surface let the internal resistance of the conductor increase, while the internal inductance decreases. In the EEC model, this is described by R_{int} and L_{int}, respectively. It should be noted that the EEC model does not include electrochemical battery reactions with time constants >1 ms as they are not relevant for the PLC frequency range of interest [45]. The model was parametrized by HF impedance measurements on the Samsung ICR18650-26J Li-ion cell using a vector network analyzer (VNA) with the shunt-through method, which is specialized for broadband low-ohmic impedance measurements [48]. The model parametrization was optimized for PLC frequencies yielding an adequate fit from 500 kHz up to 300 MHz as visible in Figure 3b. The resulting fitted values of the EEC elements are summarized in Table 1. As designated in Figure 3a, the cell impedance can be separated into an internal and an external impedance part, where the external part formed by L_{ext} will interact with the environment as demonstrated in Section 3.2.2. The value of the external inductance L_{ext} is comparable with the self-inductance of a hollow cylinder with the same physical dimensions as the 18650 cell, suggesting a similar behavior of cell and cylinder for high frequencies. For a more detailed EEC model derivation and validation, the reader is referred to our previous work [45]. As mentioned before, the cell impedance Z_{cell} is low-ohmic for low frequencies, which can be seen from the impedance modulus results in Figure 3b. For higher frequencies, the cell impedance increases because of its inductive properties and exhibits an impedance greater than 1 Ω above 1 MHz. Therefore, PLC frequencies above this frequency are preferred, although an access impedance of 1 Ω is still challenging [25]. Previous works focusing on larger prismatic Li-ion cells found similar impedance values for a 24 Ah cell [34] and significantly smaller values ($\approx$0.2 Ω at 10 MHz) for a 34 Ah cell [49].

Table 1. EEC elements of the battery model of Figure 3a including their physical interpretation and value range for the Samsung ICR18650-26J. The given frequency ranges indicate, where the elements contribute most to the overall impedance.

Element	Physical Meaning	Fitted EEC Value Range [45]	Main Frequency Range
R_e	Electrolyte, contact, and CID resistances	30 ... 40 mΩ	Broadband
R_{ion}	Ionic resistance of stacked electrode layers and electrolyte	1.0 ... 1.5 Ω	20 kHz to 10 MHz
R_w	Electrical resistance of collector windings	3 ... 7 mΩ	20 kHz to 10 MHz
L_w	Jelly roll winding inductance	130 ... 140 nH	20 kHz to 10 MHz
L_{ext}	External inductance due to the cell's length, tabs and bonding wires	15 ... 25 nH	Broadband
R_{int}	Internal/ surface resistance due to skin effect	10 ... 15 Ω	above 10 MHz
L_{int}	Internal inductance due to skin effect	3 ... 6 nH	above 10 MHz

3.2. Capacitive and Inductive Coupling Effects between Cells

For an accurate PLC channel model, it is important not only to model the Li-ion cells, but also to include coupling mechanisms among cells in the model. When Li-ion cells are placed in close proximity, capacitive coupling between adjacent cells can be observed as reported in previous works [21,22,50]. Moreover, we also expect inductive coupling to be a significant contributor to the overall PLC channel characteristics. As no literature could be found on quantifying cell-coupling mechanisms over frequency, we investigate both broadband capacitive and inductive coupling in the following.

3.2.1. Capacitive Coupling

As can be seen from the PLC demonstrator photograph (Figure 2b), the cells are placed in triplet plastic cell holders, which ensure a distance of 1 mm between adjacent cells. To measure the coupling capacitance, two Samsung ICR18650-26J were placed next to each other into an unmounted triplet cell holder. Both cells are electrically isolated from each other and one pole of each cell was connected to a VNA port as illustrated in the inset of Figure 4a. Using the VNA reflect method [45], the high ohmic impedance between the two cells was determined by measuring the reflection coefficient Γ, and the cell-to-cell coupling capacitance C_{cc} was calculated according to:

$$C_{cc} = \frac{1}{2\pi f \cdot \Im\{Z_{meas}\}} = \frac{1}{2\pi f \cdot \Im\left\{Z_0 \cdot \frac{1+\Gamma}{1-\Gamma}\right\}} \, , \tag{1}$$

with the frequency f and the characteristic impedance Z_0, which is 50 Ω in this work. As visible in the inset of Figure 4a, the "Y"-shaped VNA connector exhibits serial inductances as well as capacitive coupling between the connecting leads. These effects have been excluded by de-embedding techniques similar to [49]. To gain deeper insight into the capacitive coupling phenomenon, the cell holder was replaced by plastic spacers to alter the distance between the cells. The de-embedded measured coupling capacitances are depicted in Figure 4a for various cell distances. In addition, the raw measurement data of the "Y"-connector are given. As the results suggest, the broadband coupling capacitance is nearly constant above 1 MHz and exhibits approximately 10 pF for a distance of 1 mm. Below this frequency, the high-ohmic reactive impedance of $1/(2\pi f C_{cc})$ is assumed to significantly deteriorate the VNA measurements. Due to the constant coupling above 1 MHz, we assume that the coupling capacitance is constant over the entire frequency range and only depends on the outer metal casings of the cells and the distance in between them. To prove this, Figure 4b compares the measured coupling capacitances at 20 MHz for various distances with two commonly used capacitor models. As visible, an accurate match could be achieved between measurement and the parallel-cylinder capacitor model [51]:

$$C_{cc} = \frac{\pi \epsilon_0 \epsilon_r l}{\ln\left[\frac{D+d_{cc}}{D} + \sqrt{\left(\frac{D+d_{cc}}{D}\right)^2 - 1}\right]} \, , \tag{2}$$

with the vacuum permittivity ϵ_0, the relative permittivity ϵ_r, the cell length $l = 6.5$ cm, the cell diameter $D = 18$ mm, and the distance d_{cc} between the cells. The relative permittivity ϵ_r in (2) was set to 2.1 and can be seen as an average value of the cell surrounding. For further validation, the capacitive coupling has been simulated in CST Studio Suite® by Dassault Systemes Deutschland GmbH (Stuttgart, Germany) [52]. The 3-D EM simulation environment is depicted in Figure 5a and was used to calculate the static electric field and the coupling capacitance between two hollow metal cylinders with a 1 mm distance. The resulting electric field is presented in Figure 5b and the simulated coupling capacitance exhibits a value of 9.56 pF, which is close to the measurement value indicated in Figure 4b. As the relative permittivity of the cell holder made of thermoplastic polyester was not given in its datasheet, a typical value was chosen from literature ($\epsilon_r = 3 \ldots 4$ [53]). In conclusion, the capacitive coupling does not depend on the internal cell structure but only on the outer cell casings and their spacing. Further investigations also showed that the orientation of the cells (parallel or antiparallel cell polarity) had no influence.

(a)

(b)
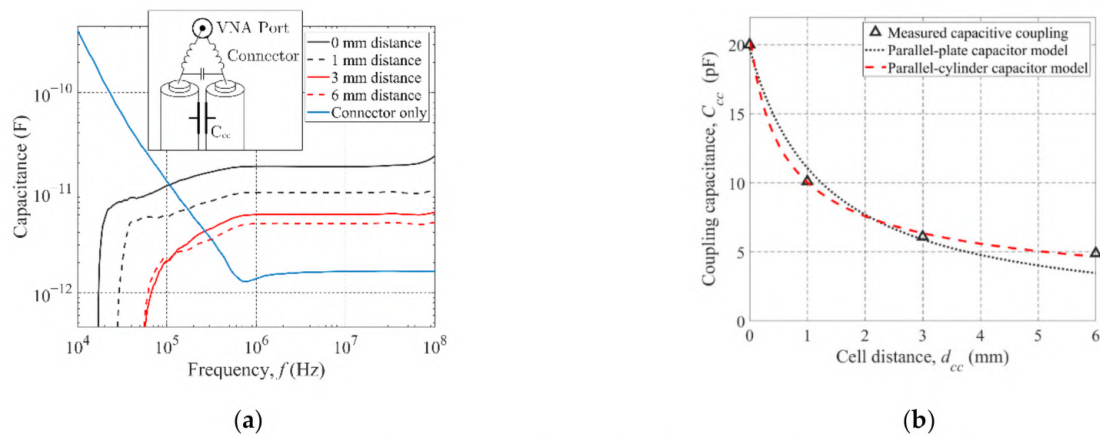
Figure 4. Measured capacitive coupling between two adjacent cylindrical cells: (**a**) Measured coupling capacitance versus frequency for various distances between two cells; (**b**) Coupling capacitance at 20 MHz extracted from the measurements (**a**). For comparison, two commonly known capacitor models are added.

(a)

(b)
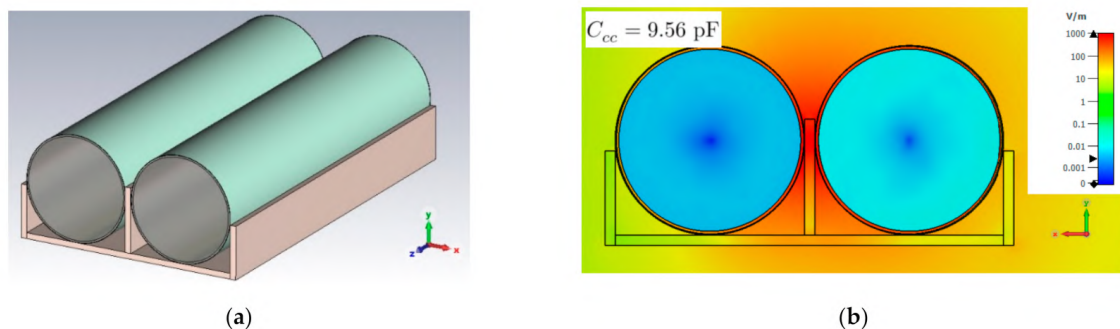
Figure 5. 3-D EM model to simulate capacitive coupling between cylindrical cells: (**a**) Model structure containing two hollow metal cylinders, PVC heat shrinking tubes, and plastic cell holder; (**b**) Static electric field distribution.

3.2.2. Inductive Coupling

If two wires are located in close proximity, a time-varying current in one wire generates a magnetic field that induces a voltage drop on the other wire. In circuit analysis, this phenomenon is described by mutual inductance [54]. In the following, we demonstrate that mutual inductive coupling can also be observed in the case of adjacent battery cells. To determine the mutual inductance M between two cylindrical cells placed in parallel, the Grover method [55] was used, which links M and the self-inductance L_{self} of a single cell to the total inductance L_{loop} of two cells forming a current loop with:

$$L_{loop} = 2\left(L_{self} - M\right). \tag{3}$$

Generally, this approach applies for linear conductors situated in parallel. To prove its validity also for cylindrical battery cells, a 3-D EM simulation was conducted using CST Studio Suite® (Dassault Systemes Deutschland GmbH, Stuttgart, Germany) A simplified 3-D cell model (depicted in Figure 6a) was used for the simulation because the derivation of a detailed 3-D cell model is out of scope of this work and can be found in literature as in [56]. The 3-D cell model consists of only one spirally wound copper (Cu) current collector foil, which is encased by a hollow metal cylinder and a PVC heat shrinking tube. Nickel (Ni) tabs are attached to the cell windings. The number of windings and tab positions match the Samsung ICR18650-26J and were derived from a computed tomography (CT) scan presented in our previous work [45]. The validity of using only one current collector instead of two is given by the fact that in [57], a strong inductive coupling was found between positive and negative current collectors leading to an effective winding inductance equal to the inductance of a single current collector as we demonstrated in [58]. Using the Partial RLC solver in the 3-D EM simulation, the self-, mutual, and loop inductance values could be determined and are summarized in Figure 6b. In the first two frequency decades of Figure 6b, the simulated self- and total inductance values decrease due to the skin effect, whereas the mutual inductance is nearly constant. The resonance visible at approximately 200 MHz is caused by the boundary conditions, which need to be set to electrical instead of open for the Partial RLC solver [52] and does not refer to the cell coupling.

As can be seen from Figure 6b, the simulated total inductance matches the calculated total inductance using (3) thus validating the Grover method for cylindrical battery cells. Solving (3) for M, the Grover method can be used to determine the mutual inductance between two cells placed in parallel by measuring their total inductance L_{loop} and the self-inductance of a single cell.

| (**a**) | (**b**) |
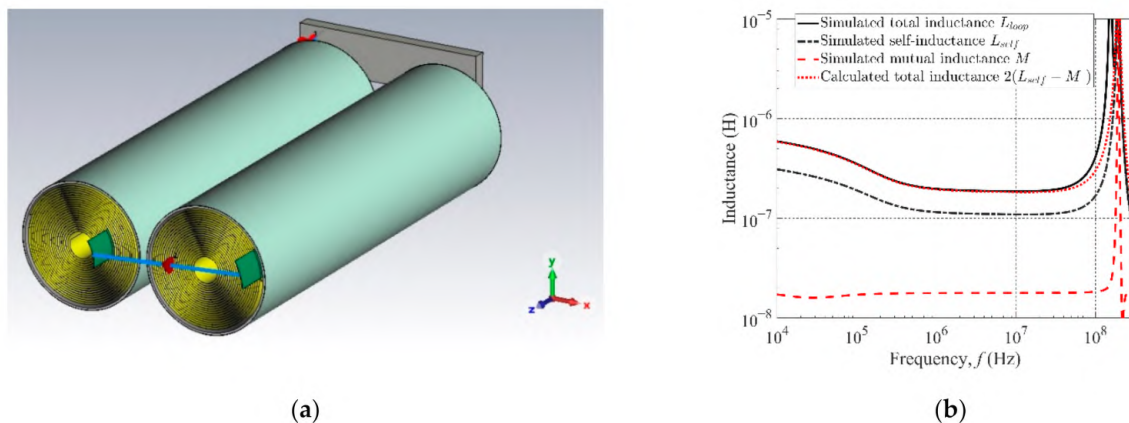
Figure 6. 3-D EM model to simulate inductive coupling between cylindrical cells: (**a**) Model structure containing two hollow metal cylinders with PVC heat shrinking tubes, one spirally wound Cu current collector, and two Ni tabs each; (**b**) Simulated and calculated loop, mutual, and self-inductances proving the validity of the Grover method [55].

For the loop inductance measurement, two 18650 cells were placed 1 mm apart and were electrically connected at one end by a solid wire as illustrated in the inset of Figure 7a. Using the VNA shunt-through method [48], the low-ohmic impedance of the serially connected cells was measured and de-embedded from the measurement setup considering lead inductances and the previously determined capacitance coupling. The resulting loop inductance of the two cells was calculated from the measured, de-embedded impedance Z using:

$$L = \frac{\Im\{Z\}}{2\pi f} . \tag{4}$$

In the same way, (4) was used to derive the self-inductance of a single cell from the impedance measurement results shown in Figure 3b.
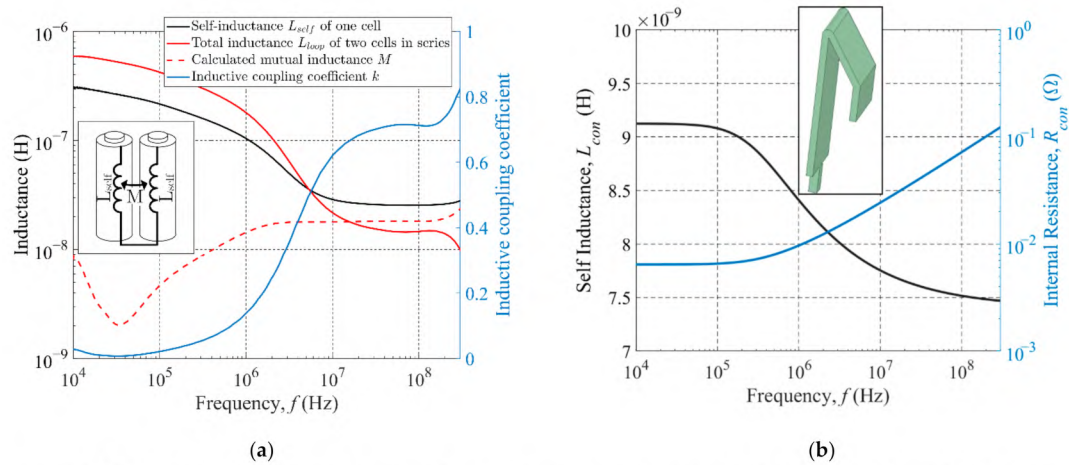
Figure 7. Inductive coupling among adjacent cells and cell connector resistance and inductance: (**a**) Measured inductance values of single cells, two serially connected cells and calculated mutual inductive coupling; (**b**) Self-partial inductance and internal resistance of the cell holder contacts, obtained from 3-D EM simulations.

The resulting mutual inductance M obtained by Equation (3) and the inductive coupling factor $k := M/\sqrt{L_{self}L_{self}} = M/L_{self}$ are summarized in Figure 7a. The inductive coupling factor is rather small below 1 MHz, yet increases significantly between 1 MHz and 20 MHz. Figure 7a also depicts the determined self-inductance L_{self} of a single cell and the total inductance L_{loop} of two cells forming a loop. Both decrease remarkably for higher frequencies, which can be explained by the current distribution inside the cell, which changes over frequency. For frequencies below 1 MHz, most of the current flows in circumferential direction along the current collector windings, thus creating a high jelly roll inductance. At the same time, the metal casing of the cell is assumed to shield the inner magnetic field leading to a small overall inductive coupling. For higher frequencies above 1 MHz, the current tends to concentrate close to the outer cell casing because there, the current experiences the least cylinder inductance and thus reactive impedance [58,59]. In this frequency range, the value of the mutual inductance is approximately constant at 18 nH. This is in accordance with the simulation results of Figure 6b as well as with the mutual inductance formula of two parallel wires according to [55]:

$$M \approx \frac{\mu_0}{2\pi}\left(\ln\left(\frac{2l}{d}\right) - 1 + \frac{d}{l}\right). \tag{5}$$

Using the cell's length $l = 6.5$ cm, the cell center distance $d = 19$ mm (i.e., 1 mm distance between the cells of 9 mm radius) and the permeability $\mu_0 = 4\pi \cdot 10^{-7}$ H/m of free space, (5) yields a mutual inductance of approximately 16 nH. Taking into account that (5) does not consider magnetic fringe field effects at the ends of the cells, the theoretical value fits the experimental results. This demonstrates that the external magnetic field of the battery being responsible for the inductive coupling resembles the external magnetic field of a cylindrical conductor with similar dimensions as the 18650, which is in accordance with the previous works [45,59]. While the mutual inductance above 1 MHz is nearly constant, the self and loop inductance values decrease significantly, which let the inductive coupling factor increase. In conclusion, for PLC frequencies above 1 MHz, significant inductive coupling has to be considered up to a coupling factor of 0.8 or mutual inductance values of 18 nH, respectively. The described experiments were also carried out for parallel cells with opposite orientation, showing no difference in the results similar to Section 3.2.1.

To include the mutual inductive coupling in the cell model of Figure 3a, two EEC cell models connected in series were fitted to the corresponding de-embedded impedance measurement of two cells. The results show that including a constant mutual inductance of 18 nH among the external inductances L_{ext} yields a meaningful match between model and measurement. Again, this demonstrates that the mutual inductance M above 1 MHz can be considered nearly constant and applies only to the external inductance L_{ext} of the battery cell.

3.3. Electrical Cell Connection and Contact Resistance

Beside the cells and their electromagnetic interaction, also the electrical intercon-nection among the cells including contact resistances have to be considered in the PLC channel modeling process. For this, the self-inductance L_{con} and resistance R_{con} of the 18,650 cell holder contacts have been determined by 3-D EM simulations. The results are illustrated in Figure 7b, exhibiting the typical progression over frequency due to the skin effect. Additional contact resistances may occur between the cell terminals and the cell holder contacts, caused by material surface roughness and passivating film layers [60]. However, cell impedance measurements showed that contact resistances become negligible for high frequencies, which can be explained by capacitive coupling across the connecting interfaces [61].

4. PLC Channel Model and Transfer Characteristics

In this Section, the PLC channel model and simulation results regarding the transfer characteristics are demonstrated. Furthermore, the channel model is validated by measure-ments on the PLC hardware demonstrator. The simulations were carried out using the circuit simulator SPICE. By cascading the model components presented in Section 3, the small-scale battery pack of Figure 2a was rebuilt in the simulation environment. Figure 8 gives an insight into the cascaded model structure, where multiple EEC cell models are con-nected in a meandering pattern with the cell connectors, each one modeled by L_{con} and R_{con} (indicated by the grey boxes in Figure 8). The model also includes capacitive and inductive coupling effects identified in the previous Section 3 by the elements C_{cc} and M, respectively. For better illustration, each internal cell impedance is marked by a yellow-colored box, showing no interaction with the environment as described in Section 3.1.
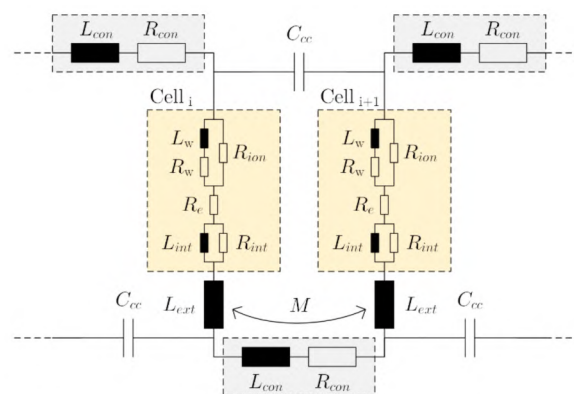
Figure 8. PLC channel model segment including cascaded battery cell models, coupling capacitances, mutual inductance, and electrical connections (marked by grey boxes). The internal impedances of the cells (i, i + 1 . . .) are marked by yellow boxes.

4.1. PLC Channel Model Validation

Since the PLC channel model components of Section 3 were parametrized in the frequency domain, it is reasonable to validate the entire channel model in the time domain. For that, the PLC hardware demonstrator introduced in Section 2 was used to generate a real 2-ASK-PLC signal with 160 mVpp across the small-scale battery pack of Figure 2b (details

on the signal generation can be found in [32]). The pack voltage and the individual cell voltages were measured and digitalized using an oscilloscope MSO58 by Tektronix GmbH (Cologne, Germany). The measured pack voltage was imported into the SPICE simulation providing an input signal to simulate the PLC voltage drops across the single cells. The results are illustrated in Figure 9a and b in case of cell 1 (leftmost cell in Figure 2b). The comparison between measurement and simulation gives a close match, thus graphically demonstrating the validity of the used PLC channel model. This is also confirmed by the low root mean square error (RMSE) between measurement and simulation, which is approximately 1.0 mV.

(a)

(b)
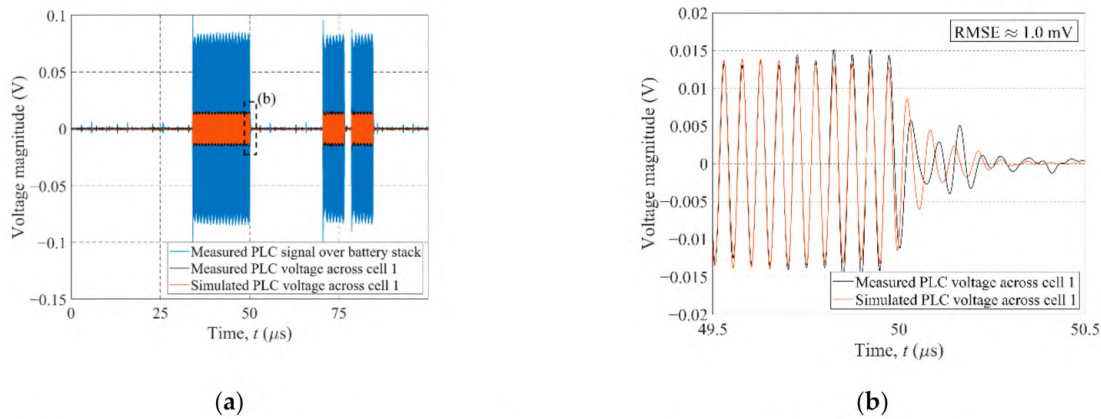
Figure 9. PLC channel model validation using a real ASK-PLC signal generated by the PLC hardware demonstrator of Figure 2b: (**a**) Measured PLC voltages across battery stack (blue) and cell 1 (red) in comparison to the simulated PLC voltage across cell 1; (**b**) Magnified scope view of (**a**) highlighting the fit between measurement and simulation.

4.2. PLC Transfer Function Simulation

The PLC channel transfer characteristics were evaluated within the simulation for both master-to-slave (downlink) and slave-to-master (uplink) communication. To define the PLC transfer function, Figure 10 redraws the PLC system of Figure 2a as two-port network for the downlink case. The transmitter (TX) of the PLC master modem is linked via the two-port network of the PLC channel to the receiver (RX) of the PLC slave modem, which is located at an arbitrary Li-ion cell within the battery pack. The PLC channel is represented by the channel model of Figure 8. As input or access impedance, the master modem sees the entire pack impedance $Z_p(f)$, whereas the slave modem sees the impedance $Z_{cell}(f)$ of a single cell. Based on this representation, the downlink transfer function is given by the relationship between the PLC voltage $V_{s,i}(f)$ across the ith slave cell and the voltage $V_m(f)$ across the PLC master modem:

$$H_d(f) = \frac{V_{s,i}(f)}{V_m(f)} \ . \tag{6}$$

If the direction of communication is reversed, transmitter and receiver are swapped in Figure 10 and the uplink transfer function $H_u(f)$ can be calculated likewise. Although $H_d(f)$ and $H_u(f)$ are in general different, we remark that they hold the property of wide sense symmetry [62]. Moreover, if $Z_m(f) = Z_s(f)$, it follows that $H_d(f) \approx H_u(f)$ [63].

Both uplink and downlink transfer functions were simulated for all six cells of the battery stack using the PLC channel model of Figure 8. For the simulations, the channel model was connected to the master's internal impedance $Z_m(f)$ via coupling capacitors to close the PLC current loop as shown in Figure 2a. Likewise, PLC slave modems were connected in parallel to the single cells. As in PLC systems, the goal is to increase the voltage amplitude rather than the power of the received signal [64], the transmitter's output impedance is low-ohmic (<2 Ω for our demonstrator), whereas the receiver's input impedance is set to high values (>100 kΩ in our case). The simulation results are given for downlink and uplink in Figure 11a,b, respectively. The outer cell nodes 1, 3, 4, 6 and the

inner nodes 2, 5 show similar transfer characteristics. A more attenuated transfer function is seen across cells 2 and 5 for both uplink and downlink, which can be explained by enhanced inductive coupling in the middle position of the triplet cell holders. Considering the downlink, the battery pack can be seen as a $1/N$ voltage divider, with N being the number of cells. Adopting this for our case, $H_d(f)$ has an ideal value of $1/6$ or -15.56 dB. As visible in Figure 11a, this value is reached by the outer cell nodes for frequencies >20 MHz. For lower frequencies, the inductance of the cell interconnections causes a higher channel attenuation. The inner cells differ from the outer cells having a 2 dB lower maximum value of $H_d(f)$ located between 1 and 2 MHz. For frequencies above 80 MHz, $H_d(f)$ of all cells is strongly affected by capacitive coupling. Similar observations can be made for the uplink case depicted in Figure 11b. However, $H_u(f)$ has a lower attenuation than $H_d(f)$, which can be attributed to the master's adjustable internal impedance Z_m. In the uplink case, Z_m forms a voltage divider with the battery pack as it is part of the PLC current loop. Therefore, by choosing a reasonably high impedance for Z_m, one can significantly improve the uplink transfer characteristics. Still, we remark that the access impedance at the slave nodes remains low, requiring higher currents to generate a viable PLC voltage compared to the downlink.
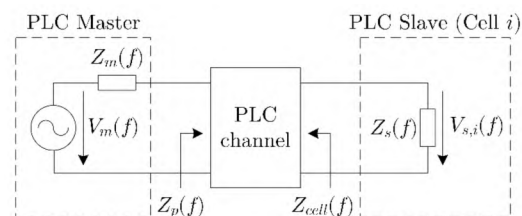
Figure 10. PLC system as a two-port network. PLC master (TX) and slave modem (RX) are connected by the PLC channel model of Figure 8 exhibiting the downlink transfer function $H_d(f)$.

(a)

(b)
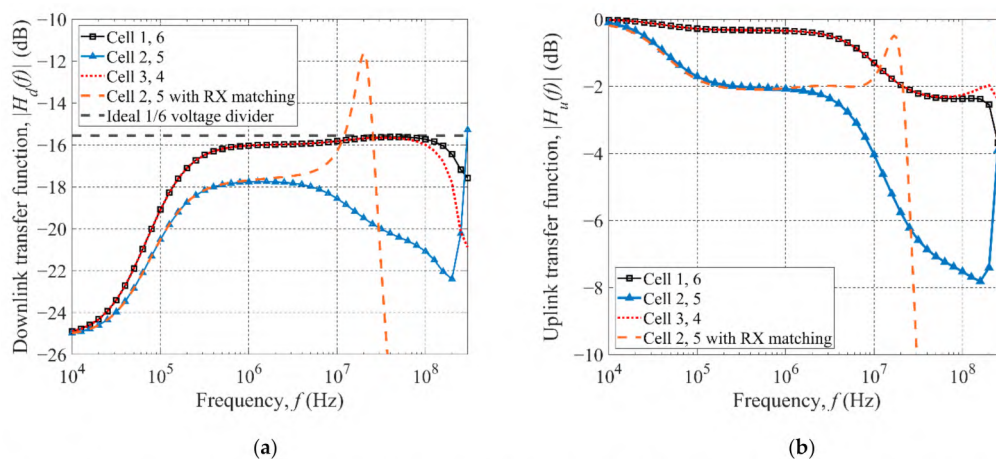
Figure 11. Simulated PLC channel transfer characteristics for the small-scale battery pack of Figure 2a: (**a**) Master-to-slave (downlink) transfer function $H_d(f)$ for all cells including an optimized transfer function by appropriate RX matching at the slave node to maximize the received PLC voltage. The ideal behavior of a $1/6$ voltage divider is added for comparison; (**b**) Slave-to-master (uplink) transfer function $H_u(f)$ for all cells including an optimized transfer function by appropriate RX matching at the master node to maximize the received PLC voltage.

Further simulations revealed that the PLC transfer characteristics can still be improved using the findings on optimized receiver impedance matching of [64], where the authors found the real part to be zero and the median value of the imaginary part close to zero in a series of case studies. Accordingly, to maximize the amplitude of the received voltage signal, the impedance of the PLC receiver is set to have the opposite imaginary value to the access impedance (i.e., the battery impedance) and a null real value. Evaluating the imaginary part $\Im\{Z(f_c)\}$ of both single cell and battery pack impedance at the PLC carrier

frequency f_c yields a positive value of the reactance due to the inductive cell behavior. Using $C = [2\pi f_c \cdot \Im\{Z(f_c)\}]^{-1}$, we obtain capacitance values of 2.0 nF and 0.5 nF for PLC slave and master modems, respectively, generating the desired opposite reactance value at f_c. Inserting the calculated capacitances as impedances Z_m and Z_s of the PLC modems for both uplink and downlink results in the optimized transfer characteristics at f_c as drawn by the dashed orange lines in Figure 11a,b.

In conclusion, the developed PLC channel model can be used for predicting and optimizing the transfer characteristics of a PLC over batteries and can be used also for large-scale battery packs in future works.

5. Coexistence Analysis

For the development of a PLC system, it is essential to address the coexistence between PLC and the existing BMS cell monitoring circuits. Possible interference scenarios need to be examined in order to mitigate them in later design stages. In the following, we will consider the disturbance of BMS CMCs in terms of voltage, current, and impedance sensing caused by PLC signals. In general, the interference is two-fold as it can occur in both directions. However, one direction can be largely excluded.

5.1. PLC Disturbance by BMS Monitoring

BMS monitoring is expected not to cause severe PLC signal distortions for the following reasons: (1) Voltage and current measurements do not require additional excitation signals that could interfere with PLC signals. (2) The frequencies of EIS measurements (typically 1 mHz–10 kHz [65]) are much lower than typical PLC carrier frequencies (>1 MHz). Therefore, no PLC interference coming from the EIS circuitry is expected.

It should be added, though, that online EIS may use a periodical square wave as excitation signal as will be described in the experimental Section 5.2.1. In this case, higher harmonics are inherently present as given by the Fourier series of a periodical square wave with amplitude $\hat{i}$ and frequency $1/t_0$:

$$\frac{4\hat{i}}{\pi} \sum_{n=1,3,5,\dots}^{\infty} \frac{1}{n} sin\left(n \cdot 2\pi \frac{1}{t_0} t \right) \tag{7}$$

By calculating the series of harmonics with (7), their attenuation with respect to the fundamental can be determined. The first harmonic is attenuated by 9.54 dB, the third harmonic by 13.98 dB etc. Given the limited EIS frequency range and the fact that EIS voltage responses must not exceed amplitudes of 10 mV to ensure linearity [11], interference with PLC signals in the megahertz range is not expected.

In the case of EIS amplitudes higher than 10 mV, the nonlinear signal response of the battery can generate higher harmonics. As reported in [66], by using nonlinear frequency response analysis (NFRA), the authors were able to detect frequency components up to the fifth harmonic. Still, the electrochemical cell processes responsible for the nonlinearities were found to occur only below 200 Hz [66], which is far below PLC carrier frequencies.

Although PLC interference by BMS monitoring can be largely excluded for the stated reasons, the CMCs attached to the battery cells may alter the PLC channel characteristics. As shown in Figure 12, the PLC access impedance across a single cell node is decreased if the CMC used in the experiments in Section 5.2.1. is connected to the cell under investigation. The resonance at approximately 1.4 MHz is likely caused by the capacitive filter characteristics of the CMC. However, the impact on the overall PLC channel characteristics can be simply mitigated by choosing a PLC carrier frequency placed deliberately above the resonance or by the integration of decoupling circuits.
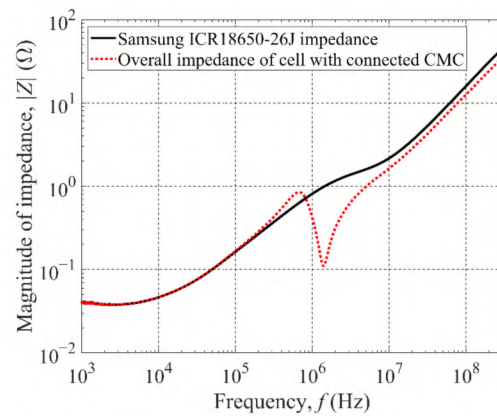
Figure 12. Difference between single cell impedance and overall access impedance for the case that a CMC is attached to the cell.

5.2. BMS Monitoring Disturbance by PLC

PLC signals may interfere with cell monitoring tasks such as voltage, current and impedance measurements, when PLC frequency components are present in the baseband (<10 kHz). Since DC current and voltage measurements need to withstand electromagnetic interference (EMI) coming from the HV power lines, BMS cell monitoring circuits are usually equipped with EMI filters such as blocking capacitors [67]. Therefore, PLC signals are supposed to be filtered out by the EMI filtering devices and do not affect DC measurements. On the other hand, EIS involves cell perturbation by a single-tone AC voltage or current and acquiring the response signal in terms of amplitude and phase. The frequency-dependent cell impedance is then derived by the relationship between voltage amplitude $\hat{v}$ and current amplitude $\hat{i}$ and their phase shift $\Delta\Phi$ at various frequencies f_{EIS}:

$$Z(f_{EIS}) = |Z(f_{EIS})|e^{j\Phi_Z(f_{EIS})} = \left.\frac{\hat{v}}{\hat{i}}e^{j\Delta\Phi}\right|_{f=f_{EIS}}. \tag{8}$$

For a rectangular excitation, the impedance is defined in a more general form considering the discrete Fourier transform (DFT) of cell voltage $V(2\pi f_k)$ and current $I(2\pi f_k)$ at the discrete frequencies f_k:

$$Z(2\pi f_k) = \frac{V(2\pi f_k)}{I(2\pi f_k)} = \frac{|V(2\pi f_k)|}{|I(2\pi f_k)|}e^{j\cdot arg\{V(2\pi f_k)\}-j\cdot arg\{I(2\pi f_k)\}}. \tag{9}$$

The signal acquisition can be, for example, realized by a bandpass delta–sigma (Δ-Σ) analog-to-digital converter (ADC) as described in [10]. Supposing a PLC signal being present and containing a frequency component equal to an EIS measurement frequency, it is expected that the spectral component of the PLC signal may pass through the EIS filter structures thus distorting the EIS measurement. Although the frequency bands of EIS (1 mHz–10 kHz) and PLC (carrier frequency > 1 MHz) are quite different, in the following, we will demonstrate in detail that certain PLC data or packet rates may interfere with EIS measurements.

5.2.1. EIS Disturbance by PLC: Experimental Setup

For EIS interference investigations, we designed an experimental CMC board, whose basic structure is shown in Figure 13. A Samsung ICR18650-26J Li-ion cell is stimulated by a PLC signal and an EIS signal at the same time. The PLC signal is created by a signal generator allowing flexibility in terms of PLC amplitude, data rate, and modulation scheme. For impedance measurements, a prototype integrated circuit (IC) by Infineon Technologies AG (Neubiberg, Germany) is used. Besides temperature and DC cell voltage measurements, the IC performs a galvanostatic EIS by forcing an adjustable sinusoidal or

rectangular (square wave) AC excitation and sensing the AC voltage response of the cell. The complex-valued cell impedance is determined by internal signal processing within the IC and can be plotted in a Nyquist plot as illustrated in Figure 13. Measurement accuracy and resolution are ensured by narrowband input filters, adjustable acquisition times and a sufficient dynamic range of the ADCs. The IC is supplied by a single Li-ion cell having a local ground reference, where it only sees the low voltage of a single cell rather than the high voltage of the entire pack.
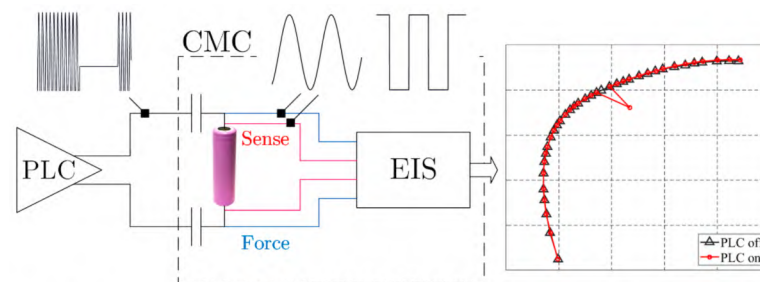
Figure 13. Experimental setup comprising a Samsung ICR18650-26J Li-ion cell mounted on a CMC board with integrated online EIS by an Infineon prototype IC. An external signal generator can be connected to the CMC providing adjustable PLC signals.

During the experiments, a variety of experimental signal parameters have been modified, which are summarized in Table 2.

Table 2. Experimental parameters of PLC and EIS signals.

	Parameter	Settings
PLC	Amplitude	10 mVpp ... 100 mVpp
	Carrier frequency	20 MHz (±1 MHz for FSK)
	Modulation scheme	2-ASK, 2-FSK, 2-PSK
	Modulation signal	Square wave, PRBS
	Bit rate	0.1 kbps ... 2 Mbps
	Time division	Continuous bit stream, data packets
EIS	Excitation current amplitude	10 mA (0.004 C), 67 mA (0.026 C)
	Response voltage for 976.6 Hz	0.8 mVpp, 5.4 mVpp
	Measurement frequency	Sweep or single point (976.6 Hz)
	Measurement time per freq. point	25 ms ... 1600 ms

During the experiments, a variety of experimental signal parameters have been modified, which are summarized in Table 2. EIS measurements were performed either for a single frequency or a complete frequency sweep as shown in Figure 13. Two different EIS excitation currents as well as different acquisition times per frequency point were used. For the PLC signals, various sinusoidal carrier amplitudes between 10 mVpp and 100 mVpp were investigated. Different narrowband digital modulation schemes such as 2-ASK, binary frequency shift keying (2-FSK), and binary phase shift keying (2-PSK) were also inspected. As modulating signal, we used a periodical square wave or a pseudo-random bit sequence (PRBS) that is sent either as permanent data stream or allocated in data packets. The modulation frequency (i.e., data rate) was altered between a few hertz and 2 MHz. For each parameter setting, the EIS measurement was conducted ten times and the results were averaged to increase the confidence level.

5.2.2. EIS Disturbance by PLC: Results and Discussion

Since the experimental parameters given in Table 2 lead to multitudinous combinations for both EIS and PLC signals, only selected interference scenarios are presented in the following. Stated beforehand, the majority of experiments did not lead to EIS interference

by PLC. As the overall results suggest, an interference only occurs, when a PLC frequency component happens to be close to an EIS measurement frequency. In the experiments, this was found for PLC data or packet rates close to an EIS frequency point. A typical EIS result distorted by PLC can be seen in the Nyquist plot of Figure 13.

Figure 14a shows a time signal measured by an oscilloscope that exemplifies the superposition of a rectangular EIS excitation and a 2-ASK PLC signal modulated by a low data rate square wave. Due to the galvanostatic EIS excitation, both the cell's voltage response and the applied PLC voltage accumulate and their sum will be measured by the EIS IC. If the frequency of the modulating square wave approaches an EIS frequency point f_{EIS}, a selective disturbance of the measurement at f_{EIS} can be observed as in Figure 13.

How close the disturber has to approach the EIS frequency to cause an interference is illustrated in Figure 14b for $f_{EIS} = 976.6$ Hz. The given percentage impedance measurement deviation is calculated from the 90% confidence interval normalized by the averaged impedance. The closer the modulation frequency is to f_{EIS}, the more severe the interference gets, which is approximately six times higher for the lower EIS excitation amplitude (5.7% for 0.8 mVpp, 0.9% for 5.4 mVpp). Only a few hertz apart from f_{EIS}, the percentage impedance deviation drops significantly.

To find the origin of the disturbance, a real 2-ASK PLC voltage signal was digitalized by an oscilloscope and the spectrum was calculated using Fast Fourier transform (FFT). The resulting FFT spectrum is shown in Figure 15a displaying one-sided true amplitudes. For comparison, Figure 15b shows the ideal spectrum of the same 2-ASK signal generated by simulation. The spectrum of the ideal ASK signal has only one main spectral component located at the carrier frequency and levels off to both sides. Therefore, ideally no significant baseband components are expected. However, when looking at the spectrum of the real signal, beside higher harmonics of the carrier, there is also an essential baseband component right at the frequency of the modulation signal. We assume that due to non-ideal modulation by the signal generator or other non-ideal down conversion effects, this spectral component is responsible for the EIS interference and may be avoided by prior bandpass-filtering of the PLC signal.

In order to evaluate how different PLC signal properties enforce the selective EIS interference seen in the Nyquist plot of Figure 13, we now intentionally set the PLC modulation frequency exactly to an EIS frequency point f_{EIS}. For the following results, the frequency $f_{EIS} = 976.6$ Hz is taken as representative for all EIS frequency points.

Figure 14c highlights the influence of different PLC amplitudes and EIS measurement times in case of a square wave modulating signal with $f_{EIS} = 976.6$ Hz. Interestingly, all EIS impedance measurements of one PLC setting are located on a sphere around the reference or "true" impedance. Larger PLC amplitudes and shorter measurement times let the impedance error and thus the radius of the sphere increase. However, from Figure 14d averaging the results of Figure 14c including 90% confidence intervals, it becomes clear that only large measurement times (800 ms, 1600 ms) can significantly reduce the impedance measurement spread. For the smallest PLC amplitude (10 mVpp), the inset of Figure 14c indicates that the spherical distribution of the impedance measurements is slightly disarranged by superimposed noise.

(a)

(b)

(c)

(d)

(e)

(f)
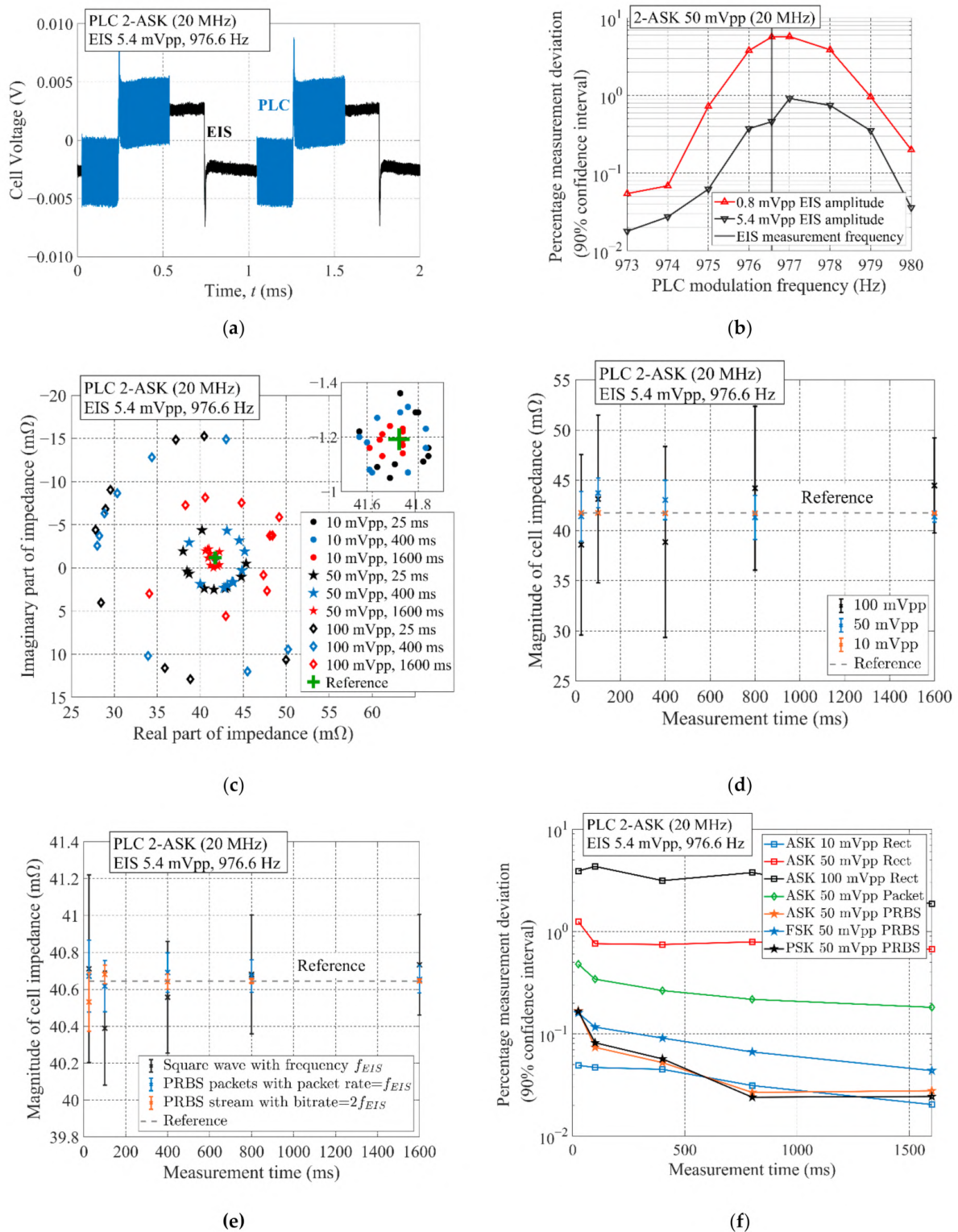
Figure 14. PLC interference with simultaneous EIS measurement: (**a**) Time signal of superimposed 2-ASK PLC and rectangular EIS voltage signals measured across the cell terminals (AC-coupled); (**b**) Percentage EIS measurement deviation for various PLC modulation frequencies around an EIS measurement frequency; (**c**) Impedance measurement results at a single frequency point for a variety of 2-ASK PLC signal amplitudes and EIS measurement times; (**d**) Representation of (**c**) by mean values and 90% confidence interval bars; (**e**) Impedance deviation for different PLC modulation signals represented by mean values and 90% confidence interval bars; (**f**) Percentage impedance deviation based on normalized 90% confidence intervals for different PLC amplitudes, modulation signals, and time divisions.
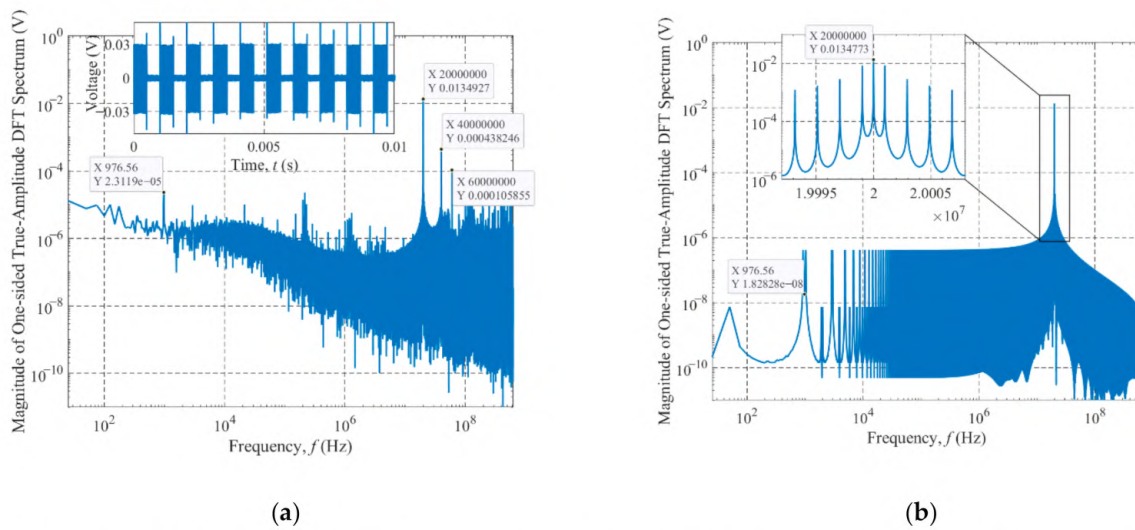
Figure 15. One-sided true amplitude DFT spectra of a 2-ASK PLC signal modulated by a periodical square wave with frequency 976.6 Hz (**a**) Real PLC signal spectrum and time signal (inset); (**b**) Ideal PLC signal spectrum calculated by simulation.

The difference between measured and true impedance seen in Figure 14c can be described by an error vector, which circles around the reference value depending on the phase relationship between PLC and EIS signal. Based on (9), the impedance error vector can be broken down into voltage and current DFT error vectors having the same circulating behavior depicted in Figure 16. Summing up the EIS-caused and PLC-caused voltage DFT vectors $V_{EIS}(2\pi f_k)$ and $V_{PLC}(2\pi f_k)$ results in the overall DFT voltage vector $V_\Sigma(2\pi f_k)$, which is seen by the EIS IC.
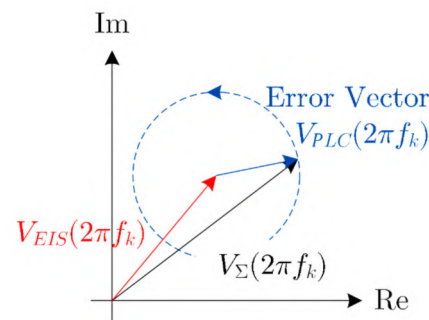
Figure 16. Argand diagram of the complex voltage DFT values for a specific discrete frequency f_k. The PLC error voltage circles around the reference voltage value $V_{EIS}(2\pi f_k)$. The sum of reference and error vector gives the actually measured voltage DFT value for f_k.

Since the EIS excitation current is still measured correctly by the IC regardless of the superimposed PLC signal, the DFT current error vector is zero, and the impedance error vector Z_{er} can be approximated by the superposition of the voltage DFT vectors at the discrete frequency f_k by the following expression:

$$Z_{er,f_k} := Z_{\Sigma,f_k} - Z_{true,f_k} = \frac{V_\Sigma(2\pi f_k) - V_{EIS}(2\pi f_k)}{I_{EIS}(2\pi f_k)} = \frac{V_{PLC}(2\pi f_k)}{I_{EIS}(2\pi f_k)} , \tag{10}$$

with the true impedance Z_{true} and the effectively measured impedance Z_Σ.

In another experiment, the impact of the modulation signal waveforms (listed in Table 2) on the EIS frequency point at f_{EIS} was evaluated using the following settings: For the PRBS modulating signal, a bit rate of $2f_{EIS}$ is chosen because the time per bit is half of the EIS period $1/f_{EIS}$. For the packet stream, PRBS data with 500 kbps are repeatedly

switched on and off with the frequency f_{EIS}. As before, the square wave modulating signal has a frequency of f_{EIS}. All three signals are 2-ASK modulated onto the sinusoidal carrier located at 20 MHz. The impedance results at f_{EIS} for the different modulation signals are averaged and displayed in Figure 14e with 90% confidence intervals. Clearly, the square wave modulation signal has the highest impact on the EIS measurement, whereas the PRBS only leads to small distortions. This can be explained by the higher fundamental content in the periodic square wave than in the PBRS. On the other hand, the PBRS packets are periodically sent with the packet rate f_{EIS}, therefore having a higher fundamental content than the continuous PBRS stream, which leads to a more severe interference. In all three cases, longer EIS measurement times lead to a decrease in measurement error.

The presented results are summarized in terms of percentage measurement deviation in Figure 14f, which again highlights the influence of different PLC signal settings. In addition, results are given for different modulation schemes (2-ASK, 2-FSK, 2-PSK), suggesting a rather small impact on the measurement deviation.

In conclusion, the most relevant factor for EIS disturbance by PLC is the modulation signal's frequency. As the typical frequency range of EIS is below 10 kHz, the critical parameter is the data packet rate rather than the data rate, which is expected to be well above the EIS frequency range. This means, interference can be largely mitigated by avoiding PLC packet rates equal to EIS measurement frequencies.

6. Conclusions

Power line communications for HV battery systems is an attractive alternative communication technique for BMS data transmission and can pave the way for advanced single-cell monitoring methods such as electrochemical impedance spectroscopy being implemented in future smart cells and smart battery systems. In this work, we developed a bottom-up PLC channel model that can predict the PLC channel transfer characteristics for both uplink (CMC to BMU) and downlink (BMU to CMC) communication in a small-scale 18650 battery pack. Using a self-made PLC hardware demonstrator, the model was successfully validated with real PLC signals on the battery pack.

The PLC channel model considers high frequency properties of cylindrical Li-ion cells as well as capacitive and inductive coupling effects among adjacent cells. Impedance characterization and modeling of a single Li-ion cell showed that for typical PLC frequencies above 1 MHz, access impedances greater than 1 Ω per cell can be expected. Investigations on the coupling mechanisms revealed that the coupling capacitance as well as the mutual inductance between adjacent cylindrical cells can be approximated over a wide frequency range by well-known formulas used for hollow metallic cylinders. Cell coupling is predominantly determined by the geometrical cell arrangement, while the direction of current flow in two adjacent cells determines the sign (positive for same, negative for opposite current direction) of the mutual inductance among them as described in [55].

The simulated PLC channel transfer characteristics vary between inner and outer cells forming the battery stack, which is due to higher mutual inductive coupling inside the stack. Capacitive coupling is observed to affect the transfer characteristics only above approximately 80 MHz.

For future work, the presented modeling approach can be used for predicting the transfer characteristics of large-scale HV battery packs as well as for designing customized PLC modems. The model can also be adapted to large-format automotive cells with higher capacity as long as they exhibit a similar rolled-up internal structure as the 18650 cells, such as prismatic cells having elliptically wound electrodes [41]. As large-scale battery packs consist of a high number of single Li-ion cells, the PLC channel is expected to have a significantly higher attenuation than for the investigated PLC demonstrator. Because the cells within a pack may be distributed three-dimensionally in space, they will not entirely follow the parallel placement as in our setup (Figure 2b). This can lead to different coupling among cells placed in series, which is expected to be smaller compared to the parallel arrangement.

The presented circuit-based PLC channel model can be used for further physical layer analysis concerning channel noise characteristics, signal-to-noise ratio and bit error rate (BER) requirements. According to the previous works [34,35], the PLC physical layer can be modeled by (1) the master-slave channel transfer characteristics as determined in this work, and (2) additive white Gaussian noise (AWGN) present for frequencies above 40 MHz. For example, desired BERs below 10^{-3} were achieved by an E_b/N_0 (energy per bit to noise power spectral density ratio) of 9 dB in [35].

For the success of PLC for BMS applications, it is important to unfold and quantify possible coexistence issues between PLC and BMS monitoring. Therefore, in the second part of our work, we investigated various interference scenarios applying a large amount of PLC signals with different settings. As the results demonstrate, BMS monitoring is not expected to interfere with PLC signals. However, monitoring circuits attached to the cell may slightly change the PLC access impedance and transfer characteristics. In contrast, PLC signals can interfere with BMS monitoring, yet only in particular cases regarding EIS. To prevent EIS distortions, PLC signals with packet rates equal to EIS measurement frequencies should to be avoided or passed through effective bandpass filter devices. DC monitoring is not affected by PLC signals since the measurement interfaces are protected by effective filter structures.

Author Contributions: Conceptualization, methodology, validation and formal analysis, T.F.L.; investigation, T.F.L., G.H.; resources, G.S. and G.H.; writing—original draft preparation, T.F.L.; writing—review and editing, G.S., G.H., M.R. and A.J.; visualization, T.F.L.; supervision, M.R. and A.J.; project administration, A.J.; funding acquisition, M.R. and A.J. All authors have read and agreed to the published version of the manuscript.

Conflicts of Interest: The authors declare no conflict of interest. The funders had no role in the design of the study; in the collection, analyses, or interpretation of data; in the writing of the manuscript, or in the decision to publish the results.

Abbreviations

2-ASK	Binary amplitude shift keying
2-PSK	Binary phase shift keying
2-FSK	Binary frequency shift keying
3-D	Three-dimensional
ADC	Analog-to-digital converter
AC	Alternating current
ASIL	Automotive safety integrity level
AWGN	Additive white Gaussian noise
BER	Bit error rate
BEV	Battery electric vehicle
BMS	Battery management system
BMU	Battery management unit
CAN	Control area network
CID	Current interrupt device
CISPR	Comité International Spécial des Perturbations Radioélectriques

CMC	Cell monitoring circuit
CRC	Cyclic redundancy check
CT	Computed tomography
DC	Direct current
DFT	Discrete Fourier transform
EEC	Equivalent electrical circuit
EIS	Electrochemical impedance spectroscopy
EM	Electromagnetic
EMC	Electromagnetic compatibility
EMI	Electromagnetic interference
EV	Electric vehicle
FFT	Fast Fourier transform
GND	Ground
HEV	Hybrid electric vehicle
HF	High frequency
HV	High voltage
IC	Integrated circuit
Li-ion	Lithium-ion
LV	Low voltage
NFRA	Nonlinear frequency response analysis
OOK	On-off keying
PCB	Printed circuit board
PLC	Power line communications
PRBS	Pseudo-random bit sequence
RMSE	Root mean square error
RX	Receiver
SOC	State of charge
SOH	State of health
TX	Transmitter
VNA	Vector network analyzer

Nomenclature

Symbols	Unit	Description
$\Delta\Phi$	$^\circ$	Phase shift between voltage and current signals
ϵ_0	$8.854 \cdot 10^{12}$ F/m	Vacuum permittivity
ϵ_r		Relative permittivity
Φ_Z	$^\circ$	Phase of complex impedance
Γ		Reflection coefficient
μ_0	$4\pi \cdot 10^{-7}$ H/m	Vacuum permeability
ϑ	$^\circ$C	Temperature
C_c	F	Power line coupling capacitor
C_{cc}	F	Cell-to-cell coupling capacitance
C_{dc}	F	DC-link capacitor
D	0.018 m	Cell diameter
d_{cc}	m	Distance between cells
f_c	Hz	Carrier frequency
f_{EIS}	Hz	EIS measurement frequency
f_k	Hz	DFT frequency point
$H_d(f), H_u(f)$	dB	Downlink and uplink PLC transfer function
$\hat{\imath}$	A	Current amplitude
l	0.065 m	Cell length
L_{con}	H	Cell connector inductance
L_{ext}	H	External cell inductance due to the cell's length, tabs and bonding wires

L_{int}	H	Internal cell inductance due to skin effect
L_{loop}	H	Loop inductance
L_{self}	H	Self-inductance
L_{w}	H	Jelly roll winding inductance of the cell
M	H	Mutual inductance
n		n^{th} frequency harmonic
R_{con}	Ω	Cell connector resistance
R_e	Ω	Electrolyte, contact, and CID resistances of the cell
R_{int}	Ω	Internal/ surface cell resistance due to skin effect
R_{ion}	Ω	Ionic resistance of stacked electrode cell layers and electrolyte
R_{w}	Ω	Electrical resistance of cell collector windings
t_0	s	Signal period
$\hat{v}$	V	Voltage amplitude
V_{EIS}	V + jV	EIS voltage DFT vector
V_m	V	PLC voltage across master modem
V_{PLC}	V + jV	PLC voltage DFT error vector
V_Σ	V + jV	Overall DFT vector
$V_{s,i}$	V	PLC voltage across i^{th} slave cell
X_L	Ω	Inductive reactance
Z_0	Ω	Characteristic impedance
Z_{cell}	Ω + jΩ	Complex cell impedance
Z_{er,f_k}	Ω + jΩ	Complex impedance error at f_k
Z_m, Z_s	Ω + jΩ	Master, slave transceiver impedance
Z_p	Ω + jΩ	Battery pack impedance
Z_{true,f_k}	Ω + jΩ	True complex impedance at f_k
Z_{Σ,f_k}	Ω + jΩ	Overall complex impedance at f_k

References

1. Blomgren, G.E. The Development and Future of Lithium Ion Batteries. *J. Electrochem. Soc.* **2017**, *164*, A5019–A5025. [CrossRef]
2. Rao, Z.; Wang, S.; Zhang, G. Simulation and experiment of thermal energy management with phase change material for ageing LiFePO4 power battery. *Energy Convers. Manag.* **2011**, *52*, 3408–3414. [CrossRef]
3. Balasingam, B.; Ahmed, M.; Pattipati, K. Battery Management Systems—Challenges and Some Solutions. *Energies* **2020**, *13*, 2825. [CrossRef]
4. Hannan, M.A.; Lipu, M.S.H.; Hussain, A.; Mohamed, A. A review of lithium-ion battery state of charge estimation and management system in electric vehicle applications: Challenges and recommendations. *Renew. Sustain. Energy Rev.* **2017**, *78*, 834–854. [CrossRef]
5. Weicker, P. *A Systems Approach to Lithiumion Battery Management*; Artech House: Norwood, MA, USA, 2014; ISBN 1608076598.
6. Wei, Z.; Zhao, J.; He, H.; Ding, G.; Cui, H.; Liu, L. Future smart battery and management: Advanced sensing from external to embedded multi-dimensional measurement. *J. Power Sources* **2021**, *489*, 229462. [CrossRef]
7. Din, E.; Schaef, C.; Moffat, K.; Stauth, J.T. A Scalable Active Battery Management System with Embedded Real-Time Electrochemical Impedance Spectroscopy. *IEEE Trans. Power Electron.* **2017**, *32*, 5688–5698. [CrossRef]
8. Koch, R.; Jossen, A. Impedance spectroscopy for battery monitoring with switched mode amplifiers. In Proceedings of the 2014 16th International Power Electronics and Motion Control Conference and Exposition, Antalya, Turkey, 21–24 September 2014; pp. 496–501, ISBN 978-1-4799-2060-0.
9. Abedi Varnosfaderani, M.; Strickland, D. A Comparison of Online Electrochemical Spectroscopy Impedance Estimation of Batteries. *IEEE Access* **2018**, *6*, 23668–23677. [CrossRef]
10. Crescentini, M.; de Angelis, A.; Ramilli, R.; Angelis, G.; de Tartagni, M.; Moschitta, A.; Traverso, P.A.; Carbone, P. Online EIS and Diagnostics on Lithium-Ion Batteries by Means of Low-Power Integrated Sensing and Parametric Modeling. *IEEE Trans. Instrum. Meas.* **2021**, *70*, 1–11. [CrossRef]
11. Barsoukov, E.; Macdonald, J.R. *Impedance Spectroscopy*; John Wiley & Sons, Inc.: Hoboken, NJ, USA, 2018; ISBN 9781119381860.
12. Andre, D.; Meiler, M.; Steiner, K.; Wimmer, C.; Soczka-Guth, T.; Sauer, D.U. Characterization of high-power lithium-ion batteries by electrochemical impedance spectroscopy. I. Experimental investigation. *J. Power Sources* **2011**, *196*, 5334–5341. [CrossRef]

13. Waag, W.; Käbitz, S.; Sauer, D.U. Experimental investigation of the lithium-ion battery impedance characteristic at various conditions and aging states and its influence on the application. *Appl. Energy* **2013**, *102*, 885–897. [CrossRef]
14. Mingant, R.; Bernard, J.; Sauvant Moynot, V.; Delaille, A.; Mailley, S.; Hognon, J.-L.; Huet, F. EIS Measurements for Determining the SoC and SoH of Li-Ion Batteries. *ECS Trans.* **2010**, *33*, 41–53. [CrossRef]
15. Love, C.T.; Virji, M.B.V.; Rocheleau, R.E.; Swider-Lyons, K.E. State-of-health monitoring of 18650 4S packs with a single-point impedance diagnostic. *J. Power Sources* **2014**, *266*, 512–519. [CrossRef]
16. Schmidt, J.P.; Arnold, S.; Loges, A.; Werner, D.; Wetzel, T.; Ivers-Tiffée, E. Measurement of the internal cell temperature via impedance: Evaluation and application of a new method. *J. Power Sources* **2013**, *243*, 110–117. [CrossRef]
17. Raijmakers, L.H.J.; Danilov, D.L.; van Lammeren, J.P.M.; Lammers, M.J.G.; Notten, P.H.L. Sensorless battery temperature measurements based on electrochemical impedance spectroscopy. *J. Power Sources* **2014**, *247*, 539–544. [CrossRef]
18. Meddings, N.; Heinrich, M.; Overney, F.; Lee, J.-S.; Ruiz, V.; Napolitano, E.; Seitz, S.; Hinds, G.; Raccichini, R.; Gaberšček, M.; et al. Application of electrochemical impedance spectroscopy to commercial Li-ion cells: A review. *J. Power Sources* **2020**, *480*, 228742. [CrossRef]
19. Hong, H.J.; Sevillano, J.R.; Kain, C.; Hofer, G.; Felber, K.; Chan, W.K. Alternatives in Battery Communication Protocols. In Proceedings of the SAE Technical Paper Series. WCX™ 17: SAE World Congress Experience, Detroit, MI, USA, 4 April 2017.
20. Maryanka, Y. Wiring reduction by battery power line communication. In *Proceedings of the IEE Seminar on Passenger Car Electrical Architecture*; IEE Seminar on Passenger Car Electrical Architecture: Birmingham, UK, 2000; p. 8.
21. Ouannes, I.; Nickel, P.; Dostert, K. Cell-wise monitoring of Lithium-ion batteries for automotive traction applications by using power line communication: Battery modeling and channel characterization. In Proceedings of the 2014 18th IEEE International Symposium on Power Line Communications and Its Applications (ISPLC), Glasgow, UK, 30 March–2 April 2014; pp. 24–29, ISBN 978-1-4799-4980-9.
22. Bolsinger, C.; Brix, J.; Dragan, M.; Birke, K.P. Investigating and modeling the transmission channel of a prismatic lithium-ion cell and module for powerline communication. *J. Energy Storage* **2017**, *10*, 11–19. [CrossRef]
23. Talie, A.P.; Pribyl, W.A.; Hofer, G. Electric Vehicle Battery Management System Using Power Line Communication Technique. In Proceedings of the 2018 14th Conference on Ph.D. Research in Microelectronics and Electronics (PRIME), Prague, Czech Republic, 2–5 July 2018; pp. 225–228, ISBN 978-1-5386-5387-6.
24. Opalko, O.; Alonso, D.; Dostert, K. Modeling of the power-line channel in automotive Li-ion batteries with Rogowski coils as coupling elements. In Proceedings of the 2016 International Symposium on Power Line Communications and its Applications (ISPLC), Bottrop, Germany, 20–23 March 2016; pp. 224–229, ISBN 978-1-4673-6643-4.
25. Tonello, A.M.; Lampe, L.; Swart, T.G. *Power Line Communications: Principles, Standards and Applications from Multimedia to Smart Grid*, 2nd ed.; John Wiley & Sons: Hoboken, NJ, USA, 2016; ISBN 978-1-118-67671-4.
26. Pittolo, A.; de Piante, M.; Versolatto, F.; Tonello, A.M. In-Vehicle Power Line Communication: Differences and Similarities Among the In-Car and the In-Ship Scenarios. *IEEE Veh. Technol. Mag.* **2016**, *11*, 43–51. [CrossRef]
27. Miller, B.P. Automotive Lithium-Ion Batteries. *Johns. Matthey Technol. Rev.* **2015**, *59*, 4–13. [CrossRef]
28. Landinger, T.F.; Schwarzberger, G.; Jossen, A. A Novel Method for High Frequency Battery Impedance Measurements. In Proceedings of the 2019 IEEE International Symposium on Electromagnetic Compatibility, Signal & Power Integrity (EMC+SIPI), New Orleans, LA, USA, 22–26 July 2019; pp. 106–110, ISBN 978-1-5386-9199-1.
29. Sendin, A.; Peña, I.; Angueira, P. Strategies for Power Line Communications Smart Metering Network Deployment. *Energies* **2014**, *7*, 2377–2420. [CrossRef]
30. Degauque, P.; Stievano, I.; Pignari, S.; Degardin, V.; Canavero, F.; Grassi, F.; Canete, F.J. Power-Line Communication: Channel Characterization and Modeling for Transportation Systems. *IEEE Veh. Technol. Mag.* **2015**, *10*, 28–37. [CrossRef]
31. Taherinejad, N.; Rosales, R.; Lampe, L.; Mirabbasi, S. Channel characterization for power line communication in a hybrid electric vehicle. In Proceedings of the 2012 IEEE International Symposium on Power Line Communications and Its Applications, Beijing, China, 27–30 March 2012; pp. 328–333, ISBN 978-1-4673-0361-3.
32. Landinger, T.F.; Schwarzberger, G.; Rose, M.; Dollhaeubl, S.; Hofer, G.; Talei, A.P.; Jossen, A. Power Line Communications in Automotive Traction Batteries: A Proof of Concept. In Proceedings of the 2020 IEEE International Symposium on Power Line Communications and its Applications (ISPLC), Málaga, Spain, 11–13 May 2020; pp. 1–5, ISBN 978-1-7281-4816-8.
33. Takanashi, M.; Harada, T.; Takahashi, A.; Tanaka, H.; Hayashi, H.; Hattori, Y. High-voltage power line communication system for hybrid vehicle. In Proceedings of the 2015 IEEE International Symposium on Power Line Communications and Its Applications (ISPLC), Austin, TX, USA, 29 March–1 April 2015; pp. 222–227, ISBN 978-1-4799-8413-8.
34. Ouannes, I.; Nickel, P.; Bernius, J.; Dostert, K. Physical Layer Performance Analysis of Power Line Communication (PLC) applied for Cell-Wise Monitoring of Automotive Lithium-Ion Batteries. In Proceedings of the 18th International OFDM Workshop 2014 (InOWo'14), Essen, Germany, 27–28 August 2014; pp. 1–8.
35. Opalko, O.; Simon, B.; Alonso, D.; Dostert, K. Physical layer and multi-carrier analysis for power line communication networks in Li-ion batteries for electric and hybrid vehicles. In Proceedings of the 2015 IEEE Vehicular Networking Conference (VNC), Kyoto, Japan, 16–18 December 2015; pp. 243–250, ISBN 978-1-4673-9411-6.
36. Vincent, T.A.; Marco, J. Development of Smart Battery Cell Monitoring System and Characterization on a Small-Module Through In-Vehicle Power Line Communication. *IEEE Access* **2020**, *8*, 220658–220671. [CrossRef]

37. Taherinejad, N.; Rosales, R.; Mirabbasi, S.; Lampe, L. A study on access impedance for vehicular power line communications. In Proceedings of the 2011 IEEE International Symposium on Power Line Communications and Its Applications, Udine, Italy, 3–6 April 2011; pp. 440–445, ISBN 978-1-4244-7751-7.
38. Osswald, P.J.; Erhard, S.V.; Noel, A.; Keil, P.; Kindermann, F.M.; Hoster, H.; Jossen, A. Current density distribution in cylindrical Li-Ion cells during impedance measurements. *J. Power Sources* **2016**, *314*, 93–101. [CrossRef]
39. Iglesias, M.; Echeverria, I.; Arteche, F.; Piedrafita, J.; Pradas, A.; de Clercq, J. EMC mapping of a power train for fully electric 4-wheel drive vehicle. In Proceedings of the 2014 International Symposium on Electromagnetic Compatibility, Gothenburg, Sweden, 1–4 September 2014; pp. 414–419, ISBN 978-1-4799-3226-9.
40. CISPR 25. *Radio Disturbance Characteristics for the Protection of Receivers Used on Board Vehicles, Boats and on Devices—Limits and Methods of Measurement*; IEC/DIN-EN 55025 Brussels, Belgium; IEC: Geneva, Switzerland, 2008.
41. Saw, L.H.; Ye, Y.; Tay, A.A.O. Integration issues of lithium-ion battery into electric vehicles battery pack. *J. Clean. Prod.* **2016**, *113*, 1032–1045. [CrossRef]
42. Reuter, M.; Tenbohlen, S.; Kohler, W. The Influence of Network Impedance on Conducted Disturbances Within the High-Voltage Traction Harness of Electric Vehicles. *IEEE Trans. Electromagn. Compat.* **2014**, *56*, 35–43. [CrossRef]
43. Korth Pereira Ferraz, P.; Schmidt, R.; Kober, D.; Kowal, J. A high frequency model for predicting the behavior of lithium-ion batteries connected to fast switching power electronics. *J. Energy Storage* **2018**, *18*, 40–49. [CrossRef]
44. Hoene, E.; Guttowski, S.; Saikly, R.; John, W.; Reichl, H. Rf-properties of automotive traction batteries. In Proceedings of the 2003 IEEE International Symposium on Electromagnetic Compatibility, 2003. EMC '03, Istanbul, Turkey, 16 May 2003; Volume 1, pp. 425–428, ISBN 0-7803-7779-6.
45. Landinger, T.F.; Schwarzberger, G.; Jossen, A. A Physical-Based High-Frequency Model of Cylindrical Lithium-Ion Batteries for Time Domain Simulation. *IEEE Trans. Electromagn. Compat.* **2020**, *62*, 1524–1533. [CrossRef]
46. Wu, Y.; Saxena, S.; Xing, Y.; Wang, Y.; Li, C.; Yung, W.; Pecht, M. Analysis of Manufacturing-Induced Defects and Structural Deformations in Lithium-Ion Batteries Using Computed Tomography. *Energies* **2018**, *11*, 925. [CrossRef]
47. Yao, X.-Y.; Pecht, M.G. Tab Design and Failures in Cylindrical Li-ion Batteries. *IEEE Access* **2019**, *7*, 24082–24095. [CrossRef]
48. Agilent Technologies, Inc. *Application Note 5989-5935EN: Ultra-Low Impedance Measurements Using 2-Port Measurements*; Agilent Technologies, Inc.: Santa Clara, CA, USA, 2007.
49. Pake Talei, A.; Pribyl, W.A.; Hofer, G. Considerations for a power line communication system for traction batteries. *Elektrotech. Inftech.* **2021**, *10*, 24. [CrossRef]
50. Teo, Y.X.; Chen, J.; Ruddle, A.R. Predicting the RF Impedance of Cells in Parallel for Automotive Traction Battery Applications. In Proceedings of the 2019 International Symposium on Electromagnetic Compatibility—EMC EUROPE, Barcelona, Spain, 2–6 September 2019; pp. 438–443, ISBN 978-1-7281-0594-9.
51. Terman, F.E. *Radio Engineers' Handbook*, 1st ed.; MacGraw-Hill: New York, NY, USA, 1943.
52. SIMULIA. *CST Studio Suite 2021*; Dassault Systemes Deutschland GmbH: Stuttgart, Germany, 2021.
53. Manas, D.; Mizera, A.; Navratil, M.; Manas, M.; Ovsik, M.; Sehnalek, S.; Stoklasek, P. The Electrical, Mechanical and Surface Properties of Thermoplastic Polyester Elastomer Modified by Electron Beta Radiation. *Polymers* **2018**, *10*, 1057. [CrossRef]
54. Leferink, F.B.J.; van Doom, M.J.C.M. Inductance of printed circuit board ground planes. In Proceedings of the 1993 International Symposium on Electromagnetic Compatibility, Dallas, TX, USA, 9–13 August 1993; pp. 327–329, ISBN 0-7803-1304-6.
55. Grover, F.W. *Inductance Calculations*; Dover Publications, Inc.: Mineola, NY, USA, 2013; ISBN 9780486318356.
56. Guo, M.; White, R.E. Mathematical model for a spirally-wound lithium-ion cell. *J. Power Sources* **2014**, *250*, 220–235. [CrossRef]
57. Schindler, S.; Danzer, M.A. Influence of cell design on impedance characteristics of cylindrical lithium-ion cells: A model-based assessment from electrode to cell level. *J. Energy Storage* **2017**, *12*, 157–166. [CrossRef]
58. Landinger, T.F.; Schwarzberger, G.; Jossen, A. High frequency impedance characteristics of cylindrical lithium-ion cells: Physical-based modeling of cell state and cell design dependencies. *J. Power Sources* **2021**, *488*, 229463. [CrossRef]
59. Ruddle, A.R.; Chen, J.; Teo, Y.X. Measurement of RF impedance for automotive 18650 cylindrical lithium ion cells. In Proceedings of the 2017 International Symposium on Electromagnetic Compatibility—EMC EUROPE, Angers, France, 4–7 September 2017; pp. 1–6, ISBN 978-1-5386-0689-6.
60. Brand, M.J.; Berg, P.; Kolp, E.I.; Bach, T.; Schmidt, P.; Jossen, A. Detachable electrical connection of battery cells by press contacts. *J. Energy Storage* **2016**, *8*, 69–77. [CrossRef]
61. Malucci, R.D. The impact of contact resistance on high speed digital signal transmission. In Proceedings of ther Forty-Eighth IEEE Holm Conference on Electrical Contacts, Orlando, FL, USA, 21–23 October 2002; pp. 212–220, ISBN 0-7803-7433-9.
62. Passerini, F.; Tonello, A.M. Secure PHY Layer Key Generation in the Asymmetric Power Line Communication Channel. *Electronics* **2020**, *9*, 605. [CrossRef]
63. Galli, S. Exact conditions for the symmetry of a loop. *IEEE Commun. Lett.* **2000**, *4*, 307–309. [CrossRef]
64. Antoniali, M.; Tonello, A.M.; Versolatto, F. A Study on the Optimal Receiver Impedance for SNR Maximization in Broadband PLC. *J. Electr. Comput. Eng.* **2013**, *2013*, 635086. [CrossRef]
65. Illig, J.; Schmidt, J.P.; Weiss, M.; Weber, A.; Ivers-Tiffée, E. Understanding the impedance spectrum of 18650 LiFePO4-cells. *J. Power Sources* **2013**, *239*, 670–679. [CrossRef]

66.   Harting, N.; Wolff, N.; Röder, F.; Krewer, U. Nonlinear Frequency Response Analysis (NFRA) of Lithium-Ion Batteries. *Electrochim. Acta* **2017**, *248*, 133–139. [CrossRef]
67.   Lelie, M.; Braun, T.; Knips, M.; Nordmann, H.; Ringbeck, F.; Zappen, H.; Sauer, D. Battery Management System Hardware Concepts: An Overview. *Appl. Sci.* **2018**, *8*, 534. [CrossRef]

6 Summary and Conclusion

Online Electrochemical Impedance Spectroscopy combined with power line communications for automotive traction batteries has been investigated as potential solution path towards smart cells and smart plug-and-play battery management systems.

The implementation of online EIS into automotive traction batteries faces several challenges such as (1) external disturbances coming from the automotive power electronics, (2) leakage currents across secondary current paths, and (3) crosstalk among online EIS circuits and other EMI effects. Using a monolithic chip solution for online EIS and data processing, it has been shown that a decentralized EIS approach with active signal generation gives reliable impedance measurement results even under strong noise with slightly negative SNR.

The impedance of a battery cell is influenced by many factors such as temperature, SOC, load current, and changes during aging. On the interpretation side of EIS measurement data, powerful estimation methods still need to demonstrate the effective use of impedance for specific state estimations such as SOH tracking without SOC knowledge. As potential alternative to completely decoupled impedance-based state estimation methods, existing techniques such as coulomb counting for SOC tracking could be used in combination with online EIS, for example, to detect the SOH of the cell. In summary, the added value of online EIS in terms of cell state prediction on the way towards smart single Li-ion cells has to be proven to outweigh its additional implementation efforts and cost.

HV PLC for in-battery communications can be implemented as classical master-to-slave topology, where the battery power line network forms the physical layer of the communications and universal bus standards such as UART can be used as top layer for data transmission. Within this thesis, a proof-of-concept study using a block-based hardware design approach was conducted, forming the foundation for further PLC system designs. Based on the proof of concept, Figure 23 proposes a more compact solution of both PLC modulator and demodulator circuits based on a 2-ASK modulation
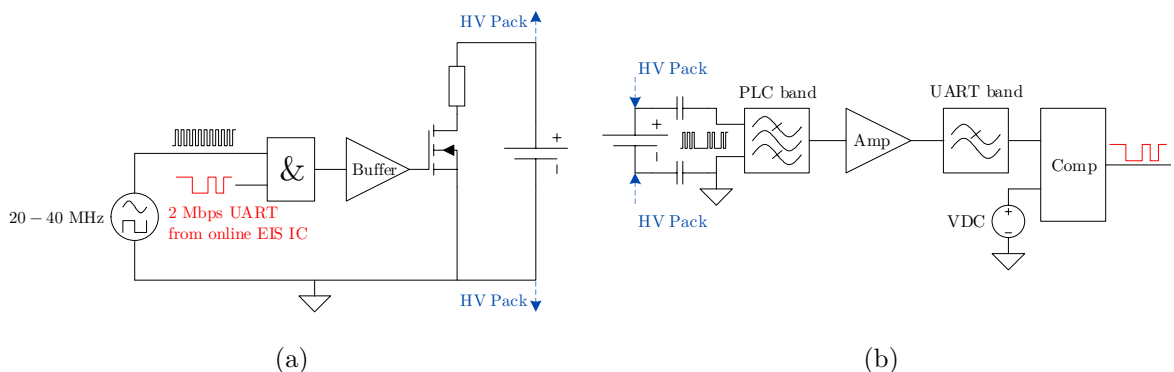
Figure 23: Concise hardware concept for an integrated PLC modem based on the proof of concept of Section 5.1. (a) Modulator concept based on periodic load switching with the modulated PLC signal. The UART signal is 2-ASK modulated by an AND gate and fed via a buffer to the switching transistor. (b) Demodulator concept based on effective filtering and amplifying of the incoming modulated PLC signal, and digitizing through a comparator with adjustable DC voltage reference.

technique, which could be used for future monolithic re-designs. The modem is intended for a single-cell-based PLC but could be attached also to a battery module when using a modulating transistor (shown in Figure 23a) with a sufficiently high maximum voltage rating.

The battery PLC channel presents a challenging communications environment consisting of many serially connected communications nodes, and differs therefore largely from the well-established PLC DC bus technology. Moreover, PLC modems need to cope with low-ohmic access impedances provided by the Li-ion battery cells but which increase with frequency thanks to the inductive nature of the cells at high frequencies. HF characterization of several 18650 Li-ion cells within this work demonstrated that access impedances around 2 Ω can be expected for frequencies above 10 MHz. For comparison, existing works on larger prismatic Li-ion cells found more spread impedance values of approximately 0.2 Ω for a 34 Ah cell [221] and 10 Ω for a 24 Ah cell [57] both at 10 MHz. Following the findings of this thesis on cell design aspects, the impedance spread may be explained by the different internal cell geometries of prismatic cells (either stacked or rolled-up electrode layers) since the jelly roll inductance contributes strongly to the cell impedance at high frequencies. Low temperatures were found to significantly increase the HF impedance of Li-ion cells around 10 MHz (from 40 °C to 0 °C by nearly 30%) because high jelly roll reactances let the temperature-dependent ionic current contribution increase. On the other hand, SOC hardly affects the HF impedance behavior.

The lower the access impedance, the more power (current) the transmitter of the PLC modem requires to drive the PLC voltage signal onto the battery cell. Signal strengths between 10 mVpp and 100 mVpp have been considered to keep the power consumption at a reasonable level. Taking an access impedance of 2 Ω and assuming an alternating bit stream with 50% duty cycle ("1010…"), an hour of continuous data transmission is expected to discharge the battery cell by 2.5 mAh to 25 mAh, neglecting quiescent and bias currents of the modem. This is in the same range as was found for wireless BMS solutions (11.2 mAh to 22.5 mAh [179]) as well as for wired BMS using a conventional CAN transceiver (typ. 15 mAh [222]).

Predicting the PLC channel transfer characteristics is challenging because electromagnetic coupling effects between adjacent battery cells cause the PLC signal voltage drop per cell to be partly "indeterministic". That means that the coupling among cells strongly depends on the specific module or pack topology and the locations of each cells within the pack. As approximation over a wide frequency range, this thesis demonstrated that EM coupling among cylindrical Li-ion cells can be well described by the coupling among hollow electrical conductors with the same dimensions as of the cell. It is assumed that this approximation can also be applied to high-capacity prismatic cells, suggesting that EM coupling may increase for larger cells due to higher capacitances and larger effective inductive loop area [223]. Taking EM coupling effects into account, an equivalent electrical circuit model of the battery power line network was developed for PLC channel simulations and was validated by the custom-made proof-of-concept demonstrator. The proposed physical-based battery model considers HF-relevant battery processes such as the ionic shunt effect, the skin effect, and other resistive-inductive loss processes, which were identified by a novel HF impedance measurement method developed in this thesis.

Using the novel measurement method for HF impedance characterization of several cylindrical Li-ion cells with different internal geometries, the ionic shunt effect was identified to be the root cause of the characteristic impedance curve bending that is often visible in the Nyquist plot above the intercept frequency describing the intercept point of the impedance locus with the imaginary axis. Accordingly, the quasiparallel interconnection between the current collector windings and the stacked active electrode layers leads to an increase in resistance and therefore to the impedance curve bending.

As time multiplexing of HV PLC signaling and battery monitoring is too time-consuming for automotive BMS applications, the coexistence of the two was investigated in this thesis, giving suggestions to avoid compatibility issues. On the one hand, voltage, current, and impedance monitoring of the BMS was found not to interfere with HV PLC signaling. However, cell monitoring circuits need to be considered by the PLC channel modeling approach as they can change the PLC access impedance. On the other hand, HV PLC signaling may distort BMS monitoring, yet only under special circumstances regarding online EIS. The results demonstrate that interference can be largely prevented by avoiding PLC packet and data rates equal to EIS measurement frequencies. DC voltage and current monitoring were found not to be distorted by PLC signaling. In conclusion, EIS with PLC for automotive HV battery management systems has been demonstrated to work properly under laboratory conditions without interoperability problems.

In future work, a first implementation of HV PLC on battery pack level could be realized by a module-to-module communication to alleviate the aforementioned challenges of HV PLC for a cell-to-cell communication. This way, access impedances could be increased and coupling effects among single cells would become less critical. Moreover, the power consumption of the PLC modem could be reduced as less excitation current is necessary to generate the PLC voltage signal across the module. Therefore, HV PLC among battery modules is expected to have improved channel transfer characteristics, increased robustness and efficiency, and could be used for an initial PLC operation on battery pack level. As potential next step, a large-scale battery pack equipped with single-cell-based monitoring circuits and PLC modems could be assembled and tested with respect to communications reliability and EMC regulations.

On the simulation side, future work can reuse the developed channel modeling approach for further channel simulations of large-scale HV battery packs, this way facilitating custom-made PLC modem design. Due to the high number of single Li-ion cells, the channel attenuation within an entire battery pack is expected to be significantly higher than found for the small stack of the PLC proof-of-concept demonstrator, which was approximately 16 dB. Accordingly, the channel attenuation for one hundred Li-ion cells connected in series can be estimated by 1/100 or 40 dB. To adapt the required PLC transmitting power, further physical layer analysis regarding channel noise characteristics, signal-to-noise ratio and bit error rate (BER) need to be performed. For this, the developed PLC channel model can be combined with an additional noise model describing the noisy automotive environment. Assuming additive white Gaussian noise in the simulation environment, related works found BERs below 10^{-3} for an E_b/N_0 (energy per bit to noise power spectral density ratio) of 9 dB, [65, 224].

Prospective studies should further address the possibilities of reusing PLC signals for impedance measurements or charge balancing to improve its added value for BMS monitoring.

List of Figures

List of Tables

List of References

[1] International Energy Agency. "Global EV Outlook" (2020). Accessed on April 9, 2021. [Online]. URL: `https://www.iea.org/reports/global-ev-outlook-2020`.

[2] European Commission. "Communication from the commission: A Clean Planet for all - A European strategic long-term vision for a prosperous, modern, competitive and climate neutral economy" (2018). Accessed on April 9, 2021. [Online]. URL: `https://eur-lex.europa.eu/legal-content/EN/TXT/?uri=CELEX:52018DC0773`.

[3] United Nations Framework Convention on Climate Change. "Adoption of the Paris agreement" (2015). Accessed on April 12, 2021. [Online]. URL: `https://unfccc.int/sites/default/files/english_paris_agreement.pdf`.

[4] S. Fluchs. "The diffusion of electric mobility in the European Union and beyond". In: *Transportation Research Part D: Transport and Environment*, vol. 86, no. 5, 102462 (2020). DOI: `10.1016/j.trd.2020.102462`.

[5] M. Giansoldati, L. Rotaris, M. Scorrano, and R. Danielis. "Does electric car knowledge influence car choice? Evidence from a hybrid choice model". In: *Research in Transportation Economics*, vol. 80, no. 6, 100826 (2020). DOI: `10.1016/j.retrec.2020.100826`.

[6] K. W. E. Cheng, B. P. Divakar, H. Wu, K. Ding, and H. F. Ho. "Battery-Management System (BMS) and SOC Development for Electrical Vehicles". In: *IEEE Transactions on Vehicular Technology*, vol. 60, no. 1 (2011), pp. 76–88. DOI: `10.1109/TVT.2010.2089647`.

[7] G. E. Blomgren. "The Development and Future of Lithium Ion Batteries". In: *Journal of The Electrochemical Society*, vol. 164, no. 1, A5019 (2017). DOI: `10.1149/2.0251701jes`.

[8] Z. Wei, J. Zhao, H. He, G. Ding, H. Cui, and L. Liu. "Future smart battery and management: Advanced sensing from external to embedded multi-dimensional measurement". In: *Journal of Power Sources*, vol. 489, 229462 (2021). DOI: `10.1016/j.jpowsour.2021.229462`.

[9] Katarina Edström. "BATTERY 2030+ roadmap" (2020). Accessed on April 12, 2021. [Online]. URL: `https://battery2030.eu/digitalAssets/861/c_861008-l_1-k_roadmap-27-march.pdf`.

[10] L. Lu, X. Han, J. Li, J. Hua, and M. Ouyang. "A review on the key issues for lithium-ion battery management in electric vehicles". In: *Journal of Power Sources*, vol. 226, no. 3 (2013), pp. 272–288. DOI: `10.1016/j.jpowsour.2012.10.060`.

[11] S. Abada, G. Marlair, A. Lecocq, M. Petit, V. Sauvant-Moynot, and F. Huet. "Safety focused modeling of lithium-ion batteries: A review". In: *Journal of Power Sources*, vol. 306 (2016), pp. 178–192. DOI: `10.1016/j.jpowsour.2015.11.100`.

[12] B. Balasingam, M. Ahmed, and K. Pattipati. "Battery Management Systems—Challenges and Some Solutions". In: *Energies*, vol. 13, no. 11, 2825 (2020). DOI: `10.3390/en13112825`.

[13] Y. Wu, S. Saxena, Y. Xing, Y. Wang, C. Li, W. Yung, and M. Pecht. "Analysis of Manufacturing-Induced Defects and Structural Deformations in Lithium-Ion Batteries Using Computed Tomography". In: *Energies*, vol. 11, no. 4, 925 (2018). DOI: `10.3390/en11040925`.

[14] A. R. M. Siddique, S. Mahmud, and B. van Heyst. "A comprehensive review on a passive (phase change materials) and an active (thermoelectric cooler) battery thermal management system and their limitations". In: *Journal of Power Sources*, vol. 401, no. 1 (2018), pp. 224–237. DOI: `10.1016/j.jpowsour.2018.08.094`.

[15] R. Xiong, S. Ma, H. Li, F. Sun, and J. Li. "Toward a Safer Battery Management System: A Critical Review on Diagnosis and Prognosis of Battery Short Circuit". In: *iScience*, vol. 23, no. 4, 101010 (2020). DOI: `10.1016/j.isci.2020.101010`.

[16] H. Rahimi-Eichi, U. Ojha, F. Baronti, and M.-Y. Chow. "Battery Management System: An Overview of Its Application in the Smart Grid and Electric Vehicles". In: *IEEE Industrial Electronics Magazine*, vol. 7, no. 2 (2013), pp. 4–16. DOI: `10.1109/MIE.2013.2250351`.

[17] B. P. Miller. "Automotive Lithium-Ion Batteries". In: *Johnson Matthey Technology Review*, vol. 59, no. 1 (2015), pp. 4–13. DOI: `10.1595/205651315X685445`.

[18] H. Dai, B. Jiang, X. Hu, X. Lin, X. Wei, and M. Pecht. "Advanced battery management strategies for a sustainable energy future: Multilayer design concepts and research trends". In: *Renewable and Sustainable Energy Reviews*, vol. 138, 110480 (2021). DOI: `10.1016/j.rser.2020.110480`.

[19] V. Reber. "New Possibilities with 800-Volt Charging". In: *Porsche Engineering MAGAZINE*, no. 1 (2016). Accessed on April 14, 2021, pp. 10–15. [Online]. URL: `https://www.porscheengineering.com/filestore/download/peg/en/pemagazin-01-2016-artikel-e-power/default/09d75d4f-3e8d-11e6-8697-0019999cd470/e-power-%C3%A2%E2%82%AC%E2%80%9C-New-Possibilities-with-800-Volt-Charging-Porsche-Engineering-Magazine-01-2016.pdf`.

[20] Y. Xing, E. W. M. Ma, K. L. Tsui, and M. Pecht. "Battery Management Systems in Electric and Hybrid Vehicles". In: *Energies*, vol. 4, no. 11 (2011), pp. 1840–1857. DOI: `10.3390/en4111840`.

[21] L. H. Saw, Y. Ye, and A. A. O. Tay. "Integration issues of lithium-ion battery into electric vehicles battery pack". In: *Journal of Cleaner Production*, vol. 113 (2016), pp. 1032–1045. DOI: `10.1016/j.jclepro.2015.11.011`.

[22] M. A. Hannan, M. S. H. Lipu, A. Hussain, and A. Mohamed. "A review of lithium-ion battery state of charge estimation and management system in electric vehicle applications: Challenges and recommendations". In: *Renewable and Sustainable Energy Reviews*, vol. 78 (2017), pp. 834–854. DOI: `10.1016/j.rser.2017.05.001`.

[23] O. Aiello. "Electromagnetic Susceptibility of Battery Management Systems' ICs for Electric Vehicles: Experimental Study". In: *Electronics*, vol. 9, no. 3, 510 (2020). DOI: `10.3390/electronics9030510`.

[24] A. Farmann and D. U. Sauer. "A comprehensive review of on-board State-of-Available-Power prediction techniques for lithium-ion batteries in electric vehicles". In: *Journal of Power Sources*, vol. 329 (2016), pp. 123–137. DOI: `10.1016/j.jpowsour.2016.08.031`.

[25] X. Lin, H. E. Perez, J. B. Siegel, and A. G. Stefanopoulou. "Robust Estimation of Battery System Temperature Distribution Under Sparse Sensing and Uncertainty". In: *IEEE Transactions on Control Systems Technology*, vol. 28, no. 3 (2020), pp. 753–765. DOI: `10.1109/TCST.2019.2892019`.

[26] M. Lelie, T. Braun, M. Knips, H. Nordmann, F. Ringbeck, H. Zappen, and D. Sauer. "Battery Management System Hardware Concepts: An Overview". In: *Applied Sciences*, vol. 8, no. 4, 534 (2018). DOI: `10.3390/app8040534`.

[27] L. H. J. Raijmakers, D. L. Danilov, J. P. M. van Lammeren, T. J. G. Lammers, H. J. Bergveld, and P. H. L. Notten. "Non-Zero Intercept Frequency: An Accurate Method to Determine the Integral Temperature of Li-Ion Batteries". In: *IEEE Transactions on Industrial Electronics*, vol. 63, no. 5 (2016), pp. 3168–3178. DOI: `10.1109/TIE.2016.2516961`.

[28] M. Ecker, P. S. Sabet, and D. U. Sauer. "Influence of operational condition on lithium plating for commercial lithium-ion batteries – Electrochemical experiments and post-mortem-analysis". In: *Applied Energy*, vol. 206, no. 9 (2017), pp. 934–946. DOI: `10.1016/j.apenergy.2017.08.034`.

[29] C. Forgez, D. Vinh Do, G. Friedrich, M. Morcrette, and C. Delacourt. "Thermal modeling of a cylindrical LiFePO4/graphite lithium-ion battery". In: *Journal of Power Sources*, vol. 195, no. 9 (2010), pp. 2961–2968. DOI: `10.1016/j.jpowsour.2009.10.105`.

[30] P. J. Osswald, M. d. Rosario, J. Garche, A. Jossen, and H. E. Hoster. "Fast and Accurate Measurement of Entropy Profiles of Commercial Lithium-Ion Cells". In: *Electrochimica Acta*, vol. 177 (2015), pp. 270–276. DOI: `10.1016/j.electacta.2015.01.191`.

[31] T. A. Vincent and J. Marco. "Development of Smart Battery Cell Monitoring System and Characterization on a Small-Module Through In-Vehicle Power Line Communication". In: *IEEE Access*, vol. 8 (2020), pp. 220658–220671. DOI: `10.1109/ACCESS.2020.3043657`.

[32] United Nations Economic Commission for Europe. "Global Technical Regulation on Electric Vehicle Safety (EVS)" (2018). Accessed on April 13, 2021. [Online]. URL: `https://unece.org/fileadmin/DAM/trans/main/wp29/wp29wgs/wp29gen/wp29r egistry/ECE-TRANS-180a20e.pdf`.

[33] E. Din, C. Schaef, K. Moffat, and J. T. Stauth. "A Scalable Active Battery Management System With Embedded Real-Time Electrochemical Impedance Spectroscopy". In: *IEEE Transactions on Power Electronics*, vol. 32, no. 7 (2017), pp. 5688–5698. DOI: `10.1109/TPEL.2016.2607519`.

[34] R. Koch and A. Jossen. "Impedance spectroscopy for battery monitoring with switched mode amplifiers". In: *2014 IEEE 16th International Power Electronics and Motion Control Conference and Exposition*. Antalya, Turkey, 2014, pp. 496–501. ISBN: 9781479920600. DOI: `10.1109/EPEPEMC.2014.6980542`.

[35] M. Abedi Varnosfaderani and D. Strickland. "A Comparison of Online Electrochemical Spectroscopy Impedance Estimation of Batteries". In: *IEEE Access*, vol. 6 (2018), pp. 23668–23677. DOI: `10.1109/ACCESS.2018.2808412`.

[36] M. Crescentini, A. de Angelis, R. Ramilli, G. de Angelis, M. Tartagni, A. Moschitta, P. A. Traverso, and P. Carbone. "Online EIS and Diagnostics on Lithium-Ion Batteries by Means of Low-Power Integrated Sensing and Parametric Modeling". In: *IEEE Transactions on Instrumentation and Measurement*, vol. 70 (2021), pp. 1–11. DOI: `10.1109/TIM.2020.3031185`.

[37] D. A. Howey, P. D. Mitcheson, V. Yufit, G. J. Offer, and N. P. Brandon. "Online Measurement of Battery Impedance Using Motor Controller Excitation". In: *IEEE Transactions on Vehicular Technology*, vol. 63, no. 6 (2014), pp. 2557–2566. DOI: `10.1109/TVT.2013.2293597`.

[38] D. Andre, M. Meiler, K. Steiner, C. Wimmer, T. Soczka-Guth, and D. U. Sauer. "Characterization of high-power lithium-ion batteries by electrochemical impedance spectroscopy. I. Experimental investigation". In: *Journal of Power Sources*, vol. 196, no. 12 (2011), pp. 5334–5341. DOI: `10.1016/j.jpowsour.2010.12.102`.

[39] W. Waag, S. Käbitz, and D. U. Sauer. "Experimental investigation of the lithium-ion battery impedance characteristic at various conditions and aging states and its influence on the application". In: *Applied Energy*, vol. 102 (2013), pp. 885–897. DOI: `10.1016/j.apenergy.2012.09.030`.

[40] R. Mingant, J. Bernard, V. Sauvant-Moynot, A. Delaille, S. Mailley, J.-L. Hognon, and F. Huet. "EIS Measurements for Determining the SoC and SoH of Li-Ion Batteries". In: *ECS Transactions*, vol. 33, no. 39 (2010), pp. 41–53. DOI: `10.1149/1.3589920`.

[41] A. Cuadras and O. Kanoun. "SoC Li-ion battery monitoring with impedance spectroscopy". In: *2009 6th International Multi-Conference on Systems, Signals and Devices*. Djerba, Tunisia, 2009, pp. 1–5. ISBN: 9781424443451. DOI: `10.1109/SSD.2009.4956761`.

[42] C. T. Love, M. B. V. Virji, R. E. Rocheleau, and K. E. Swider-Lyons. "State-of-health monitoring of 18650 4S packs with a single-point impedance diagnostic". In: *Journal of Power Sources*, vol. 266 (2014), pp. 512–519. DOI: `10.1016/j.jpowsour.2014.05.033`.

[43] S. F. Schuster, M. J. Brand, C. Campestrini, M. Gleissenberger, and A. Jossen. "Correlation between capacity and impedance of lithium-ion cells during calendar and cycle life". In: *Journal of Power Sources*, vol. 305 (2016), pp. 191–199. DOI: `10.1016/j.jpowsour.2015.11.096`.

[44] M. Kiel, D. U. Sauer, P. Turpin, M. Naveed, and E. Favre. "Validation of single frequency Z measurement for standby battery state of health determination". In: *INTELEC 2008 IEEE 30th International Telecommunications Energy Conference*. San Diego, CA, 2008, pp. 1–7. ISBN: 9781424420551. DOI: `10.1109/INTLEC.2008.4664020`.

[45] J. P. Schmidt, S. Arnold, A. Loges, D. Werner, T. Wetzel, and E. Ivers-Tiffée. "Measurement of the internal cell temperature via impedance: Evaluation and application of a new method". In: *Journal of Power Sources*, vol. 243 (2013), pp. 110–117. DOI: `10.1016/j.jpowsour.2013.06.013`.

[46] R. R. Richardson, P. T. Ireland, and D. A. Howey. "Battery internal temperature estimation by combined impedance and surface temperature measurement". In: *Journal of Power Sources*, vol. 265 (2014), pp. 254–261. DOI: `10.1016/j.jpowsour.2014.04.129`.

[47] L. H. J. Raijmakers, D. L. Danilov, J. P. M. van Lammeren, M. J. G. Lammers, and P. H. L. Notten. "Sensorless battery temperature measurements based on electrochemical impedance spectroscopy". In: *Journal of Power Sources*, vol. 247 (2014), pp. 539–544. DOI: `10.1016/j.jpowsour.2013.09.005`.

[48] L. Zhou, L. He, Y. Zheng, X. Lai, M. Ouyang, and L. Lu. "Massive battery pack data compression and reconstruction using a frequency division model in battery management systems". In: *Journal of Energy Storage*, vol. 28, 101252 (2020). DOI: `10.1016/j.est.2020.101252`.

[49] Y. Maryanka. "Wiring reduction by battery power line communication". In: *IEE Seminar on Passenger Car Electrical Architecture.* Birmingham, UK, 2000, pp. 8/1–8/4. DOI: `10.1049/ic:20000453`.

[50] A. M. Tonello, L. Lampe, and T. G. Swart (Eds.). *Power line communications: Principles, standards and applications from multimedia to smart grid.* Chichester, UK, Hoboken, NJ, USA: John Wiley & Sons, 2016. ISBN: 9781118676714.

[51] S. Carcangiu, A. Fanni, and A. Montisci. "Optimization of a Power Line Communication System to Manage Electric Vehicle Charging Stations in a Smart Grid". In: *Energies*, vol. 12, no. 9, 1767 (2019). DOI: `10.3390/en12091767`.

[52] P. Mlýnek, M. Rusz, L. Benešl, J. Sláčik, and P. Musil. "Possibilities of Broadband Power Line Communications for Smart Home and Smart Building Applications". In: *Sensors*, vol. 21, no. 1, 240 (2021). DOI: `10.3390/s21010240`.

[53] S. Barmada, M. Raugi, M. Tucci, Y. Maryanka, and O. Amrani. "PLC systems for electric vehicles and Smart Grid applications". In: *2013 IEEE 17th International Symposium on Power Line Communications and Its Applications.* Johannesburg, 2013, pp. 23–28. ISBN: 9781467360166. DOI: `10.1109/ISPLC.2013.6525819`.

[54] T. F. Landinger, G. Schwarzberger, G. Hofer, M. Rose, and A. Jossen. "Power Line Communications for Automotive High Voltage Battery Systems: Channel Modeling and Coexistence Study with Battery Monitoring". In: *Energies*, vol. 14, no. 7, 1851 (2021). DOI: `10.3390/en14071851`.

[55] P. Brinda and P. Usha Rani. "A Comprehensive View on Information Metering, Monitoring and Measurement of a Smartgrid". In: *IOP Conference Series: Materials Science and Engineering*, vol. 1070, no. 1, 12092 (2021). DOI: `10.1088/1757-899X/1070/1/012092`.

[56] A. Pittolo, M. de Piante, F. Versolatto, and A. M. Tonello. "In-Vehicle Power Line Communication: Differences and Similarities Among the In-Car and the In-Ship Scenarios". In: *IEEE Vehicular Technology Magazine*, vol. 11, no. 2 (2016), pp. 43–51. DOI: `10.1109/MVT.2015.2480098`.

[57] I. Ouannes, P. Nickel, and K. Dostert. "Cell-wise monitoring of Lithium-ion batteries for automotive traction applications by using power line communication: battery modeling and channel characterization". In: *2014 18th IEEE International Symposium on Power Line Communications and Its Applications (ISPLC)*. Glasgow, United Kingdom, 2014, pp. 24–29. ISBN: 9781479949809. DOI: `10.1109/ISPLC.2014.6812322`.

[58] O. Opalko. *Powerline-Kommunikation für Batteriemanagement-Systeme in Elektro- und Hybridfahrzeugen*. Dissertation. Karlsruhe, Germany: KIT Scientific Publishing, 2017. ISBN: 9783731506478.

[59] A. Pake Talei, W. A. Pribyl, and G. Hofer. "Considerations for a power line communication system for traction batteries". In: *e & i Elektrotechnik und Informationstechnik*, vol. 138 (2021), pp. 3–14. DOI: `10.1007/s00502-020-00861-2`.

[60] C. Bolsinger, J. Brix, M. Dragan, and K. P. Birke. "Investigating and modeling the transmission channel of a prismatic lithium-ion cell and module for powerline communication". In: *Journal of Energy Storage*, vol. 10 (2017), pp. 11–19. DOI: `10.1016/j.est.2016.12.001`.

[61] A. Scherer. "A Smart Battery Management System for Electric Vehicles using Powerline Communication". Master's thesis. Munich: Technical University of Munich, 2013. Accessed on April 20, 2021. [Online]. URL: `https://robotics.ee.uwa.edu.au/theses/2013-REV-BMS-Scherer.pdf`.

[62] A. Schiffer. "Entwurf und Bewertung eines Systems zur Datenübertragung mittels der Energieversorgungsleitungen im Kraftfahrzeug". Dissertation. Munich: Technical University of Munich, 2001. Accessed on August 25, 2021. [Online]. URL: `https://mediatum.ub.tum.de/601518`.

[63] A. Pake Talei, W. A. Pribyl, and G. Hofer. "Electric Vehicle Battery Management System Using Power Line Communication Technique". In: *2018 IEEE 14th Conference on Ph.D. Research in Microelectronics and Electronics (PRIME)*. Prague, Czech Republic, 2018, pp. 225–228. ISBN: 9781538653876. DOI: `10.1109/PRIME.2018.8430304`.

[64] M. Takanashi, T. Harada, A. Takahashi, H. Tanaka, H. Hayashi, and Y. Hattori. "High-voltage power line communication system for hybrid vehicle". In: *2015 IEEE International Symposium on Power Line Communications and Its Applications (ISPLC)*. Austin, TX, USA, 2015, pp. 222–227. ISBN: 9781479984138. DOI: `10.1109/ISPLC.2015.7147618`.

[65] O. Opalko, B. Simon, D. Alonso, and K. Dostert. "Physical layer and multi-carrier analysis for power line communication networks in Li-ion batteries for electric and hybrid vehicles". In: *2015 IEEE Vehicular Networking Conference (VNC)*. Kyoto, Japan, 2015, pp. 243–250. ISBN: 9781467394116. DOI: `10.1109/VNC.2015.7385583`.

[66] P. Weicker. *A systems approach to lithium-ion battery management*. Norwood, MA, USA: Artech House, 2014. ISBN: 9781608076598.

[67] H. Dai, B. Jiang, and X. Wei. "Impedance Characterization and Modeling of Lithium-Ion Batteries Considering the Internal Temperature Gradient". In: *Energies*, vol. 11, no. 1, 220 (2018). DOI: `10.3390/en11010220`.

[68] J. Illig, J. P. Schmidt, M. Weiss, A. Weber, and E. Ivers-Tiffée. "Understanding the impedance spectrum of 18650 LiFePO4-cells". In: *Journal of Power Sources*, vol. 239 (2013), pp. 670–679. DOI: `10.1016/j.jpowsour.2012.12.020`.

[69] S. Schindler and M. A. Danzer. "Influence of cell design on impedance characteristics of cylindrical lithium-ion cells: A model-based assessment from electrode to cell level". In: *Journal of Energy Storage*, vol. 12 (2017), pp. 157–166. DOI: `10.1016/j.est.2017.05.002`.

[70] H. Beelen, K. M. Shivakumar, L. H. J. Raijmakers, M. C. F. Donkers, and H. J. Bergveld. "Towards impedance-based temperature estimation for Li-ion battery packs". In: *International Journal of Energy Research*, vol. 44, no. 4 (2020), pp. 2889–2908. DOI: `10.1002/er.5107`.

[71] M. Park, X. Zhang, M. Chung, G. B. Less, and A. M. Sastry. "A review of conduction phenomena in Li-ion batteries". In: *Journal of Power Sources*, vol. 195, no. 24 (2010), pp. 7904–7929. DOI: `10.1016/j.jpowsour.2010.06.060`.

[72] P. J. Osswald, S. V. Erhard, A. Noel, P. Keil, F. M. Kindermann, H. Hoster, and A. Jossen. "Current density distribution in cylindrical Li-Ion cells during impedance measurements". In: *Journal of Power Sources*, vol. 314 (2016), pp. 93–101. DOI: `10.1016/j.jpowsour.2016.02.070`.

[73] T. F. Landinger, G. Schwarzberger, and A. Jossen. "High frequency impedance characteristics of cylindrical lithium-ion cells: Physical-based modeling of cell state and cell design dependencies". In: *Journal of Power Sources*, vol. 488, 229463 (2021). DOI: `10.1016/j.jpowsour.2021.229463`.

[74] M. J. Brand. *Lithium-ion battery cells and systems under dynamic electric loads*. Dissertation. Munich, Germany: Herbert Utz Verlag GmbH, 2018. ISBN: 9783831647526.

[75] A. Jossen. "Fundamentals of battery dynamics". In: *Journal of Power Sources*, vol. 154, no. 2 (2006), pp. 530–538. DOI: `10.1016/j.jpowsour.2005.10.041`.

[76] M. A. Danzer. "Generalized Distribution of Relaxation Times Analysis for the Characterization of Impedance Spectra". In: *Batteries*, vol. 5, no. 3, 53 (2019). DOI: `10.3390/batteries5030053`.

[77] O. Heaviside. *Electrical Papers: Volume 1*. Cambridge: Cambridge University Press, 1892. ISBN: 9781108028561.

[78] C. H. Hamann, A. Hamnett, and W. Vielstich. *Electrochemistry*. 2nd ed. Weinheim, Germany: Wiley-VCH, 2007. ISBN: 9783527310692.

[79] V. S. Bagotsky. *Fundamentals of electrochemistry*. 2nd ed. Hoboken, NJ, USA: John Wiley and Sons, 2006. ISBN: 9780471700586.

[80] J. Newman and K. E. Thomas-Alyea. *Electrochemical Systems*. 3rd ed. Hoboken, NJ, USA: John Wiley & Sons, 2004. ISBN: 9780471477567.

[81] D. Linden and T. B. Reddy (Eds.). *Handbook of batteries*. 3rd ed. New York, NY, USA: McGraw-Hill, 2002. ISBN: 9780071359788.

[82] A. Jossen and W. Weydanz. *Moderne Akkumulatoren richtig einsetzen.* 2nd ed. Goettingen, Germany: MatrixMedia, 2019. ISBN: 9783946891185.

[83] P. Iurilli, C. Brivio, and V. Wood. "On the use of electrochemical impedance spectroscopy to characterize and model the aging phenomena of lithium-ion batteries: a critical review". In: *Journal of Power Sources*, vol. 505, 229860 (2021). DOI: `10.1016/j.jpowsour.2021.229860`.

[84] N. Meddings, M. Heinrich, F. Overney, J.-S. Lee, V. Ruiz, E. Napolitano, S. Seitz, G. Hinds, R. Raccichini, M. Gaberšček, and J. Park. "Application of electrochemical impedance spectroscopy to commercial Li-ion cells: A review". In: *Journal of Power Sources*, vol. 480, 228742 (2020). DOI: `10.1016/j.jpowsour.2020.228742`.

[85] E. Barsoukov and J. R. Macdonald. *Impedance Spectroscopy.* Hoboken, NJ, USA: John Wiley & Sons, 2018. ISBN: 9781119381860.

[86] P. Delahay. *Double-layer and electrode kinetics.* London, New York: Interscience Publishers, a Division of John Wiley & Sons, 1965. ISBN: 9780608101996.

[87] S. Buller. *Impedance based simulation models for energy storage devices in advanced automotive power systems.* Dissertation. Aachen, Germany: Shaker, 2003. ISBN: 9783832212254.

[88] Z. Kerner and T. Pajkossy. "On the origin of capacitance dispersion of rough electrodes". In: *Electrochimica Acta*, vol. 46, 2-3 (2000), pp. 207–211. DOI: `10.1016/S0013-4686(00)00574-0`.

[89] M. Petzl, M. Kasper, and M. A. Danzer. "Lithium plating in a commercial lithium-ion battery - A low-temperature aging study". In: *Journal of Power Sources*, vol. 275 (2015), pp. 799–807. DOI: `10.1016/j.jpowsour.2014.11.065`.

[90] J.-A. Choi, S. H. Kim, and D.-W. Kim. "Enhancement of thermal stability and cycling performance in lithium-ion cells through the use of ceramic-coated separators". In: *Journal of Power Sources*, vol. 195, no. 18 (2010), pp. 6192–6196. DOI: `10.1016/j.jpowsour.2009.11.020`.

[91] Y. Xie, H. Zou, H. Xiang, R. Xia, D. Liang, P. Shi, S. Dai, and H. Wang. "Enhancement on the wettability of lithium battery separator toward nonaqueous electrolytes". In: *Journal of Membrane Science*, vol. 503 (2016), pp. 25–30. DOI: `10.1016/j.memsci.2015.12.025`.

[92] M. Brand, S. Glaser, J. Geder, S. Menacher, S. Obpacher, A. Jossen, and D. Quinger. "Electrical safety of commercial Li-ion cells based on NMC and NCA technology compared to LFP technology". In: *2013 World Electric Vehicle Symposium and Exhibition (EVS27).* Barcelona, Spain, 2013, pp. 1–9. ISBN: 9781479938322. DOI: `10.1109/EVS.2013.6914893`.

[93] S. J. An, J. Li, C. Daniel, D. Mohanty, S. Nagpure, and D. L. Wood. "The state of understanding of the lithium-ion-battery graphite solid electrolyte interphase (SEI) and its relationship to formation cycling". In: *Carbon*, vol. 105, no. 4 (2016), pp. 52–76. DOI: `10.1016/j.carbon.2016.04.008`.

[94] J. Vetter, P. Novák, M. R. Wagner, C. Veit, K.-C. Möller, J. O. Besenhard, M. Winter, M. Wohlfahrt-Mehrens, C. Vogler, and A. Hammouche. "Ageing mechanisms in lithium-ion batteries". In: *Journal of Power Sources*, vol. 147, 1-2 (2005), pp. 269–281. DOI: `10.1016/j.jpowsour.2005.01.006`.

[95] M. J. Armstrong, C. O'Dwyer, W. J. Macklin, and J. D. Holmes. "Evaluating the performance of nanostructured materials as lithium-ion battery electrodes". In: *Nano Research*, vol. 7, no. 1 (2014), pp. 1–62. DOI: `10.1007/s12274-013-0375-x`.

[96] F. Kindermann. "Implications of Current Density Distribution in Lithium-Ion Battery Graphite Anodes on SEI Formation". Dissertation. Munich: Technical University of Munich, 2017. Accessed on August 25, 2021. [Online]. URL: `https://mediatum.ub.tum.de/1380608`.

[97] A. Patil, V. Patil, D. Wook Shin, J.-W. Choi, D.-S. Paik, and S.-J. Yoon. "Issue and challenges facing rechargeable thin film lithium batteries". In: *Materials Research Bulletin*, vol. 43, 8-9 (2008), pp. 1913–1942. DOI: `10.1016/j.materresbull.2007.08.031`.

[98] V. A. Agubra and J. W. Fergus. "The formation and stability of the solid electrolyte interface on the graphite anode". In: *Journal of Power Sources*, vol. 268, no. 8 (2014), pp. 153–162. DOI: `10.1016/j.jpowsour.2014.06.024`.

[99] J. M. Tarascon. "The Li-Ion Battery: 25 Years of Exciting and Enriching Experiences". In: *Interface magazine*, vol. 25, no. 3 (2016), pp. 79–83. DOI: `10.1149/2.F08163if`.

[100] K. Edström, T. Gustafsson, and J. O. Thomas. "The cathode–electrolyte interface in the Li-ion battery". In: *Electrochimica Acta*, vol. 50, 2-3 (2004), pp. 397–403. DOI: `10.1016/j.electacta.2004.03.049`.

[101] C. Daniel and J. O. Besenhard. *Handbook of Battery Materials*. Weinheim, Germany: Wiley-VCH, 2011. ISBN: 9783527637188.

[102] K. Smith and C.-Y. Wang. "Solid-state diffusion limitations on pulse operation of a lithium ion cell for hybrid electric vehicles". In: *Journal of Power Sources*, vol. 161, no. 1 (2006), pp. 628–639. DOI: `10.1016/j.jpowsour.2006.03.050`.

[103] A. Fick. "V. On liquid diffusion". In: *The London, Edinburgh, and Dublin Philosophical Magazine and Journal of Science*, vol. 10, no. 63 (1855), pp. 30–39. DOI: `10.1080/14786445508641925`.

[104] E. Warburg. "Ueber die Spitzenentladung". In: *Annalen der Physik*, vol. 303, no. 1 (1899), pp. 69–83. DOI: `10.1002/andp.18993030104`.

[105] T. J. Heil. "Ersatzschaltbild-basierte Modellierung der Diffusion und des Ladungsdurchtritts in Lithium-Ionen-Zellen". Dissertation. Munich: Technical University of Munich, 2021. Accessed on July 27, 2021. [Online]. URL: `https://mediatum.ub.tum.de/?id=1575045`.

[106] B. A. Boukamp. "Derivation of a Distribution Function of Relaxation Times for the (fractal) Finite Length Warburg". In: *Electrochimica Acta*, vol. 252 (2017), pp. 154–163. DOI: `10.1016/j.electacta.2017.08.154`.

[107] S. Buller, M. Thele, R. W. De Doncker, and E. Karden. "Impedance-Based Simulation Models of Supercapacitors and Li-Ion Batteries for Power Electronic Applications". In: *IEEE Transactions on Industry Applications*, vol. 41, no. 3 (2005), pp. 742–747. DOI: `10.1109/TIA.2005.847280`.

[108] M. Oldenburger, B. Bedürftig, A. Gruhle, F. Grimsmann, E. Richter, R. Findeisen, and A. Hintennach. "Investigation of the low frequency Warburg impedance of Li-ion cells by frequency domain measurements". In: *Journal of Energy Storage*, vol. 21, no. 12 (2019), pp. 272–280. DOI: `10.1016/j.est.2018.11.029`.

[109] C. Ho, I. D. Raistrick, and R. A. Huggins. "Application of A-C Techniques to the Study of Lithium Diffusion in Tungsten Trioxide Thin Films". In: *Journal of The Electrochemical Society*, vol. 127, no. 2 (1980), pp. 343–350. DOI: `10.1149/1.2129668`.

[110] P. L. Moss, G. Au, E. J. Plichta, and J. P. Zheng. "An Electrical Circuit for Modeling the Dynamic Response of Li-Ion Polymer Batteries". In: *Journal of The Electrochemical Society*, vol. 155, no. 12, A986 (2008). DOI: `10.1149/1.2999375`.

[111] S. Gantenbein, M. Weiss, and E. Ivers-Tiffée. "Impedance based time-domain modeling of lithium-ion batteries: Part I". In: *Journal of Power Sources*, vol. 379 (2018), pp. 317–327. DOI: `10.1016/j.jpowsour.2018.01.043`.

[112] R. Koch. "On-line Electrochemical Impedance Spectroscopy for Lithium-Ion Battery Systems". Dissertation. Munich: Technical University of Munich, 2017. Accessed on July 27, 2021. [Online]. URL: `https://mediatum.ub.tum.de/1343447`.

[113] S. Ludwig, I. Zilberman, M. F. Horsche, T. Wohlers, and A. Jossen. "Pulse resistance based online temperature estimation for lithium-ion cells". In: *Journal of Power Sources*, vol. 490, 229523 (2021). DOI: `10.1016/j.jpowsour.2021.229523`.

[114] A. Barai, K. Uddin, W. D. Widanage, A. McGordon, and P. Jennings. "A study of the influence of measurement timescale on internal resistance characterisation methodologies for lithium-ion cells". In: *Scientific reports*, vol. 8, no. 1, 21 (2018). DOI: `10.1038/s41598-017-18424-5`.

[115] M. Mathew, S. Janhunen, M. Rashid, F. Long, and M. Fowler. "Comparative Analysis of Lithium-Ion Battery Resistance Estimation Techniques for Battery Management Systems". In: *Energies*, vol. 11, no. 6, 1490 (2018). DOI: `10.3390/en11061490`.

[116] A. Lievre, A. Sari, P. Venet, A. Hijazi, M. Ouattara-Brigaudet, and S. Pelissier. "Practical Online Estimation of Lithium-Ion Battery Apparent Series Resistance for Mild Hybrid Vehicles". In: *IEEE Transactions on Vehicular Technology*, vol. 65, no. 6 (2016), pp. 4505–4511. DOI: `10.1109/TVT.2015.2446333`.

[117] G. Giordano, V. Klass, M. Behm, G. Lindbergh, and J. Sjoberg. "Model-Based Lithium-Ion Battery Resistance Estimation From Electric Vehicle Operating Data". In: *IEEE Transactions on Vehicular Technology*, vol. 67, no. 5 (2018), pp. 3720–3728. DOI: `10.1109/TVT.2018.2796723`.

[118] P. Keil. "Aging of Lithium-Ion Batteries in Electric Vehicles". Dissertation. Munich: Technical University of Munich, 2017. Accessed on July 27, 2021. [Online]. URL: `https://mediatum.ub.tum.de/1355829`.

[119] L. Deleebeeck and S. Veltzé. "Electrochemical impedance spectroscopy study of commercial Li-ion phosphate batteries: A metrology perspective". In: *International Journal of Energy Research*, vol. 44, no. 9 (2020), pp. 7158–7182. DOI: `10.1002/er.5350`.

[120] D. Klotz, M. Schönleber, J. P. Schmidt, and E. Ivers-Tiffée. "New approach for the calculation of impedance spectra out of time domain data". In: *Electrochimica Acta*, vol. 56, no. 24 (2011), pp. 8763–8769. DOI: `10.1016/j.electacta.2011.07.096`.

[121] P. Keil and A. Jossen. "Aufbau und Parametrierung von Batteriemodellen". In: *9. DESIGN&ELEKTRONIK-Entwicklerforum Batterien & Ladekonzepte, 2012.* Accessed on August 25, 2021 [Online]. URL: `https://mediatum.ub.tum.de/doc/1162416/1162416.pdf`.

[122] J. E. B. Randles. "Kinetics of rapid electrode reactions". In: *Discussions of the Faraday Society*, vol. 1 (1947), pp. 11–19. DOI: `10.1039/df9470100011`.

[123] D. Andrea. *Battery management systems for large lithium-ion battery packs.* Boston, MA, USA: Artech House, 2010. ISBN: 9781608071043.

[124] R. Dorn, R. Schwartz, and B. Steurich. "Battery management system". In: *Lithium-Ion Batteries: Basics and Applications*, R. Korthauer (Ed.). Berlin, Heidelberg: Springer-Verlag, 2018, pp. 165–175. ISBN: 9783662530696. DOI: `10.1007/978-3-662-53071-9_14`.

[125] G. Plett. *Battery Management Systems, Volume I.* Norwood, MA, USA: Artech House, 2015. ISBN: 9781630810245.

[126] B. Pattipati, B. Balasingam, G. V. Avvari, K. R. Pattipati, and Y. Bar-Shalom. "Open circuit voltage characterization of lithium-ion batteries". In: *Journal of Power Sources*, vol. 269, no. 3 (2014), pp. 317–333. DOI: `10.1016/j.jpowsour.2014.06.152`.

[127] C. Fleischer, W. Waag, H.-M. Heyn, and D. U. Sauer. "On-line adaptive battery impedance parameter and state estimation considering physical principles in reduced order equivalent circuit battery models". In: *Journal of Power Sources*, vol. 260 (2014), pp. 276–291. DOI: `10.1016/j.jpowsour.2014.01.129`.

[128] B. Liebhart, L. Komsiyska, and C. Endisch. "Passive impedance spectroscopy for monitoring lithium-ion battery cells during vehicle operation". In: *Journal of Power Sources*, vol. 449, 227297 (2020). DOI: `10.1016/j.jpowsour.2019.227297`.

[129] U. Tröltzsch, O. Kanoun, and H.-R. Tränkler. "Characterizing aging effects of lithium ion batteries by impedance spectroscopy". In: *Electrochimica Acta*, vol. 51, 8-9 (2006), pp. 1664–1672. DOI: `10.1016/j.electacta.2005.02.148`.

[130] M. Urquidi-Macdonald, S. Real, and D. D. Macdonald. "Applications of Kramers—Kronig transforms in the analysis of electrochemical impedance data—III. Stability and linearity". In:

Electrochimica Acta, vol. 35, no. 10 (1990), pp. 1559–1566. DOI: `10.1016/0013-4686(90)80010-L`.

[131] X. Wang, X. Wei, Q. Chen, J. Zhu, and H. Dai. "Lithium-ion battery temperature on-line estimation based on fast impedance calculation". In: *Journal of Energy Storage*, vol. 26, 100952 (2019). DOI: `10.1016/j.est.2019.100952`.

[132] H. Zappen, F. Ringbeck, and D. Sauer. "Application of Time-Resolved Multi-Sine Impedance Spectroscopy for Lithium-Ion Battery Characterization". In: *Batteries*, vol. 4, no. 4, 64 (2018). DOI: `10.3390/batteries4040064`.

[133] A. Tomaszewska, Z. Chu, X. Feng, S. O'Kane, X. Liu, J. Chen, C. Ji, E. Endler, R. Li, L. Liu, Y. Li, S. Zheng, S. Vetterlein, M. Gao, J. Du, M. Parkes, M. Ouyang, M. Marinescu, G. Offer, and B. Wu. "Lithium-ion battery fast charging: A review". In: *eTransportation*, vol. 1, 100011 (2019). DOI: `10.1016/j.etran.2019.100011`.

[134] C. Lyu, T. Zhang, W. Luo, G. Wei, B. Ma, and L. Wang. "SOH Estimation of Lithium-ion Batteries Based on Fast Time Domain Impedance Spectroscopy". In: *2019 14th IEEE Conference on Industrial Electronics and Applications (ICIEA)*. Xi'an, China, 2019, pp. 2142–2147. ISBN: 9781538694909. DOI: `10.1109/ICIEA.2019.8834119`.

[135] E. Locorotondo, S. Scavuzzo, L. Pugi, A. Ferraris, L. Berzi, A. Airale, M. Pierini, and M. Carello. "Electrochemical Impedance Spectroscopy of Li-Ion battery on-board the Electric Vehicles based on Fast nonparametric identification method". In: *2019 IEEE International Conference on Environment and Electrical Engineering and 2019 IEEE Industrial and Commercial Power Systems Europe (EEEIC / I&CPS Europe)*. Genoa, Italy, 2019, pp. 1–6. ISBN: 9781728106533. DOI: `10.1109/EEEIC.2019.8783625`.

[136] J. Sihvo, T. Messo, T. Roinila, and R. Luhtala. "Online Internal Impedance Measurements of Li-ion Battery Using PRBS Broadband Excitation and Fourier Techniques: Methods and Injection Design". In: *2018 International Power Electronics Conference*. Niigata, Japan, 2018, pp. 2470–2475. ISBN: 9784886864055. DOI: `10.23919/IPEC.2018.8507565`.

[137] J. P. Christophersen, C. G. Motloch, J. L. Morrison, I. B. Donnellan, and W. H. Morrison. "Impedance Noise Identification for State-of-Health Prognostics". In: *43rd Power Sources Conference*. Philadelphia, PA, USA, INL/CON-08-14101, 2008. Accessed on August 25, 2021. [Online]. URL: `https://www.osti.gov/biblio/936627`.

[138] K. Godfrey (Ed.). *Perturbation signals for system identification*. New York, NY, USA: Prentice Hall, 1993. ISBN: 9780136564140.

[139] T. Roinila and T. Messo. "Online Grid-Impedance Measurement Using Ternary-Sequence Injection". In: *IEEE Transactions on Industry Applications*, vol. 54, no. 5 (2018), pp. 5097–5103. DOI: `10.1109/TIA.2018.2825938`.

[140] J. Sihvo, T. Messo, T. Roinila, R. Luhtala, and D. I. Stroe. "Online identification of internal impedance of Li-ion battery cell using ternary-sequence injection". In: *2018 IEEE Energy Conversion Congress and Exposition (ECCE)*. Portland, OR, USA, 2018, pp. 2705–2711. ISBN: 9781479973125. DOI: `10.1109/ECCE.2018.8558147`.

[141] K. Takano, K. Nozaki, Y. Saito, K. Kato, and A. Negishi. "Impedance Spectroscopy by Voltage-Step Chronoamperometry Using the Laplace Transform Method in a Lithium-Ion Battery". In: *Journal of The Electrochemical Society*, vol. 147, no. 3, 922 (2000). DOI: `10.1149/1.1393293`.

[142] R. Mingant, J. Bernard, and V. Sauvant-Moynot. "Novel state-of-health diagnostic method for Li-ion battery in service". In: *Applied Energy*, vol. 183, no. 8 (2016), pp. 390–398. DOI: `10.1016/j.apenergy.2016.08.118`.

[143] R. Koch and A. Jossen. "Speed Optimized Multisine Stimuli for Electrochemical Impedance Spectroscopy with a Switched Mode Excitation". In: *2014 IEEE Vehicle Power and Propulsion Conference (VPPC)*. Coimbra, Portugal, 2014, pp. 1–6. ISBN: 9781479967834. DOI: `10.1109/VPPC.2014.7007135`.

[144] J. P. Schmidt and E. Ivers-Tiffée. "Pulse-fitting – A novel method for the evaluation of pulse measurements, demonstrated for the low frequency behavior of lithium-ion cells". In: *Journal of Power Sources*, vol. 315 (2016), pp. 316–323. DOI: `10.1016/j.jpowsour.2016.03.026`.

[145] B.-Y. Chang and S.-M. Park. "Electrochemical impedance spectroscopy". In: *Annual review of analytical chemistry*, vol. 3 (2010), pp. 207–229. DOI: `10.1146/annurev.anchem.012809.102211`.

[146] Y. Hoshi, N. Yakabe, K. Isobe, T. Saito, I. Shitanda, and M. Itagaki. "Wavelet transformation to determine impedance spectra of lithium-ion rechargeable battery". In: *Journal of Power Sources*, vol. 315 (2016), pp. 351–358. DOI: `10.1016/j.jpowsour.2016.03.048`.

[147] D. Depernet, O. Ba, and A. Berthon. "Online impedance spectroscopy of lead acid batteries for storage management of a standalone power plant". In: *Journal of Power Sources*, vol. 219, no. 2 (2012), pp. 65–74. DOI: `10.1016/j.jpowsour.2012.07.053`.

[148] X. Wei, X. Wang, and H. Dai. "Practical On-Board Measurement of Lithium Ion Battery Impedance Based on Distributed Voltage and Current Sampling". In: *Energies*, vol. 11, no. 1, 64 (2018). DOI: `10.3390/en11010064`.

[149] R. Koch, C. Riebel, and A. Jossen. "On-line electrochemical impedance spectroscopy implementation for telecommunication power supplies". In: *2015 IEEE International Telecommunications Energy Conference (INTELEC)*. Osaka, Japan, 2015, pp. 1–6. ISBN: 9781479965823. DOI: `10.1109/INTLEC.2015.7572384`.

[150] T. Serni, E. Locorotondo, L. Pugi, L. Berzi, M. Pierini, and V. Cultrera. "A Low Cost Programmable Hardware for Online Spectroscopy of Lithium Batteries". In: *2020 IEEE 20th Mediterranean Electrotechnical Conference (MELECON)*. Palermo, Italy, 2020, pp. 57–62. ISBN: 9781728152004. DOI: `10.1109/MELECON48756.2020.9140641`.

[151] N. Lohmann, P. Haussmann, P. Wesskamp, J. Melbert, and T. Musch. "Employing Real Automotive Driving Data for Electrochemical Impedance Spectroscopy on Lithium-Ion Cells". In: *SAE International Journal of Alternative Powertrains*, vol. 4, no. 2 (2015), pp. 308–317. DOI: `10.4271/2015-01-1187`.

[152] A. Karger, L. Wildfeuer, A. Maheshwari, N. Wassiliadis, and M. Lienkamp. "Novel method for the on-line estimation of low-frequency impedance of lithium-ion batteries". In: *Journal of Energy Storage*, vol. 32, 101818 (2020). DOI: `10.1016/j.est.2020.101818`.

[153] O. Bohlen. "Impedance based battery monitoring". Dissertation. Aachen: RWTH Aachen University, 2008. Accessed on August 25, 2021. [Online]. URL: `http://publications.rwth-aachen.de/record/50539`.

[154] W. Waag, S. Käbitz, and D. U. Sauer. "Application-specific parameterization of reduced order equivalent circuit battery models for improved accuracy at dynamic load". In: *Measurement*, vol. 46, no. 10 (2013), pp. 4085–4093. DOI: `10.1016/j.measurement.2013.07.025`.

[155] Keysight Technologies, Inc. "Ultra-Low Impedance Measurements Using 2-Port Measurements". Santa Rosa, CA, USA, Application Note 5989-5935EN, 2014. Accessed on August 25, 2021. [Online]. URL: `https://www.keysight.com/de/de/assets/7018-08474/application-notes/5989-5935.pdf`.

[156] X. Wang, X. Wei, H. Dai, and Q. Wu. "State Estimation of Lithium Ion Battery Based on Electrochemical Impedance Spectroscopy with On-Board Impedance Measurement System". In: *2015 IEEE Vehicle Power and Propulsion Conference (VPPC)*. Montreal, QC, Canada, 2015, pp. 1–5. ISBN: 9781467376372. DOI: `10.1109/VPPC.2015.7353021`.

[157] S. Guttowski, S. Weber, E. Hoene, W. John, and H. Reichl. "EMC issues in cars with electric drives". In: *2003 IEEE Symposium on Electromagnetic Compatibility. Symposium Record (Cat. No.03CH37446)*. Boston, MA, USA, 2003, pp. 777–782, vol. 2. ISBN: 9780780378350. DOI: `10.1109/ISEMC.2003.1236706`.

[158] T. F. Landinger, S. Mikl, F. Rasras, G. Hofer, G. Schwarzberger, M. Rose, and A. Jossen. "Interference Scenarios during Single Cell Impedance Measurements in Automotive Battery Packs". In: *Kraftwerk Batterie 2021*. Accessed on July 6, 2021. [Online]. URL: `https://battery-power.eu/wp-content/uploads/2021/04/Landinger-2021-Interference-Scenarios-during-Single-Cell-Impedance-Measurements.pdf`.

[159] K. Williston (Ed.). *Digital Signal Processing: World Class Designs*. 1st ed. Burlington, MA, USA: Elsevier, 2009. ISBN: 9780080950822.

[160] L. H. J. Raijmakers, K. M. Shivakumar, M. C . F. Donkers, M. J. G. Lammers, and H. J. Bergveld. "Crosstalk Interferences on Impedance Measurements in Battery Packs". In: *IFAC-PapersOnLine*, vol. 49, no. 11 (2016), pp. 42–47. DOI: `10.1016/j.ifacol.2016.08.007`.

[161] D. E. Alonso. *Wireless Data Transmission for the Battery Management System of Electric and Hybrid Vehicles*. Dissertation. Karlsruhe, Germany: KIT Scientific Publishing, 2017. ISBN: 9783731506706

[162] A. Hauser and R. Kuhn. "High-voltage battery management systems (BMS) for electric vehicles". In: *Advances in Battery Technologies for Electric Vehicles*: Elsevier, 2015, pp. 265–282.

[163] H. J. Hong, J. R. Sevillano, C. Kain, G. Hofer, K. Felber, and W. K. Chan. "Alternatives in Battery Communication Protocols". In: *SAE Technical Paper Series*, vol. 1, 1212 (2017). DOI: `10.4271/2017-01-1212`.

[164] J. Douglass. "Battery management architectures for hybrid/electric vehicles". In: *Electronic Prodict Design*, March (2009). [Online]. URL: `https://www.analog.com/media/en/technical-documentation/technical-articles/epd_march_2009-battery_management_architectures_for_hybrid-electric_vehicles.pdf`.

[165] Robert Bosch GmbH. "CAN Specification: Version 2.0". Stuttgart, Germany: 1991.

[166] M. Zheng, B. Qi, and H. Wu. "A Li-ion battery management system based on CAN-bus for electric vehicle". In: *2008 3rd IEEE Conference on Industrial Electronics and Applications.* Singapore, 2008, pp. 1180–1184. ISBN: 9781424417179. DOI: `10.1109/ICIEA.2008.4582704`.

[167] R. Xiong and W. Shen. *Advanced battery management technologies for electric vehicles.* Hoboken, NJ, USA: John Wiley & Sons, 2018. ISBN: 9781119481645.

[168] M. Brandl, H. Gall, M. Wenger, V. Lorentz, M. Giegerich, F. Baronti, G. Fantechi, L. Fanucci, R. Roncella, R. Saletti, S. Saponara, A. Thaler, M. Cifrain, and W. Prochazka. "Batteries and battery management systems for electric vehicles". In: *2012 Design, Automation & Test in Europe Conference & Exhibition (DATE).* Dresden, Germany, 2012, pp. 971–976. ISBN: 9781457721458. DOI: `10.1109/DATE.2012.6176637`.

[169] Infineon Technologies AG. "TLE9012AQU: Li-Ion Battery Monitoring and Balancing IC". Datasheet, 2020. Accessed on July 9, 2021. [Online]. URL: `https://www.infineon.com/dgdl/Infineon-TLE9012AQU-DataSheet-v01_00-EN.pdf?fileId=5546d46272aa54c00172e07a3ba42ef3`.

[170] Maxim Integrated, Corp. "MAX11068: 12-Channel, High-Voltage Sensor, Smart Data-Acquisition Interface". Datasheet, 2020. Accessed on July 9, 2021. [Online]. URL: `https://datasheets.maximintegrated.com/en/ds/MAX11068.pdf`.

[171] Texas Instruments, Corp. "bq76PL536A-Q1 3-to-6 Series Cell Lithium-Ion Battery Monitor and Secondary Protection IC for EV and HEV Applications". Datasheet, 2016. Accessed on July 9, 2021. [Online]. URL: `https://www.ti.com/lit/ds/symlink/bq76pl536a-q1.pdf?ts=1625840216791&ref_url=https%253A%252F%252Fwww.google.com%252F`.

[172] Analog Devices, Inc. "LTC6803-1/LTC6803-3: Multicell Battery Stack Monitor". Datasheet, 2011. Accessed on July 9, 2021. [Online]. URL: `https://www.analog.com/media/en/technical-documentation/data-sheets/680313fa.pdf`.

[173] C. Shell, J. Henderson, H. Verra, and J. Dyer. "Implementation of a wireless battery management system (WBMS)". In: *2015 IEEE International Instrumentation and Measurement Technology Conference (I2MTC) Proceedings.* Pisa, Italy, 2015, pp. 1954–1959. ISBN: 9781479961146. DOI: `10.1109/I2MTC.2015.7151581`.

[174] P. Schiepel, J. Ernsting, F. Rittweger, G. Müller, K.-R. Riemschneider, and C. Modrzynski. "Measurement data communication within vehicle battery modules by plastic light guide bodies". In: *Kraftwerk Batterie 2021.* Accessed on July 13, 2021. [Online]. URL: `https://battery-power.eu/poster2/623/`.

[175] V. Roscher, M. Schneider, P. Durdaut, N. Sassano, S. Pereguda, E. Mense, and K.-R. Riemschneider. "Synchronisation using wireless trigger-broadcast for impedance spectroscopy of battery cells". In: *2015 IEEE Sensors Applications Symposium (SAS).* Zadar, Croatia, 2015, pp. 1–6. ISBN: 9781479961177. DOI: `10.1109/SAS.2015.7133608`.

[176] T. Faika, T. Kim, and M. Khan. "An Internet of Things (IoT)-Based Network for Dispersed and Decentralized Wireless Battery Management Systems". In: *2018 IEEE Transportation Electrification Conference and Expo (ITEC).* Long Beach, CA, USA, 2018, pp. 1060–1064. ISBN: 9781538630488. DOI: `10.1109/ITEC.2018.8450161`.

[177] X. Huang, X. Sui, D.-I. Stroe, and R. Teodorescu. "A Review of Management Architectures and Balancing Strategies in Smart Batteries". In: *IECON 2019 - 45th Annual Conference of the IEEE Industrial Electronics Society.* Lisbon, Portugal, 2019, pp. 5909–5914. ISBN: 9781728148786. DOI: `10.1109/IECON.2019.8926687`.

[178] S. A. Mathew, R. Prakash, and P. C. John. "A smart wireless battery monitoring system for Electric Vehicles". In: *2012 12th International Conference on Intelligent Systems Design and Applications (ISDA).* Kochi, India, 2012, pp. 189–193. ISBN: 9781467351195. DOI: `10.1109/ISDA.2012.6416535`.

[179] C. Behrens, O. Bischoff, M. Lueders, and R. Laur. "Energy-efficient topology control for wireless sensor networks using online battery monitoring". In: *Advances in Radio Science*, vol. 5 (2007), pp. 205–208. DOI: `10.5194/ars-5-205-2007`.

[180] "IEEE Standard for Low-Rate Wireless Networks". In: *IEEE Std. 802.15.4-2020* (2020), pp. 1–800. DOI: `10.1109/IEEESTD.2020.9144691`.

[181] A. Rahman, M. Rahman, and M. Rashid. "Wireless Battery Management System of Electric Transport". In: *IEEE Transactions on Vehicular Technology*, vol. 260, 12029 (2017). DOI: `10.1088/1757-899X/260/1/012029`.

[182] T. Takeuchi and T. Terada. "Evaluation of Wireless Communication Performance in a Li-ion Battery System". In: *Journal of Automation and Control Engineering*, vol. 2, no. 1 (2014), pp. 26–30. DOI: `10.12720/joace.2.1.26-30`.

[183] J.-L. Lafrenz, P. Scheff, M. Ricco, T. Kerekes, R. L. Olsen, R. Teodorescu, and M. Liserre. "Application Layer Design for Smart Battery Pack Control with Wi-Fi® Feedback". In: *2018 IEEE Energy Conversion Congress and Exposition (ECCE).* Portland, OR, USA, 2018, pp. 5586–5590. ISBN: 9781479973125. DOI: `10.1109/ECCE.2018.8557584`.

[184] M. Schneider, S. Ilgin, N. Jegenhorst, R. Kube, S. Puttjer, K.-R. Riemschneider, and J. Vollmer. "Automotive battery monitoring by wireless cell sensors". In: *2012 IEEE International Instrumentation and Measurement Technology Conference Proceedings.* Graz, Austria, 2012, pp. 816–820. ISBN: 9781457717727. DOI: `10.1109/I2MTC.2012.6229439`.

[185] D. Alonso, O. Opalko, M. Sigle, and K. Dostert. "Towards a Wireless Battery Management System: Evaluation of Antennas and Radio Channel Measurements Inside a Battery Emulator". In: *2014 IEEE 80th Vehicular Technology Conference (VTC2014-Fall)*. Vancouver, BC, Canada, 2014, pp. 1–5. ISBN: 9781479944491. DOI: `10.1109/VTCFall.2014.6966212`.

[186] D. Alonso, O. Opalko, and K. Dostert. "Parametrization of automotive lithium-ion batteries and its influence on the wireless in-battery channel". In: *2016 10th European Conference on Antennas and Propagation (EuCAP)*. Davos, Switzerland, 2016, pp. 1–5. ISBN: 9788890701863. DOI: `10.1109/EuCAP.2016.7481269`.

[187] G. Zimmer. "Wireless Battery Management Systems Highlight Industry's Drive for Higher Reliability". White Paper. Analog Devices, Inc., 2020. Accessed on July 12, 2021. [Online]. URL: `https://www.analog.com/media/en/technical-documentation/technical-articles/S65-Wireless_BMS_EN.pdf`.

[188] R. Pell. *Maxim to demo wireless automotive BMS at CES.* Accessed on July 12, 2021. [Online]. URL: `https://www.eenewsautomotive.com/news/maxim-demo-wireless-automotive-bms-ces-0`.

[189] Texas Instruments, Corp. "CC2662R-Q1 SimpleLink™ Wireless BMS MCU". Datasheet, 2020. Accessed on July 12, 2021. [Online]. URL: `https://www.ti.com/lit/ds/symlink/cc2662r-q1.pdf?ts=1626102710103&ref_url=https%253A%252F%252Fwww.ti.com%252Fproduct%252FCC2662R-Q1`.

[190] V. R. H. Lorentz, M. M. Wenger, J. L. Grosch, M. Giegerich, M. P. M. Jank, M. Marz, and L. Frey. "Novel cost-efficient contactless distributed monitoring concept for smart battery cells". In: *2012 IEEE International Symposium on Industrial Electronics.* Hangzhou, China, 2012, pp. 1342–1347. ISBN: 9781467301596. DOI: `10.1109/ISIE.2012.6237285`.

[191] S. Galli, A. Scaglione, and Z. Wang. "For the Grid and Through the Grid: The Role of Power Line Communications in the Smart Grid". In: *Proceedings of the IEEE*, vol. 99, no. 6 (2011), pp. 998–1027. DOI: `10.1109/JPROC.2011.2109670`.

[192] A. A. Atayero, A. A. Alatishe, and Y. A. Ivanov. "Power Line Communication Technologies: Modeling and Simulation of PRIME Physical Layer". In: *World Congress on Engineering and Computer Science.* San Francisco, CA, USA, 2012, pp. 931–936. Accessed on August 25, 2021. [Online]. URL: `http://eprints.covenantuniversity.edu.ng/917/#.YSaBZ6hxdPZ`.

[193] *Signaling on Low-Voltage Electrical Installations in the Frequency Range 3 kHz-148.5 kHz,* CENELEC Std. EN 50065-1, 1992.

[194] *PoweRline Intelligent Metering Evolution (PRIME).* Accessed on July 15, 2021. [Online]. URL: `https://www.prime-alliance.org/`.

[195] *G3-PLC Alliance.* Accessed on July 15, 2021. [Online]. URL: `https://www.g3-plc.com/home/`.

[196] *G.9960: Unified high-speed wireline-based home networking transceivers - System architecture and physical layer specification,* International Telecommunication Union (ITU). Accessed on July 15, 2021. [Online]. URL: `https://www.itu.int/rec/T-REC-G.9960`.

[197] "IEEE Standard for Broadband over Power Line Networks: Medium Access Control and Physical Layer Specifications". In: *IEEE Std. 1901-2010* (2010), pp. 1–1586. DOI: `10.1109/IEEESTD.2010.5678772`.

[198] A. M. Tonello and A. Pittolo. "Considerations on narrowband and broadband power line communication for smart grids". In: *2015 IEEE International Conference on Smart Grid Communications (SmartGridComm).* Miami, FL, USA, 2015, pp. 13–18. ISBN: 9781467382892. DOI: `10.1109/SmartGridComm.2015.7436269`.

[199] M. Antoniali, M. de Piante, and A. M. Tonello. "PLC noise and channel characterization in a compact electrical car". In: *2013 IEEE 17th International Symposium on Power Line Communications and Its Applications.* Johannesburg, South Africa, 2013, pp. 29–34. ISBN: 9781467360166. DOI: `10.1109/ISPLC.2013.6525820`.

[200] P. Degauque, I. Stievano, S. Pignari, V. Degardin, F. Canavero, F. Grassi, and F. J. Canete. "Power-Line Communication: Channel Characterization and Modeling for Transportation Systems". In: *IEEE Vehicular Technology Magazine*, vol. 10, no. 2 (2015), pp. 28–37. DOI: `10.1109/MVT.2015.2411111`.

[201] J. Amanor-Boadu, A. Guiseppi-Elie, and E. Sánchez-Sinencio. "The Impact of Pulse Charging Parameters on the Life Cycle of Lithium-Ion Polymer Batteries". In: *Energies*, vol. 11, no. 8, 2162 (2018). DOI: `10.3390/en11082162`.

[202] A. Foote and O. C. Onar. "A review of high-power wireless power transfer". In: *2017 IEEE Transportation Electrification Conference and Expo (ITEC).* Chicago, IL, USA, 2017, pp. 234–240. ISBN: 9781509039531. DOI: `10.1109/ITEC.2017.7993277`.

[203] J. Wang, K. Zou, C. Chen, and L. Chen. "A high frequency battery model for current ripple analysis". In: *Twenty-Fifth Annual IEEE Applied Power Electronics Conference and Exposition (APEC).* Palm Springs, CA, USA, 2010, pp. 676–680. ISBN: 9781424447824. DOI: `10.1109/APEC.2010.5433598`.

[204] M. Reuter, S. Tenbohlen, and W. Kohler. "The Influence of Network Impedance on Conducted Disturbances Within the High-Voltage Traction Harness of Electric Vehicles". In: *IEEE Transactions on Electromagnetic Compatibility*, vol. 56, no. 1 (2014), pp. 35–43. DOI: `10.1109/APEC.2010.5433598`.

[205] F. C. Laman. "Inductive Impedance of a Spirally Wound Li/MoS_2 Cell". In: *Journal of The Electrochemical Society*, vol. 133, no. 12, 2441 (1986). DOI: `10.1149/1.2108430`.

[206] S. M. R. Islam, S.-Y. Park, and B. Balasingam. "Circuit parameters extraction algorithm for a lithium-ion battery charging system incorporated with electrochemical impedance spectroscopy". In: *2018 IEEE Applied Power Electronics Conference and Exposition (APEC).* San Antonio, TX, USA, 2018, pp. 3353–3358. ISBN: 9781538611807. DOI: `10.1109/APEC.2018.8341584`.

[207] T. F. Landinger, G. Schwarzberger, and A. Jossen. "A Novel Method for High Frequency Battery Impedance Measurements". In: *2019 IEEE International Symposium on Electromagnetic Compatibility, Signal & Power Integrity (EMC+SIPI)*. New Orleans, LA, USA, 2019, pp. 106–110. ISBN: 9781538691991. DOI: 10.1109/ISEMC.2019.8825315.

[208] Keysight Technologies, Inc. "Performing Impedance Analysis with the E5061B ENA Vector Network Analyzer". Santa Rosa, CA, USA, Application Note 5991-0213EN, 2018. Accessed on August 25, 2021. [Online]. URL: https://www.keysight.com/de/de/assets/7018-03423/application-notes/5991-0213.pdf.

[209] Samsung SDI Co., Ltd. "ICR18650-26J". Specification of Product. Yongin, South Korea, 2016.

[210] P. Korth Pereira Ferraz, R. Schmidt, D. Kober, and J. Kowal. "A high frequency model for predicting the behavior of lithium-ion batteries connected to fast switching power electronics". In: *Journal of Energy Storage*, vol. 18 (2018), pp. 40–49. DOI: 10.1016/j.est.2018.04.024.

[211] *Radio disturbance characteristics for the protection of receivers used on board vehicles, boats and on devices - Limits and methods of measurement,* Std. IEC/DIN-EN 55025/ CISPR 25, Brussels, Belgium, 2008.

[212] *Road vehicles - Component test methods for electrical disturbances from narrowband radiated electromagnetic energy - Part 2: Absorber-lined shielded enclosure,* ISO 11452-2:2019-01, 2019.

[213] HomePlug Powerline Alliance, Inc. "Home Plug Green PHY. The Standard For In-Home Smart Grid Powerline Communications", 2010. Accessed on July 27, 2021. [Online]. URL: https://content.codico.com/fileadmin/media/download/datasheets/powerline-communication/plc-homeplug-green-phy/homeplug_green_phy_whitepaper.pdf.

[214] Z. Sheng, D. Tian, V. C. M. Leung, and G. Bansal. "Delay Analysis and Time-Critical Protocol Design for In-Vehicle Power Line Communication Systems". In: *IEEE Transactions on Vehicular Technology*, vol. 67, no. 1 (2018), pp. 3–16. DOI: 10.1109/TVT.2017.2770182.

[215] Yamar Electronics, Ltd. Power line communication transceivers ICs. Accessed on July 15, 2021. [Online]. URL: https://yamar.com/.

[216] Y. Maryanka and O. Amrani. "DC powerline communications for management of high voltage battery packs", 2013. Accessed on July 28, 2021. [Online]. URL: https://yamar.com/articles/Battery-monitoring-system-with-powerline-communication.pdf.

[217] T. A. Vincent and J. Marco. "Development of Smart Battery Cells through Sensor Instrumentation and In-Vehicle Power Line Communication". In: *2020 IEEE International Symposium on Power Line Communications and its Applications (ISPLC)*. Málaga, Spain, 2020, pp. 1–5. ISBN: 9781728148168. DOI: 10.1109/ISPLC48789.2020.9115411.

[218] A. Stepanov, M. Vorobyov, and I. Galkin. "Battery monitoring using high frequency impedance modulation through series power line". In: *IECON 2012 - 38th Annual Conference on IEEE*

Industrial Electronics Society. Montreal, QC, Canada, 2012, pp. 5148–5152. ISBN: 9781467324212. DOI: `10.1109/IECON.2012.6389553`.

[219] K. Cermak and M. Bartl. "Decentralized Battery Management System". In: *Proceedings of the 2014 15th International Scientific Conference on Electric Power Engineering (EPE).* Brno-Bystrc, Czech Republic, 2014, pp. 599–603. ISBN: 9781479938070. DOI: `10.1109/EPE.2014.6839509`.

[220] N. Harting, N. Wolff, F. Röder, and U. Krewer. "Nonlinear Frequency Response Analysis (NFRA) of Lithium-Ion Batteries". In: *Electrochimica Acta*, vol. 248 (2017), pp. 133–139. DOI: `10.1016/j.electacta.2017.04.037`.

[221] A. Pake Talei, W. A. Pribyl, and G. Hofer. "Wide Frequency Range Impedance Measurement of a Li- ion Prismatic Cell for Power Line Communication Technique". In: *2019 16th International Conference on Synthesis, Modeling, Analysis and Simulation Methods and Applications to Circuit Design (SMACD).* Lausanne, Switzerland, 2019, pp. 109–112. ISBN: 9781728112015. DOI: `10.1109/SMACD.2019.8795281`.

[222] Infineon Technologies AG. "TLE9250V: Z8F57889424". Application Note, 2020. Accessed on August 2, 2021. [Online]. URL: `https://www.infineon.com/dgdl/Infineon-Z8F57889424_TLE9250V-ApplicationNotes-v01_40-EN.pdf?fileId=5546d4625 debb399015e14c1ebda5987`.

[223] Texas Instruments, Corp. "Designing EMI/EMC Safe Battery Pack". Application Report, 2016. Accessed on August 2, 2021. [Online]. URL: `https://www.ti.com/lit/an/slua776/slua776.pdf?ts=1627870582887&ref_url=https%253A%252F%252Fwww.google.com%252F`.

[224] I. Ouannes, P. Nickel, J. Bernius, and K. Dostert. "Physical Layer Performance Analysis of Power Line Communication (PLC) applied for Cell-Wise Monitoring of Automotive Lithium-Ion Batteries". In: *OFDM 2014; 18th International OFDM Workshop 2014 (InOWo'14).* Essen, Germany, 2014, pp. 1–8.

[225] E. Zeidler. *Springer-Taschenbuch der Mathematik.* Wiesbaden: Springer Fachmedien Wiesbaden, 2013. ISBN: 9783835101234.

Appendix

Rectangular online EIS Excitation for higher Signal-to-Noise Ratio

In this appendix, the higher SNR of active rectangular EIS excitation compared to sinusoidal excitation is derived. Based on Figure 13a, the online EIS measurement setup can be redrawn as large signal equivalent electrical circuit using the Thevenin equivalent circuit model of the battery and the varying load impedance of the switching transistor R_L while neglecting the current shunt resistor as shown in Figure A.1a. The resulting small signal current excitation drawn from the cell can be modeled according to Figure A.1b. By dynamically changing the load resistor R_L, an alternating excitation current $i(t)$ is generated, which causes an additional AC voltage drop across the overall cell impedance Z_{bat}. The two different excitation current waveforms – sinusoidal and rectangular – are illustrated in Figure A.2a and can be mathematically formulated as

$$i_{sin}(t) = \hat{i} \left[\sin \left(2\pi \frac{1}{T} t \right) + 1 \right] , \tag{A.1}$$

$$i_{rect}(t) = 2 \cdot \hat{i} \sum_{n=-\infty}^{\infty} \text{rect} \left(\frac{t - nT - T/4}{T/2} \right) , \tag{A.2}$$

with the time period T and the amplitude $\hat{i}$ as indicated in Figure A.2. The DC offset of the signal waveforms is due to the online excitation principle, which performs EIS only in discharge mode. The average electric charge $\bar{q}$ drawn from the battery can be calculated for both excitation waveforms by

$$\bar{q}_{sin} = \int_0^T i_{sin}(t) dt = \left[\hat{i} \cdot t - \frac{T}{2\pi} \cos \left(2\pi \frac{1}{T} t \right) \right]_0^T = \hat{i} \cdot T , \tag{A.3}$$

$$\bar{q}_{rect} = \int_0^T i_{rect}(t) dt = [2 \cdot \hat{i} \cdot t]_0^{T/2} = \hat{i} \cdot T = \bar{q}_{sin} . \tag{A.4}$$
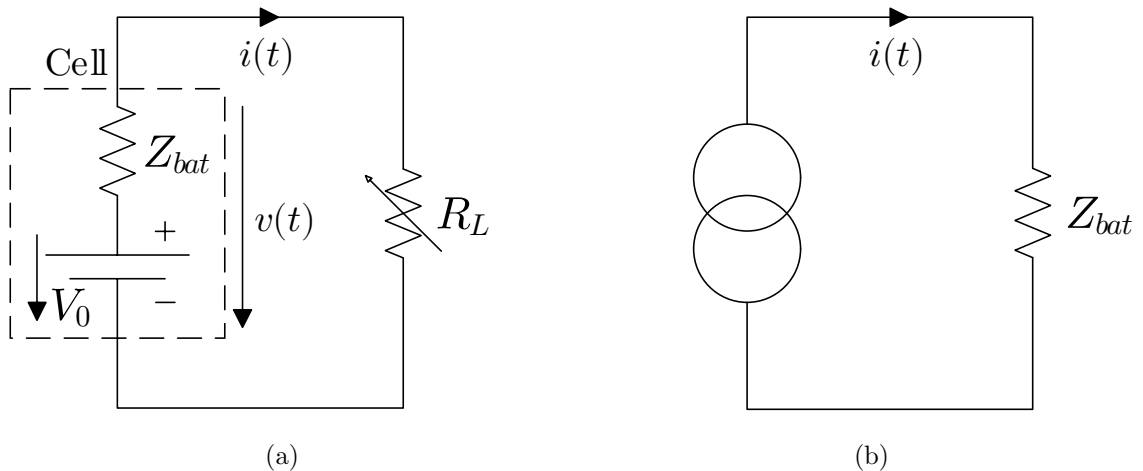
Figure A.1: (a) Online EIS excitation principle using a varying load impedance Z_L. The dashed box marks the Thevenin equivalent circuit of the battery cell with the equilibrium voltage V_0 and the overall cell impedance Z_{bat}. (b) Small signal EEC using a current source and Z_{bat}.
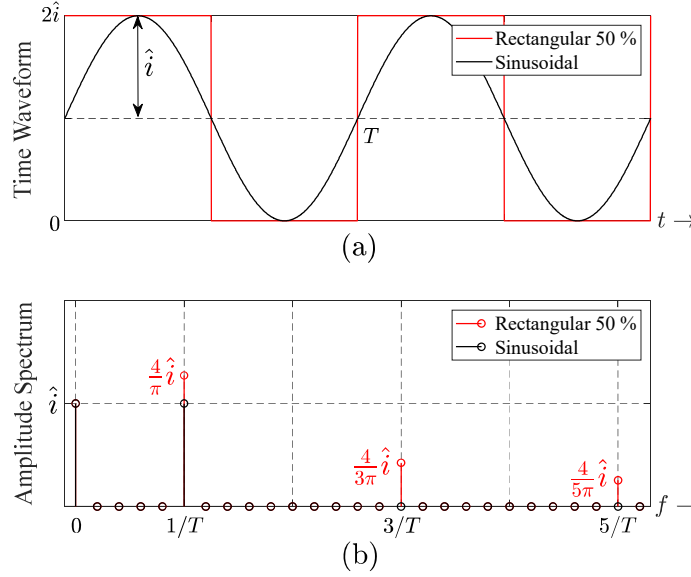
Figure A.2: Time domain (a) and frequency domain view (b) of sinusoidal and rectangular waveforms with same peak-to-peak current value and same average current drawn from the battery, according to the schematic of Figure A.1a.

Following Eqs. (A.3) and (A.4), the drawn charge is identical for both excitations with same peak-to-peak current values. The ratio of consumed energies of both excitation waveforms is

$$\frac{E_{rect}}{E_{sin}} = \frac{\int_0^T v(t) \cdot i_{rect}(t)dt}{\int_0^T v(t) \cdot i_{sin}(t)dt} \cong \frac{\int_0^T V_0 \cdot i_{rect}(t)dt}{\int_0^T V_0 \cdot i_{sin}(t)dt} = \frac{V \cdot \bar{q}_{rect}}{V \cdot \bar{q}_{sin}} = 1 \tag{A.5}$$

while neglecting the small AC voltage across Z_{bat} (< 10 mV, see Section 3.2.1) that is superimposed to V_0.

The Fourier series representations of both sinusoidal and rectangular waveforms are listed in Table A.1 and are illustrated in Figure A.2b. Both the amplitude spectrum and the values of the Fourier series coefficients reveal that the fundamental of the rectangular waveform is $\frac{4}{\pi} \triangleq 2.1$ dB higher than the fundamental of the sinusoidal waveform, although the same amount of energy respectively charge is drawn from the battery in both cases. In case of superimposed noise with equal power spectral density, the SNR during rectangular current excitation is therefore 2.1 dB higher than in the case of conventional sinusoidal excitation.

Table A.1: Fourier series of sinusoidal and rectangular current waveforms.

Waveform	Fourier series representation [225]	Single tones (amplitude, frequency)
$i_{sin}(t)$	$\hat{i} + \hat{i} \cdot \sin\left(2\pi\frac{1}{T}t\right)$	$(\hat{i}, f = 0)$, $(\hat{i}, f = \frac{1}{T})$
$i_{rect}(t)$	$\hat{i} + \frac{4}{\pi}\hat{i} \cdot \sum_{n=1,3,5,...}^{\infty} \frac{1}{n}\sin(n \cdot 2\pi\frac{1}{T}t)$	$(\hat{i}, f = 0)$, $(\frac{4}{\pi}\hat{i}, f = \frac{1}{T})$, $(\frac{4}{3\pi}\hat{i}, f = \frac{3}{T})$,...